UNIVERSITY OF SOUTHAMPTON

FACULTY OF ENGINEERING AND THE ENVIROMENT

ASTRONAUTICS RESEARCH GROUP

Development and Validation of Microvibration Models for a Satellite Reaction Wheel Assembly

By

Zhe Zhang

Thesis for the degree of Doctor of Philosophy

January 2013

UNIVERSITY OF SOUTHAMPTON

Faculty of Engineering and the Environment

Doctor of Philosophy

Development and Validation of Microvibration Models for a Satellite Reaction Wheel Assembly

by Zhe Zhang

ABSTRACT

Microvibrations are a critical concern on satellites equipped with instruments with high stability requirements. Amongst many sources of microvibration onboard, reaction wheel and momentum wheel assemblies are often considered the most significant. This thesis presents the development and validation of microvibration models for a cantilever configured wheel assembly designed with a soft-suspension system. Wheel assembly-induced microvibrations under hard-mounted and coupled boundary conditions are studied. In particular, the wheel assembly semi-analytical microvibration model in a hard-mounted boundary condition is developed with harmonic excitations and the traditionally ignored broadband noise excitations are included. Some peculiar dynamics such as nonlinearity in the motor and high damping of the soft-suspension system are observed from the hard-mounted measurements conducted on a bespoke dynamometer. Modeling strategies for these peculiar dynamics are developed and implemented in the wheel assembly microvibration modeling. This includes a systematic approach to extract stiffness and damping values of the suspension system, considering nonlinearity and high damping from measurements. The microvibrations produced by the wheel assembly in a coupled boundary condition are studied using a seismic mass to support the wheel assembly. A coupled microvibration measurement system, which allows the wheel assembly interface loads to be reconstructed by measuring the response accelerations on the seismic mass, is designed, built and validated. In addition, the wheel assembly driving point static and dynamic accelerance are measured and analytical expressions of the driving point dynamic accelerance are derived. The coupled microvibrations are predicted with wheel assembly static accelerance, dynamic accelerance and the standard method (i.e. no wheel accelerance). The predicted results have shown that the method developed in this thesis which uses the wheel assembly dynamic accelerance accurately simulates the microvibrations observed in practice.

格物，致知，诚意，正心，修身，齐家，治国，平天下

–《礼记·大学》

TABLE OF CONTENTS

LIST OF FIGURES

LIST OF TABLES

DECLARATION OF AUTHORSHIP

I, Zhe Zhang

declare that the thesis entitled

Development and Validation of Microvibration Models for a Satellite Reaction Wheel Assembly

and the work presented in the thesis are both my own, and have been generated by me as the result of my own original research. I confirm that:

- this work was done wholly or mainly while in candidature for a research degree at this University;
- where any part of this thesis has previously been submitted for a degree or any other qualification at this University or any other institution, this has been clearly stated;
- where I have consulted the published work of others, this is always clearly attributed;
- where I have quoted from the work of others, the source is always given. With the exception of such quotations, this thesis is entirely my own work;
- I have acknowledged all main sources of help;
- where the thesis is based on work done by myself jointly with others, I have made clear exactly what was done by others and what I have contributed myself;
- parts of this work have been published as:

Journal Papers

- Zhang, Z., Aglietti, G. S., and Zhou, W. *Microvibrations Induced by a Cantilevered Wheel Assembly with a Soft-Suspension System*, AIAA Journal, Vol. 49, No. 5, 2011, pp. 1067-1079.

- Zhou, W., Aglietti, G. S., and Zhang, Z. *Modelling and Testing of a Soft Suspension Design for a Reaction/momentum Wheel Assembly*, Journal of Sound and Vibration, Vol. 330, No. 18-19, 2011, pp. 4596-4610.

- Zhang, Z., Aglietti, G. S., and Ren, W. *Coupled Microvibration Analysis of a Reaction Wheel Assembly including Gyroscopic Effects in its Accelerance*, accepted by Journal of Sound and Vibration in December 2012.

Conference Papers

- Zhang, Z., Zhou, W., Aglietti, G. S., and Bianchi, G. *Modelling Microvibrations emitted by Satellites Reaction Wheel Assemblies*, The 10th International Conference on Recent Advances in Structural Dynamics (RASD), Southampton, UK, 2010.

- Zhang, Z., Ren, W., and Aglietti, G. S. *Microvibration Modeling, Validation and Coupled Analysis of a Reaction Wheel in Satellite*, The 12th European Conference on Spacecraft Structures, Materials & Environmental Testing (ECSSMET), Noordwijk, the Netherlands, 2012.

- Zhang, Z., Aglietti, G. S., and Le Page, B. H. *Microvibration Modelling and Testing of a Satellite Reaction Wheel Assembly*, The 10th International Conference on Vibrations in Rotating Machinery (VIRM), London, UK, 2012.

- Zhang, Z., Aglietti, G. S., and Ren, W. *Microvibration Model Development and Validation of a Cantilevered Reaction Wheel Assembly*, The 2nd International Conference on Vibration, Structural Engineering and Measurement (ICVSEM), Shanghai, China, 2012.

- Remedia, M., Aglietti, G. S., Zhang, Z., Le Page, B. H., and Richardson, G. *Modeling Methodologies for Microvibration-related Analysis of Spacecraft Structures*, The 12th European Conference on Spacecraft Structures, Materials & Environmental Testing (ECSSMET), Noordwijk, the Netherlands, 2012.

- Remedia, M., Aglietti, G. S., Zhang, Z., Le Page, B. H., and Richardson, G. *A General Methodology to Study the Transmission of Micro-vibrations in Satellites*, The 63rd International Astronautical Congress (IAC), Naples, Italy, 2012.

Internal Technical Report

- Zhang, Z., Remedia, M., Aglietti, G. S., Le Page, B. H., and Richardson, G. *Methodology for Analysis of Structure-Borne Micro-Vibration*. Internal Report for ESA and SSTL joint project, ITT No. AO/1-6135/09/NL/NA, 2011.

Signed:

Date:

ACKNOWLEGEMENTS

I would like to thank Satellite Services B.V. (SSBV) Space and Ground Systems UK (formerly Satellite Services Ltd, SSL) for their generosity in supplying the wheel assembly during my four years of research at the University of Southampton. I would also like to thank Surrey Satellite Technology Ltd (SSTL) for the partial funding of my Ph.D. under the contract with European Satellite Agency (ESA) for the project: ITT No. AO/1-6135/09/NL/NA (Methodology for Analysis of Structure-Borne Micro-Vibration). The majority of the work presented in this thesis has served as an input to this ESA project.

I also want to express my gratitude to the people who have supported me on this journey. Firstly, I would like to thank my supervisor Professor Guglielmo S. Aglietti for his guidance and help, not only in my research but also in life. His enthusiasm and dedication to his work have set me an exceptional example to follow which I hope to emulate in my life. In addition, I would like to thank Dr. Nicholas K. Lincoln for helping me operate the wheel assembly, Dr. Weiyong Zhou and Professor Weijia Ren for their advice on the theory and experimentation, Mr. Marcello Remedia for his help in MATLAB programming and Dr. Angelo Grubišić for checking my written English. Finally, I would like to thank my family and my girlfriend Lan Luan for their constant love over these years, despite the distance which separates us. Without them I would have never finished this thesis.

NOMENCLATUE

Abbreviations

AOCS	attitude and orbit control system
AS	amplitude spectrum
BW	backward whirl
CoM	center of mass
CRMS	cumulative root mean square
CSD	cross-spectral density
DC	direct current
DoF	degree of freedom
ECSS	European Cooperation on Space Standardization
EoM	equation of motion
Eq.	equation
ESA	European Space Agency
FE	finite element
FFT	fast Fourier transformation
FW	forward whirl
MWA	momentum wheel assembly
OPD	optical path difference
rpm	revolutions per minute
PSD	power spectral density
RBE	rigid body element
RMS	root mean square
RWA	reaction wheel assembly
SEA	statistical energy analysis
SMVMS	seismic mass vibration measurement system
SSBV	Satellite Service Besloten Vennootschap
SSTL	Surry Satellite Technology Limited
w.r.t.	with respect to
WA	wheel assembly

Spacecraft and Instrumentation

ARTEMIS	the Advanced Relay and TEchnology MISsion
FIRST	Far Infra-Red and Submillimeter Telescope
GOCE	Gravity field and steady-state Ocean Circulation Explorer
GOES	Geostationary Operational Environmental Satellites
HST	Hubble Space Telescope
ISS	International Space Station
JWST	James Webb Space Telescope
LST	Large Space Telescope
MTG	Meteosat Third Generation
OICETS	Optical Inter-orbit Communications Engineering Test Satellite
PAX	PSDE (Payload and Spacecraft Demonstration and Experimentation program) Accelerometer Experiment
SDO	Solar Dynamics Observatory
SIM	Space Interferometry Mission
SOHO	SOlar and Heliospheric Observatory
SPOT	Système Pour l'Observation de la Terre
STS	Space Transportation System
TPF	Terrestrial Planet Finder

Symbols

a = acceleration

a, b, c = WA first rotation frame

A = accelerance

$\boldsymbol{A}$ = accelerance matrix

c = damping

C = seismic mass CoM

C_i = harmonic amplitude coefficient

$\boldsymbol{C}$ = damping matrix

d = shaft length

d_0 = distance from mass imbalance to seismic mass CoM

d_i = distance from accelerometer to seismic mass CoM

d_{ii} = distance between any two accelerometers

f = frequency

$\boldsymbol{f}$ = forcing vector

F = arbitrary force

$\boldsymbol{G}$ = gyroscopic matrix

$\boldsymbol{G}_f$ = “load filter” between WA hard-mounted and coupled microvibrations

h = axial distance from dynamic mass imbalance to flywheel CoM/harmonic number

i, j = imaginary unit

I = moment of inertia

$\boldsymbol{I}$ = inertia tensor/unit matrix

k = stiffness

$\boldsymbol{K}$ = stiffness matrix

l = moment arm/axial distance from suspension system to seismic mass CoM

L = Lagrangian

m = general mass/mass imbalance

M = mass/moment

$\boldsymbol{M}$ = mass matrix

n = number of harmonics

N = total number of data in a signal

O = CoM of specific part as mentioned in thesis/coordinate origin

P = power in a signal

$\boldsymbol{q}$ = complex coordinates

Q = work done

$\boldsymbol{Q}$ = forcing vector

r = flywheel displacement in complex coordinates/general displacement/radius/root mean square value

R = correlation function

$\boldsymbol{R}$ = coordinate system transformation matrix

s = Laplace transformation sign, a complex number

S = power spectral density

t = time

T = kinetic energy

$\boldsymbol{u}$ = displacement vector of flywheel CoM

U = potential energy

v = velocity

$\boldsymbol{V}$ = translational velocity vector of flywheel CoM

W = broadband noise excitation

x, y, z = displacement in WA body frame/general displacement

x', y', z' = WA second rotation frame

$\boldsymbol{x}$ = displacement vector

X = displacement in Laplace transform

X, Y, Z = displacement in WA inertial frame

Y = mobility

μ = mean value of a signal

α = receptance

ζ = damping ratio

θ, φ, ψ = rotations about three WA orthogonal axes x, y and z respectively

λ = complex frequency

ξ = WA generalized coordinates

σ = decay rate/variance of a signal

τ = time step

Φ = element in spectral density matrix

ϕ = flywheel rotations in complex coordinates

$\mathbf{\Phi}$ = spectral density matrix

ω = general angular velocity

ω_0 = natural frequency

$\boldsymbol{\omega}$ = angular velocity vector

Ω = constant flywheel spin/angular speed

Subscripts

a = accelerometer

b = blocked

c = seismic mass/coupled

d, s = dynamic and static mass imbalance

nq = Nyquist frequency

p = hard-mounted microvibration measurement platform coordinate system

r = torsional spring and dashpot/rotational DoF

R = total in rotational DoF

s = WA-seismic mass coupled system/structure

ss = flywheel-base system

t = linear spring and dashpot/translational DoF

w = WA

w_t, w_r = WA translational and rotational DoF respectively

x, y, z = in the three translational DoF respectively

x_w, y_w, z_w = flywheel x, y and z DoF respectively

y_wz_w, x_wz_w = flywheel yz-plane and xz-plane respectively

θ, φ, ψ = in the three rotational DoF respectively

Superscripts

at = flywheel axial translational DoF

H = Hermitian

rr = radial rotational DoF

rt = radial transnational DoF

T = transpose

1. Introduction

1.1. Satellite Stability

Satellite microvibrations and related issues have interested satellite engineers and researchers for more than four decades. In this context, we refer to microvibrations as low level mechanical disturbances which affect payload performance. Microvibrations are mostly a concern for optical/imaging missions such as space astronomy and earth observation, where high levels of pointing accuracy are required. However microvibration issues are not limited to optical instruments. Modern communication satellites have also received attention regarding onboard microvibrations for inter-space/space-ground communications; OICETS [1-3] is a typical example. Other missions, such as the in-orbit scientific research satellite GOCE [4, 5], or microgravity experiments on ISS Columbus module [6] and other spacelab [7], etc., all pose challenging environments for microvibration control and mitigation. It has to be noted that at times, microvibration issues are also referred to as microgravity issues when the focus is on the disturbance of the microgravity environment in particular.

One clear example to illustrate the effects of satellite microvibrations is the image quality of onboard telescopes or cameras where microvibrations may result in geometric distortions in the image. In Figure 1-1 such distortions can be observed as zigzag

Figure 1-1 Effects of microvibrations on geometric distortions [8]

patterns on geometrically straight features such as roads.

Figure 1-2 presents a computed star image output on the detector of the European Space Agency (ESA)'s FIRST telescope model on SPOT 4 with and without microvibrations from Reaction Wheel Assemblies (RWAs) and cryocoolers [9]. It is clear that microvibration is a significant cause of distortion of the initially diffraction-limited star image.

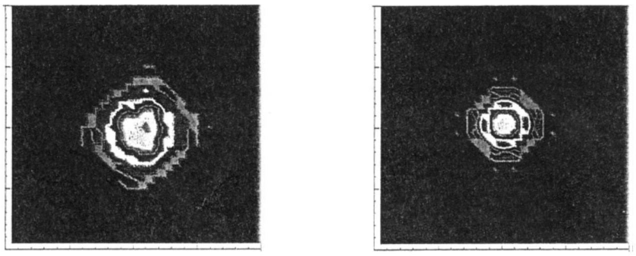

a) With microvibrations b) Without microvibrations

Figure 1-2 Effects of microvibrations on a telescope star image quality [9]

Microvibrations are usually in the range of micro-g's (μg) typically occurring at frequencies from a few Hz up to 1 kHz [10]. In some extreme cases microvibrations below 1 to 2 Hz are also of concern [11]. Generally, microvibrations cannot be controlled or reduced by the Attitude and Orbit Control System (AOCS) of satellites because they usually involve the flexible modes of the satellite structure (rather than its rigid body motion) and because the satellite AOCS usually has an upper controllable frequency limit of a few Hz, whereas microvibrations generally occur at higher frequencies [12].

The importance of microvibration in satellite engineering, and in particular the desire to develop methods to deal effectively with these phenomena has been confirmed in 2010 by the ESA, who commissioned a study entitled: *Methodology for Analysis of Structure-Borne Micro-Vibration*; and part of the research described in this thesis has contributed to this study (see [8] for more detail). In 2012 a handbook was produced by the ESA European Cooperation on Space Standardization (ECSS) which included a chapter on satellite microvibrations and in particular the analysis methodologies (see [13] for more detail). However this area still demands further development.

1.2. Microvibrations on Satellite

Onboard satellites there is a range of more frequently used equipment and/or events which can generate low level mechanical vibrations, i.e. microvibration sources. Amongst them are high speed rotation devices, e.g. RWAs and Momentum Wheel Assemblies (MWAs) [14], cryocoolers [15-17] and pointing mechanisms [18, 19] which are generally the most important sources. However other mechanisms such as tape recorders [20], thrusters, switches [5], filter wheels [21] and some onboard events such as solar-array thermal elastic bending [22], fuel-sloshing [23-25], thermal snaps in structure and at joints [26], cracks in thermal insulation blankets [27, 28] and foil [29], etc., are also microvibration sources. The microvibrations caused by these sources are transmitted through the satellite structure and excite the structure or elements of the instrument, influencing its performance. The items of interest excited by the microvibrations are often termed as receivers [30]. The dynamics of the microvibration sources will also couple with those of the satellite structure, making the microvibration dynamics yet more complicated.

The propagation of microvibrations can be presented schematically as in Figure 1-3. Note that in some cases the vibrations can be transmitted by some payload elements to the satellite structure, thus in this case the payload is the source and also the vibration receiver [31].

Figure 1-3 Propagation of microvibrations on satellites

Research on satellite microvibrations and its control started approximately in the early 1970's driven mainly by the HST project (previously known as LST) [32-34]. HST had a pointing stability requirement of 0.02 micro-radians, and a significant amount of work was performed to improve its optical performance during its design and more than 22 years' life in orbit. For example, the solar arrays and driving mechanisms of HST were replaced in 1993 (STS-61) and 2002 (STS-109) primarily to reduce the disturbances generated by their thermal bending and drive mechanisms. Other satellites in the early

90’ such as the communication satellite OLYMPUS [35-39] and the SPOT earth observation satellite family [40, 41] also have been affected by microvibrations. For example, an accelerometer package (PAX) was installed on OLYMPUS to monitor the satellite micro-dynamic performance produced by various mechanisms when the satellite was on orbit.

Since the late 90’s microvibration analysis has become increasingly important in the design of satellites carrying instruments with high stability requirements, ARTEMIS [42-46], SPOT 4 [47-49], GOES [50] and SOHO [51] were just a few typical examples. Microvibration research during that time was systematically developed and the field gradually became more mature. Research techniques were largely based on the satellite system level microvibration tests on the ground and analytical studies of satellite structure dynamics. For example, satellite structure models were created using Finite Element (FE) and Statistical Energy Analysis (SEA) methods for ARTEMIS microvibration analysis and the simulated results were validated from on-ground satellite microvibration tests. These techniques at the present time have been accepted as the standard approach in satellite microvibration analysis and significant effort is still spent to improve them analytically and experimentally, for example in [52-54].

Figure 1-4 shows the increased angular resolution (sharpness of images) of optical payloads on some typical earth observation satellites launched between 1970 to 2010 [55]. Meanwhile, other research [56] shows that the angular resolution of earth observation satellites improves roughly 10-times every decade.

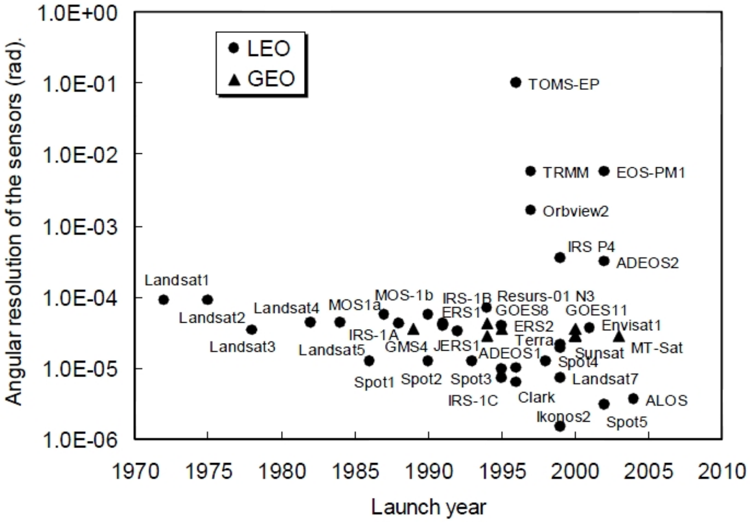

Figure 1-4 Angular resolution of earth observation satellite (1970 to 2010) [55]

At the present time, satellites' telescopes and cameras angular resolutions have been significantly improved and scientific instruments have become more complex, however they are also more vibration-sensitive. Satellite microvibration analysis and control is now a predefined step in almost all modern high precision satellite design, in many cases they are critical to the mission success. For example GOCE [4, 5], HINODE (SOLAR-B) [57-59], SDO [18, 60, 61], and future satellites such as SOLAR-C [62] in Japan, JWST [63, 64] in the United States, MTG [65] in Europe and recently canceled TPF [66, 67] and SIM project [68-70].

Amongst them, SOLAR-B has a pointing stability requirement of 0.17 micro-radians over 10 seconds. SOLAR-C will have a pointing stability requirement of 0.07 micro-radians over 10 seconds. The JWST fine pointing requirement is 0.02 micro-radians (similar to HST). SIM and TPF impose even more challenging requirements as for these missions the payloads are interferometers. For SIM the allowable Optical Path Difference (OPD) between the 2 collectors is approximately 10 nm. For TFP the OPD requirement is tighter and there are 4 collectors. GOCE's main instrument, the gradiometer, on the other hand is particularly sensitive to micro-disturbance events rather than the onboard mechanism-generated microvibrations.

Microvibration analysis of these satellites takes advantages of modern computer technologies, in many cases using the "integrated modeling and simulation" which is a technique capable of performing the complete satellite microvibration analysis (or sometimes called jitter analysis, pointing error analysis) in one-off computation. Typical examples such as [11, 71-75], where all potential microvibration sources and other subsystems such as AOCS, pointing or guidance control, thermal control, payload vibration isolation control system, sensor noises, etc., even external disturbances such as solar radiation pressure are all integrated into one framework and analyzed by computer (typically in the time domain). In this manner, the payload performance can be simulated more closely to reality, i.e. the in orbit working condition. This analysis technique is considered to be the mainstream for future large space projects. A typical example of satellite microvibration integrated modeling analysis process is shown in Figure 1-5. Note that the RWA-induced microvibrations are particularly important in this process.

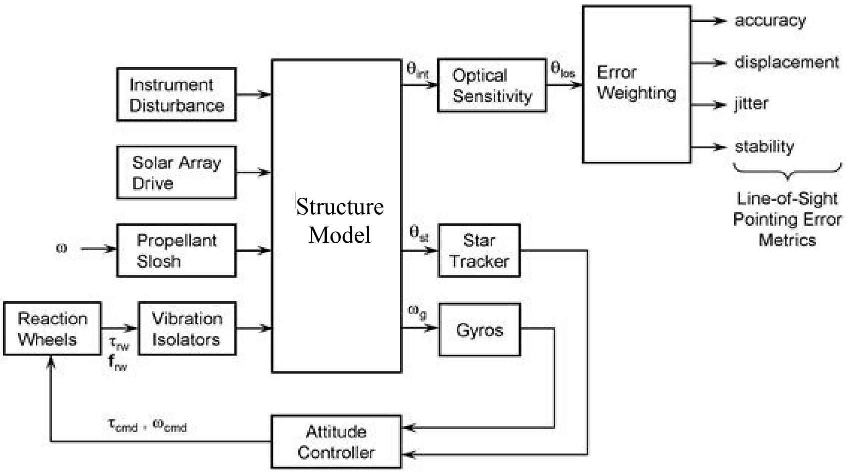

Figure 1-5 Typical example of satellite microvibration integrated modeling process (here also called the pointing error analysis) [76]

Microvibration research in satellite design has become exceptionally important and this trend is expected to continue. During all analysis, microvibration source characterization is usually the first step in the analysis approach. The high speed rotation devices, in particular the Wheel Assemblies (WAs), including RWAs and MWAs, are considered one of the most important microvibration sources and thus far have received the majority of attention [77]. Figure 1-6 shows two typical WAs with mid-span configuration and cantilever configuration respectively.

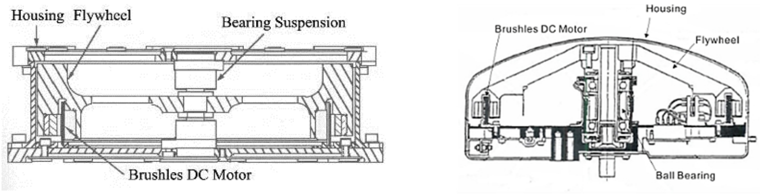

a) Mid-span configuration b) Cantilever configuration

Figure 1-6 Typical RWA and MWA configurations

A large number of projects have been conducted on WA-induced microvibrations in almost every aspect and also their influences to the satellite payload performance analysis. However, the development of higher performance payload (thus stringent structure stability) pushes further WA designs toward low microvibration emissions and improvements in modeling capabilities to faithfully simulate the dynamics of the physical hardware.

1.3. Open Issues in the State of the Art

Although WA dynamics have been studied for a considerable time, there are still open issues which are briefly introduced below and will be further discussed in the relevant chapters of this thesis.

Firstly, all the models the author encountered during his survey of the state of the art described mid-span configurations (see Figure 1-6 a) for example) whereas the dynamic analysis of the cantilever configured WAs (see Figure 1-6 b) for example) seem to have been neglected or at least not published. Although the conceptual procedure to model mid-span or cantilever configured WAs is the same, the cantilevered configuration has some peculiarities that produce different dynamic characteristics which cannot be observed in a mid-span configuration. In addition, most of the practical models consider a flywheel supported by a suspension system rigid enough to push the WA resonances beyond the rotation frequency (typically up to 5000 rpm or 80 Hz). For various reasons it is possible to design WAs which includes a soft-suspension system, but it was not possible to find publications discussing satellite WA implementing this type of design.

Secondly, the vibrations produced by a WA when spinning are dominated by the flywheel mass imbalances and this can be accurately modeled from first principles; higher harmonics can be modeled as multiples of fundamental harmonics and are also well established in the literature. However, the functioning WA also produces broadband (noise) excitations and they have often been ignored in the previous model developments. Meanwhile, the only broadband excitation modeling method available in the literature was not well developed with limited application. The desire to improve the model accuracy now requires broadband frequencies and lower amplitude vibrations to also be accurately modeled and implemented in the overall WA microvibration model.

Finally, most models simply considered the vibrations emitted by a WA rigidly connected to the ground (this type of boundary condition is also called hard-mounted or blocked, and corresponds to an infinitely rigid support), and then apply these loads to the supporting structure. In reality when a source is coupled with a supporting structure, which clearly cannot be infinitely rigid, the loads transmitted are different from those produced by the source hard-mounted. This is due to the dynamic coupling between the structure of the source and that of the supporting structure, and to achieve accurate simulations this effect has to be included. In practice, the effect of the coupling can be modeled using a parameter termed accelerance (or its inverse, dynamic mass), which is the ratio between the loads applied at the mounting point of the equipment and the accelerations there. The main issues here are the practical difficulties in estimating this parameter and the fact that the gyroscopic effects have not been included with any reasonable degree of accuracy in the models developed within the literature.

To clarify the terminology, “rigid-suspended” and “soft-suspended” refer to the WA internal suspension system, i.e. the configuration that links the flywheel to the rest of the mechanism. In this thesis, rigid-suspension refers to the conventional rigid (ball) bearing system; soft-suspension refers to the newly designed web-spring flexible suspension system. The terminology “hard-mounted” and “coupled” refer to the boundary configuration that WA base connects to the external structure. In particular, a hard-mounted boundary condition refers to the WA rigidly connects to the structure, i.e. no motion between the two bodies. A coupled boundary condition refers to the WA connection to a movable structure.

1.4. Objectives of this Work

The main objective of this thesis is to provide a methodology to model the microvibrations produced by a WA which somehow addresses the issues which still remain open in the current state of the art, and hence delivers models which better correlate with the dynamic behavior of the real hardware. In particular, the focus of this thesis is on the microvibrations generated from a cantilever configured WA that designed with a soft-suspension system, however the methodologies developed here from modeling and testing can also be applied to the mid-span configured WAs and with rigid supports (see [52, 78] for example).

In order to achieve the goal, the research methodology followed two stages:

i. Microvibration source characterization (i.e. analysis at WA subsystem level); this part of the work involves modeling and testing of the WA in a hard-mounted boundary condition and has been published by the author in [79-83].

ii. Source-structure coupled microvibration analysis (i.e. analysis at WA-structure system level); in this part of the work the WA is mounted on a rigid seismic mass, which is used as the supporting structure. Coupled microvibrations induced by the WA are measured and predicted with the consideration of their driving point accelerance. This work has been published by the author in [79-82, 84].

i) The first task is thus to derive a mathematical model for the microvibrations emitted by the cantilever configured WA. With respect to (w.r.t.) previous designs, here we considered a WA with a soft-suspension system which has the advantage of producing less vibration at high frequencies. A further improvement w.r.t. previous mathematical model is that in addition to the main harmonics produced by flywheel and motor-bearing system, here we also include the broadband excitations produced in the WA (i.e. caused by internal components in the motor such as raceways, balls and cages, etc.).

To validate the mathematical model of the WA and extract some of the model parameters, rather than using a commercially available dynamometric platform (e.g. a Kistler table), we have developed a performance-competitive measurement platform which uses simpler components. Due to the WA design and the consequent dynamic characteristics such as nonlinearity in the motor and high damping of the soft-suspension system, a new method is developed to extract the model parameters (e.g. stiffness and damping) as a systematic procedure for WA microvibration modeling.

ii) The goal of this part of the work is to improve the existing coupled microvibration analysis method described in the literature in order to improve the accuracy of the system level WA-structure microvibration simulation. The work includes the development of a coupled microvibration measurement system using common accelerometers rather than the complex load cell used in the literature. A WA-seismic mass coupled system is designed and its dynamic model is derived.

This part of the work also focuses on the development of methods to model the WA driving point accelerance and their implementation in the coupled microvibration predictions. In particular, several modeling cases of the WA accelerance (include those available in the literature) are considered and are compared with each other to reveal the advantages of the method developed in this thesis.

1.5. Thesis Layout

The overall structure of the thesis is organized into eight chapters which are briefly outlined in this section. The flow chart in Figure 1-7 on the next page summarizes the work and shows the relationships between chapters. The first two chapters (Part 1) set the scene for the development of the work, whereas the rest of the thesis can be split in two parts (Part 2 and 3), which are consistent with the description of the tasks in the previous section.

More in detail, following from the introduction presented in this chapter, in Chapter 2 WA microvibration studies in the literature are reviewed. This includes the commonly accepted experimental and analytical microvibration analysis methods at both WA subsystem and system levels. In particular, issues found in the current WA hard-mounted and coupled microvibration analysis methods are discussed. Chapters 3 to 5 deal with WA hard-mounted microvibrations, i.e. to characterize WA at subsystem level. In Chapter 3, the Equations of Motion (EoMs) of WA-induced microvibrations are derived. The derivation process is based on an energy method and fundamental harmonic excitations due to the flywheel mass imbalances in different conditions are considered. In Chapter 4, a microvibration measurement system is designed to measure the WA-induced microvibrations in a hard-mounted boundary condition. The measured microvibrations are analyzed, including the peculiar nonlinearity and high damping characteristics. Comparisons in microvibrations are also discussed between the soft-suspended WA and the conventional rigid-suspended WA. Chapter 5 includes the simulation of WA hard-mounted microvibrations and their validation with the test results. Simulation processes for harmonic and broadband excitations are introduced. The systematic approach that has been developed to extract the WA model parameters is also explained.

Chapter 6 and 7 deal with WA-seismic mass coupled microvibrations, i.e. to characterize the WA at system level. In Chapter 6, the WA-seismic mass coupled microvibration model is derived primarily based on the hard-mounted case presented in Chapter 3 but with slight modifications to the WA interface boundary condition. Next, the design and calibration of a coupled microvibration measurement system is introduced. The coupled microvibrations induced by the WA are measured and analyzed.

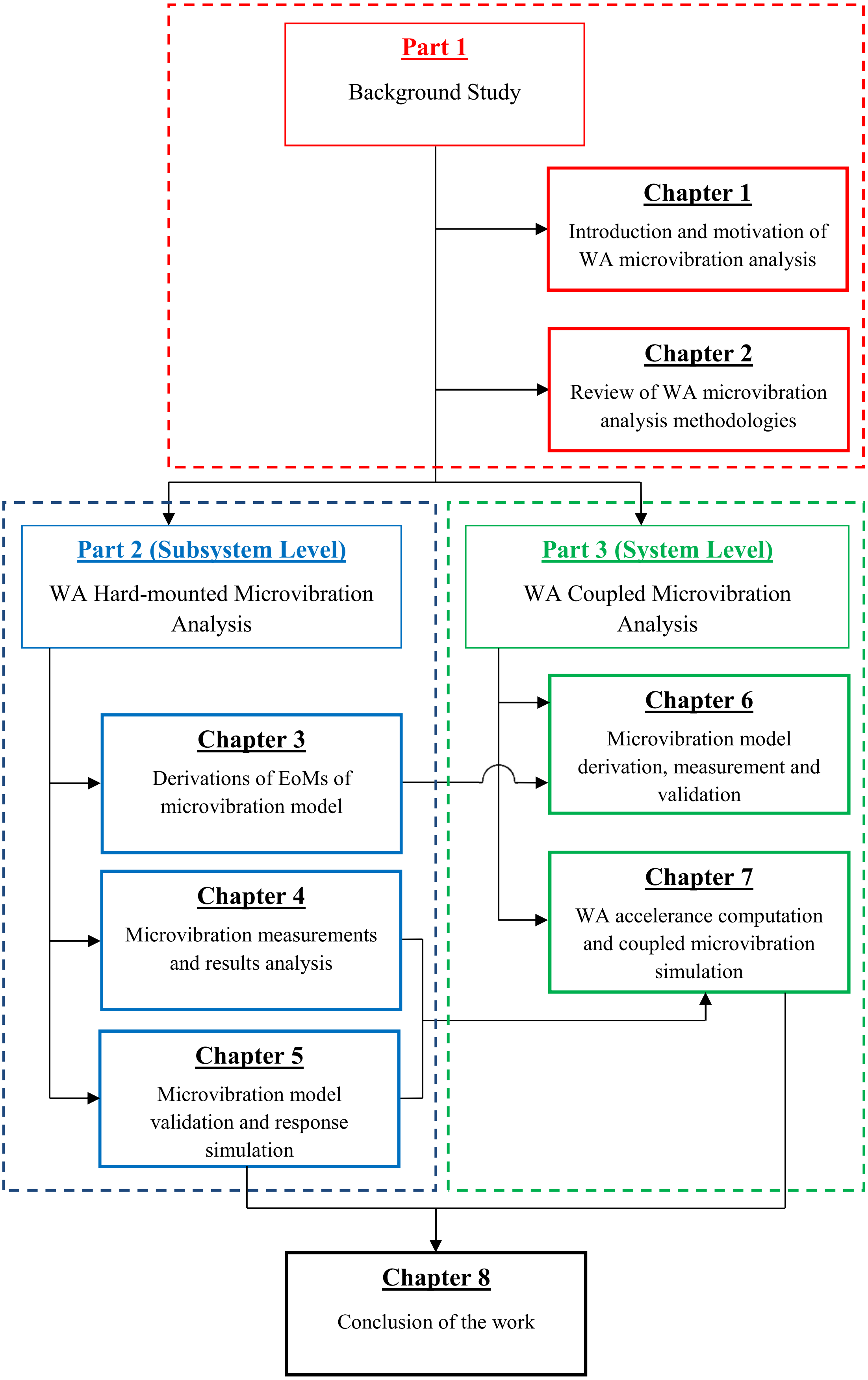

Figure 1-7 Research approach and thesis structure

Also the coupled microvibration model is validated. Chapter 7 focuses on the important issues regarding WA driving point accelerance and improvements to the coupled microvibration analysis methods developed in the literature. The WA driving point accelerance in a static condition (i.e. a non-spinning flywheel) are first studied with a WA accelerance measurement system and also from a WA FE model. The WA driving point accelerance in a dynamic condition (i.e. considering gyroscopic effects in the spinning flywheel) is studied next. In particular, analytical expressions of the WA dynamic accelerance are derived from the WA microvibration model in a “free-free” boundary condition, which is also presented. The microvibrations are predicted from the coupled microvibration analysis method for different WA accelerance and results are compared. Both hard-mounted test results presented in Chapter 3 and the coupled test results presented in Chapter 6 are used during predictions. Finally, conclusions of the work presented in this thesis and possible future work are inferred in Chapter 8.

2. Wheel Assembly Microvibration Analysis Background

In this chapter, the fundamentals of WAs and their microvibrations are introduced. These well-established studies are the foundation in all WA microvibration analysis and they are essential to the work presented in this thesis. The theories of previous WA hard-mounted and coupled microvibration analysis methodologies are introduced. In particular, some typical WA microvibration models are presented and most importantly, the merits and issues in these models and the difficulties encountered in the current analysis methodologies are discussed. The importance of the coupling effect between a WA and its supporting structure is also demonstrated with a simple example.

2.1. Wheel Assemblies

Both RWAs and MWAs are part of the satellite AOCS. Electro-mechanically they are similar and often use the same technology [85]. RWAs are used for satellite attitude control and particularly useful when the satellite needs to be rotated precisely. MWAs are used to store momentum and provide stability to the satellite. A typical RWA or MWA consists of a flywheel mounted on a shaft suspended by bearings and driven by a brushless Direct Current (DC) motor. The whole assembly is often protected by a housing cover. The mechanical configuration of a RWA or MWA can be either mid-span or cantilever configured (see Figure 2-1 a) and b) for example).

a) Mid-span with a rigid suspension	b) Cantilevered with a rigid suspension	c) Cantilevered with a soft-suspension	d) WA under study

Figure 2-1 Typical WA configurations and the WA under study

RWAs usually have a nominally zero speed (or several hundred rpm to avoid stiction problems near zero speed [86]) and can spin in either direction. If the rotation speed can go up to 5000-10000 rpm and maintained, it can be used as a MWA to provide momentum bias to the satellite. Some of them can have functions of both, especially for small satellites [87]. Often they have more complex control system and structures compared to typical WAs due to smart design [88].

The WA used in this thesis is cantilever configured. It is shown in Figure 2-1 c) and d). In addition, the WA is designed with a soft-suspension system instead of the conventional rigid suspension system (see Figure 2-1 for comparisons). The WA is designed to allow utilization either as a RWA or MWA and it can spin up to approximately 10000 rpm.

Note that in practice often three or four WAs are installed on a satellite and each tilt with an angle, hence vibrations transmitted to the satellite may also influenced by their installations [89]. In this thesis, microvibrations induced by a single WA are considered.

2.2. Wheel Assembly-induced Microvibrations

2.2.1. Harmonics and Broadband Noise

Due to their mode of operation, WA-induced microvibrations are continuous. In particular, they generate high amplitude and high frequency microvibrations which are tonal, occurring at known ratios of the angular speed of a spinning flywheel. Since frequency and magnitude of microvibrations both change with angular speed, they may interact with the WA internal flexibilities (i.e. structural modes) at some speeds in the speed band (i.e. critical speeds) and greatly amplify response levels (i.e. resonances). This effect is usually temporary, lasting only as long as the exciting frequency matches a WA resonant frequency, but the resulting amplification is usually unacceptably large.

As first summarized in [14] and updated later in [90], typical sources of microvibration from a WA can be broken down into three categories:

- Flywheel mass imbalances; from the modeling point of view, this includes static and dynamic mass imbalances, which both generate microvibrations at fundamental harmonics of the angular speed.

- Bearing irregularities; they are caused by lubricant dynamics and irregularities in the balls, races and cage, which generate microvibrations at sub- and higher harmonics of the angular speed.

- Motor irregularities; brushless DC motor noise is usually due to the ripple and cogging, which generate very high frequency microvibrations.

In addition, WA-induced microvibrations always have a low level broadband vibrational characteristic accompanied with the tonal vibrations [61].

From the above discussion and in WA microvibration modeling, the total excitations from the WA can be broken down into two types: harmonic excitations and broadband excitations. If a linear assumption is applied, they can be superimposed as the total input excitations to the WA structural model. The complete microvibration model allows WA-induced loads to be predicted with the consideration of gyroscopic effects, WA flexibilities and amplifications. This process is depicted in Figure 2-2.

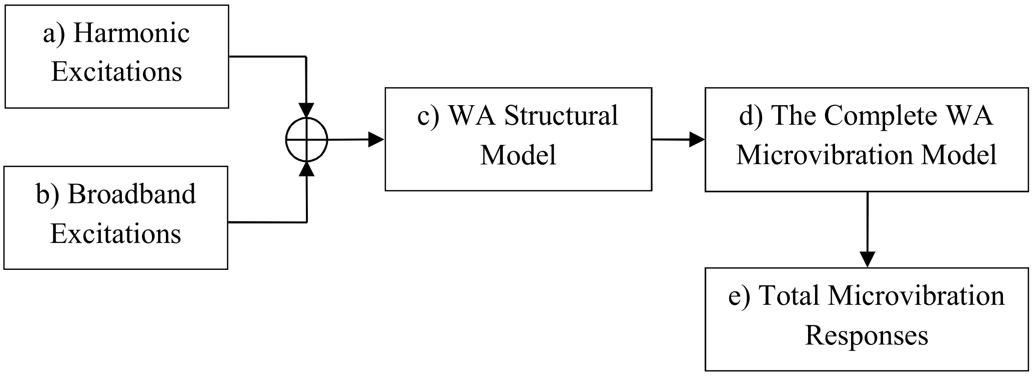

Figure 2-2 WA microvibration modeling process

2.2.2. Wheel Assembly Structural Modes

WA structural modes depend largely on the WA's configuration. Generally a typical WA can be modeled as a single Degree of Freedom (DoF) system in axial translational DoF, with a two-DoFs system in each radial (or in-plane) DoF, thus five DoFs are included in the model. Note that torque vibrations are often ignored due to the flywheel angular speed domination, i.e. the flywheel spin speed driven by the motor is much larger than the perturbation angular speed in the torque DoF.

This WA model results in three dominant modes referred to respectively as the axial translational mode, the radial translational mode and the radial rotational (or “rocking”) mode. They are depicted respectively in Figure 2-3 for a mid-span configured WA.

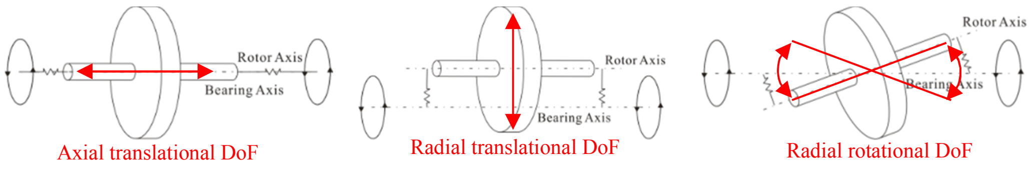

a) Axial translational mode

b) Radial translational mode

c) Radial “rocking” mode

Figure 2-3 Structural modes of a typical mid-span configured WA

Among the three structural modes in Figure 2-3 for a mid-span configured WA, the axial and radial translational modes are speed-independent. The “rocking” mode is speed-dependent and whirls are caused by the gyroscopic procession of the spinning flywheel.

Figure 2-4 shows typical Campbell diagram of mid-span and cantilever configured WAs.

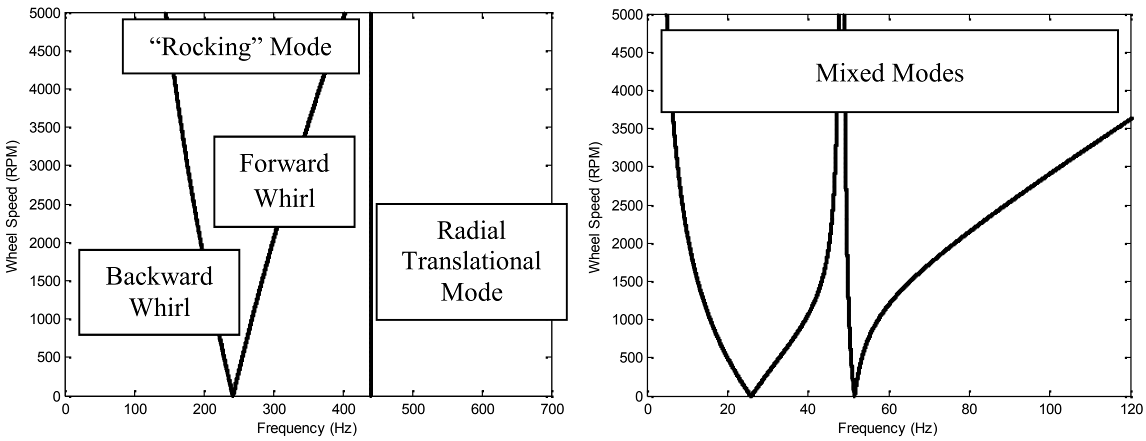

a) Mid-span configured WA

b) Cantilever configured WA

Figure 2-4 Example of Campbell diagrams of mid-span and cantilever configured WAs

In theory the “rocking” mode of an axisymmetric WA splits into two speed-dependent natural frequencies (or whirls) from static (i.e. at zero rpm): backward (or precession) whirl and forward (or nutation) whirl. The backward whirl decreases in frequency as speed increases, while the forward whirl is opposite [91]. It is also clear from Figure 2-3 and Figure 2-4 a) that the three structural modes are decoupled from each other, especially between the radial translational mode and the “rocking” mode. In contrast for a cantilever configured WA, the two radial modes are coupled, thus it is no more possible to speak of radial translational mode or “rocking” mode [92] (see Figure 2-4 b) for example). The structural modes of a cantilever configured WA are depicted in Figure 2-5.

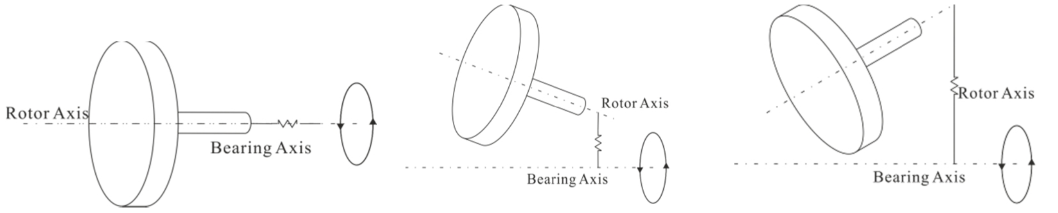

a) Axial translational mode b) Mixed radial mode c) Alternative radial mode

Figure 2-5 Structural modes of a typical cantilever configured WA

In this case, the axial translational mode remains uncoupled from the radial modes, but the radial translational mode and the “rocking” mode are combined into a mixed radial mode in each radial DoF. Also, in this case the four radial modes are all speed-dependent. In practice, these coupled motions in radial DoFs make the overall modeling process much more complicated than that for a conventional mid-span configured WA.

2.3. Typical Microvibration Analysis Methodologies

In the traditional WA microvibration analysis, WA-induced loads are measured in a hard-mounted configuration, in which the WA is mounted on a rigid surface and its interface is constrained to have zero motion. As flywheel spins, load cells are used to measure the resulting forces and moments at the interface. The dynamic models developed under such boundary condition are called the WA hard-mounted microvibration models. However in practice, the hard-mounted boundary condition is not an accurate representation of the WA when it is mounted on a satellite structure. In other words, the hard-mounted microvibrations differ from the coupled microvibrations that would actually exist at the WA-structure interface if the two bodies are coupled together. In order to improve the modeling accuracy, WA-structure coupled analysis methodologies are developed.

Although hard-mounted microvibration analysis methodologies have been well developed in the literature, coupled cases have not. The literature shows only a few works which lack maturity in both analysis theory and experimental work. In this section, some typical WA microvibration analysis methodologies (hard-mounted and coupled) developed in the literature are reviewed. Problems and difficulties encountered in them are also discussed.

2.3.1. Wheel Assembly Internal Microvibration Source Characterization

In the earlier works of WA microvibration analysis such as [93-95], studies were primarily based on the general WA microvibration test results and modeling for specific vibrational features. Harmonic characteristics were well understood and some empirical models were attempted. For example, WA-induced microvibrations were first modeled assuming they consist of discrete and superimposed harmonics in [96]. Microvibrations from the WA internal components such as bearing, motor and flywheel, etc. were carefully characterized and modeled in a series of works published in [97-99] and later similar works were also seen in [100-102] for another WA. Also during this time, microvibration test platforms [103-106] and test methods [107-109] were greatly developed for WA microvibration analysis. For example, the detailed microvibration analysis of a typical WA ball bearing system at low frequencies were studied in [110-112] by using a specially designed air floating vibration measurement platform in [113]. The complete harmonic analysis of a WA was published in [114], it was performed with a customized vibration measurement system. Similar works in [115-117] should also be noted. In [118] on the other hand, an envelope analysis technique was developed to localize imperfections in the WA bearing, where the measured microvibration data were used for condition monitoring of ball bearings in the WAs. By detecting the modulation of the resonance frequency from imperfection signals, the technique could detect signals, which were six times lower than the noise level. The measurement platform used in this study was introduced in detail in [119], it was designed based on similar principles of a Kistler table. As in general, microvibration measurement platforms are designed during WA microvibration research.

In general, characterizations of WA internal components are very useful for understanding their internal microvibration sources, and for this reason the results are mainly used for WA design purposes. For microvibration analysis at satellite system level however, they are in general impractical to be used as the inputs to a satellite model. In this case, the complete WA needs to be considered as a single source or “black box” and being characterized as a whole, i.e. at subsystem level. WA-induced microvibrations at subsystem level and system level are the main concerns in this thesis. Reviews of their literature works are presented in the rest this chapter.

2.3.2. Wheel Assembly Hard-mounted Microvibration Analysis

When modeling a mechanism which causes vibrational energy to enter the system, there are two fundamental approaches: the analytical approach and the empirical approach, as defined from [120]:

- *The analytical approach relies on physically modeling the mechanism that causes the vibration and to assign realistic values to the physical parameters of the model.*

- *The empirical approach consists in creating an empirical model of its dynamic response via the analysis of experimental test data.*

Often, the two approaches need to be combined and refer to one another. In this case it is known as the semi-empirical (or semi-analytical or hybrid) approach. The detailed WA microvibration study at subsystem level were first reported in [121], in which an empirical model of microvibrations induced by a mid-span configured WA in a hard-mounted boundary condition was developed. In particular, programs were written based on the developed modeling method to extract harmonic excitation parameters from test results. Later, these parameters were used in the semi-analytical model development in [122]. Gyroscopic effects derived from the analytical model were integrated with the empirical model, thus the complete microvibration model was a hybrid.

In general, relationships between each model described above are depicted in Figure 2-6 on the next page.

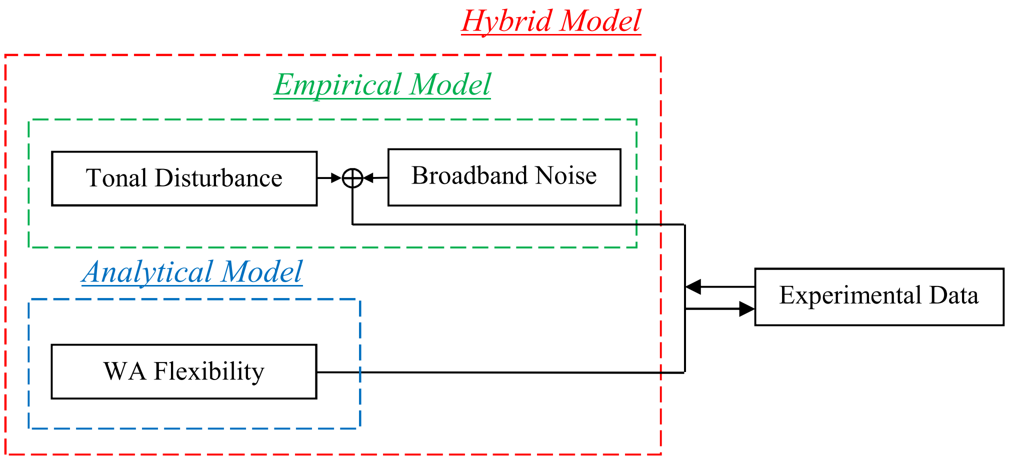

Figure 2-6 Relationships of WA hard-mounted microvibration models

This analysis approach generally has been accepted and widely used in the WA microvibration analysis. Subsequently, similar WA microvibration models (either analytical, empirical or hybrid) developed in the literature were based on this modeling principle. For example, WA-induced microvibrations in radial DoFs were measured and the closed-form harmonic response expressions were derived in [123]. Similar work was also published in [124], but in this case frictions due to bearing system and irregularities in motor, etc. were also included in the model. Responses were only simulated in the time domain however. Similar WA microvibrations were modeled but primarily used for the measurement platform design in [125], and also a similar one in [126]. In order to improve the WA empirical model accuracy, an energy compensation method was developed to correct the measured microvibration data in [127, 128], and later harmonic parameters obtained from the improved test results were used in the semi-analytical model development in [129, 130]. The closed-form harmonic response expressions in each WA DoF was presented and simulated directly in the frequency domain in [131], and also a similar one in [132]. Even simpler analytical expressions of harmonic responses were derived in [133], in which the model considers resonances on harmonics (include those from gyroscopic effects) to be the dynamic amplifications such as in the conventional vibration problems, and thus avoid deriving the whole EoMs. In [134] a complete WA microvibration analytical model was derived not only considering the flywheel mass imbalances but also irregularities in the bearing system (i.e. balls and raceway, etc.) were physically modeled.

A WA broadband excitation modeling method was first introduced in [61], and it was concluded that no purely analytical model was able to simulate broadband excitations and they had to be modeled in other ways. Based on this work, a hybrid broadband excitation model was developed in [135], where an arbitrary broadband forcing function was realized as a speed dependent polynomial. This method assumes the broadband noise was speed-dependent and requires both an analytical “shape function” of vibration and test results at each speed. Apart from these examples, there seems to be no other work has attempted the modeling of WA broadband noises.

In brief, WA-induced microvibrations in hard-mounted boundary conditions are well studied up to the present. Various microvibration models, measurement platforms and analysis methodologies have been developed or designed. The microvibrations measured and simulated in this way can be used directly as the inputs in the satellite model in order to predict the payload performance. This is the standard microvibration analysis method and has been widely used in satellite system level microvibration analysis. Studies in [61] and [136] are two typical examples.

Tackling Open Issues

- The Cantilevered Configuration

All microvibration models mentioned above and others in the literature were derived for the mid-span configured WAs. In practice, there is another group of WAs with cantilevered configurations, i.e. a flywheel and its Center of Mass (CoM) at one side of the shaft, however their microvibration studies were not found. Due to the cantilevered configuration, their structural models are very different from those of the mid-span configured WAs, for example, the coupled motions in radial DoFs as mentioned earlier. It is thus necessary to derive its EoMs and characterize its dynamics and later used for the system level microvibration analysis. This can be considered as the problem in Figure 2-2 part c) in a typical WA microvibration modeling.

- The Generalized Harmonic Excitations

In previous WA microvibration modeling, there was generally no resonance on the fundamental harmonics in the test speed band (say up to 4000 rpm) due to the rigid suspension system used in the WAs which has their structural modes at relatively high frequencies (e.g. above 200 Hz in Figure 2-4 a)). However in practice this is not always true, for example, a MWA spins at 10000 rpm or for a relatively flexibly suspended WA. In these cases, fundamental harmonics may severely interact with the WA structural modes in the speed band analyzed and cause significant dynamic amplifications before and after the resonances. If under such conditions, the traditional harmonics modeling methods cannot model them precisely, since there are several aspects that were not considered. For example, the extraction of harmonic parameters can only be performed up to some speeds much earlier before the resonances due to resonance dynamic amplifications. In contrast, the responses in the whole speed band were used in the literature for extractions without considering resonance dynamic amplifications. Damping values must also be taken care at the fundamental harmonic resonances since they may exhibit very different values compared to those on higher harmonics (where damping values were often extracted in the traditional modeling methods). Other possible dynamics such as nonlinearity may also occur at fundamental harmonic resonances due to the excessive loads transmitted in the motor.

In brief, typical issues and hence variables, in the simulation of generalized harmonic excitations include:

- Flywheel mass imbalances are often not exactly known, but the minimum performance values from manufacture are usually given (e.g. the typical static mass imbalance is less than 5 g.mm for the WA under study).

- Fundamental harmonic responses severely interact with WA structural modes in the speed band analyzed, thus a nonlinearity effect may also occur.

- In practice, amplitudes of harmonic responses are not exactly proportional to the angular speed squared, such as also found in [137].

- Influences of resonance dynamic amplifications must be considered in the modeling.

In addition, all above issues are interrelated hence making the simulation of generalized harmonic excitations much more complicated than those shown in the literature. This can be considered as the problem in Figure 2-2 part a).

- Broadband Excitations

Issues related to the continuous broadband excitations have recently become increasingly important in WA microvibration analysis. From recent studies such as in [13], there is a trend that microvibrations are becoming more concerned in the high frequency band with even lower amplitudes. It is thus necessary to consider the broadband type excitations onboard satellites. In general this includes sensor noises and mechanism-generated noises that often accompanied with other vibrations. In previous WA microvibration analysis, excitations due to broadband noises were generally ignored, with only harmonic excitations were considered and thus responses.

As introduced earlier, very limited information is available on WA broadband excitations and responses modeling in the literature. Traditionally, the broadband noises need to be extracted from vibration test results at each speed, i.e. speed-dependent. In the meantime, analytical expressions, i.e. “shape functions”, used to describe the general response level of broadband noises must also be derived at each speed to capture the broadband amplifications in the responses. This however, significantly increases the simulation efforts especially if the analysis is performed at many speeds, thus the method was not practical. It is therefore also necessary to develop an efficient and accurate method for WA broadband excitations and responses modeling. This can be considered as the problem in Figure 2-2 part b).

2.3.3. Wheel Assembly-Structure Coupled Microvibration Analysis

The following example is presented to demonstrate the importance of structure coupling within a coupled system. Consider for example the maximum magnitude of the force produced by the simple systems with two counter-rotating masses of two cases shown in Figure 2-7 a) and b) respectively.

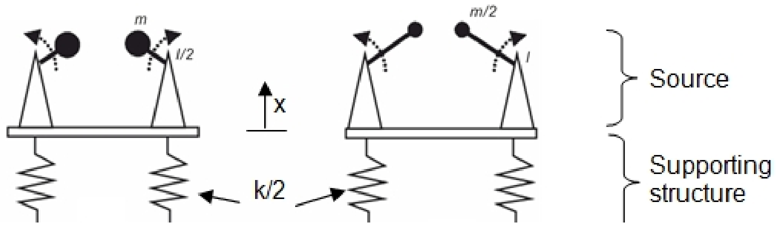

a) mass: *m*; arm: *l*/2 b) mass: *m*/2; arm: *l*

Figure 2-7 Schematic of possible source of vibrations

In both cases, if the source is hard-mounted (i.e. base displacement, *x*, equals to zero and in this case the supporting structure is rigid as stiffness, *k*, tends to infinity), the maximum force is thus:

$$F_{\max} = ml\omega^2 \tag{2.1}$$

where ω is the angular speed, m (or m/2 in Figure 2-7 b)) is the attached mass value, $l/2$ (or l in Figure 2-7 b)) is rotation arm of the mass.

While Eq. (2.1) is true for a hard-mounted boundary condition, when the source is actually mounted on a flexible structure the system shown in Figure 2-7 b) can produce twice the force as in Figure 2-7 a).

To demonstrate this, we examine the system in Figure 2-7 a) and allow movement of the support (i.e. $x \neq 0$), which in practice corresponds to the source supported by a structure with a total finite stiffness equals to k. The vertical equilibrium can be expressed as:

$$2m\left(-\frac{l}{2}\omega^2 \sin\left(\omega t\right) + \ddot{x}\right) + kx = 0 \tag{2.2}$$

where t is time, and the solution of this equation can be written as:

$$x = \frac{ml\omega^2}{k - 2m\omega^2}\sin\left(\omega t\right) \text{ with } \omega \neq \omega_0 = \sqrt{\frac{k}{2m}} \tag{2.3}$$

where ω_0 is the natural frequency of the system described.

Therefore for a high angular speed, i.e. $\omega \geq \omega_0$, the displacement x tends towards $l/2$ and consequently the force transmitted to the support will be:

$$F_{a)}\Big|_{\omega>>\omega_0} = \frac{kl}{2} \tag{2.4}$$

If we now consider the system in Figure 2-7 b), the vertical equilibrium can be written as:

$$m\left(-l\omega^2 \sin\left(\omega t\right) + \ddot{x}\right) + kx = 0 \tag{2.5}$$

and its solution:

$$x = \frac{ml\omega^2}{k - m\omega^2}\sin\left(\omega t\right) \text{ with } \omega \neq \omega_0 = \sqrt{\frac{k}{m}} \tag{2.6}$$

If we now consider for a high angular speed, i.e. $\omega \geq \omega_0$, the displacement x tends to l and consequently the force transmitted to the support will be:

$$F_{b)}\Big|_{\omega>>\omega_0} = kl \tag{2.7}$$

The value is twice the force generated by the source in Figure 2-7 a).

In a coupled system, the loads exchanged at the interface between a source and its supporting structure depend on the source internal dynamics (i.e. the forces and moments in the blocked configuration, produced by mass imbalances and other possible internal component irregularities) and the reactions due to the coupling (and consequent motion of the interface).

Although the basic theory has been known for some time, the issues related to the WA-structure coupled microvibrations were first reported in [138], where both the WA and structure were considered as rigid bodies with internal flexibilities. Concepts of the coupled microvibration modeling were formulated and relationships between the loads generated by the WA and performance of the structure were derived. It was also realized that some frequency-dependent qualities (WA and supporting structure driving point dynamic mass or accelerance) were critical in the coupled microvibration analysis.

The work was further developed in [139, 140], where an experimental method was developed to measure the WA driving point dynamic mass in a static condition (here static refers to a WA without the flywheel spinning). A six-DoF load cell was used to measure the reaction loads and several accelerometers were used to measure accelerations, both qualities were derived at the WA base interface, i.e. the driving point. The coupled microvibrations predicted with WA static accelerance clearly showed advantages over the standard one, however even this method had flaws, as it only considered WA dynamic mass with the non-spinning flywheel and used it to predict the coupled microvibrations at a broadband speed. In practice when the flywheel is spinning this not only produces microvibrations (e.g. because of its mass imbalances, etc.), but also the dynamic mass of the WA varies as functions of angular speed. Due to gyroscopic effects, the WA dynamic mass becomes quite different from that of the non-spinning case in a broadband speed.

This problem has been studied in [74, 141, 142]. In these works, an analytical method was developed to obtain the WA accelerance with gyroscopic effects, i.e. the WA driving point accelerance in a dynamic condition or WA dynamic accelerance. Analytical expressions of the WA dynamic accelerance were derived from the WA hard-mounted microvibration model. In this case however, the accelerance expressions only considered the flywheel mass and inertias but ignored the stiffness and damping values of the suspension system. The gyroscopic effects of the spinning flywheel (and thus dynamic accelerance) derived were implemented in the coupled microvibration analysis, and even though the predicted results were improved from previous ones.

Other related work involving WA-structure coupling issues was also seen in [143] and [144], however it was not for WA coupled microvibration analysis but rather for WA measurement platform and mounting bracket design respectively. Other than that, there is no other method for WA-structure coupled microvibration analysis.

Tackling Open Issues

- Accelerance Measurements

From the literature review, there was only one experimental method available to measure the WA dynamic mass (or accelerance) and in the static condition only. In this thesis, rather than using the complex load cell to measure forces and moments at the WA interface, an alternative and simpler measurement method is introduced. The method utilizes maximum two common unidirectional force sensors to measure the input forces, and eight accelerometers to measure the response accelerations, both applied directly at the WA base interface. In addition, the system is also used to measure WA accelerance in the dynamic condition.

- Dynamic Accelerance

The method to derive the WA dynamic accelerance in the literature however, has some fundamental approximations in the model. First of all, the WA-structure coupled microvibration analysis requires the WA accelerance to be derived in a “free-free” boundary condition, where forces and accelerations should be obtained at the WA base interface, i.e. the driving point. Thus rather than using the WA hard-mounted microvibration model, the model in the “free-free” boundary condition should be used. Next, from WA static accelerance tests, the results have clearly shown the influence of stiffness and damping within the suspension system, even when the flywheel is not spinning, in other words, WA accelerance is not constant in the frequency domain at any speed if the WA base interface is taken as the driving point. Therefore, rather than completely ignoring the stiffness and damping of the suspension system in the dynamic accelerance derivations, they should be included in the modeling. In doing so, this has a significant impact in the WA dynamic accelerance calculated and also in the coupled microvibrations predicted.

2.4. Summary

WAs as one of the most important microvibration sources have been studied by many researchers and there is a relative wealth of publications. Aside from the analysis of the

WA internal components dynamics, WA-induced microvibrations were also widely studied at subsystem level, both experimentally and analytically. In general, WA microvibration analysis can be categorized into two group w.r.t. the WA boundary condition: hard-mounted and coupled. Difficulties are still encountered in the currently available analysis methods for both hard-mounted (where no cantilever configured WA microvibration model exists, neither an accurate and efficient broadband noise modeling method) and coupled analysis (with lack of a reliable method to include gyroscopic effects in the WA driving point accelerance calculation), and require improvement for future satellite design.

3. Wheel Assembly Hard-mounted Microvibration Model Derivation

In this chapter, an analytical microvibration model of cantilever configured WA with a soft-suspension system due to flywheel mass imbalances is derived in the hard-mounted boundary condition. The derivation is carried out using an energy (or Lagrangian) method. The soft-suspension system is modeled as a combination of linear and torsional springs and dashpots. Under linear assumptions, analytical expressions of kinetic energy, potential energy and work done can be expressed for the flywheel mass balanced case and subsequently for the statically and dynamically mass imbalanced cases. EoMs of each case are derived in succession in this chapter. At the end of this chapter, the linearized EoMs of a fully flywheel mass imbalanced WA are derived.

3.1. Energy Method

In the WA model the flywheel is assumed as a rigid disk, while rotations of a rigid body can be described using Euler angles in an energy method. Generally, Euler angles are used to define the rigid body rotations and relate one coordinate frame to another. Consider the CoM of a balanced flywheel is *O* and is free to rotate about any axis as shown in Figure 3-1.

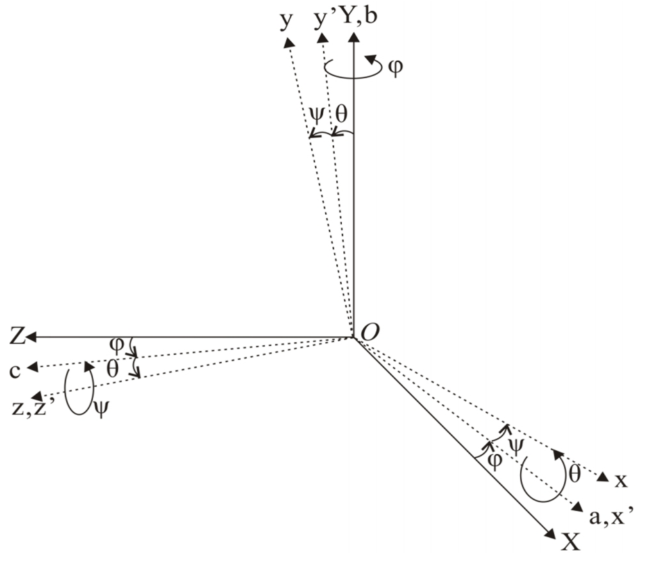

Figure 3-1 Euler angles and transformations between each coordinate frame

Euler angles are formed in sequence by rotating each of the three orthogonal axes in the corresponding frame termed the "Euler angles convention". The commonly used convention in rotordynamics is the *Z*-convention, since the *Z*-axis is usually defined as the shaft pointing direction and also in this thesis. Let the ground-fixed inertial frame, *XYZ*, and the body-fixed frame, *xyz*, coincide at the origin *O* before rotation starts. Under *Z*-convention, the first rotation angle, φ, is formed by rotating the rigid body about the *Y*-axis. This defines the first rotation frame, *abc*. The next rotation angle, θ, is formed by rotating the rigid body about the *a*-axis. This defines the second rotation frame, $x'y'z'$. The final rotation angle, ψ, is formed by rotating the rigid body about z'-axis. The final rotation also represents the spinning of the flywheel (i.e. in torque DoF) and defines the body-fixed frame, *xyz*.

After the final rotation, three angles: φ, θ and ψ, are formed, they are the Euler angles. In other words, the initial body frame, *xyz*, is rotated through the three Euler angles w.r.t the inertial frame, *XYZ*. Using this method, the complete rotation of a rigid body about its CoM can be mathematically described. The transformation matrices between frames are given in Appendix A.

EoMs of the WA microvibration model are derived using Lagrange's equations. The general form of Lagrange's equations is:

$$\frac{d}{dt}\left(\frac{\partial L}{\partial \dot{\xi}_n}\right)-\frac{\partial L}{\partial \xi_n}=Q_i \tag{3.1}$$

where ξ_n is the generalized coordinates, Q_i is the work done and L is known as "Lagrangian" and defined as the difference between the total kinetic energy, T, and the total potential energy, U, of the system.

$$L\left(\xi_1\cdots\xi_n,\ \dot{\xi}_1\cdots\dot{\xi}_n,\ t\right)=T-U \tag{3.2}$$

The dot denotes the first derivative of the variable w.r.t. time, *t*.

From Eq. (3.2) it is thus necessary to find the total kinetic energy, *T*, the total potential energy, *U*, and the total work done, Q_i, of the system. To derive the fully mass imbalanced WA microvibration model, three cases are considered one after another:

- Mass balanced flywheel;
- Statically mass imbalanced flywheel;
- Dynamically mass imbalanced flywheel;

EoMs are derived for each case and then the final EoMs of the fully mass imbalanced WA are derived. They are presented in the rest of this chapter.

3.2. Coordinate System

After some simplifications, the cantilever configured WA with the soft-suspension system in the hard-mounted boundary condition can be considered as the model shown in Figure 3-2. This model is able to capture the five structural modes of the WA and also gyroscopic effects of the spinning flywheel.

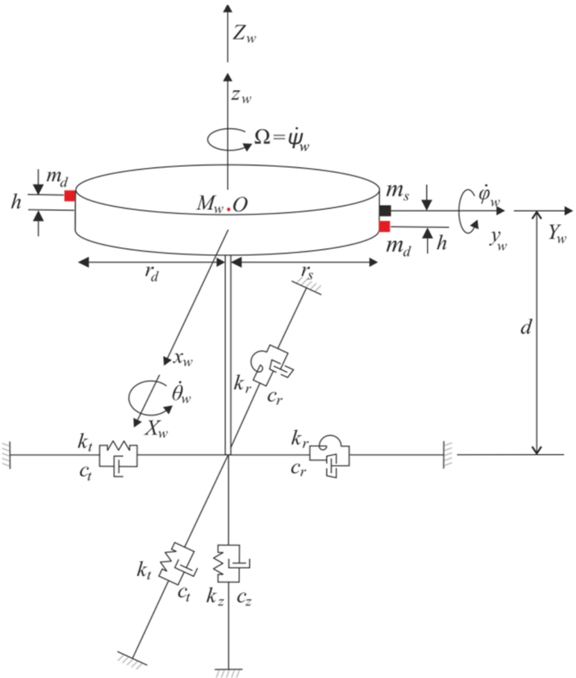

Figure 3-2 Simplified model of cantilever configured WA with the soft-suspension system in the hard-mounted boundary condition

Firstly, the WA is assumed axisymmetric about its shaft. Due to the cantilevered configuration, the rigid flywheel (or rotor) is modeled at one side of the suspension system. The inertial (or fixed) frame, $X_wY_wZ_w$, and the body (or rotating) frame, $x_wy_wz_w$, coincide at the flywheel CoM, O, while z_w-axis (or Z_w-axis) is defined as the shaft pointing axis. Subscript "*w*" indicates "WA only" as for the hard-mounted boundary condition. Rotations about the three axes are θ_w, φ_w and ψ_w. Assuming steady speed rotation, i.e. $\Omega = \dot{\psi}_w$, Ω is the flywheel angular speed. As mentioned previously, the flywheel is modeled as a rigid disk with mass M_w. It is connected by a massless and rigid shaft with length d to the soft-suspension system.

The soft-suspension system is modeled as a combination in five DoFs. This includes two pairs of linear spring and dashpot, two pairs of torsional spring and dashpot, each in one of the two radial translational DoFs and a linear spring and dashpot in the axial translational DoF. Due to axisymmetry of the suspension system, the linear spring stiffness, k_t, is the same in the two radial translational DoFs, and the torsional spring stiffness, k_r, as well the dashpot damping coefficients, c_t and c_r. In axial translational DoF, linear spring stiffness and dashpot damping coefficient are k_z and c_z respectively.

In practice, the generalized coordinates in the WA microvibration model are five: x_w, y_w, z_w, θ_w and φ_w. The rotation angle, ψ_w, is not considered as a Lagrangian coordinate due to the flywheel steady speed rotation assumption and thus domination over angular speed perturbation in torque DoF (this assumption is used throughout the thesis, thus the complete WA microvibration analysis presented is steady speed analysis rather than transient speed analysis). Following this modeling approach there are thus five motions in the microvibration model: two same radial translational motions; two same radial rotational motions and one independent axial translational motion. All EoMs are derived in terms of the body frame, $x_wy_wz_w$, or in other words, w.r.t. the inertial frame, $X_wY_wZ_w$.

3.3. Kinetic Energy

For a mass balanced flywheel, the total kinetic energy, T_w, is the sum of the total translational kinetic energy, T_{w_t}, and the rotational kinetic energy, T_{w_r}, of the flywheel.

$$T_w = T_{w_t} + T_{w_r} \tag{3.3}$$

Note that due to steady speed rotation and at typical angular speed, the kinetic energy of the spinning flywheel (i.e. Ω related) dominates over the kinetic energy due to torsional microvibrations (i.e. φ_w related). When ignoring the kinetic energy of torsional microvibrations, T_{w_t} then includes the kinetic energy in the two radial translational DoFs and axial translational DoF, while T_{w_r} includes only those in the two radial rotational DoFs.

3.3.1. Flywheel Displacement and Velocity

For a mass balanced flywheel, the geometric center of the flywheel coincides with its CoM (i.e. no offset from the static mass imbalance) and the flywheel axis of symmetry coincides with the spin axis (i.e. no axis misalignment from the dynamic mass imbalance). In this case, the position of the flywheel CoM, *O*, at any instant time in the rotational plane can be depicted as:

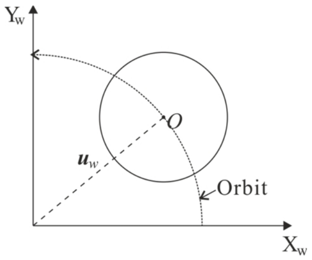

Figure 3-3 Position of the flywheel CoM during spinning (rotational plane)

Considering that in axial translational DoF, the total translational displacement vector, $\boldsymbol{u}_w$, of the flywheel CoM can be expressed as:

$$\boldsymbol{u}_w = \begin{Bmatrix} x_w \\ y_w \\ z_w \end{Bmatrix} \tag{3.4}$$

The translational velocity vector, $\boldsymbol{V}_w$, of the flywheel CoM is thus:

$$\boldsymbol{V}_w = \begin{Bmatrix} \dot{x}_w \\ \dot{y}_w \\ \dot{z}_w \end{Bmatrix} \tag{3.5}$$

The angular velocity vector, $\boldsymbol{\omega}_w$, of the flywheel CoM is computed as the sum of three angular velocities acting in different directions: $\dot{\varphi}_w$ about the Y_w-axis, $\dot{\theta}_w$ about the a_w-axis, and $\dot{\psi}_w$ about the z_w-axis. Using the appropriate transformation matrices given in Appendix A, also let $\dot{\psi}_w = \Omega$ due to steady speed rotation, $\boldsymbol{\omega}_w$ in the body frame can be expressed as:

$$\boldsymbol{\omega}_w = \boldsymbol{R}_2 \left(\boldsymbol{R}_1 \begin{Bmatrix} 0 \\ \dot{\varphi}_w \\ 0 \end{Bmatrix} + \begin{Bmatrix} \dot{\theta}_w \\ 0 \\ 0 \end{Bmatrix} \right) + \begin{Bmatrix} 0 \\ 0 \\ \dot{\psi}_w \end{Bmatrix} = \begin{Bmatrix} \dot{\theta}_w \cos\psi_w + \dot{\varphi}_w \cos\theta_w \sin\psi_w \\ -\dot{\theta}_w \sin\psi_w + \dot{\varphi}_w \cos\theta_w \cos\psi_w \\ -\dot{\varphi}_w \sin\theta_w + \Omega \end{Bmatrix} \tag{3.6}$$

where the two transformation matrices, $\boldsymbol{R}_1$ and $\boldsymbol{R}_2$ are taken from Appendix A.

$$\boldsymbol{R}_1 = \begin{bmatrix} 1 & 0 & 0 \\ 0 & \cos\theta_w & \sin\theta_w \\ 0 & -\sin\theta_w & \cos\theta_w \end{bmatrix} \tag{3.7}$$

$$\boldsymbol{R}_2 = \begin{bmatrix} \cos\psi_w & \sin\psi_w & 0 \\ -\sin\psi_w & \cos\psi_w & 0 \\ 0 & 0 & 1 \end{bmatrix} \tag{3.8}$$

3.3.2. Translational and Rotational Kinetic Energy

Substituting the translational velocity vector Eq. (3.5) into the total translational kinetic energy, T_{w_t}, thus:

$$T_{w_t} = \frac{1}{2} \boldsymbol{V}_w^T M_w \boldsymbol{V}_w = \frac{1}{2} M_w \left(\dot{x}_w^2 + \dot{y}_w^2 + \dot{z}_w^2 \right) \tag{3.9}$$

where superscript "*T*" indicates the transpose of a vector. Substituting the rotational velocity vector Eq. (3.6) into the rotational kinetic energy, T_{w_r}, thus:

$$T_{w_r} = \frac{1}{2} \boldsymbol{\omega}_w^T \boldsymbol{I} \boldsymbol{\omega}_w = \frac{1}{2} \left[\left(\dot{\theta}_w^2 + \dot{\varphi}_w^2 \cos^2\theta_w \right) I_r + \left(\dot{\varphi}_w^2 \sin^2\theta_w + \Omega^2 - 2\Omega\dot{\varphi}_w \sin\theta_w \right) I_z \right] \tag{3.10}$$

where ***I*** is inertia tensor of the flywheel. Remembering that for an axisymmetric flywheel, the transversal moments of inertia, I_r, about the two radial translational DoFs are equal. Furthermore, if the flywheel is an infinite thin disc, the polar moment of inertia, $I_z = 2I_r$. In general, the inertia tensor of the flywheel in body frame can be expressed as:

$$\boldsymbol{I} = \begin{bmatrix} I_r & 0 & 0 \\ 0 & I_r & 0 \\ 0 & 0 & I_z \end{bmatrix} \tag{3.11}$$

Finally, the total kinetic energy, T_w, of a mass balanced WA is derived:

$$T_w = \frac{1}{2}\left[M_w\left(\dot{x}_w^2 + \dot{y}_w^2 + \dot{z}_w^2\right) + \left(\dot{\theta}_w^2 + \dot{\varphi}_w^2 \cos^2\theta_w\right) I_r + \left(\dot{\varphi}_w^2 \sin^2\theta_w + \Omega^2 - 2\Omega\dot{\varphi}_w \sin\theta_w\right) I_z \right] \tag{3.12}$$

3.4. Potential Energy

The only internal forces and moments acting on the flywheel in the WA are due to the elastic reactions and damping of the suspension system. For potential energy derivations, the flywheel radial motions are assumed to be independent from the axial translational motion, i.e. there is no dynamic coupling between axial and radial DoFs. Meanwhile due to WA axisymmetry, dynamics in the two perpendicular radial DoFs (x_w and y_w) are assumed equal. Under these assumptions, the differing sign convention in the two perpendicular planes $x_w z_w$ and $y_w z_w$ compels the use of opposite signs for the off-diagonal elements in the stiffness matrices of the two planes. This means if the stiffness matrix in any of the two planes is derived, the stiffness matrix in the other plane can be immediately obtained by altering the sign for the off-diagonal elements. The "virtual displacement method" is used to derive the stiffness matrix of the suspension system.

The total potential energy, U_w, is the sum of the potential energy, $U_{x_w z_w}$, in $x_w z_w$-plane and, $U_{y_w z_w}$, in $y_w z_w$-plane. This includes the translational and rotational potential energy in the two radial DoFs and in axial translational DoF, thus U_w is expressed as:

$$U_w = U_{x_w z_w} + U_{y_w z_w} + U_{z_w} \tag{3.13}$$

Derivation of each potential energy in Eq. (3.13) is shown as following.

3.4.1. Potential Energy in $y_w z_w$-plane

The WA model in $y_w z_w$-plane is depicted in Figure 3-4:

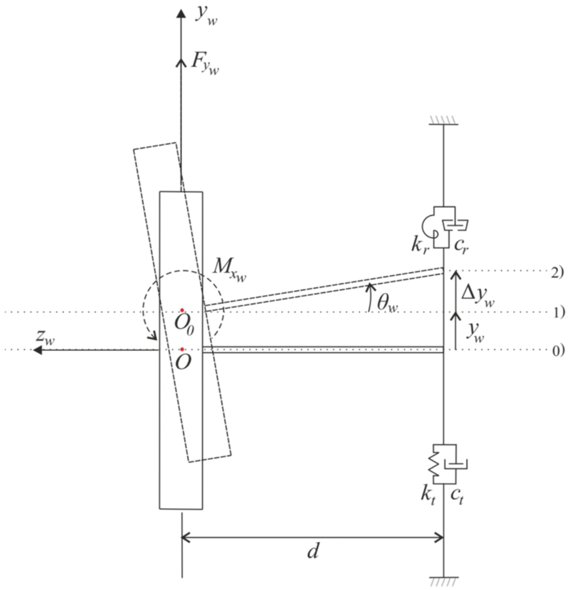

Figure 3-4 WA model in $y_w z_w$-plane

Firstly, apply a virtual displacement, y_w, at the flywheel CoM, O, positively (i.e. upward in y_w-axis), the linear spring produces an extensive force, F_{y_w}, and let the new CoM to be O_0. Next, apply a virtual rotation, θ_w, at O_0 positively (i.e. anticlockwise), the torsional spring then produces an extensive moment, M_{x_w}. Since the rotational angle is assumed to be small, then $\Delta y_w = \theta_w d$. Also, since only linear spring can produce extensive or compressive forces, the total extension will be the sum of y_w and Δy_w. Hence the total force, F_{y_w}, in $y_w z_w$-plane can be expressed as:

$$F_{y_w} = k_t y_w + k_t d\theta_w \tag{3.14}$$

The total moment, M_{x_w}, also includes two components: one produced by the torsional spring and the other one produced by the linear spring. The displacement of the linear spring is the sum of y_w and Δy_w, and the rotation of torsional spring is θ_w. Hence the total moment, M_{x_w}, in $y_w z_w$-plane can be expressed as:

$$M_{x_w} = k_t d y_w + \left(k_r + k_t d^2\right)\theta_w \tag{3.15}$$

Forming Eqs. (3.14) and (3.15) into a matrix, gives:

$$\begin{bmatrix} F_{y_w} \\ M_{x_w} \end{bmatrix} = \begin{bmatrix} k_t & k_t d \\ k_t d & k_r + k_t d^2 \end{bmatrix} \begin{bmatrix} y_w \\ \theta_w \end{bmatrix} \tag{3.16}$$

The stiffness matrix in $y_w z_w$-plane, $\boldsymbol{K}_{y_w z_w}$, is thus:

$$\boldsymbol{K}_{y_w z_w} = \begin{bmatrix} k_t & k_t d \\ k_t d & k_r + k_t d^2 \end{bmatrix} \tag{3.17}$$

The potential energy in $y_w z_w$-plane (radial DoFs only) is derived as the following:

$$U_{y_w z_w} = \frac{1}{2} \begin{Bmatrix} y_w \\ \theta_w \end{Bmatrix}^T \boldsymbol{K}_{y_w z_w} \begin{Bmatrix} y_w \\ \theta_w \end{Bmatrix} = \frac{1}{2}\left(k_t y_w^2 + 2k_t d \theta_w y_w + k_r \theta_w^2 + k_t d^2 \theta_w^2\right) \tag{3.18}$$

This includes the translational component in y_w-axis and rotational component about x_w-axis.

3.4.2. Potential Energy in $x_w z_w$-plane

The WA model in $x_w z_w$-plane is depicted in Figure 3-5:

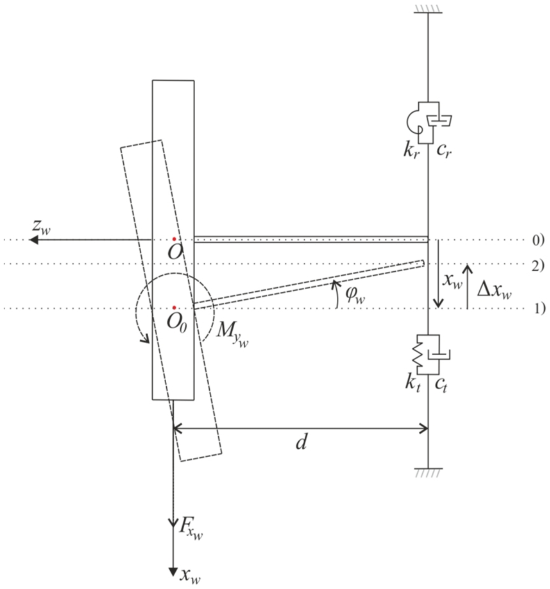

Figure 3-5 WA model in x_wz_w-plane

Similarly, apply a virtual displacement, x_w, at the flywheel CoM, O, positively (i.e. downward in x_w-axis), the linear spring then produces a compressive force, F_{x_w}. Let the new CoM be O_0. Next, apply a virtual rotation, φ_w, at O_0 positively (i.e. anticlockwise), torsional spring then produces an extensive moment, M_{y_w}. Since the rotational angle is assumed to be small, then $\Delta x_w = \varphi_w d$. Since only linear spring can produce extensive or compressive forces, the total extension is thus the sum of x_w and Δx_w. Note that in this case x_w and Δx_w are in opposite directions. Hence the total force, F_{x_w}, in x_wz_w-plane can be obtained as:

$$F_{x_w} = k_t x_w - k_t d\varphi_w \tag{3.19}$$

The total moment, M_{y_w}, can be obtained in a similar manner as that in y_wz_w-plane:

$$M_{y_w} = -k_t d x_w + \left(k_r + k_t d^2\right)\varphi_w \tag{3.20}$$

The stiffness matrix in x_wz_w-plane, $\boldsymbol{K}_{x_wz_w}$, is thus:

$$\boldsymbol{K}_{x_wz_w} = \begin{bmatrix} k_t & -k_t d \\ -k_t d & k_r + k_t d^2 \end{bmatrix} \tag{3.21}$$

Comparing Eqs. (3.17) and (3.21), the two stiffness matrices have opposite signs in the off-diagonal elements and diagonal elements are the same, verifying the earlier statement.

The total potential energy in $x_w z_w$-plane (radial DoFs only) is thus derived as:

$$U_{x_w z_w} = \frac{1}{2}\begin{Bmatrix} x_w \\ \varphi_w \end{Bmatrix}^T \boldsymbol{K}_{x_w z_w} \begin{Bmatrix} x_w \\ \varphi_w \end{Bmatrix} = \frac{1}{2}\left(k_t x_w^2 - 2k_t \varphi_w d x_w + k_r \varphi_w^2 + k_t d^2 \varphi_w^2\right) \tag{3.22}$$

Note that from Eqs. (3.18) and (3.22), the potential energy in radial DoFs in each plane is contributed from three components: the linear spring, the torsional spring and their coupled influences. In axial translational DoF, the potential energy, U_{z_w}, is independent from others and can be derived as:

$$U_{z_w} = \frac{1}{2} k_z z_w^2 \tag{3.23}$$

The total potential energy of the flywheel, U_w, is thus:

$$U_w = \frac{1}{2}\left(k_t x_w^2 - 2k_t \varphi_w d x_w + k_r \varphi_w^2 + k_t d^2 \varphi_w^2 + k_t y_w^2 + 2k_t d \theta_w y_w + k_r \theta_w^2 + k_t d^2 \theta_w^2 + k_z z_w^2\right) \tag{3.24}$$

3.5. Work Done

To complete the mass balanced WA microvibration model, the work done by the linear and torsional dashpots must be included. For simplicity, the damping of the suspension system is assumed to be viscous type. It is modeled as linear and torsional dashpots in parallel to linear and torsional springs. Using the virtual displacement method, the virtual work done by the soft-suspension system, δQ, can be written as:

$$\delta Q = F_i \delta x_i \tag{3.25}$$

where F_i are the forces or moments produced by dashpots; δx_i are the corresponding virtual displacements or rotations.

Since both linear and torsional dashpots are viscous type, the damping forces, Q_i, are the product of the damping coefficients and the corresponding velocities in each DoF. Hence Eq. (3.25) can also be written as:

$$\delta Q = -c_i \dot{x}_i \delta x_i \tag{3.26}$$

where c_i are the damping coefficients of dashpots.

From Figure 3-2, dashpots can be considered exhibiting “similar” effects to the system as the springs, i.e. springs provide restoring forces with dashpots provide damping forces. The work done expressions by the dashpots must also have similar forms as the potential energy expressions.

3.5.1. Work Done in $y_w z_w$-plane

Examining Eqs. (3.14) and (3.15), the damping force and moment produced by the linear and torsional dashpots can be obtained respectively as:

$$F'_{y_w} = -\left(c_t \dot{y}_w + c_t d \dot{\theta}_w\right) \tag{3.27}$$

$$M'_{x_w} = -\left(c_t d \dot{y}_w + \left(c_r + c_t d^2\right)\dot{\theta}_w\right) \tag{3.28}$$

Writing Eqs. (3.27) and (3.28) into matrix form, gives:

$$\begin{bmatrix} F'_{y_w} \\ M'_{x_w} \end{bmatrix} = -\begin{bmatrix} c_t & c_t d \\ c_t d & c_r + c_t d^2 \end{bmatrix} \begin{bmatrix} \dot{y}_w \\ \dot{\theta}_w \end{bmatrix} \tag{3.29}$$

From Eq. (3.29), the virtual work done in $y_w z_w$-plane, $\delta \boldsymbol{W}_{y_w z_w}$, is thus:

$$\delta \boldsymbol{W}_{y_w z_w} = -\begin{bmatrix} c_t & c_t d \\ c_t d & c_r + c_t d^2 \end{bmatrix} \begin{bmatrix} \dot{y}_w \delta y_w \\ \dot{\theta}_w \delta \theta_w \end{bmatrix} \tag{3.30}$$

and the damping matrix in $y_w z_w$-plane, $\boldsymbol{C}_{y_w z_w}$, is:

$$\boldsymbol{C}_{y_w z_w} = \begin{bmatrix} c_t & c_t d \\ c_t d & c_r + c_t d^2 \end{bmatrix} \tag{3.31}$$

3.5.2. Work Done in $x_w z_w$-plane

Examining Eqs. (3.19) and (3.20), the damping force and moment produced by the linear and torsional dashpots can be obtained respectively as:

$$F'_{x_w} = -\left(c_t \dot{x}_w - c_t d \dot{\varphi}_w\right) \tag{3.32}$$

$$M'_{y_w} = -\left(-c_t d \dot{x}_w + \left(c_r + c_t d^2\right) \dot{\varphi}_w\right) \tag{3.33}$$

Writing Eqs. (3.32) and (3.33) into matrix form, gives:

$$\begin{bmatrix} F'_{x_w} \\ M'_{y_w} \end{bmatrix} = -\begin{bmatrix} c_t & -c_t d \\ -c_t d & c_r + c_t d^2 \end{bmatrix} \begin{bmatrix} \dot{x}_w \\ \dot{\varphi}_w \end{bmatrix} \tag{3.34}$$

The virtual work done in $x_w z_w$-plane, $\delta \boldsymbol{W}_{x_w z_w}$, is thus:

$$\delta \boldsymbol{W}_{x_w z_w} = -\begin{bmatrix} c_t & -c_t d \\ -c_t d & c_r + c_t d^2 \end{bmatrix} \begin{bmatrix} \dot{x}_w \delta x_w \\ \dot{\varphi}_w \delta \varphi_w \end{bmatrix} \tag{3.35}$$

and the damping matrix in $x_w z_w$-plane, $\boldsymbol{C}_{x_w z_w}$, is:

$$\boldsymbol{C}_{x_w z_w} = \begin{bmatrix} c_t & -c_t d \\ -c_t d & c_r + c_t d^2 \end{bmatrix} \tag{3.36}$$

In axial translational DoF, only linear dashpot exists, thus:

$$\delta W_{z_w} = -c_z \dot{z}_w \delta z_w \tag{3.37}$$

3.6. Equations of Motion in Physical Coordinates

The linearized Lagrangian, L_w, can be obtained by substituting the kinetic energy (i.e. Eq. (3.12) in linearized form) and the potential energy (i.e. Eq. (3.24) in linearized form) into Eq. (3.2), it gives:

$$\begin{aligned} L_w &= T_w - U_w \\ &= \frac{1}{2}\left[M_w \left(\dot{x}_w^2 + \dot{y}_w^2 + \dot{z}_w^2 \right) + \left(\dot{\theta}_w^2 + \dot{\varphi}_w^2 \right) I_r + \left(\Omega^2 - 2\Omega \dot{\varphi}_w \theta_w \right) I_z \right] \\ &-\frac{1}{2}\left(k_t x_w^2 - 2k_t \varphi_w d x_w + k_r \varphi_w^2 + k_t d^2 \varphi_w^2 + k_t y_w^2 + 2k_t d \theta_w y_w + k_r \theta_w^2 + k_t d^2 \theta_w^2 + k_z z_w^2 \right) \end{aligned} \tag{3.38}$$

Considering, the five EoMs w.r.t. the five generalized coordinates: x_w, y_w, z_w, θ_w and φ_w can be written from Eq. (3.1) respectively as:

$$\begin{cases} \dfrac{d}{dt}\left(\dfrac{\partial L_w}{\partial \dot{x}_w} \right) - \dfrac{\partial L_w}{\partial x_w} = F'_{x_w} \\ \dfrac{d}{dt}\left(\dfrac{\partial L_w}{\partial \dot{y}_w} \right) - \dfrac{\partial L_w}{\partial y_w} = F'_{y_w} \\ \dfrac{d}{dt}\left(\dfrac{\partial L_w}{\partial \dot{z}_w} \right) - \dfrac{\partial L_w}{\partial z_w} = F'_{z_w} \\ \dfrac{d}{dt}\left(\dfrac{\partial L_w}{\partial \dot{\theta}_w} \right) - \dfrac{\partial L_w}{\partial \theta_w} = M'_{x_w} \\ \dfrac{d}{dt}\left(\dfrac{\partial L_w}{\partial \dot{\varphi}_w} \right) - \dfrac{\partial L_w}{\partial \varphi_w} = M'_{y_w} \end{cases} \tag{3.39}$$

The EoM w.r.t. x_w is thus derived as:

$$M_w \ddot{x}_w + \left(c_t \dot{x}_w - c_t d \dot{\varphi}_w \right) + \left(k_t x_w - k_t d \varphi_w \right) = 0 \tag{3.40}$$

The EoM w.r.t. y_w is thus derived as:

$$M_w \ddot{y}_w + \left(c_t \dot{y}_w + c_t d \dot{\theta}_w\right) + \left(k_t y_w + k_t d \theta_w\right) = 0 \tag{3.41}$$

The EoM w.r.t. z_w is thus derived as:

$$M_w \ddot{z}_w + c_z \dot{z}_w + k_z z_w = 0 \tag{3.42}$$

The EoM w.r.t. θ_w is thus derived as:

$$\ddot{\theta}_w I_r + \Omega I_z \dot{\varphi}_w + \left(c_t d \dot{y}_w + \left(c_r + c_t d^2\right)\dot{\theta}_w\right) + \left(k_t d y_w + \left(k_r + k_t d^2\right)\theta_w\right) = 0 \tag{3.43}$$

The EoM w.r.t. φ_w is thus derived as:

$$\ddot{\varphi}_w I_r - \Omega I_z \dot{\theta}_w + \left(-c_t d \dot{x}_w + \left(c_r + c_t d^2\right)\dot{\varphi}_w\right) + \left(-k_t d x_w + \left(k_r + k_t d^2\right)\varphi_w\right) = 0 \tag{3.44}$$

Collecting the generalized coordinates from Eqs. (3.40) to (3.44) and composing into matrix form, gives:

$$\begin{bmatrix} M_w & 0 & 0 & 0 & 0 \\ 0 & I_r & 0 & 0 & 0 \\ 0 & 0 & M_w & 0 & 0 \\ 0 & 0 & 0 & I_r & 0 \\ 0 & 0 & 0 & 0 & M_w \end{bmatrix} \begin{Bmatrix} \ddot{x}_w \\ \ddot{\varphi}_w \\ \ddot{y}_w \\ \ddot{\theta}_w \\ \ddot{z}_w \end{Bmatrix} + \begin{bmatrix} c_t & -c_t d & 0 & 0 & 0 \\ -c_t d & c_r + c_t d^2 & 0 & -\Omega I_z & 0 \\ 0 & 0 & c_t & c_t d & 0 \\ 0 & \Omega I_z & c_t d & c_r + c_t d^2 & 0 \\ 0 & 0 & 0 & 0 & c_z \end{bmatrix} \begin{Bmatrix} \dot{x}_w \\ \dot{\varphi}_w \\ \dot{y}_w \\ \dot{\theta}_w \\ \dot{z}_w \end{Bmatrix}$$
$$+ \begin{bmatrix} k_t & -k_t d & 0 & 0 & 0 \\ -k_t d & k_r + k_t d^2 & 0 & 0 & 0 \\ 0 & 0 & k_t & k_t d & 0 \\ 0 & 0 & k_t d & k_r + k_t d^2 & 0 \\ 0 & 0 & 0 & 0 & k_t \end{bmatrix} \begin{Bmatrix} x_w \\ \varphi_w \\ y_w \\ \theta_w \\ z_w \end{Bmatrix} = \begin{Bmatrix} 0 \\ 0 \\ 0 \\ 0 \\ 0 \end{Bmatrix} \tag{3.45}$$

Remembering that for a mass balanced flywheel there are no excitations in the system, thus the terms on the right-hand-side of Eq. (3.45) are zero. Note that in both stiffness and damping matrices, the translational and rotational motion couples with each other due to the WA cantilevered configuration, i.e. there are non-zero off-diagonal elements in the two matrices. This is the main difference from the conventional mid-span configured WAs in which the motions in radial translational and rotational DoFs are uncoupled, i.e. all off-diagonal elements are zero. The coupled motions in radial DoFs make the microvibration analysis more complicated for the cantilever configured WA. For example, the closed-form expressions of responses cannot be derived for each radial DoF for the cantilever configured WA, and the five DoFs in Eq. (3.45) are best to be solved numerically.

3.7. Equations of Motion in Complex Coordinates

Eq. (3.45) can be decomposed into radial motions (i.e. a biquadratic equation in radial DoFs) and an independent equation in axial translational DoF. Complex coordinates can be used to simplify Eq. (3.45) which allows the WA structural modes to be derived in their analytical forms. Firstly, define the vector of complex coordinates, r and ϕ, as:

$$\begin{cases} r = x_w + iy_w \\ \phi = \varphi_w - i\theta_w \end{cases} \tag{3.46}$$

The real part of the coordinates refers to the motions in $x_w z_w$-plane and the imaginary part refers to the motions in $y_w z_w$-plane. Note that the minus sign in front of θ_w remedies the different conventions of sign in the two planes. Multiplying the y_w translational equation (i.e. Eq. (3.41)) by imaginary unit i and adding the x_w translational equation (i.e. Eq. (3.40)), it gives:

$$M_w\ddot{r} + \left(c_t\dot{r} - c_t d\dot{\phi}\right) + \left(k_t r - k_t d\phi\right) = 0 \tag{3.47}$$

Multiplying the x_w rotational equation (i.e. Eq. (3.43)) by $-i$ and adding it to the y_w rotational equation (i.e. Eq. (3.44)), it gives:

$$I_r\ddot{\phi} - i\Omega I_z\dot{\phi} + \left(\left(c_r + c_t d^2\right)\dot{\phi} - c_t d\dot{r}\right) + \left(\left(k_r + k_t d^2\right)\phi - k_t dr\right) = 0 \tag{3.48}$$

Eqs. (3.47) and (3.48) can be written into a more compact form as:

$$\boldsymbol{M}\ddot{\boldsymbol{q}}_w + \left(\boldsymbol{C} - i\Omega\boldsymbol{G}\right)\dot{\boldsymbol{q}}_w + \boldsymbol{K}\boldsymbol{q}_w = 0 \tag{3.49}$$

where the vector of complex coordinates, $\boldsymbol{q}_{\mathrm{w}}$, mass matrix, $\boldsymbol{M}$, gyroscopic matrix, $\boldsymbol{G}$, stiffness matrix, $\boldsymbol{K}$, and damping matrix, $\boldsymbol{C}$, are derived respectively as:

$$\boldsymbol{q}_w = \begin{Bmatrix} r \\ \phi \end{Bmatrix},\ \boldsymbol{M} = \begin{bmatrix} M_w & 0 \\ 0 & I_r \end{bmatrix},\ \boldsymbol{G} = \begin{bmatrix} 0 & 0 \\ 0 & I_z \end{bmatrix},\ \boldsymbol{K} = \begin{bmatrix} k_t & -k_t d \\ -k_t d & k_r + k_t d^2 \end{bmatrix},\ \boldsymbol{C} = \begin{bmatrix} c_t & -c_t d \\ -c_t d & c_r + c_t d^2 \end{bmatrix} \tag{3.50}$$

Note that in this case all above matrices are symmetric about their diagonals when using complex coordinates. In contrast, the gyroscopic matrix is skew-symmetric in physical coordinates, remembering that from Eq. (3.45):

$$\boldsymbol{G} = \begin{bmatrix} 0 & -\Omega I_z \\ \Omega I_z & 0 \end{bmatrix} \tag{3.51}$$

The EoM in axial translational DoF is independent from others and can be simply written as:

$$M_w \ddot{z}_w + c_z \dot{z}_w + k_t z_w = 0 \tag{3.52}$$

Natural frequencies of the WA can be obtained from the general solutions of the homogeneous equation of the undamped and free system. Since the damping of suspension system is usually very small, damped natural frequencies of the system are not so different from the undamped ones. Thus to characterize flywheel structural modes and their interactions with harmonics, an undamped and free system is used.

As mentioned previously, radial translational DoFs are elastically coupled with rotational DoFs in each plane. The free whirling of the undamped system can be solved from the homogeneous equation associated with Eq. (3.49) in an undamped form. By introducing a solution of the type:

$$\begin{Bmatrix} r \\ \phi \end{Bmatrix} = \begin{Bmatrix} r_0 \\ \phi_0 \end{Bmatrix} e^{i\omega t} \tag{3.53}$$

As solution of the Eigen-problem are imaginary, it is useful to directly use a real frequency, ω, as an unknown rather than complex frequency, λ (defined as $\lambda = \sigma \pm i\omega$, where σ is the decay rate). Placing their first and second time derivative vectors into Eqs. (3.47) and (3.48), the following algebraic linear equations are readily obtained:

$$\begin{cases} r_0\left(k_t - M_w\omega^2\right) + \phi_0\left(-k_t d\right) = 0 \\ r_0\left(-k_t d\right) + \phi_0\left(k_r + k_t d^2 + \Omega I_z \omega - I_r \omega^2\right) = 0 \end{cases} \tag{3.54}$$

Its characteristic equation is derived as:

$$\det\begin{bmatrix} k_t - M_w\omega^2 & -k_t d \\ -k_t d & k_r + k_t d^2 + \Omega I_z \omega - I_r \omega^2 \end{bmatrix} = 0 \tag{3.55}$$

Therefore the cross-product of Eq. (3.55) gives expressions of natural frequencies or the WA structural modes in radial DoFs as:

$$\omega^4 - \Omega\frac{I_z}{I_r}\omega^3 - \left(\frac{k_t}{M_w} + \frac{k_r + k_t d^2}{I_r}\right)\omega^2 + \Omega\frac{k_t I_z}{M_w I_r}\omega + \frac{k_t k_r}{M_w I_r} = 0 \tag{3.56}$$

Eq. (3.56) includes four solutions and thus four structural modes of the WA: two radial translational modes and two “rocking” modes. The four solutions in Eq. (3.56) are all speed-dependent qualities, and as expected they are coupled and very difficult to be solved analytically. Instead, its numerical solutions can be easily computed and the results are presented as Campbell diagrams.

The natural frequency in axial translational DoF is simply derived as:

$$\omega_z = \sqrt{\frac{k_z}{M_w}} \tag{3.57}$$

Validation of the EoM is discussed in Chapter 5.

Interactions between the forward whirl and the fundamental harmonic yield the condition for forward synchronous critical speed. By inserting $\omega = \Omega$ into Eq. (3.56), the following quadratic equation can be obtained:

$$\Omega^4 M_w \left(I_z - I_r\right) - \Omega^2 \left[\left(I_z - I_r\right) k_t - M_w \left(k_r + k_t d^2\right)\right] - k_t k_r = 0 \tag{3.58}$$

The synchronous critical speed is thus derived from Eq. (3.58) as:

$$\Omega_{cr} = \sqrt{\frac{k_t \left(I_z - I_r\right) - M_w \left(k_r + k_t d^2\right) \pm \sqrt{\left[k_t \left(I_z - I_r\right) - M_w \left(k_r + k_t d^2\right)\right]^2 + 4 M_w \left(I_z - I_r\right) k_t k_r}}{2 M_w \left(I_z - I_r\right)}} \tag{3.59}$$

Note that in Eq. (3.59), if $I_z > I_r$ (i.e. a thin disc), one of the solution is imaginary and only one synchronous critical speed exists.

3.8. Statically Mass Imbalanced Flywheel

To derive the EoMs of a fully mass imbalanced flywheel, the statically mass imbalanced case is first considered and the dynamically mass imbalanced case next. The static mass imbalance can be modeled as a point mass, m_s, placed at radius, r_s, on the flywheel (see Figure 3-2 for detail). Note that amplitudes of the imbalance force are defined as the values proportional to the radial distance from the mass imbalance to the shaft axis. This radial distance however, does not have to be the flywheel radius in practice. In the modeling, the radial distance is expressed as r_s rather than the flywheel radius, although they are the same in Figure 3-2. The same argument applies to the dynamic mass imbalances presented in the Section 3.9.

From Figure 3-2, the point mass is placed in y_w-axis, the position of the point mass can be written in the body frame as:

$$\boldsymbol{u}_{m_s} = \begin{Bmatrix} 0 \\ r_s \\ 0 \end{Bmatrix} \tag{3.60}$$

Since the analysis is carried out w.r.t. the inertial frame, Eq. (3.60) needs to be transformed from the body frame to the inertial frame. Using the transformation matrix given in Appendix A, the position of point mass can be written in the body frame as:

$$\boldsymbol{U}_{m_{s\_rotational}} = \begin{bmatrix} \left(-\cos\varphi_w \sin\Omega t + \sin\varphi_w \sin\theta_w \cos\Omega t\right) r_s \\ \left(\cos\theta_w \cos\Omega t\right) r_s \\ \left(\sin\varphi_w \sin\Omega t + \cos\varphi_w \sin\theta_w \cos\Omega t\right) r_s \end{bmatrix} \tag{3.61}$$

Eq. (3.61) describes the total rotational displacement of the point mass w.r.t. inertial frame.

Consider that flywheel is also free to move in the three translational DoFs, the total translational displacement vector of the point mass can be written as:

$$\boldsymbol{U}_{m_{s\_translational}} = \begin{Bmatrix} x_w \\ y_w \\ z_w \end{Bmatrix} \tag{3.62}$$

Hence the total displacement vector, $\boldsymbol{U}_{m_s}$, of the point mass is expressed as the sum of rotational and translational displacements:

$$\boldsymbol{U}_{m_s} = \begin{Bmatrix} \left(-\cos\varphi_w \sin\Omega t + \sin\varphi_w \sin\theta_w \cos\Omega t\right) r_s + x_w \\ \left(\cos\theta_w \cos\Omega t\right) r_s + y_w \\ \left(\sin\varphi_w \sin\Omega t + \cos\varphi_w \sin\theta_w \cos\Omega t\right) r_s + z_w \end{Bmatrix} \tag{3.63}$$

The point mass velocity vector, $\boldsymbol{V}_{m_s}$, can be obtained by differentiating Eq. (3.63) w.r.t. time. Thus the kinetic energy expression of the point mass can be derived:

$$
\begin{aligned}
T_{m_s} &= \frac{1}{2} m_s \boldsymbol{V}_{m_s}^T \boldsymbol{V}_{m_s} \\
&= \frac{1}{2} m_s \Big\{ \dot{x}_w^2 + \dot{y}_w^2 + \dot{z}_w^2 + r_s^2 \left[\dot{\varphi}_w^2 \left(1 - \cos^2 \Omega t \cos^2 \theta_w\right) + \dot{\theta}_w^2 \cos^2 \Omega t + \Omega^2 \right] \\
&-2 r_s \dot{y}_w \left(\dot{\theta}_w \cos \Omega t \sin \theta_w + \Omega \cos \theta_w \sin \Omega t \right) \\
&+2 r_s^2 \dot{\varphi}_w \left(-\Omega \sin \theta_w + \dot{\theta}_w \cos \Omega t \cos \theta_w \sin \Omega t \right) \\
&+2 r_s \dot{x}_w \Big[\dot{\theta}_w \cos \Omega t \cos \theta_w \sin \varphi_w - \Omega \left(\cos \Omega t \cos \varphi_w + \sin \Omega t \sin \theta_w \sin \varphi_w \right) \\
&\qquad + \dot{\varphi}_w \left(\cos \Omega t \cos \varphi_w \sin \theta_w + \sin \Omega t \sin \varphi_w \right) \Big] \\
&+ r_s \dot{z}_w \big(-2\Omega \cos \varphi_w \sin \Omega t \sin \theta_w + 2\Omega \cos \Omega t \sin \varphi_w + 2\dot{\theta}_w \cos \Omega t \cos \theta_w \cos \varphi_w \\
&+2 \dot{\varphi}_w \cos \varphi_w \sin \Omega t - 2 \dot{\varphi}_w \cos \Omega t \sin \theta_w \sin \varphi_w \big) \Big\}
\end{aligned}
\tag{3.64}
$$

With the kinetic energy of the mass balanced WA (i.e. Eq. (3.9)), the total kinetic energy of the statically mass imbalanced flywheel can be derived. It is expressed in compact form as:

$$
\begin{aligned}
T_{w+m_s} &= \frac{1}{2} \Big[\left(M_w + m_s \right) \left(\dot{x}_w^2 + \dot{y}_w^2 + \dot{z}_w^2 \right) + \dot{\theta}_w^2 \left(m_s r_s^2 \cos^2 \Omega t + I_r \right) \\
&+ \dot{\varphi}_w^2 \left(m_s r_s^2 - m_s r_s^2 \cos^2 \Omega t \cos^2 \theta_w + \cos^2 \theta_w I_r + \sin^2 \theta_w I_z \right) \\
&+ \Omega^2 \left(m_s r_s^2 + I_z \right) - 2 m_s r_s \dot{y}_w \left(\dot{\theta}_w \cos \Omega t \sin \theta_w + \Omega \cos \theta_w \sin \Omega t \right) \\
&+2 m_s r_s \dot{x}_w \big(\dot{\theta}_w \cos \Omega t \cos \theta_w \sin \varphi_w - \Omega \cos \Omega t \cos \varphi_w - \Omega \sin \Omega t \sin \theta_w \sin \varphi_w \\
&\qquad + \dot{\varphi}_w \cos \Omega t \cos \varphi_w \sin \theta_w + \dot{\varphi}_w \sin \Omega t \sin \varphi_w \big) \\
&+2 \dot{\varphi}_w \left(m_s r_s^2 \dot{\theta}_w \cos \Omega t \cos \theta_w \sin \Omega t - m_s r_s^2 \sin \theta_w - \Omega \sin \theta_w I_z \right) \\
&+ m_s r_s \dot{z}_w \big(-2\Omega \cos \varphi_w \sin \Omega t \sin \theta_w + 2\Omega \cos \Omega t \sin \varphi_w + 2\dot{\theta}_w \cos \Omega t \cos \theta_w \cos \varphi_w \\
&+2 \dot{\varphi}_w \cos \varphi_w \sin \Omega t - 2 \dot{\varphi}_w \cos \Omega t \sin \varphi_w \sin \varphi_w \big) \Big]
\end{aligned}
\tag{3.65}
$$

Eq. (3.65) can be simplified considering that small angle assumption, small mass imbalance assumption, also the fact that the flywheel spin speed (i.e. **Ω**) is much larger than any perturbation speed in the five DoFs. The detailed simplification process is given in Appendix B. The final expression is shown as:

$$
\begin{aligned}
T_{w+m_s} &\approx \frac{1}{2} \Big[M_w \left(\dot{x}_w^2 + \dot{y}_w^2 + \dot{z}_w^2 \right) + \dot{\theta}_w^2 I_r + \dot{\varphi}_w^2 I_r + \Omega^2 I_z - 2 m_s r_s \dot{y}_w \Omega \sin \Omega t \\
&-2 m_s r_s \dot{x}_w \Omega \cos \Omega t - 2 \dot{\varphi}_w \Omega \theta_w I_z \Big]
\end{aligned}
\tag{3.66}
$$

The potential energy and work done expressions derived for the mass balanced WA are not changed in the statically mass imbalanced flywheel model. Hence the linearized Lagrangian of the statically mass imbalanced flywheel model can be derived as:

$$
\begin{aligned}
&L_{w+m_s} = T_{w+m_s} - U_w \\
&= \frac{1}{2}\Big[M_w\left(\dot{x}_w^2 + \dot{y}_w^2 + \dot{z}_w^2\right) + \dot{\theta}_w^2 I_r + \dot{\varphi}_w^2 I_r + \Omega^2 I_z - 2m_s r_s \dot{y}_w \Omega \sin\Omega t \\
&-2m_s r_s \dot{x}_w \Omega \cos\Omega t - 2\dot{\varphi}_w \Omega \theta_w I_z \Big] \\
&-\frac{1}{2}\left(k_t x_w^2 - 2k_t \varphi_w d x_w + k_r \varphi_w^2 + k_t d^2 \varphi_w^2 + k_t y_w^2 + 2k_t d \theta_w y_w + k_r \theta_w^2 + k_t d^2 \theta_w^2\right)
\end{aligned}
\tag{3.67}
$$

The EoMs of the statically mass imbalanced flywheel can be derived for the five DoFs as:

$$
\begin{cases}
M_w \ddot{x}_w + k_t x_w - k_t d \varphi_w = -m_s r_s \Omega^2 \sin\Omega t - \left(c_t \dot{x}_w - c_t d \dot{\varphi}_w\right) \\
M_w \ddot{y}_w + k_t y_w + k_t d \theta_w = m_s r_s \Omega^2 \cos\Omega t - \left(c_t \dot{y}_w + c_t d \dot{\theta}_w\right) \\
\ddot{\theta}_w I_r + \Omega \dot{\varphi}_w I_z + k_t d y_w + (k_r + k_t d^2)\theta_w = -\left(c_t d \dot{y}_w + \left(c_r + c_t d^2\right)\dot{\theta}_w\right) \\
\ddot{\varphi}_w I_r - \Omega \dot{\theta}_w I_z - k_t d x_w + (k_r + k_t d^2)\varphi_w = -\left(-c_t d \dot{x}_w + \left(c_r + c_t d^2\right)\dot{\varphi}_w\right) \\
M_w \ddot{z}_w + k_z z_w = -c_z \dot{z}_w
\end{cases}
\tag{3.68}
$$

When composing in matrix form:

$$
\begin{aligned}
&\begin{bmatrix} M_w & 0 & 0 & 0 & 0 \\ 0 & I_r & 0 & 0 & 0 \\ 0 & 0 & M_w & 0 & 0 \\ 0 & 0 & 0 & I_r & 0 \\ 0 & 0 & 0 & 0 & M_w \end{bmatrix}
\begin{Bmatrix} \ddot{x}_w \\ \ddot{\varphi}_w \\ \ddot{y}_w \\ \ddot{\theta}_w \\ \ddot{z}_w \end{Bmatrix}
+ \begin{bmatrix} c_t & -c_t d & 0 & 0 & 0 \\ -c_t d & c_r + c_t d^2 & 0 & -\Omega I_z & 0 \\ 0 & 0 & c_t & c_t d & 0 \\ 0 & \Omega I_z & c_t d & c_r + c_t d^2 & 0 \\ 0 & 0 & 0 & 0 & c_z \end{bmatrix}
\begin{Bmatrix} \dot{x}_w \\ \dot{\varphi}_w \\ \dot{y}_w \\ \dot{\theta}_w \\ \dot{z}_w \end{Bmatrix} \\
&+ \begin{bmatrix} k_t & -k_t d & 0 & 0 & 0 \\ -k_t d & k_r + k_t d^2 & 0 & 0 & 0 \\ 0 & 0 & k_t & k_t d & 0 \\ 0 & 0 & k_t d & k_r + k_t d^2 & 0 \\ 0 & 0 & 0 & 0 & k_z \end{bmatrix}
\begin{Bmatrix} x_w \\ \varphi_w \\ y_w \\ \theta_w \\ z_w \end{Bmatrix}
= \begin{Bmatrix} -m_s r_s \Omega^2 \sin\Omega t \\ 0 \\ m_s r_s \Omega^2 \cos\Omega t \\ 0 \\ 0 \end{Bmatrix}
\end{aligned}
\tag{3.69}
$$

As seen from Eq. (3.69), the addition of the static mass imbalance on the flywheel produces a forcing term in each of the two radial translational DoFs. The two forcing terms have amplitudes proportional to angular speed squared with frequencies of angular speeds. Although the radial translational mode and the "rocking" mode couples with each other for a cantilever configured WA, static mass imbalance does not influence the flywheel radial rotational motions. From the definition of the static mass imbalance, this only causes the flywheel CoM offsets from its spin axis (although does not appear in Eq. (3.69) due to the small mass imbalance assumption), thus it only excites the radial translational modes. Note also that the static mass imbalance on the flywheel does not change the flywheel total mass if small mass assumption is used. This left the left-hand-side of the equation unchanged as in the mass balanced model.

3.9. Dynamically Mass Imbalanced Flywheel

To complete the WA microvibration model, dynamic mass imbalances must be added to the flywheel to capture its radial moment microvibrations. Physically, dynamic mass imbalances are caused by misalignment of the principle axis of flywheel and its spin axis. Dynamic mass imbalances are modeled using two identical point masses, m_d, placed 180° apart at a radial distance, r_d, and a shaft distance, $2h$, on flywheel (see Figure 3-2 for detail). The two point masses create a moment when flywheel spins. Positions of the two point masses can be described in the body frame as:

$$\boldsymbol{u}_{m_{d1}} = \begin{Bmatrix} 0 \\ r_d \\ -h \end{Bmatrix} \tag{3.70}$$

$$\boldsymbol{u}_{m_{d2}} = \begin{Bmatrix} 0 \\ -r_d \\ h \end{Bmatrix} \tag{3.71}$$

Eq. (3.70) and (3.71) define the position of dynamic mass imbalances. Using the same transformation matrix given in Appendix A, the rotational displacements of the two dynamic mass imbalances w.r.t. the inertial frame can be derived. Furthermore, the two point masses can also move in the three translational DoFs, the total displacement vector of the two mass imbalances, $\boldsymbol{U}_{m_{d1}}$ and $\boldsymbol{U}_{m_{d2}}$, can be derived respectively as:

$$\boldsymbol{U}_{m_{d1}} = \begin{bmatrix} \left(-\cos\varphi_w \sin\Omega t + \sin\varphi_w \sin\theta_w \cos\Omega t\right) r_d - h\sin\varphi_w \cos\theta_w + x_w \\ \left(\cos\theta_w \cos\Omega t\right) r_d + h\sin\theta_w + y_w \\ \left(\sin\varphi_w \sin\Omega t + \cos\varphi_w \sin\theta_w \cos\Omega t\right) r_d - h\cos\varphi_w \cos\theta_w + z_w \end{bmatrix} \quad (3.72)$$

$$\boldsymbol{U}_{m_{d2}} = \begin{bmatrix} -\left(-\cos\varphi_w \sin\Omega t + \sin\varphi_w \sin\theta_w \cos\Omega t\right) r_d + h\sin\varphi_w \cos\theta_w + x_w \\ -\left(\cos\theta_w \cos\Omega t\right) r_d - h\sin\theta_w + y_w \\ -\left(\sin\varphi_w \sin\Omega t + \cos\varphi_w \sin\theta_w \cos\Omega t\right) r_d + h\cos\varphi_w \cos\theta_w + z_w \end{bmatrix} \quad (3.73)$$

The two velocity vectors can be obtained by differentiating Eqs. (3.72) and (3.73) w.r.t. time. The total kinetic energy of the two dynamic mass imbalances can be derived as:

$$\begin{aligned} T_{m_d} = m_d \Big\{ & \dot{x}_w^2 + \dot{y}_w^2 + \dot{z}_w^2 + r_d^2\Omega^2 + \dot{\varphi}_w^2 \Big[h^2\cos^2\theta_w + r_d^2\left(1 - \cos^2\Omega t \cos^2\theta_w\right) \\ & - 2 r_d h \sin\theta_w \cos\theta_w \cos\Omega t \Big] \\ & + \dot{\theta}_w^2\left(r_d^2\cos^2\Omega t + h^2\right) - 2 r_d \dot{\theta}_w \sin\Omega t \left[h\Omega - \dot{\varphi}_w\left(r_d\cos\theta_w\cos\Omega t + h\sin\theta_w\right)\right] \\ & - 2 r_d \dot{\varphi}_w \Omega\left(r_d\sin\theta_w - h\cos\Omega t\cos\theta_w\right)\Big\} \end{aligned} \quad (3.74)$$

The total kinetic energy of the fully mass imbalanced flywheel is the sum of the mass balanced WA with both statically and dynamically mass imbalanced cases. It is derived to be Eq. (3.75) that is shown on the next page.

The same assumptions used for simplifying the statically mass imbalanced case are also applied to Eq. (3.75). The simplified total kinetic energy of the fully mass imbalanced flywheel is derived. Details are shown in Appendix B with the final result is derived to be Eq. (3.76) that is shown on the next page.

$$
\begin{aligned}
T_{w+m_s+m_d} &= \frac{1}{2}\Big[\left(M_w + m_s + 2m_d\right)\left(\dot{x}_w^2 + \dot{y}_w^2 + \dot{y}_w^2\right) \\
&+\dot{\theta}_w^2\left(m_s r_s^2 \cos^2 \Omega t + I_r + 2m_d r_d^2 \cos^2 \Omega t + 2m_d h^2\right) \\
&+\dot{\varphi}_w^2\Big(m_s r_s^2 - m_s r_s^2 \cos^2 \Omega t \cos^2 \theta_w + \cos^2 \theta_w I_r + \sin^2 \theta_w I_z + 2m_d h^2 \cos^2 \theta_w + 2m_d r_d^2 \\
&\qquad - 2m_d r_d^2 \cos^2 \Omega t \cos^2 \theta_w - 4m_d r_d h \sin \theta_w \cos \theta_w \cos \Omega t\Big) \\
&+\Omega^2\left(m_s r_s^2 + I_z + 2m_d r_d^2\right) - 2m_s r_s \dot{y}_w\left(\dot{\theta}_w \cos \Omega t \sin \theta_w + \Omega \cos \theta_w \sin \Omega t\right) \\
&+2m_s r_s \dot{x}_w\Big(\dot{\theta}_w \cos \Omega t \cos \theta_w \sin \varphi_w - \Omega \cos \Omega t \cos \varphi_w - \Omega \sin \Omega t \sin \theta_w \sin \varphi_w \\
&\qquad +\dot{\varphi}_w \cos \Omega t \cos \varphi_w \sin \theta_w + \dot{\varphi}_w \sin \Omega t \sin \varphi_w\Big) \\
&+2\dot{\varphi}_w\left(m_s r_s^2 \dot{\theta}_w \cos \Omega t \cos \theta_w \sin \Omega t - m_s r_s^2 \sin \theta_w - \Omega \sin \theta_w I_z\right) \\
&-4r\dot{\theta}_w \sin \Omega t\left(m_d h \Omega - m_d \dot{\varphi}_w r_d \cos \Omega t \cos \theta_w - m_d \dot{\varphi}_w h \sin \theta_w\right) \\
&-4r_d \dot{\varphi}_w \Omega\left(m_d r_d \sin \theta_w - m_d h \cos \Omega t \cos \theta_w\right) \\
&+m_s r_s \dot{z}_w\Big(-2\Omega \cos \varphi_w \sin \Omega t \sin \theta_w + 2\Omega \cos \Omega t \sin \varphi_w + 2\dot{\theta}_w \cos \Omega t \cos \theta_w \cos \varphi_w \\
&+2\dot{\varphi}_w \cos \varphi_w \sin \Omega t - 2\dot{\varphi}_w \cos \Omega t \sin \varphi_w \sin \varphi_w\Big)\Big]
\end{aligned}
\tag{3.75}
$$

$$
\begin{aligned}
T_{w+ms+md} &\approx M_w\left(\dot{x}_w^2 + \dot{y}_w^2 + \dot{z}_w^2\right) + \dot{\theta}_w^2 I_r + \dot{\varphi}_w^2 I_r + \Omega^2 I_z - 2m_s r_s \dot{y}_w \Omega \sin \Omega t \\
&-2m_s r_s \dot{x}_w \Omega \cos \Omega t - 2\dot{\varphi}_w \Omega \theta_w I_z - 4r_d m_d h \dot{\theta}_w \Omega \sin \Omega t - 4r_d \dot{\varphi}_w \Omega\left(m_d r_d \theta_w - m_d h \cos \Omega t\right)
\end{aligned}
\tag{3.76}
$$

The total potential energy and work done remain unchanged, thus the linearized Lagrangian of the fully mass imbalanced flywheel can be derived as:

$$
\begin{aligned}
L_{w+m_s} &= T_{w+m_s+m_d} - U_w \\
&= M_w\left(\dot{x}_w^2 + \dot{y}_w^2 + \dot{z}_w^2\right) + \dot{\theta}_w^2 I_r + \dot{\varphi}_w^2 I_r + \Omega^2 I_z - 2m_s r_s \dot{y}_w \Omega \sin \Omega t - 2m_s r_s \dot{x}_w \Omega \cos \Omega t \\
&\qquad - 2\dot{\varphi}_w \Omega \theta_w I_z - 4r_d m_d h \dot{\theta}_w \Omega \sin \Omega t - 4r_d \dot{\varphi}_w \Omega\left(m_d r_d \theta_w - m_d h \cos \Omega t\right) \\
&-\frac{1}{2}\left(k_t x_w^2 - 2k_t \varphi_w d x_w + k_r \varphi_w^2 + k_t d^2 \varphi_w^2 + k_t y_w^2 + 2k_t d \theta_w y_w + k_r \theta_w^2 + k_t d^2 \theta_w^2\right)
\end{aligned}
\tag{3.77}
$$

EoMs of the fully mass imbalanced flywheel can be expressed by inserting Eq. (3.77) into Eq. (3.39). In order to get the simplest form, small displacement and small mass imbalance assumptions, etc. are also applied to the rotational EoMs, the results are shown as Eq. (3.78) on the next page.

Eq. (3.78) is composed into matrix form and shown in Eq. (3.79). Note that due to small mass assumption, the left-hand-side of Eq. (3.79) remains unchanged.

$$\begin{cases} M_w\ddot{x}_w + k_t x_w - k_t d\varphi_w = -m_s r_s \Omega^2 \sin\Omega t - \left(c_t\dot{x}_w - c_t d\dot{\varphi}_w\right) \\ M_w\ddot{y}_w + k_t y_w + k_t d\theta_w = m_s r_s \Omega^2 \cos\Omega t - \left(c_t\dot{y}_w + c_t d\dot{\theta}_w\right) \\ \ddot{\theta}_w I_r + \Omega\dot{\varphi}_w I_z + k_t d y_w + (k_r + k_t d^2)\theta_w = 2m_d r_d h\Omega^2 \cos\Omega t - \left(c_t d\dot{y}_w + \left(c_r + c_t d^2\right)\dot{\theta}_w\right) \\ \ddot{\varphi}_w I_r - \Omega\dot{\theta}_w I_z - k_t d x_w + (k_r + k_t d^2)\varphi_w = 2m_d r_d h\Omega^2 \sin\Omega t - \left(-c_t d\dot{x}_w + \left(c_r + c_t d^2\right)\dot{\varphi}_w\right) \\ M_w\ddot{z} + k_z z_w = -c_z\dot{z}_w \end{cases} \tag{3.78}$$

On the right-hand-side however, moment excitations from the two dynamic mass imbalances appear in radial rotational DoFs. The two moment excitations also have magnitudes proportional to the angular speed squared with frequencies equal to angular speeds. Note that in practice, the exponent on angular speed on right-hand-side of Eq. (3.79) might be slightly different from two. This is further discussed in Chapter 5.

$$\begin{aligned} &\begin{bmatrix} M_w & 0 & 0 & 0 & 0 \\ 0 & I_r & 0 & 0 & 0 \\ 0 & 0 & M_w & 0 & 0 \\ 0 & 0 & 0 & I_r & 0 \\ 0 & 0 & 0 & 0 & M_w \end{bmatrix} \begin{Bmatrix} \ddot{x}_w \\ \ddot{\varphi}_w \\ \ddot{y}_w \\ \ddot{\theta}_w \\ \ddot{z}_w \end{Bmatrix} + \begin{bmatrix} c_t & -c_t d & 0 & 0 & 0 \\ -c_t d & c_r + c_t d^2 & 0 & -\Omega I_z & 0 \\ 0 & 0 & c_t & c_t d & 0 \\ 0 & \Omega I_z & c_t d & c_r + c_t d^2 & 0 \\ 0 & 0 & 0 & 0 & c_z \end{bmatrix} \begin{Bmatrix} \dot{x}_w \\ \dot{\varphi}_w \\ \dot{y}_w \\ \dot{\theta}_w \\ \dot{z}_w \end{Bmatrix} \\ &+ \begin{bmatrix} k_t & -k_t d & 0 & 0 & 0 \\ -k_t d & k_r + k_t d^2 & 0 & 0 & 0 \\ 0 & 0 & k_t & k_t d & 0 \\ 0 & 0 & k_t d & k_r + k_t d^2 & 0 \\ 0 & 0 & 0 & 0 & k_z \end{bmatrix} \begin{Bmatrix} x_w \\ \varphi_w \\ y_w \\ \theta_w \\ z_w \end{Bmatrix} = \begin{Bmatrix} -m_s r_s \Omega^2 \sin\Omega t \\ 2m_d r_d h\Omega^2 \sin\Omega t \\ m_s r_s \Omega^2 \cos\Omega t \\ 2m_d r_d h\Omega^2 \cos\Omega t \\ 0 \end{Bmatrix} \end{aligned} \tag{3.79}$$

3.10. The Complete Model

Although Eq. (3.79) captures the WA structural modes, gyroscopic effects, fundamental harmonics and their amplifications, the model does not include sub- and higher harmonics, neither the broadband excitations. The methods for modeling these extra excitations in this thesis are based on an empirical approach. Their model parameters are extracted from WA microvibration test results, while their physical causes are not modeled. Sub- and higher harmonics are assumed as integer multiples of fundamental harmonics for each DoF. Parameters for harmonic excitations modeling include the amplitude coefficients, C_i, and harmonic number, h_i, where i in this case is the number of harmonics considered in each DoF.

Broadband excitations on the other hand are expressed as W at this stage. The detailed modeling of harmonics and broadband noises are presented in Chapter 5. At this stage, they can be superimposed with harmonics in the excitation vector on the right-hand-side of Eq. (3.79), thus:

$$\begin{Bmatrix} F_x \\ M_y \\ F_y \\ M_x \\ F_z \end{Bmatrix} = \begin{Bmatrix} -\sum_{i=1}^{n_{rt}} C_i^{rt}\Omega^2 \sin\left(h_i^{rt}\Omega t\right) + W \\ \sum_{i=1}^{n_{rr}} C_i^{rr}\Omega^2 \sin\left(h_i^{rr}\Omega t\right) + W \\ \sum_{i=1}^{n_{rt}} C_i^{rt}\Omega^2 \cos\left(h_i^{rt}\Omega t\right) + W \\ \sum_{i=1}^{n_{rr}} C_i^{rr}\Omega^2 \cos\left(h_i^{rr}\Omega t\right) + W \\ \sum_{i=1}^{n_{at}} C_i^{at}\Omega^2 \sin\left(h_i^{at}\Omega t\right) + W \end{Bmatrix} \tag{3.80}$$

where superscripts "*rt*", "*rr*" and "*at*" indicate radial translational DoF, radial rotational DoF and axial translational DoF respectively; n is the total number of harmonics. Note that if for fundamental harmonics (i.e. n=1, h_1 =1), C_1 are then the mass imbalances.

3.11. Summary

In this chapter, the analytical microvibration model of the cantilever configured WA with a soft-suspension system in a hard-mounted boundary condition has been derived. An energy method was used throughout the derivation process. The linearized EoM of the mass balanced microvibration model was derived first. This initial model (or the WA structure model) was able to capture the WA structural modes and gyroscopic effects but not excitations. Statically and dynamically mass imbalanced microvibration models were then derived respectively by introducing fundamental harmonic excitations to the WA structural model. The two models have successfully captured the microvibrations due to the mass imbalances. By also obtaining higher harmonics and broadband excitations (they will be discussed in detail in Chapter 5), the EoMs of the complete WA microvibration model is obtained.

4. Wheel Assembly Hard-mounted Microvibration Test

In this chapter, the WA microvibration measurements in the hard-mounted boundary condition are introduced. Microvibrations generated by the WA are measured using a specially designed platform. From the test results, the measured microvibrations of the soft-suspended WA are more complex than those generated from conventional designs (i.e. flywheel mid-span configured with a rigid suspension system). It is found that nonlinearity in the motor and high damping of the soft-suspension system severely affect the induced microvibrations in WA radial DoFs, especially at the fundamental harmonic resonances. Therefore extractions of model parameters such as stiffness and damping values of the suspension system from the test results and strategies for implementing them in the response simulation must be addressed carefully. In addition, comparisons between the soft-suspended WA and the conventional rigid-suspended design are also given through microvibration test results. Signal processing techniques that are commonly used in this thesis are also briefly introduced.

4.1. Test Setup

A microvibration measurement platform has been designed as part of this work to measure the WA-induced microvibrations in the hard-mounted boundary condition. The detailed introductions and calibrations of the platform are given in Appendix C. The platform is able to measure the WA-induced forces from the three installed force sensors. The six resulting reaction forces and moments: F_x, F_y, F_z, M_x, M_y and M_z, are reconstructed from the measured forces. In order to achieve this, it requires three independent test setups between the WA and platform (see Figure 4-1 for each setup).

Tests and test setups are explained as following:

- The normal setup; the WA was mounted on the platform vertically, i.e. the flywheel spin axis (z_w-axis) was parallel to the measurement platform vertical axis (z_p-axis) (see Figure 4-1 a)). The measurement platform was fixed on the top of a mass cube which was fixed on a shaker bench. This setup was to measured F_z, M_x and M_y simultaneously.

- The x_w-axis orientated setup; WA was mounted on the back plate of the platform. In this case, the WA x_w-axis was parallel to the platform z_p-axis. The platform itself (with WA) was mounted on one vertical side of the mass cube (see Figure 4-1 b)). This setup was primarily to measure F_x.

- The y_w-axis orientated setup; this setup was similar to the F_x test setup. The WA was oriented by 90° clockwise about its spin axis, thus the WA y_w-axis was parallel to platform z_p-axis (see Figure 4-1 c)). This setup was primarily to measure F_y.

Note that in all tests, the shaker bench was lifted by air cushions to isolate from ground-borne noise. M_z was calculated from F_x and F_y, it did not require a particular test setup.

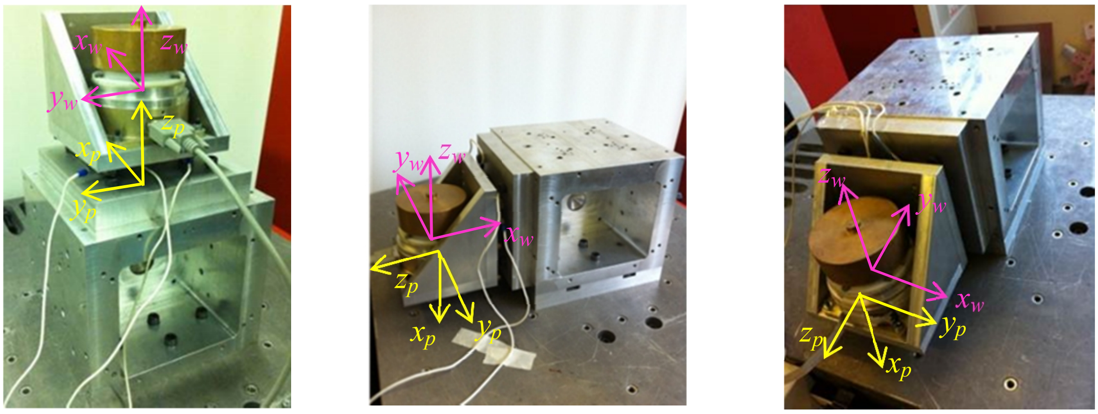

a) Normal b) x_w-axis orientated c) y_w-axis oriented

Figure 4-1 Test setups for WA hard-mounted microvibration measurements

In addition, the WA had a device implemented which allowed the soft-suspension system to be blocked so that the WA behaves like rigid suspended (see Figure 4-2 a) for detail). In contrast, a web-spring (i.e. the soft-suspension system) was used in the soft-suspended WA (see Figure 4-2 b)).

With each test setup, microvibrations were measured for both soft- and rigid-suspended WAs. In each test, the speed step was set at 60 rpm (or 1 Hz) in order not to lose any useful information (i.e. mainly to capture amplifications at fine frequencies). The

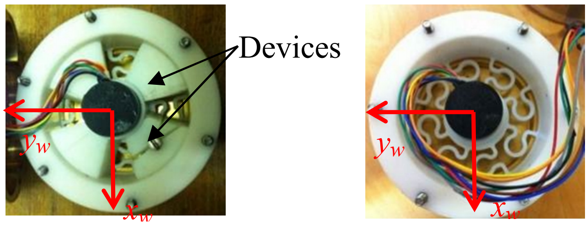

a) Rigid-suspended WA b) Soft-suspended WA

Figure 4-2 Rigid- and soft-suspended WAs (suspension system only)

flywheel was controlled to spin from 60 to 6000 rpm and signals were acquired for 5s at each speed. Signals from the force sensors were sampled at 2048 Hz with a block size of 2048, giving the frequency resolution of 1 Hz and the useful frequency band up to 1000 Hz (with anti-aliasing filter considered).

4.2. Signal Processing

Generally, dynamic analysis of rotational machinery is performed in the frequency domain. Signal processing techniques in the frequency domain such as Power Spectral Density (PSD), Amplitude Spectrum (AS), spectral map, Root Mean Square (RMS) value, Cumulative Root Mean Square (CRMS) value plot, waterfall plot and order tracking plot, etc., are the common analysis tools. Introductions of the signal processing techniques used in this thesis are given in Appendix E. In brief, most signals have been processed in the time domain first and then transformed into the frequency domain using Fast Fourier Transformation (FFT). The transformed signals were further processed to generate the PSD, AS and RMS value, etc. The software package M+P Smart Office was used to acquire signals and MATLAB was used to process all signals and generate plots throughout the thesis unless mentioned otherwise.

- In the time domain, the mean value in the signal was first removed as they were often measured with offsets from the zero lines. In addition, in order to produce the frequency resolution to be 1 Hz, five segments were chosen and thus 2048 samples per segment with a length of each segment to be 1s, 50% overlap was also applied.

- In the frequency domain, FFT was performed on the processed time domain signals. Hanning window was applied to each segment. PSD, AS, RMS value and CRMS value, etc. were then calculated from the FFT results accordingly.

For example, PSD and CRMS value plot of F_x at 1800 rpm for the soft- and rigid-suspended WAs are shown in Figure 4-3.

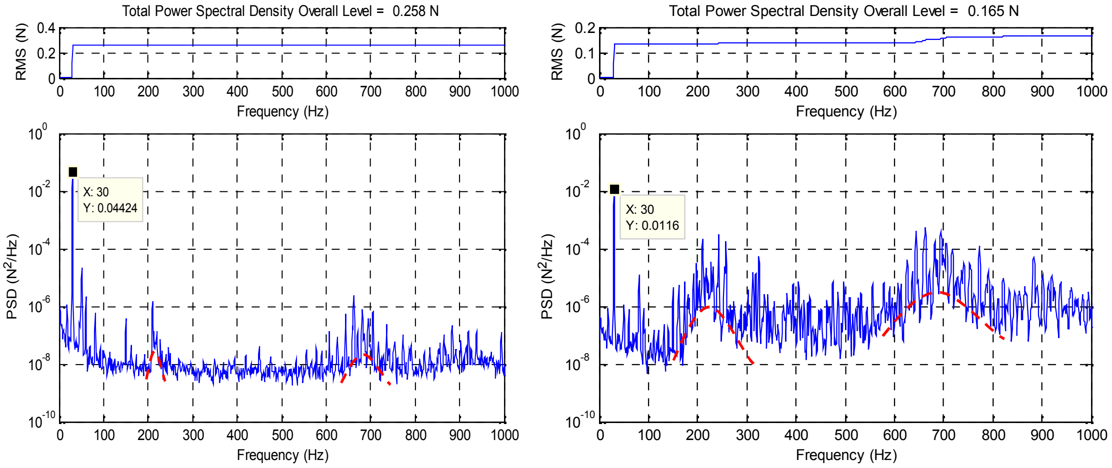

a) Soft-suspended WA b) Rigid-suspended WA

Figure 4-3 PSD and CRMS value plots of the soft- and rigid-suspended WAs (F_x at 1800 rpm)

In Figure 4-3 a) and b), the largest spike in each plot is at 1800 rpm (or 30 Hz) due to the fundamental harmonic. They are also clearly seen in the CRMS value plots where the largest step occurs at 30 Hz in both cases indicating the largest energy contribution at these frequencies.

Comparing the measured microvibrations from the two WAs, the soft-suspended WA has much smaller response amplitudes in PSD in general, especially beyond 200 Hz. Also the corresponding CRMS value plot is approximately flat after the fundamental harmonic indicating there is no significant energy variation. However this is not the case for the rigid-suspended WA. There are two distinct “mound” shaped amplifications around 220 Hz and 690 Hz respectively. These are the modes of the motor-bearing system that have been constantly excited by broadband noise. Note that the two modes are also seen in the soft-suspended WA microvibrations, but their influences are significantly reduced. Because the interested frequency band in this study is up to 500 Hz, microvibrations beyond 500 Hz are ignored and are not discussed further. The detailed discussions on the soft- and rigid-suspended WAs are presented in Section 4.8.

According to Parseval's theorem (shown in Appendix E), the total power of a signal in the time and frequency domain must be the same. This statement can also be used to assess the quality of the signal processing techniques that have been used to transform the signal between the two domains. For example, the total RMS value of F_x in the time and frequency domain were calculated at all speeds for the soft- and rigid-suspended WAs. They are shown in Figure 4-4 a) and b) respectively.

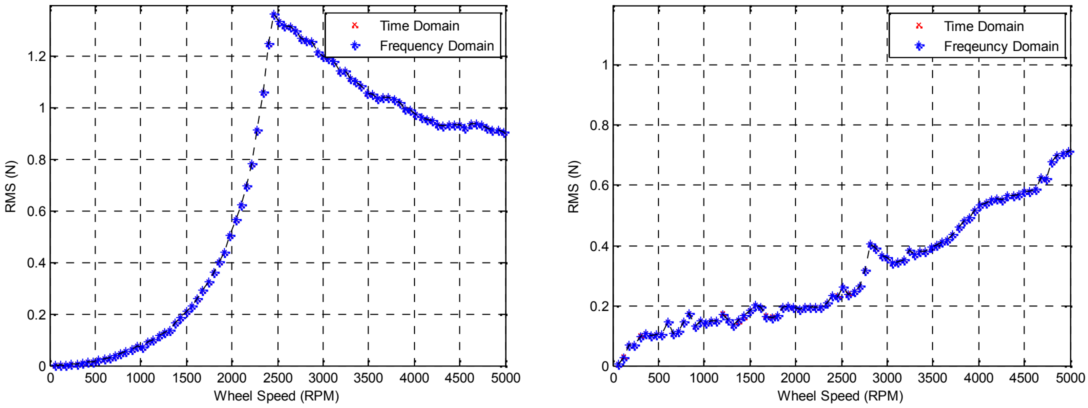

a) Soft-suspended WA b) Rigid-suspended WA

Figure 4-4 Total RMS value of F_x in the time and frequency domain

Firstly from Figure 4-4, the identical RMS values in the time and frequency domain for each WA at each speed indicate the good signal processing that has been performed. In Figure 4-4 a), the RMS value first increases from 60 rpm with a parabola shape up to about 2500 rpm and reaches the maximum value at resonance. The curve then steady decreases and finally becomes comparatively flat from about 4000 rpm. This can also be seen from Figure 4-5 shown on the next page where WA fundamental harmonic responses are plotted up to 8000 rpm (the figures are taken from another set of microvibration tests for the same WA that was performed by the author and his colleague in [81]). Note that the relatively round resonant peaks in the soft-suspended WA (i.e. "spring") are due to the coarse speed rate (per 120 rpm) tested.

These observed dynamic characteristics have shown one important design feature of the WA: to produce relatively steady and quiet vibrations at high spin speeds. This is clear if comparing to the conventional WA in Figure 4-4 b) and also in Figure 4-5, where the resonance of rigid case is much higher (beyond 8000 rpm) and accompanied with some abrupt and small amplifications at lower speeds. Results in Figure 4-4 a) indicate that the soft-suspended WA has a greater potential to work at very high speeds (e.g. above 4000 rpm) with good performance in terms of induced microvibrations.

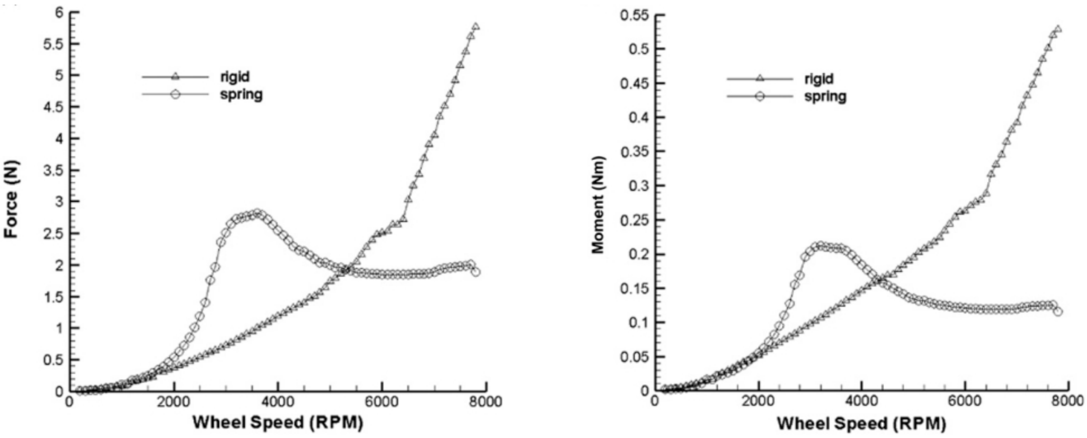

a) Radial force b) Radial moment

Figure 4-5 Fundamental harmonic response forces and moments generated by the soft- and rigid-suspended WA (0 to 8000 rpm) [81]

It should be mentioned that WA resonances or any amplification information, e.g. resonant frequencies and amplitudes, as well harmonic responses, cannot be revealed from the total RMS value plots such as shown in Figure 4-4. The total RMS value of a signal at a spin speed is defined as the total energy contributed from all vibration features in the frequency band at that speed. For a WA this typically includes harmonic responses, broadband noise and all resonant amplifications. In order to accurately analyze the WA-induced microvibrations, other signal processing techniques must be used, such as PSD waterfall plots and spectral maps. The total RMS value plot however, is very useful for broadband excitations modeling. These signal processing techniques are frequently applied to the vibration signals studied in the thesis.

4.3. Background Noise

All vibration tests presented in this thesis were performed in the Astronautics Dynamics Laboratory of the University of Southampton. In order to minimize the environmental influences on measured data, the commonly accepted procedures and treatments for space system microvibration tests have been followed. Some of them are:

- All tests were conducted at nights and weekends;
- Air cushions (of shaker) were used to isolate the ground-borne noise;

- Aluminum foil was wrapped over power cables to avoid electromagnetic interactions;
- Human activities (speaking, walking and typing, etc.) were restricted;

The typical background noise of the three force sensors is plotted in the time domain in Figure 4-6 a). Background noise of F_z and vibration responses of F_z at 600 rpm for the two WAs is plotted in the frequency domain in Figure 4-6 b).

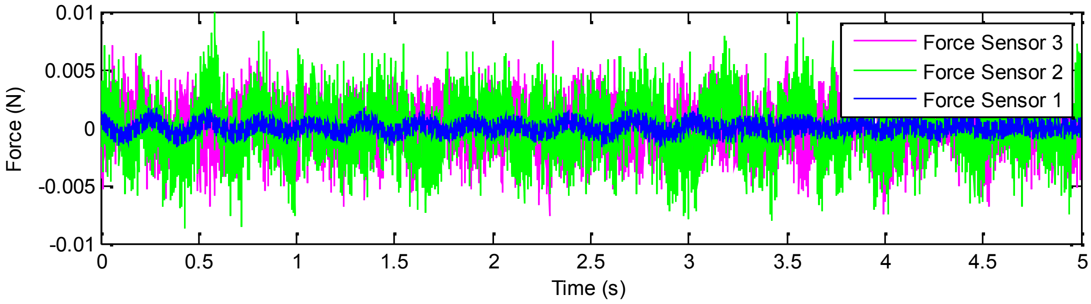

a) Background noise of the three force sensors (in the time domain)

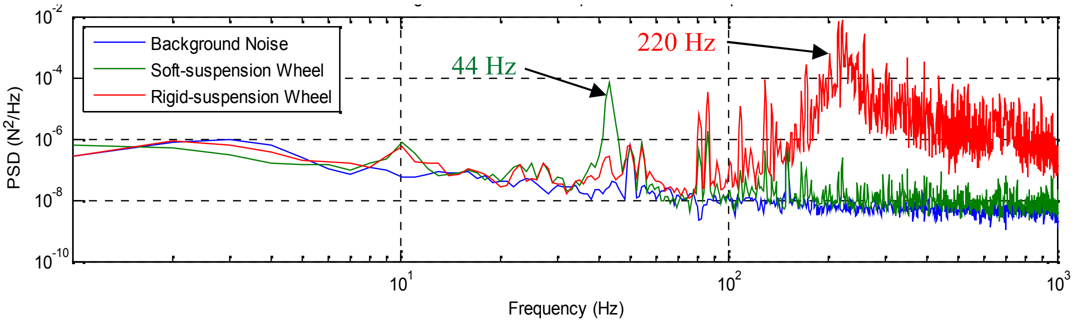

b) Background noise and vibrations of F_z at 600 rpm (in the frequency domain)

Figure 4-6 Typical background noise of force sensors

With reference to Appendix C, force sensor 1 is an order of magnitude more sensitive (~100 mv/N) than the other two force sensors (~10 mv/N), thus its background noise amplitudes (with electronics switched on) is much smaller as shown in Figure 4-6 a), the 0-p amplitude is about 0.5 mN compared to 2.5 mN.

In Figure 4-6 b), the total RMS value of the background noise of F_z for the soft-suspended WA is about 3.5 mN up to 1000 Hz. This mainly arises from the amplifications at 50 Hz (and its integer multiples) due to the UK mains frequency. In practice these amplifications cannot be completely avoided and significant efforts have been made to reduce them. In summary, the background noise shows no significant influence to the WA-induced microvibrations and they can be ignored.

On the other hand in Figure 4-6 b), the spikes around 44 Hz and 220 Hz for the soft- and rigid-suspended WAs respectively are the WA structural modes excited by broadband noise. Compare the two types of WAs, the soft-suspension system effectively shifts the natural frequency of rigid-suspended WA to a lower value, hence microvibrations of the soft-suspended WA are much quieter from 200 Hz; a useful observation for broadband excitations modeling (shown in Chapter 5).

4.4. Soft-suspended Wheel Assembly Microvibration Force Test Results

Figure 4-7 shown on the next page presents spectral maps and PSD waterfall plots of the three measured microvibration forces, F_x, F_y and F_z, for the soft-suspended WA. Note that in order to correctly present the color in spectral maps, amplitudes are scaled as 10log (amplitudes). PSD waterfall plots are plotted in a linear scale in amplitude with a maximum frequency up to 500 Hz and a maximum speed up to 5000 rpm.

Typical dynamic characteristics of WA-induced microvibrations are observed in each DoF. For example in Figure 4-7 a), different harmonic responses and structural modes are clearly present. In particular, the red line is the fundamental harmonic with the largest responses from flywheel mass imbalances. Other speed-varying lines are higher harmonics and have shown much smaller responses and are due to irregularities in the motor-bearing system. There are approximately twelve harmonics can be identified in the figure, but only the first four or five are relatively important.

There are also non-speed-varying (or vertical) lines presented in the figure which are identified to be WA structural modes and natural frequencies of the motor-bearing system. First of all, the broadband vertical line around 220 Hz (±10 Hz) is a mode due to the motor-bearing system in the WA. The vertical line begins at 50 Hz is identified to be the WA radial translational mode. Similar observations are also seen in F_y in Figure 4-7 b) and F_z in Figure 4-7 c). In these cases, the WA structural mode starts at about 50 Hz (radial translational mode) and 44 Hz (axial translational mode) respectively.

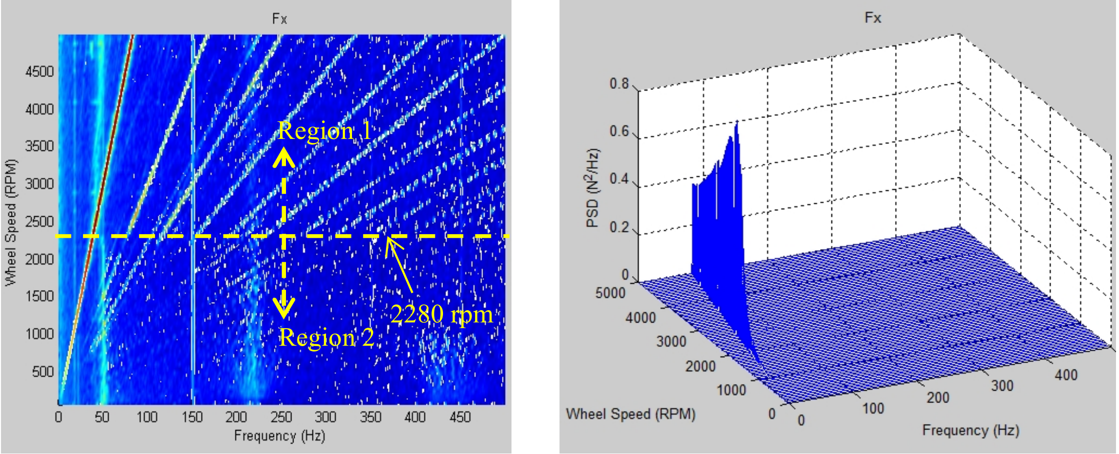

a) F_x spectral map

d) F_x PSD waterfall plot

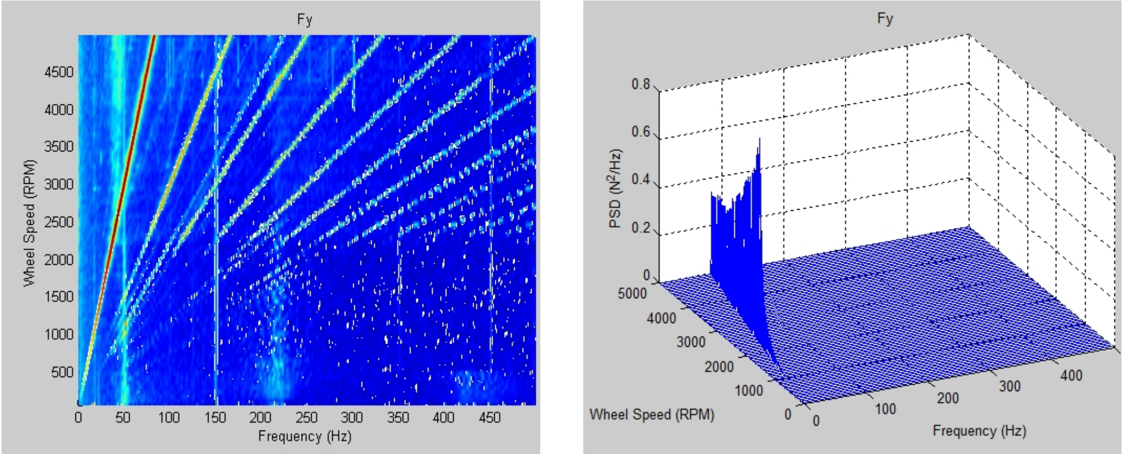

b) F_y spectral map

e) F_y PSD waterfall plot

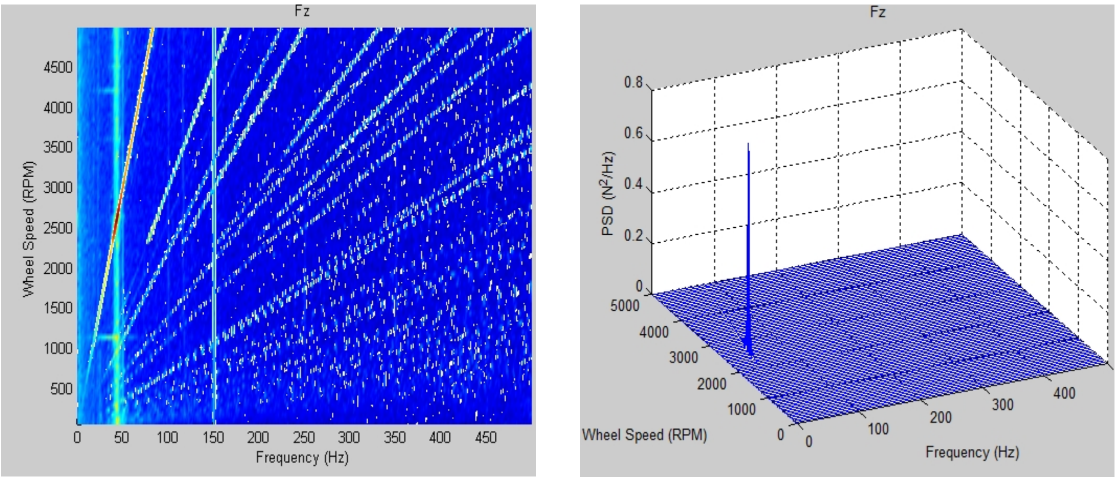

c) F_z spectral map

f) F_z PSD waterfall plot

Figure 4-7 Spectral maps and PSD waterfall plots of measured forces (soft-suspended WA)

Note that the platform natural frequencies are not shown in the frequency band as they are much higher than 500 Hz (see Appendix C for detail). Also, another relatively faint vertical line at 150 Hz is from the background noise as introduced earlier in Section 4.3. Meanwhile, the 50 Hz vertical line from the background noise coincides with the WA radial translational mode at 50 Hz and slightly larger than the axial translational mode at 44 Hz. In practice, although the mains frequencies appear in the spectral maps and coincide with WA structural modes, their responses have much smaller amplitudes (see also Section 4.3) and do not significantly influence the WA microvibration test results.

Aside from the typical WA dynamic characteristics introduced above, some peculiar dynamic features of the WA are seen in Figure 4-7. From spectral maps of F_x and F_y in Figure 4-7 a) and b), it is observed that higher harmonic responses are not clearly present until 2280 rpm and then suddenly appear with very high responses. This causes two distinct regions along the speed axis which separates at about 2280 rpm in radial DoF microvibrations.

The zoomed spectral map of F_x at approximately 2280 rpm is shown in Figure 4-8 a). The largest spike in F_x is identified at resonance and at approximately 2460 rpm (or 41 Hz) on the fundamental harmonic (also with reference to Figure 4-7 d)). A similar observation is found in F_y and at approximately 2400 rpm (or 40 Hz). The zoomed spectral map of F_z is shown in Figure 4-8 b) with the largest spike occurring at resonance at 2640 rpm (or 44 Hz).

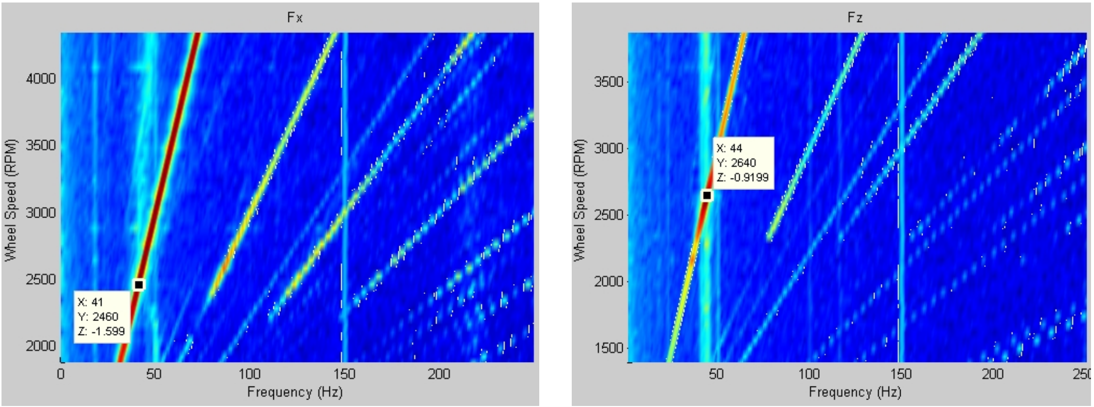

a) F_x b) F_z

Figure 4-8 Zoomed spectral maps of F_x and F_z around 2280 rpm for the soft-suspended WA

Note that in Figure 4-8 a) after the resonance, a vaguely speed-varying line appeared from 2460 rpm (or 41 Hz) in place of the constant radial translational mode at low speeds. This speed-varying line is in fact one of the whirls of the WA "rocking" mode. Similar observations are also seen in F_y. In brief, the sudden structural mode changes in radial DoFs are due to nonlinearity in the responses. For this reason, the speed (i.e. 2280 rpm) where the two regions separate is called the "separation speed" in this thesis. The nonlinear region in radial DoF is found between 38 to 50 Hz and approximately centered around 40 Hz at the resonance. Further discussions on nonlinearity in WA microvibrations are shown in Section 4.6.

In F_z, the WA axial translational mode starts at 44 Hz and remains unchanged in the speed band (see Figure 4-7 c) for detail). Note that nonlinearity has much less influences in F_z and the axial translational mode is not influenced by it before and after 2280 rpm (see Figure 4-8 b) for detail).

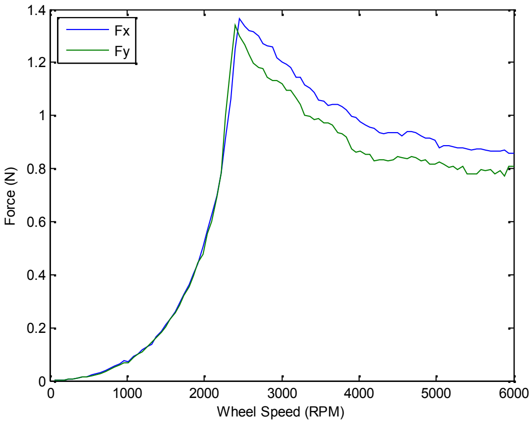

a) Fundamental harmonic responses

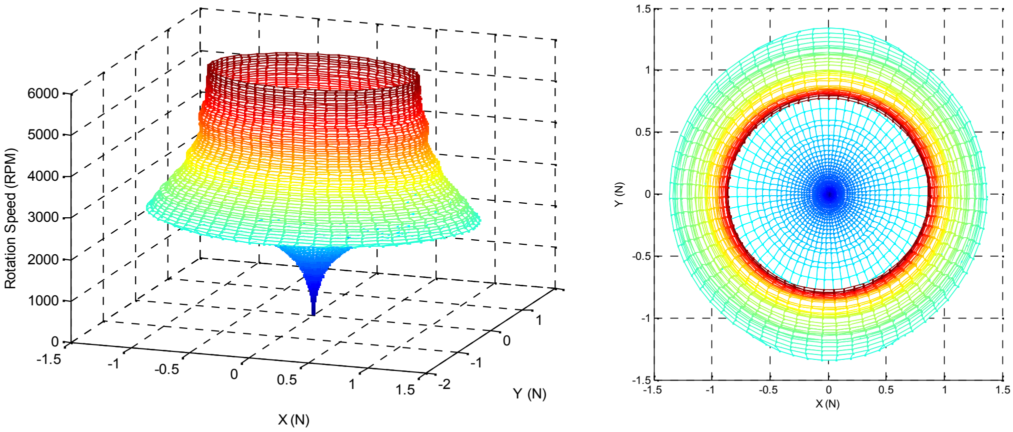

b) "Force tube" (normal view)

c) "Force tube" (top view)

Figure 4-9 F_x and F_y fundamental harmonic responses (measurements)

Next we compare F_x and F_y responses to assess the WA axisymmetry. Firstly from Figure 4-7, they produce similar microvibrations in the speed band. The fundamental harmonic responses of F_x and F_y are extracted from the test results and plotted in Figure 4-9 a). They are also plotted as the “force tube” in Figure 4-9 b) and c).

Generally in Figure 4-9 a), the two curves of F_x and F_y have a similar shape. At the starting speed (60 rpm), both curves increase approximately with the proportion of angular speed squared into parabola shapes before resonances. Resonance occurs at 2460 rpm (or 41 Hz) in F_x, while at 2400 rpm (or 40 Hz) in F_y. After the resonance, F_x amplitudes are approximately 1.1 times higher than F_y, but both curves decrease at a similar rate.

Figure 4-9 b) an c) present the “force tube” plots which provide a clear view of the evolution of the fundament harmonic response amplitudes in the speed band. At each speed, F_x and F_y fundamental harmonic response amplitudes are used as the length of the semi-major and semi-minor axes of an ellipse respectively. Ellipses at each speed are generated and plotted together along the speed axis.

In Figure 4-9 b), the “force tube” starts from 60 rpm in both directions and increases to the maximum values at resonances. Up to this point, the circumference of the tube is approximately circular, while an ellipse circumference is clearly formed at resonances and afterwards until approximately 4000 rpm. This can be clearly seen in Figure 4-9 c). The tendency of another circular circumference starts from approximately 4000 rpm with slowly decreasing response amplitudes and is reasonably formed at the end of test speed. This is due to the self-centering effect of rotational machinery at high speeds.

In practice, the difference in the harmonic response amplitudes in radial DoFs may be due to many reasons, e.g. different degrees of irregularities in the motor-bearing system or the influences of bearing friction and damping, etc. These influences generally have major impacts on the higher harmonic responses due to their causes. For fundamental harmonic amplitudes such as those seen in Figure 4-9, the main reason may arise from the motor harnesses in the WA (see Figure 4-10 for detail).

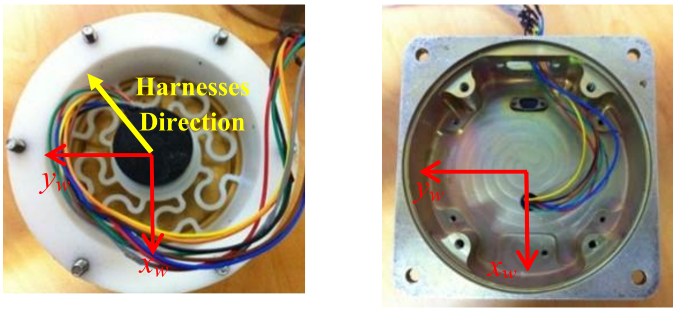

a) Suspension system b) WA base

Figure 4-10 Motor harnesses in the WA

In this case, the motor harnesses can be considered as a single DoF spring-dashpot system and thus adding extra stiffness and damping in both radial DoFs due to its orientation w.r.t. the WA coordinate system (see the yellow arrow in Figure 4-10 a)). Therefore the resonant frequencies and amplitudes in the two radial DoFs are slightly different. In the microvibration modeling, stiffness and damping values of the suspension system in the two radial DoFs can be tuned to match the test results, so in this way the influences of harnesses to the harmonic responses can be included. Alternatively, they can be estimated from the test results or physically modeled.

On the other hand in Figure 4-7, F_z generally has much smaller amplitudes in the speed band apart from the resonance at 2640 rpm compared to responses in radial DoFs. The total RMS values of F_x and F_z are calculated and plotted together in Figure 4-11 a). The fundamental harmonic response amplitudes of F_z are also extracted from the microvibration test results and plotted in Figure 4-11 b).

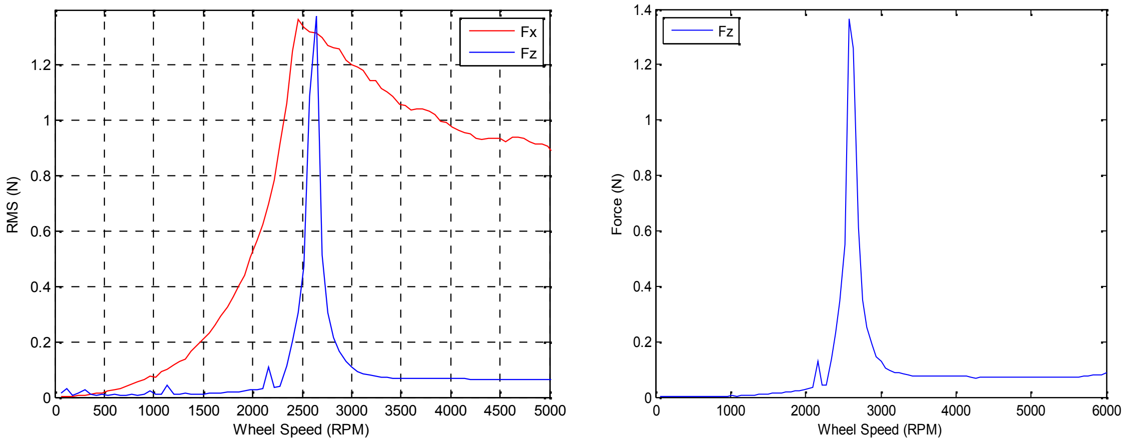

a) Total RMS values of F_x and F_z b) F_z fundamental harmonic responses

Figure 4-11 RMS values and fundamental harmonic responses of F_z

Remembering that in the WA hard-mounted microvibration model derived in Chapter 3, harmonic excitations only appear in radial DoFs, if so, the static and dynamic mass imbalances assumed in the model have no influence in axial translational DoF. However, this is not true as seen from F_z test results. From Figure 4-7 c) and Figure 4-11, fundamental harmonic responses are clearly present in F_z. In practice microvibrations in axial translational DoF arise for various reasons such as uneven distribution of flywheel mass imbalances (thus fundamental harmonics) and/or irregularities in bearing and motor components (thus higher harmonics). Also from Chapter 3, it is assumed that motion in axial translational DoF is uncoupled from those in radial DoFs, but in practice it may be influenced by them. In the WA microvibration modeling, dynamics in axial translational DoF are simply considered as an independent one DoF mass-spring-dashpot system, with all harmonic excitations modeled empirically. Note that in many cases, resonance amplitudes of F_z can be more significant than those of F_x and F_y, although responses elsewhere could be much smaller.

4.5. Soft-suspended Wheel Assembly Microvibration Moment Test Results

Figure 4-13 presents spectral maps and PSD waterfall plots of the measured microvibration moments, M_x, M_y and M_z, of the soft-suspended WA respectively. Similar to the microvibration forces shown in Section 4.4, harmonic responses and amplifications in the microvibration moments are also clearly present. In addition, the WA "rocking" mode is captured in radial moments M_x and M_y (see Figure 4-13 a) and b)). The "rocking" mode starts around 27 Hz from static and a "V" shape is formed as speed increases. The zoomed plot of the "rocking" mode is shown in Figure 4-12.

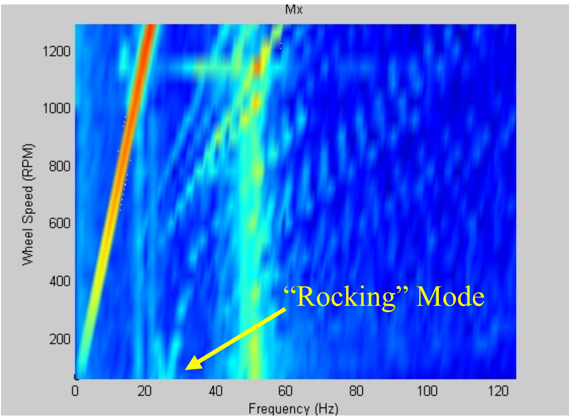

Figure 4-12 WA "rocking" mode in M_x

In Figure 4-12, the two branches of the “rocking” mode are the forward and backward whirls respectively. In addition, the radial translational mode at 50 Hz is also captured in M_x due to the “side effects” of the flywheel “rocking” motion (note that the reverse is not true since radial translational motions do not necessarily excite the “rocking” mode which only appears in M_x and M_y). Since microvibration moment test results (such as Figure 4-12) capture all WA structural modes in radial DoFs, they are preferred as the inputs for the microvibration model validations in radial DoFs (details are presented in Chapter 5). Also nonlinearity is more significant in the measured moments. The two distinct regions (separate at 2280 rpm) are clearly seen in Figure 4-13 a) and b).

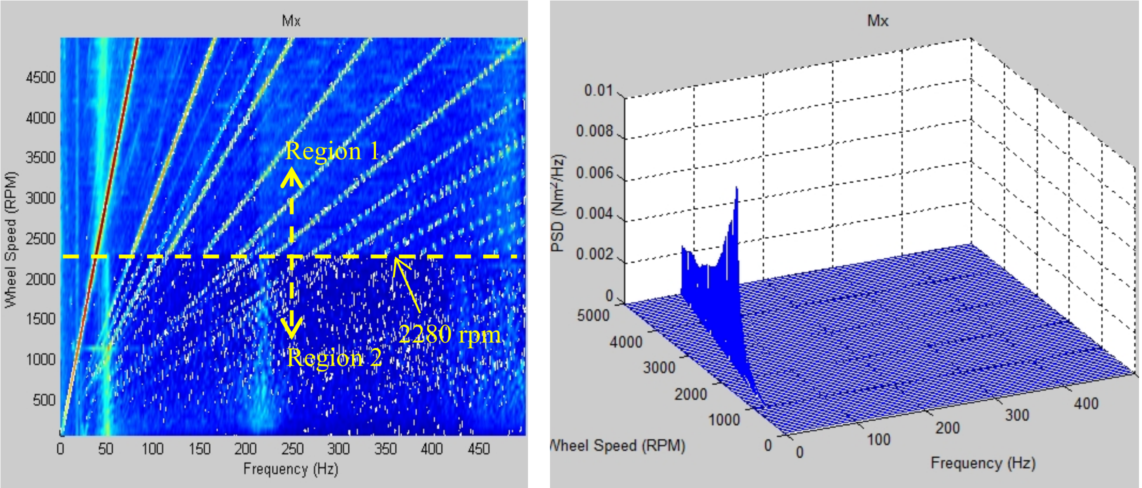

a) M_x spectral map

d) M_x PSD waterfall plot

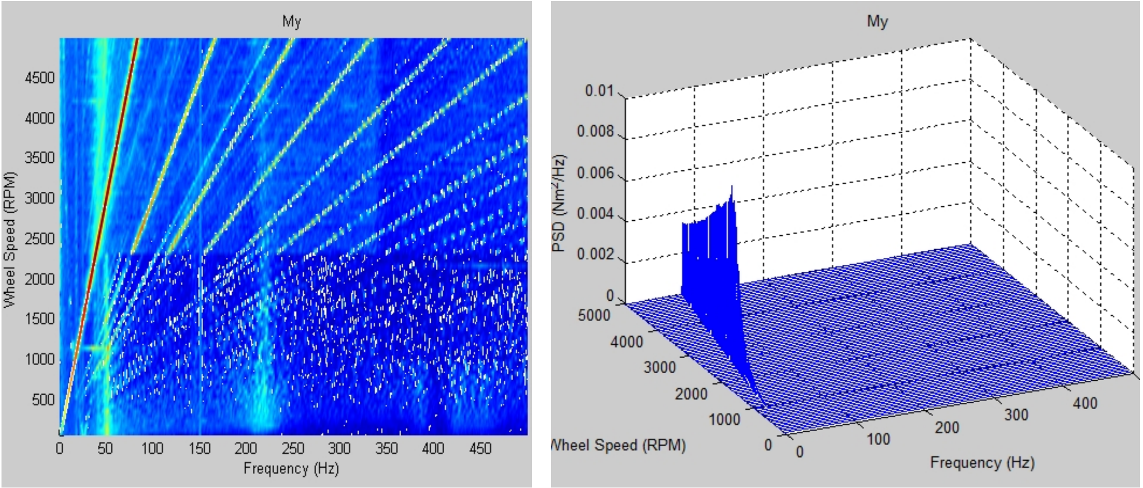

b) M_y spectral map

e) M_y PSD waterfall plot

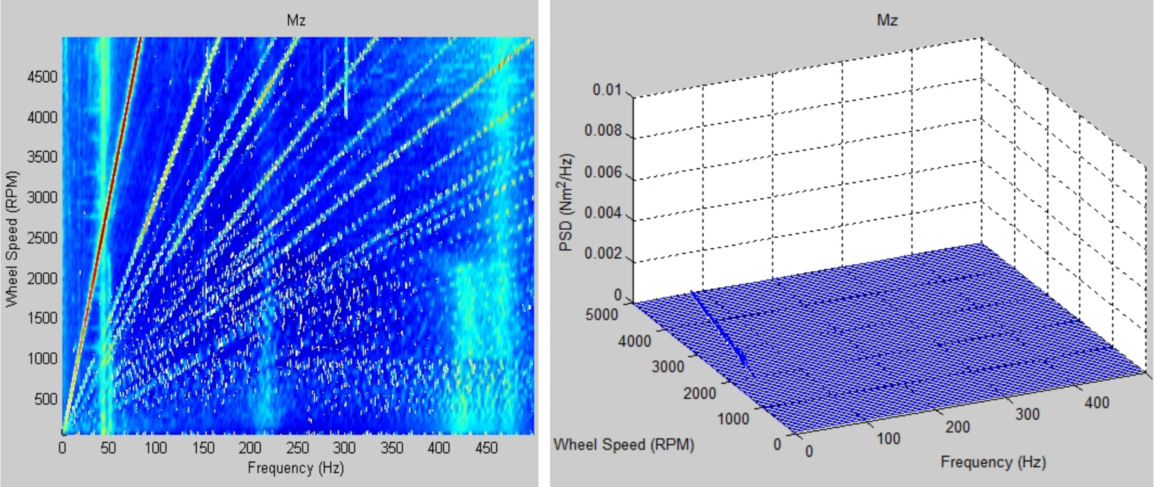

c) M_z spectral map f) M_z PSD waterfall plot

Figure 4-13 Spectral maps and PSD waterfall plots of measured moments (soft-suspended WA)

At this point of the study, the stiffness of the soft-suspension system can be determined for the WA microvibration modeling. The final stiffness and natural frequencies are given in Table 4-1. They are determined from both microvibration test results presented in this chapter and results calculated from the WA FE model (with sine-sweep tests verified, details are shown in Appendix D).

WA Structural Mode	Natural Frequency	Stiffness
Radial Translational mode	50 Hz	6.9×10^4 N/m
“Rocking” mode	27 Hz (at static)	15 Nm/rad
Axial Translational mode	44 Hz	5.8×10^4 N/m

Table 4-1 Stiffness and natural frequencies of the WA soft-suspension system

Next, comparing the PSD waterfall plots of M_x and M_y in Figure 4-13 d) and e), it is clear that there are also some differences in the fundamental harmonic responses. The M_x and M_y fundamental harmonic responses are extracted from the test results and are plotted in Figure 4-14 a). The “moment tube” is also generated and plotted in Figure 4-14 b) and c).

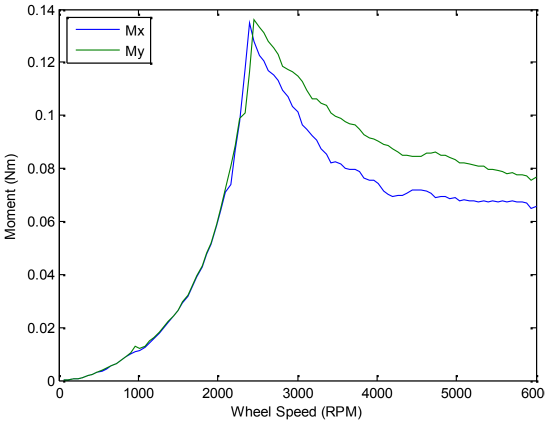

a) Fundamental harmonic responses

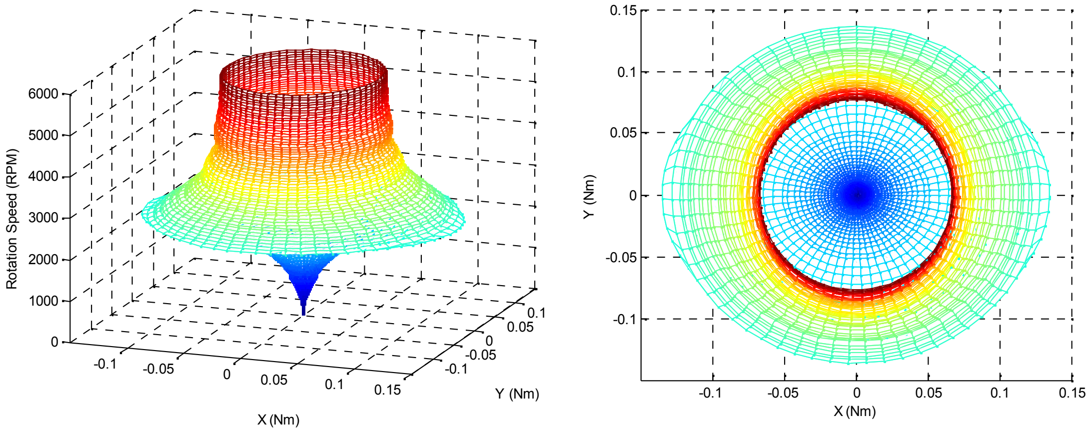

b) "Moment tube" (normal view)

c) "Moment tube" (top view)

Figure 4-14 M_x and M_y fundamental harmonic responses (measurements)

In Figure 4-14 a), the two curves are almost identical at low speeds and grow into parabola shapes until resonances. Similar to F_x and F_y, the two resonances have different resonant frequencies (2400 rpm (or 40 Hz) for M_x and 2460 rpm (or 41 Hz) for M_y) and resonant amplitudes. After the resonances, M_x decreases at a slightly faster rate than M_y, while response amplitudes of M_y are approximately 1.2 times larger than those of M_x.

The torque microvibrations, M_z, in Figure 4-13 c) and f) have much smaller response amplitudes compared to those of M_x and M_y. In practice, M_z are often ignored for typical WA microvibration analysis, but they are the relatively dominant microvibrations at very low speeds, e.g. in crossing-zero microvibration analysis. In this thesis, M_z are ignored and thus the number of DoFs studied reduces to five.

4.6. Nonlinearity

In order to investigate nonlinearity observed in the WA microvibration test results, high and low level input sine-sweep tests were performed to the hard-mounted WA. The detailed introduction of the tests, results and discussions are presented in Appendix D. In this section, the results from the high level input sine-sweep tests in WA radial x_w-DoF are presented as they are more representative and reveal the nonlinearity in the WA. The test setup and results are shown in Figure 4-15.

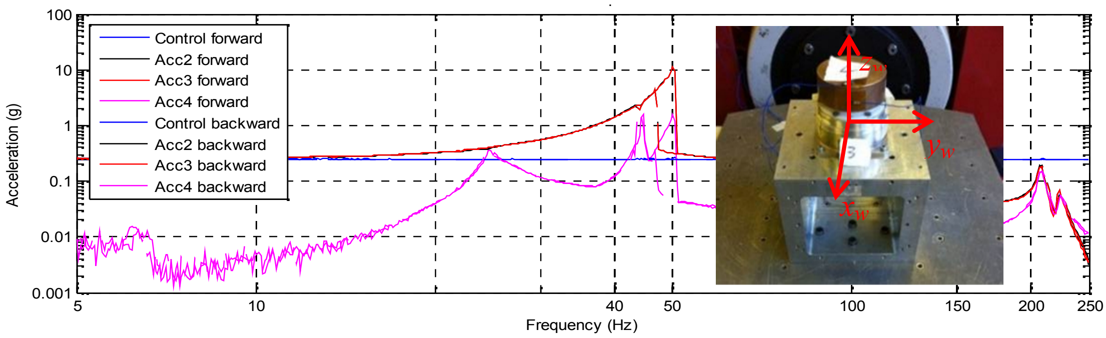

Figure 4-15 High level input sine-sweep test (WA radial x_w-DoF)

In this test, the WA was excited by the shaker from 5 to 250 Hz with an input level 0.25 g. This input level was high enough to excite the nonlinearity in the WA. Forward and backward sine-sweep tests were performed. Three accelerometers were attached to the flywheel. Accelerometer no. 2 and 3 were attached in x_w-axis to measure the radial translational mode, while accelerometer no. 4 was attached on the flywheel top surface in z_w-axis to primarily measure the “rocking” mode. Results are plotted as solid and dashed lines for the forward and backward sine-sweep tests respectively in Figure 4-15. Firstly, in the forward sine-sweep test results the radial translational mode is detected at about 50 Hz from accelerometer no. 2 and 3, while in the backward sine-sweep test results it is detected at about 46 Hz. All other modes are almost identical such as the “rocking” mode around 27 Hz, the axial translational mode at 44 Hz and the two modes above 200 Hz due to the motor-bearing system. This difference in the forward and backward sine-sweep test results is due to nonlinearity. The region between 46 to 50 Hz is the nonlinear (response) region. Note that in practice, as in the flywheel spinning condition, the nonlinear region in the test results may be slightly different (e.g. from 38 to 50 Hz as in our case as shown in Section 4.4 and 4.5). Meanwhile, the sudden decline of responses in each plot after the resonance also indicates nonlinearity occurred there.

The physical causes of nonlinearity are not studied in this thesis however, it was found from WA microvibration test results that it was due to the bearing system inside the motor (here also referred as the motor-bearing system). Nonlinearity influences in the WA microvibration analysis are discussed throughout this thesis however.

4.7. Higher Harmonic Responses

Responses of any harmonic can be extracted from the WA microvibration test results, their plots in the speed band are called the "order tracking plot of harmonics". In WA microvibration analysis, harmonics are usually expressed as fundamental harmonic (H1), second harmonic (H2), half harmonic (H0.5), H2.3, etc. Responses of the first five integer higher harmonics, i.e. H2 to H6, in F_x, M_y and F_z are extracted and plotted in Figure 4-16 a), b) and c) respectively.

Generally, the amplitudes of higher harmonic responses are much smaller compared to those of the fundamental harmonics. They also grow approximately with the square of the angular speed until the "separation speed" at 2280 rpm, and large amplifications occur due to nonlinearity (see H2 responses around 2500 rpm for example). Afterwards, the responses in radial DoFs decline at slower rates and became approximately flat from 3500 rpm as the flywheel self-centering effects become influential. Note that higher harmonic responses of F_z are much smaller compared to those of F_x as expected (except H2 around 2500 rpm due to nonlinearity).

Apart from harmonic responses, WA structural modes can also be identified from higher harmonics, e.g. resonances on H2 in F_x and M_y at 1500 rpm, and on H3 at 1000 rpm, etc., are the radial translational mode (50 Hz); resonances in F_z on H2 at 1320 rpm and on H3 at about 900 rpm, etc., are the axial translational mode (44 Hz).

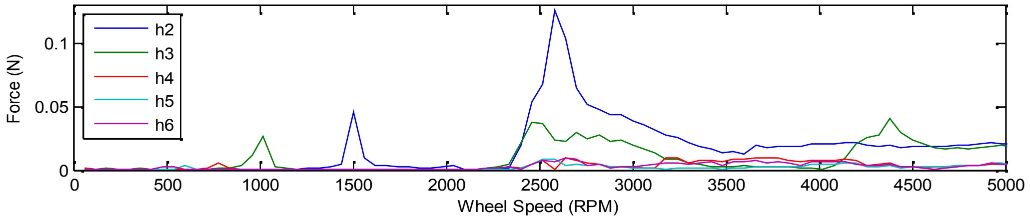

a) F_x

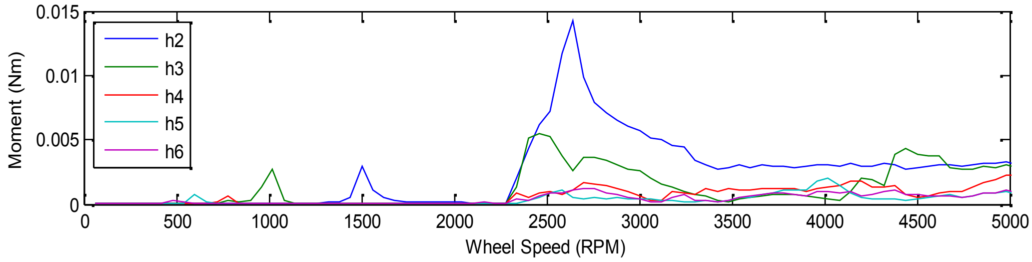

b) M_y

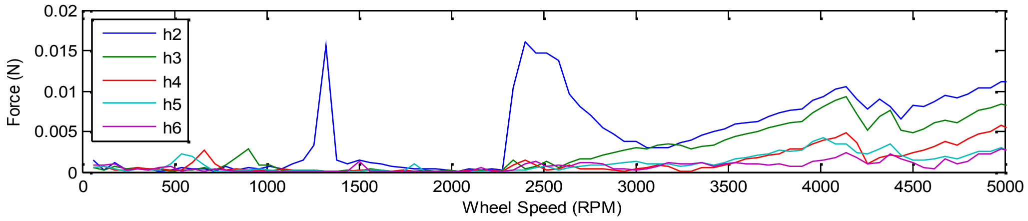

c) F_z

Figure 4-16 Order tracking plots of the soft-suspended WA (H2 to H6)

Order tracking plots are useful for higher harmonic excitations modeling, model parameters are extracted from them. Detailed work is presented in Chapter 5.

4.8. Rigid-suspended Wheel Assembly Microvibration Test Results

In this thesis the microvibration test results of a rigidly-suspended WA (see Figure 4-2 b)) are also presented but only used to compare and assess the design of the soft-suspended WA in terms of microvibrations generated. A microvibration model of the rigid-suspended WA is beyond the scope of this thesis. Microvibration test results are plotted in Figure 4-17 for the spectral maps and PSD waterfall plots of F_x, F_z and M_y.

Firstly from Figure 4-17 a), b) and c), WA structural modes have disappeared in the frequency band as they are beyond the maximum frequency plotted due to the rigid suspension used in the WA. Therefore for the rigid-suspended WA, the fundamental harmonic responses grow in the speed band without amplifications with the WA structural modes (see Figure 4-17 d), e) and f) for detail). The dynamic characteristics shown in Figure 4-17 are the typical patterns for conventional WA designs. In addition, two distinct horizontal “belts” between 2100 to 2340 rpm and 4440 to 4860 rpm appear in each DoF are from the motor-bearing system but their causes are unknown and are beyond the scope of this thesis.

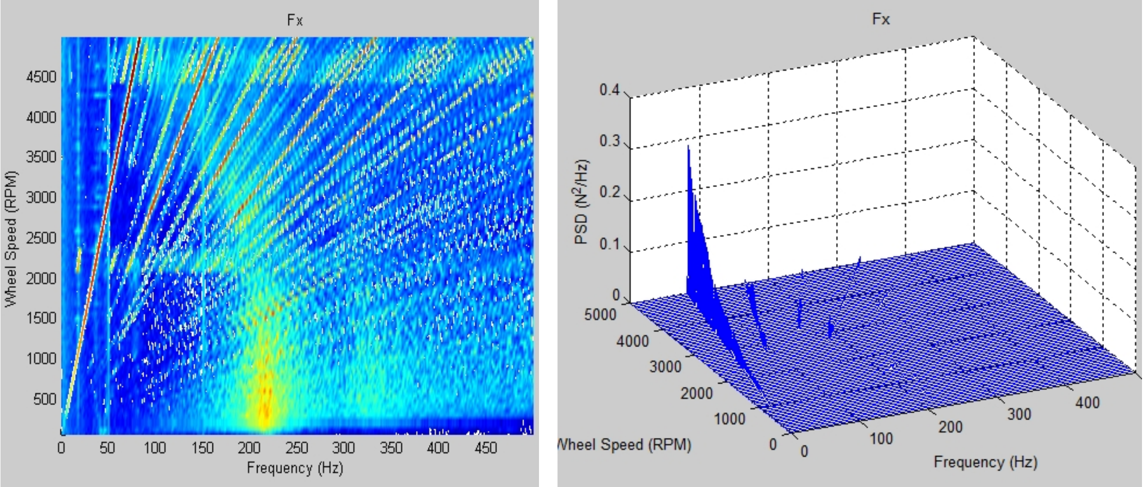

a) F_x spectral map d) F_x PSD waterfall plot

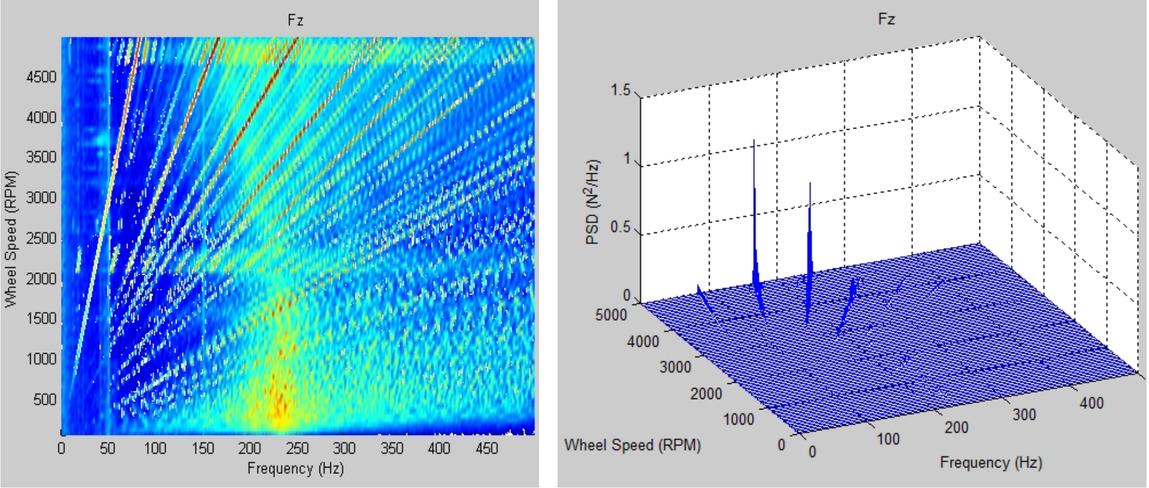

b) F_z spectral map e) F_z PSD waterfall plot

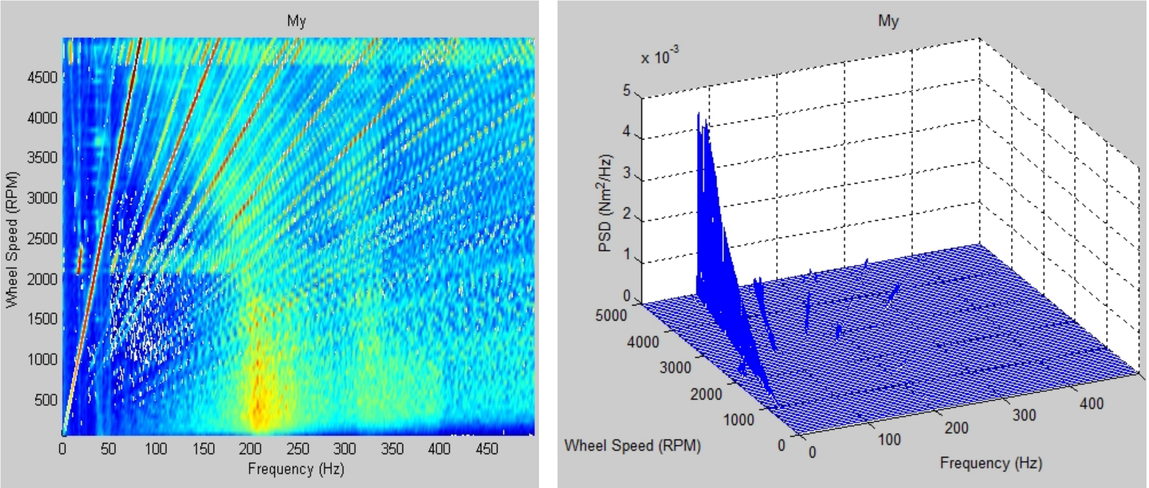

c) M_y spectral map f) M_y PSD waterfall plot

Figure 4-17 Spectral maps and waterfall plots of measured microvibrations (rigid-suspended WA)

Figure 4-17 also shows one important conclusion concerning the nonlinearity observed in the WA microvibration test results. Remembering that in the rigid-suspended WA, the soft-suspension system is completely locked, thus the nonlinearity observed in Figure 4-17 is caused by the internal components of the motor (or the motor-bearing system) rather than the web-spring of the soft-suspension system. However the study of motor-bearing system dynamics is beyond the scope of this thesis.

Figure 4-18 shows the zoomed CRMS value plots of F_x at 1800 rpm for the soft- and rigid-suspended WAs between 100 to 1000 Hz (its complete plot is shown in Figure 4-3). Note that RMS values of the two types of WAs are matched at 100 Hz in order to provide a clear comparison in the frequency band.

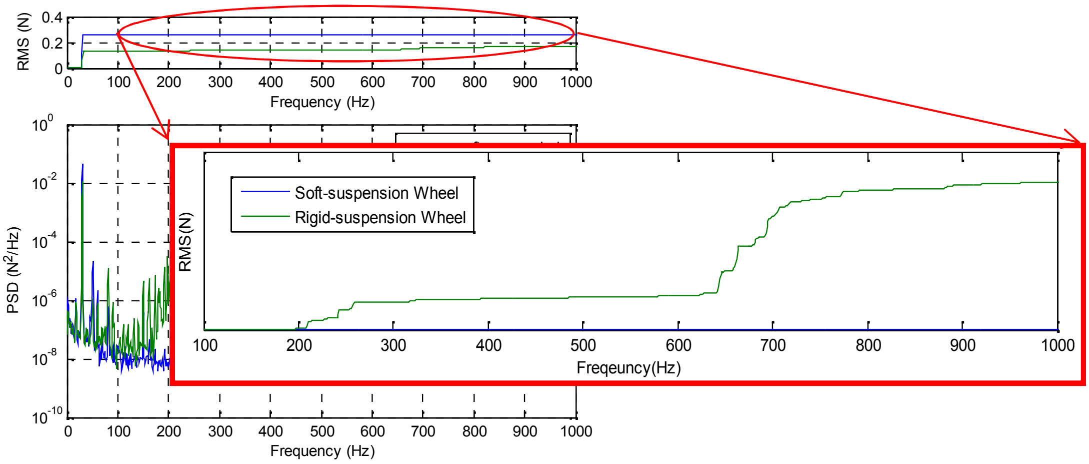

Figure 4-18 CRMS value plots of F_x at 1800 rpm for the soft- and rigid-suspended WAs (100 to 1000 Hz)

From Figure 4-18, microvibrations induced by the soft-suspended WA have much lower amplitudes in the frequency band between 200 to 1000 Hz. The blue curve (i.e. the soft-suspended case) is almost constant indicating no significant energy contribution in the response in this frequency band. On the green curve (i.e. the rigid-suspended case) however, the first major step occurs at about 220 Hz (between 200 to 260 Hz) due to the natural frequency of the motor-bearing system. It is stabilized from approximately 260 Hz and remained effectively flat until the second major step at about 690 Hz (between 640 to 700 Hz) due to also the motor-bearing system. Note that there are also some smaller steps on the green curve that are generated from the motor-bearing system since the microvibration forces and moments are not sufficiently damped because the rigid suspension used in the WA. These microvibrations are transmitted almost entirely through the rigid-suspension system and to the WA base and are thus being measured.

The comparison presented in Figure 4-8 indicates that the soft-suspended WA has improved dynamic performances at high frequencies in terms of microvibrations generated. Remembering that structural modes of the WA under study are designed at low frequencies (below 70 Hz), if at typical angular speeds, e.g. 2400 rpm (or 40 Hz) for RWAs, or 6000 rpm (or 100 Hz) for MWAs, there is no significant amplification on the fundamental harmonics in these bands, i.e. microvibrations induced by the soft-suspended WA are much quieter. This shows one of advantages of the soft-suspended WA over the conventional rigid designs.

4.9. Summary

In this chapter the WA-induced microvibrations in six-DoFs have been measured and analyzed. Apart from the typical dynamic characteristics such as harmonics and WA structural modes, nonlinearity and high damping were also seen in the responses and they are particularly influential in WA radial DoFs. Nonlinearity occurs at approximately 2280 rpm and causes the primary resonances (those on fundamental harmonics) in radial DoFs to be somewhat shifted. Responses after the resonances also grow at higher levels accompanied with amplitude fluctuations. It was also seen the fundamental harmonic responses in radial DoFs are significantly damped by the soft-suspension system. While in axial translational DoF, nonlinearity was not significant and harmonic responses present low damping. WA microvibration modeling strategies are briefly discussed, particularly regarding harmonic excitations modeling with consideration of nonlinearity and high damping of the WA. In particular, a systematic approach has been presented to extract suspension system stiffness and damping values (details are given in Appendix D). The measured results and modeling strategies are used in the next chapter for the WA microvibration response simulation. In addition, the soft-suspended WA exhibits much lower microvibration responses at frequencies above 200 Hz when compared to the conventional designs, which is one of its design advantages.

5. Wheel Assembly Hard-mounted Microvibration Model Validation and Response Prediction

In this chapter, the WA hard-mounted microvibration model derived in Chapter 3 is validated with the hard-mounted microvibration test results measured in Chapter 4, the full microvibration responses are predicted from the validated model. WA structural modes are first validated through Campbell diagram. Nonlinearity in the motor and high damping characteristics of the soft-suspension system are further discussed with the validation results. The detailed modeling of harmonic and broadband excitations is also introduced in this chapter. In particular, a parameter "trade-off" method is developed to estimate parameters for the harmonic excitations modeling. Linear harmonic responses are simulated from the WA microvibration model with damping values obtained in linear and nonlinear conditions. The frequently ignored broadband excitations are modeled empirically utilizing bandstop filters and applied to vibrations at different WA angular speeds to assess its modeling accuracy and efficiency in practice.

5.1. Wheel Assembly Structural Modes

The validation of WA structural modes is carried out by comparing the structural modes calculated from the WA hard-mounted microvibration model to the WA hard-mounted microvibration test results. If assuming an undamped and free system in Eq. (3.45), the classic Eigenvalue problem is solved. If damping values are small, natural frequencies of a damped system do not differ significantly from those in an undamped condition. For example in our case, damping ratios of the suspension system is about 0.02 in WA axial translational DoF (see Appendix D for detail), which is small enough such that the undamped natural frequencies are calculated to be the WA structural modes.

Remembering that from Chapter 3 the dynamics in the four radial DoFs are coupled for a cantilever configured WA, the closed-form expression of harmonic response cannot be derived for each radial DoF. The four radial EoMs need be solved simultaneously and numerically. The axial translational DoF on the other hand is independent from the four radial DoFs and its EoM is solved independently. Comparisons of analytical structural modes and microvibration test results are plotted as Campbell diagrams (up to 120 Hz) in Figure 5-1 a) and b) for the radial and axial translational DoFs respectively. In each figure, WA structural modes are plotted as black lines. The first five integer harmonics (H1 to H5) and one fractional harmonic (H2.7) are also plotted. They are highlighted as white lines in Figure 5-1 a).

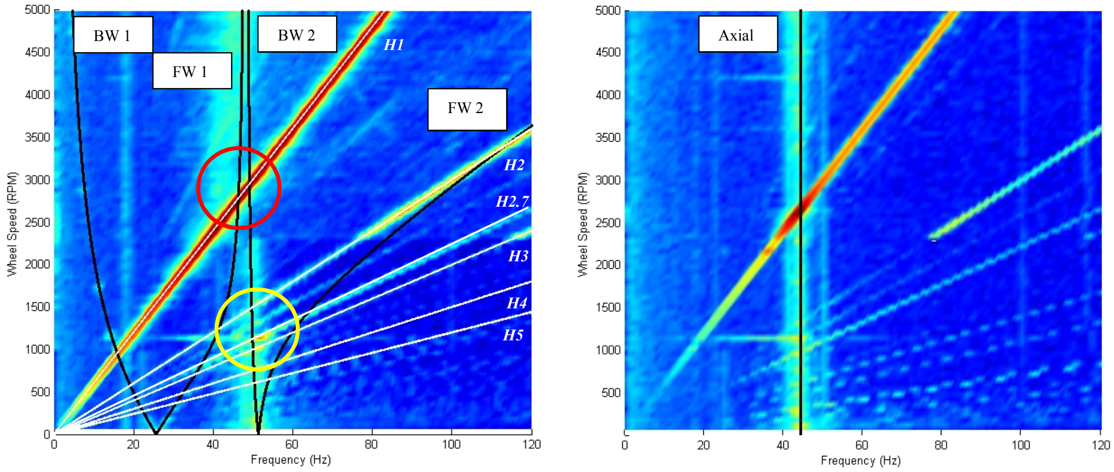

a) Radial DoFs (M_x) b) Axial translational DoF (F_z)

Figure 5-1 Campbell diagrams of WA structural modes compared to the microvibration test results

In general from Figure 5-1, all simulated WA structural modes are correlated well to the test results. In Figure 5-1 a), four whirls (two Forward Whirls (FW1 and FW2) and two Backward Whirls (BW1 and BW2)) are calculated from the WA hard-mounted microvibration model. It is clear that none of them are constant with speed due to the coupled translational and “rocking” motions in each radial DoF. Since the flywheel CoM is very close to the soft-suspension system, mathematically BW2 becomes approximately a vertical line and thus identified to be the radial translational mode. BW1 on the other hand is hardly seen in the test results with only several “points” presented, however the microvibration model has precisely captured this whirl. FW1 has clearly presented below 500 rpm and above 2400 rpm in the test results. FW1 and BW1 are together identified to be the “rocking” mode of WA. It begins at about 27 Hz from static and splits into two whirls as speed increases and eventually a “V” shape is formed. FW2 on the other hand is clearly present below 1200 rpm and above 2280 rpm (i.e. the “separation speed”). In particular, FW2 grows at a much higher rate when joined by H2 after the “separation speed”. In the low speed region, FW2 are excited by several close higher harmonics and thus large responses. In axial translational DoF in Figure 5-1 b), the independent axial translational mode starts from 44 Hz and as expected, remains constant in both simulated and test results.

Mathematically, the well correlated WA structural modes shown in Figure 5-1 have verified the undamped and free EoMs of the model. This includes the model parameters such as suspension stiffness and flywheel properties (mass and moment of inertias, etc.).

5.2. Nonlinearity and High Damping

Remembering that from Chapter 4 the WA harmonic responses exhibit nonlinearity and high damping at resonances, particularly in radial DoFs. With reference to the WA structural modes shown in Figure 5-1, these peculiar dynamic characteristics are further explained and modeling strategies are presented in this section. The development of the peculiar harmonic responses is first explained graphically in Figure 5-2.

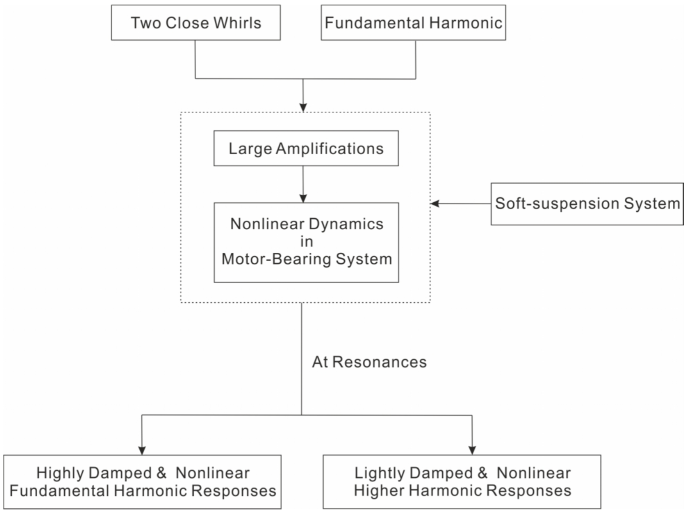

Figure 5-2 Development of nonlinear and highly damped harmonic responses

Firstly, from the Campbell diagram shown in Figure 5-1 a), it is clear that the two whirls FW1 and BW2 approach to each other as angular speed increases from static and later intersected by H1. The consequence of the interaction produces large amplifications in that region (high-lighted with a red circle) where H1 responses are significantly amplified by the two WA structural modes almost simultaneously. These large amplifications produce large input loads to the motor-bearing system and thus cause nonlinearity. In practice however, these amplifications do not show sharp spikes at resonances in radial DoFs since they are significantly reduced by the damping of the soft-suspension system, thus producing relatively flat shapes (see Figure 4-9 a) and Figure 4-11 b) for comparison). Consequently, fundamental harmonic responses in radial DoFs are highly damped at resonances.

In contrast, for the higher harmonic responses in radial DoFs in Figure 5-1 a), although BW2 and FW2 are excited by a number of close higher harmonics below 1200 rpm but the resonant amplitudes are not significantly damped. This is due to the fact that in general, higher harmonic responses have much smaller amplitudes, i.e. small inputs to the motor-bearing system, and also in this case the intersecting region is located at low speeds (high-lighted with a yellow circle in the figure). After the resonances, harmonic responses become nonlinear but are still not significantly damped (see Figure 4-16 a) and b) for example). In practice these dynamic characteristics make the modeling of higher harmonic excitations much more complicated than those in traditional cases, and this is mainly due to the different damping characteristics observed in the test results.

Nonlinearity also causes other issues in the WA microvibration response modeling. For example in Figure 5-1 a), there is a slight difference in the primary resonant frequencies between the simulated results (2680 rpm or 45 Hz) and test results (2400 rpm or 40 Hz), that is also caused by nonlinearity. Since the WA microvibration model is derived based on linear assumptions, it cannot precisely simulate the nonlinear influences such as the resonance shifting introduced here. The WA microvibration model presented in this thesis is able to closely simulate WA dynamics when compared to the experimental data.

The work presented in this section is used as the basis for harmonic excitations modeling in Section 5.3 and for determining WA suspension system damping values in Appendix D. Both results are used to simulate WA harmonic responses in Section 5.4.

5.3. Harmonic Excitations

Remembering that from Chapter 3 harmonics can be broken down into fundamental harmonics and higher harmonics. The fundamental harmonic excitations are derived as sinusoidal functions in each DoF (see also the complete derivation in Appendix B). Higher harmonic excitations due to irregularities in the motor however, are not physically modeled. They are assumed, for simplicity, as integer multiples of frequencies of fundamental harmonics and their amplitudes are modeled empirically by extracting parameters from the WA microvibration test results. Therefore the full harmonic excitation in each DoF is in fact the superposition of all harmonics considered. In this section the simulation of harmonic excitations is introduced. Due to WA axisymmetry, harmonic responses, F_y, F_z and M_x, are used for the WA microvibration model validation.

The harmonic excitations modeling method developed in this thesis is based on the microvibration test results, i.e. an empirical method. A program was first written to find a quantity termed as the "cut-off speed" from fundamental harmonic responses test results for each DoF. The "cut-off speed" is defined as the maximum speed where dynamic amplification caused by resonance on harmonics has not yet significantly influenced the response amplitudes in the test results. The rest can be considered as a "trade-off" process between the speed power and mass imbalances (both are variables in this process) until the simulated harmonic excitations (or inputs) closely correlate to the test results up to the "cut-off speed". This modeling process is presented in detail in Figure 5-3.

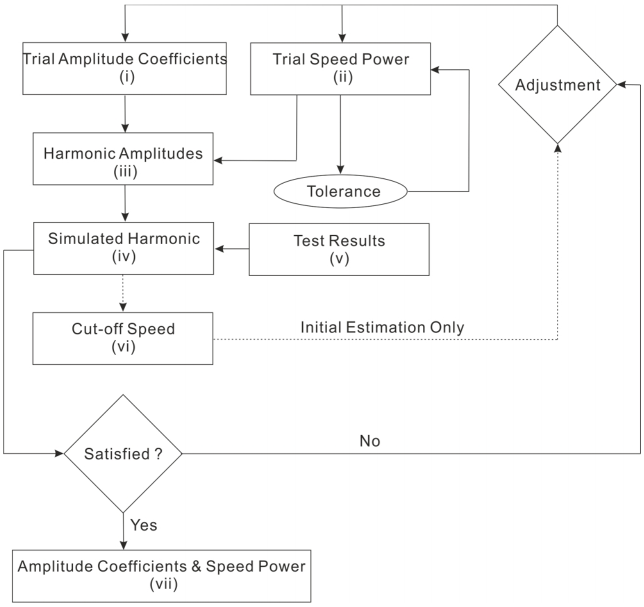

Figure 5-3 Harmonic excitation simulation process

The first step is to locate the "cut-off speed" for each DoF. This is primarily performed on the fundamental harmonics. Initially, the trial amplitude coefficients of harmonics are taken as the mass imbalances from the WA specification (i). Assume also the trial speed power to be square (or two) (ii), and the harmonic amplitudes can be estimated (iii). This process is repeated at every speed and the fundamental harmonic amplitudes in the speed band are simulated (iv). After comparing the simulated inputs to the corresponding test results for each DoF (v), adjustments are made in the trial amplitude coefficients and trial speed powers until they match each other from static, and the suitable speed range or the “cut-off speed” can be found for each DoF (v). The average value of “cut-off speed” of all DoFs is used as the final value and it is used constantly in the rest of modeling process for simulation of harmonics in all DoFs. Note that during the parameter adjustment process in Figure 5-3, the speed power is limited within the defined tolerance (i.e. ±15% from two). The final “cut-off speed” is found to be 1500 rpm. Finally, the same simulation process is applied to the higher harmonics, and in this case only up to the “cut-off speed” as it is already determined before. The speed power and amplitude coefficients of harmonic inputs are adjusted until the simulated inputs and the test results are closely correlated up to this speed (vii).

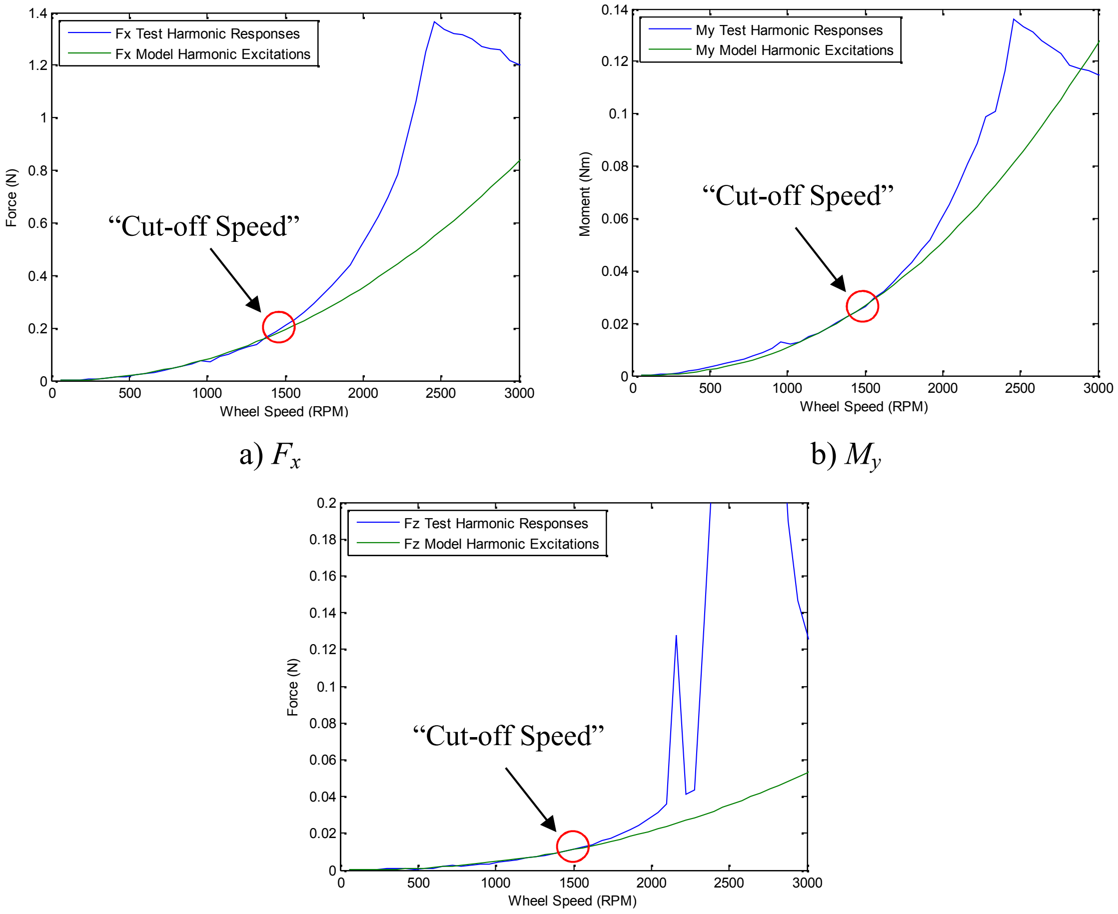

a) F_x b) M_y

c) F_z

Figure 5-4 Simulated fundamental harmonic excitations

Figure 5-4 shows the final simulated fundamental harmonic excitations for F_x, M_y and F_z (plotted up to 3000 rpm only for clear views). The corresponding test results of fundamental harmonic responses are also plotted. In later modeling (Section 5.4), the harmonic inputs curves shown here are implemented to the WA structural model, and the harmonic responses can be simulated. Since the “cut-off speed” is found to be 1500 rpm, the simulated fundamental harmonic excitations correlated well to the test results up to this speed in each DoF. After the “cut-off speed”, the test results begin to be significantly amplified by resonances, while the simulated harmonic excitations continue to grow with the speed power defined.

The simulation results of H5 harmonic excitations of F_x, M_y and F_z are shown in Figure 5-5 for example.

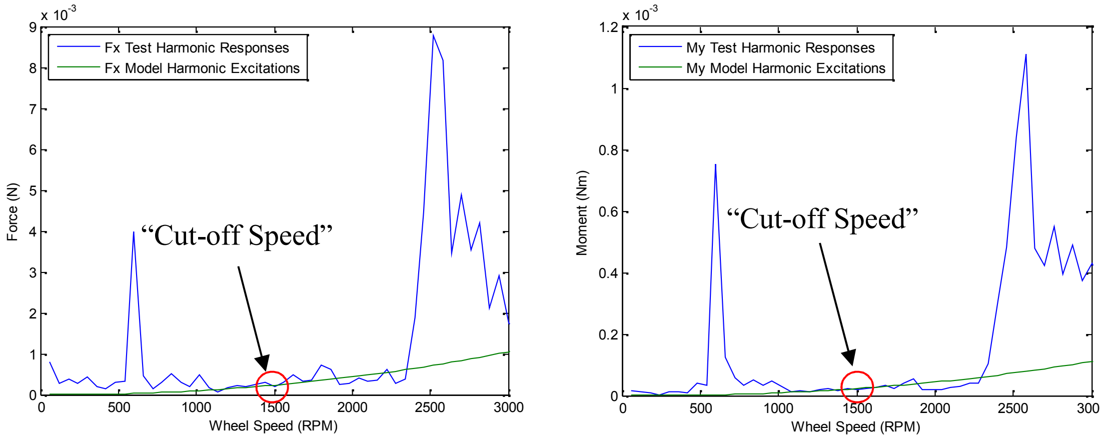

a) F_x b) M_y

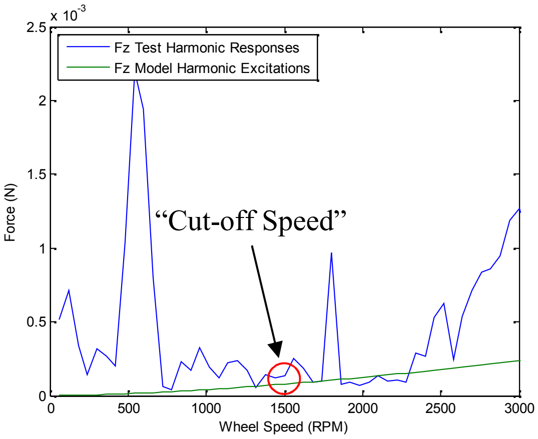

c) F_z

Figure 5-5 Simulated H5 harmonic excitations

In general in Figure 5-5, the simulated higher harmonic excitations have also correlated well with the general response levels of the test results up to approximately 1500 rpm apart from resonances in the low speed region. The appearance of resonances at low speeds on higher harmonics is the reason why the “cut-off speed” is only estimated from the fundamental harmonic response test results.

The complete simulation of harmonic excitations of F_x, M_y and F_z are plotted as AS waterfall plots in Figure 5-6. They are used as the harmonic inputs to the WA structural model. Note that higher harmonic excitations have much smaller amplitudes when compared to those of the fundamental harmonics.

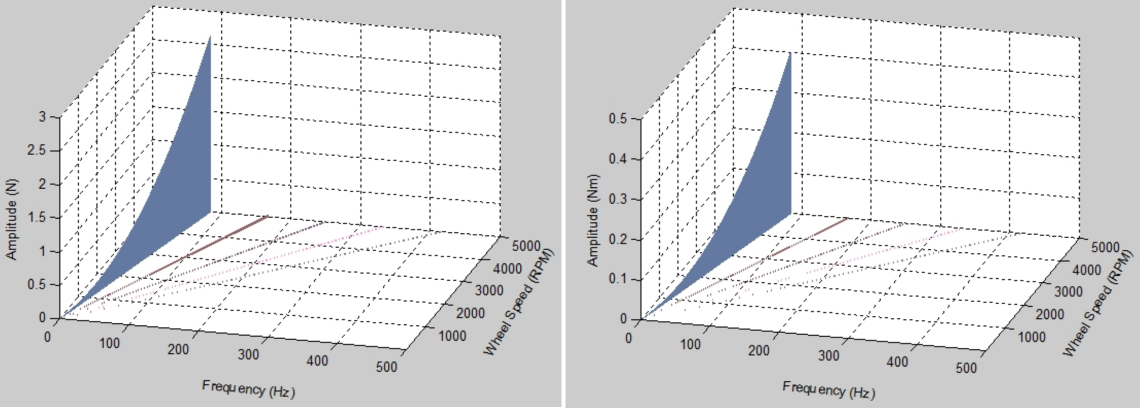

a) F_x b) M_y

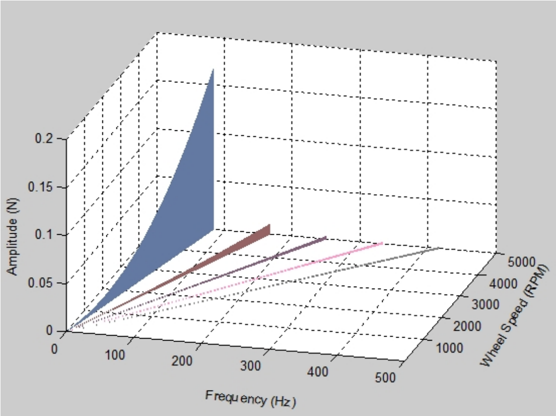

c) F_z

Figure 5-6 The complete simulated harmonic excitations (H1 to H5)

The final amplitude coefficients and speed powers of harmonic excitations obtained from this simulation method are given in Table 5-1.

Harmonic Number	Amplitude Coefficient (kg.m)	Speed Power	Amplitude Coefficient (kg.m^2)	Speed Power	Amplitude Coefficient (kg.m)	Speed Power
	F_x		M_y		F_z	
H1	4.5×10^{-6}	2.12	3.26×10^{-7}	2.25	1.35×10^{-7}	2.24
H2	4×10^{-8}		1×10^{-9}		8×10^{-9}	
H3	1×10^{-8}		3×10^{-10}		2×10^{-9}	
H4	5×10^{-9}		1×10^{-10}		1×10^{-9}	
H5	4×10^{-9}		2×10^{-10}		8×10^{-10}	

Table 5-1 Amplitude coefficients and speed powers of the simulated harmonic excitations

Note that the trial mass imbalance of fundamental harmonic excitation in F_z is assumed to be 3% of the static mass imbalance. Amplitude coefficients of higher harmonic excitations are extracted from order tracking plots of test results shown in Figure 4-16. Note also that the estimated speed powers are well retained within the tolerance defined (i.e. ±15% from two). Model parameters of harmonic excitations in Table 5-1 are applied in the WA microvibration model in order to simulate the harmonic responses.

5.4. Linear Harmonic Responses

Linear harmonic response forces and moments are simulated from the WA microvibration model using the state space approach in MATLAB. In general:

$$\boldsymbol{M}\ddot{\boldsymbol{x}}(t)+\boldsymbol{C}\dot{\boldsymbol{x}}(t)+\boldsymbol{K}\boldsymbol{x}(t)=\boldsymbol{Q}(t) \tag{5.1}$$

If the system is linear, its state space form can be derived. Let $\boldsymbol{x}_1(t)=\boldsymbol{x}(t)$ and $\boldsymbol{x}_2(t)=\dot{\boldsymbol{x}}(t)$, Eq. (5.1) then becomes:

$$\begin{bmatrix}\ddot{\boldsymbol{x}}_1(t)\\ \ddot{\boldsymbol{x}}_2(t)\end{bmatrix}=\begin{bmatrix}0 & \boldsymbol{I}\\ -\boldsymbol{M}^{-1}\boldsymbol{K} & -\boldsymbol{M}^{-1}\boldsymbol{C}\end{bmatrix}\begin{bmatrix}\boldsymbol{x}_1(t)\\ \boldsymbol{x}_2(t)\end{bmatrix}+\begin{bmatrix}0\\ \boldsymbol{M}^{-1}\end{bmatrix}\boldsymbol{Q}(t) \tag{5.2}$$

$$\boldsymbol{x}(t)=\begin{bmatrix}I & 0\end{bmatrix}\begin{bmatrix}\boldsymbol{x}_1(t)\\ \boldsymbol{x}_2(t)\end{bmatrix} \tag{5.3}$$

Using the linear dynamic system simulation function in MATLAB, the response displacements, $\boldsymbol{x}(t)$, and velocities, $\dot{\boldsymbol{x}}(t)$, can be simulated in the time domain for each DoF. After that, the linear harmonic response forces and moments can be calculated using the following equations:

$$F_x = k_t x_w \tag{5.4}$$

$$M_y = k_r \theta_w \tag{5.5}$$

$$F_z = k_z z_w \tag{5.6}$$

where all stiffness values are obtained previously.

5.4.1. Harmonic Responses with Linear Damping Parameters

In the WA microvibration model, harmonic responses are simulated for two conditions based on the suspension system damping. Remembering that from microvibration test results, the resonant amplitudes of fundamental harmonics are damped very differently in radial and axial DoFs by the soft-suspension system. Therefore rather than testing the damping values randomly to match the corresponding test results for each harmonic, in this thesis a systematic approach of calculating and implementing the damping values in the WA microvibration model is developed. The detailed introductions of obtaining damping values are presented in Appendix D. In this and the proceeding section, the implementation of damping values in the WA microvibration model is introduced.

Remembering that from the F_z microvibration test results presented in Chapter 4 (see Figure 4-7 f) for example), light damping is exhibited in axial translational DoF. This indicates the damping value estimated from the sine-sweep test must be performed with a low level input in order not to raise the high damping characteristics in the soft-suspension system, which should be the normal working condition.

From the low level input sine-sweep tests introduced in Appendix D, the damping ratio obtained is estimated approximately 0.02. Since nonlinearity is not raised in this case, this damping value is called the “linear damping” value for simplicity. Using the state space approach, the fundamental harmonic responses of F_x, M_y and F_z are simulated from Eq. (3.79). The simulated results are presented in Figure 5-7 and are also compared to the test results.

In Figure 5-7, the simulated fundamental harmonic responses have correlated well to the test results in F_z (see Figure 5-7 c)), however presenting a large disparity at the resonant amplitudes in the other two DoFs. Clearly, the damping value applied in radial DoFs is too small and is required to be increased. Rather than randomly increasing them in the model, i.e. a trial approach, a reliable and accurate method is introduced to obtain a high degree of damping values. They are discussed in Section 5.4.2.

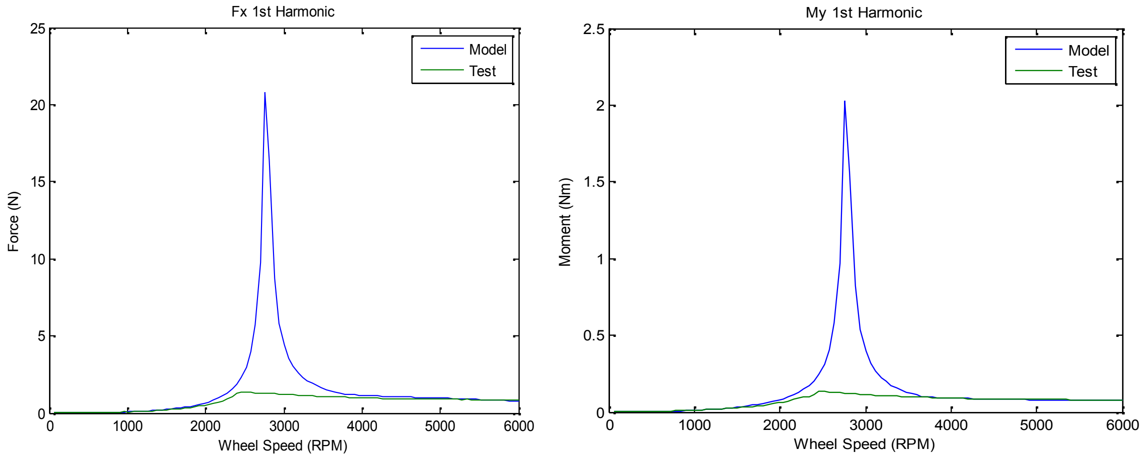

a) F_x

b) M_y

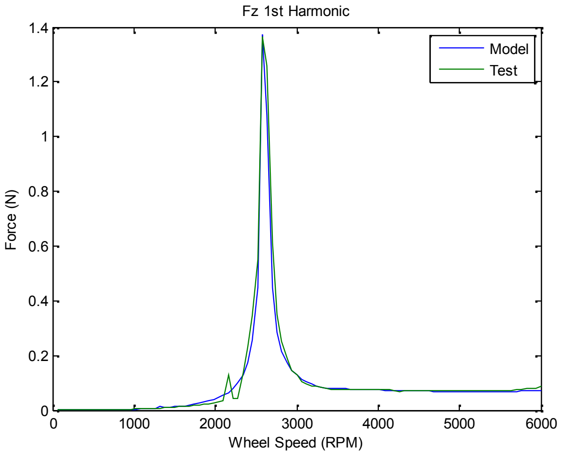

c) F_z

Figure 5-7 Simulated fundamental harmonic responses (linear damping values used)

Spectral map and AS waterfall plot of the simulated harmonic responses of F_z (H1 to H5) are presented in Figure 5-8.

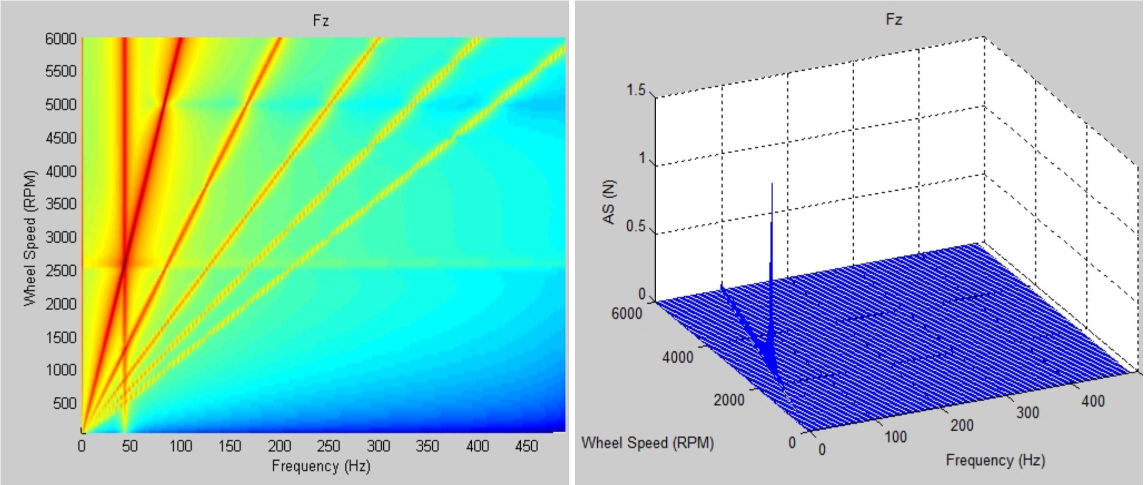

a) F_z spectral map b) F_z AS waterfall plot

Figure 5-8 Spectral map and AS waterfall plot of the simulated harmonic responses of F_z

The simulated higher harmonic responses and PSD waterfall plot of F_z are presented in Figure 5-9 a) and b) respectively.

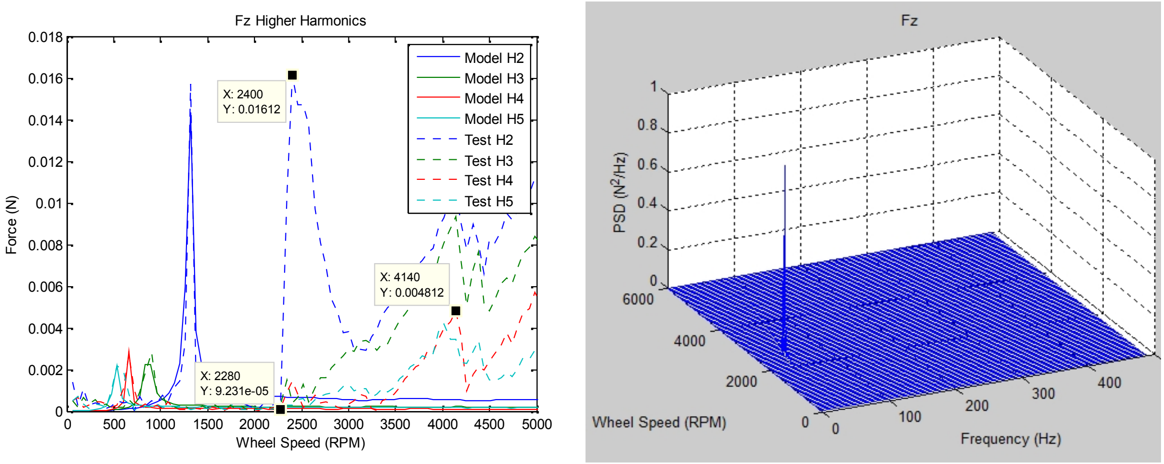

a) F_z higher harmonics (H2 to H5) b) F_z PSD waterfall plot

Figure 5-9 Simulated F_z harmonic responses

Remembering from the test results that the dynamics in axial translational DoF are not significantly influenced by nonlinearity and the amplitudes of harmonic responses grow and reduce smoothly before and after the resonance respectively. However this is not the case for higher harmonic responses. From the test results such as those shown in Figure 5-9 a), several unidentified responses are observed at speeds above 2400 rpm. For example, a large amplification at approximately 2400 rpm abruptly appears on H2, and afterwards, the responses generally maintain at much higher levels. Note also that several unidentified amplifications which appear horizontally at approximately 4100 rpm, this is similar to the horizontal response belts seen in Figure 4-17. They are generated from unknown sources in the motor and are beyond the scope of this thesis.

The linear WA microvibration model however, cannot simulate these unidentified higher harmonic responses, but it has accurately captured the dynamics at low speeds. This includes the harmonic responses, structural modes and their interactions. Therefore the linear damping value from low level input sine-sweep tests is also proved to be suitable for the modeling of higher harmonic responses in axial translational DoF. PSD waterfall plot of the simulated harmonic responses of F_z is presented in Figure 5-9 b). These are almost identical to the test results in Figure 4-7 f).

5.4.2. Harmonic Responses with Nonlinear Damping Parameters

Remembering that from high level input sine-sweep tests introduced in Appendix D, the input accelerations are large enough to raise nonlinearity in the WA suspension system, the damping values obtained in the tests are called “nonlinear damping” values for simplicity. The damping ratio estimated is approximately 0.15 in radial DoFs. The damping value is calculated and applied in the WA microvibration model. The fundamental harmonic responses are simulated for F_x and M_y and compared to the test results. These are shown in Figure 5-10 a) and b) respectively.

In Figure 5-10 a) and b), the simulated fundamental harmonic responses in both cases are much better correlated to the test results compared to those with linear damping values applied in Figure 5-7 a) and b), especially at resonances. As mentioned earlier, the slight differences in resonant frequencies between model and test results are due to resonance frequency shifting observed in the test results that the linear WA microvibration model cannot simulate. Aside from this, the fundamental harmonic responses are well simulated by the model.

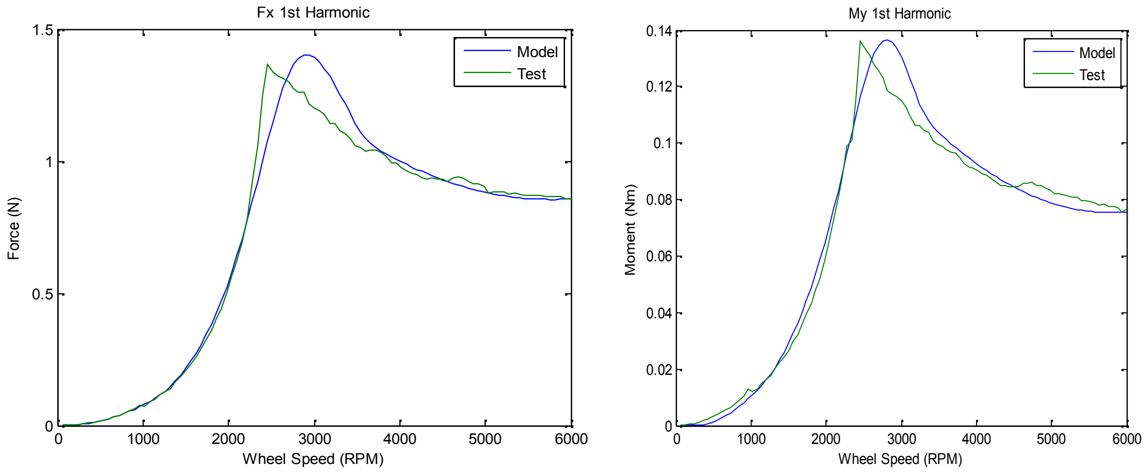

a) F_x b) M_y

Figure 5-10 Simulated fundamental harmonic responses in radial DoFs (nonlinear damping values used)

Higher harmonic responses in radial DoFs are also simulated from the WA microvibration model using nonlinear damping value however it failed to capture their resonant amplitudes correctly. Since the nonlinear damping value is constantly used in all harmonic response simulations in radial DoFs, it not only affects the fundamental harmonics but also higher harmonics and thus shows relatively flat shaped spikes such as those in Figure 5-10. This contradicts the observations in the test results such as in Figure 4-16 a) and b), where sharp resonant spikes appear on every higher harmonic response.

Technically one possible approach to solve this problem is to use the linear damping value for higher harmonic response simulations in radial DoFs, but the overall process becomes more complicated since different damping values would be used in different harmonics in each radial DoF and the complete EoM must be solved simultaneously as introduced earlier. However, the modeling method introduced in this thesis would become inefficient from the practical point of view, although all harmonic responses can be accurately simulated in this way.

AS waterfall plots and spectral maps of the simulated harmonic responses of F_x and M_y are plotted in Figure 5-11.

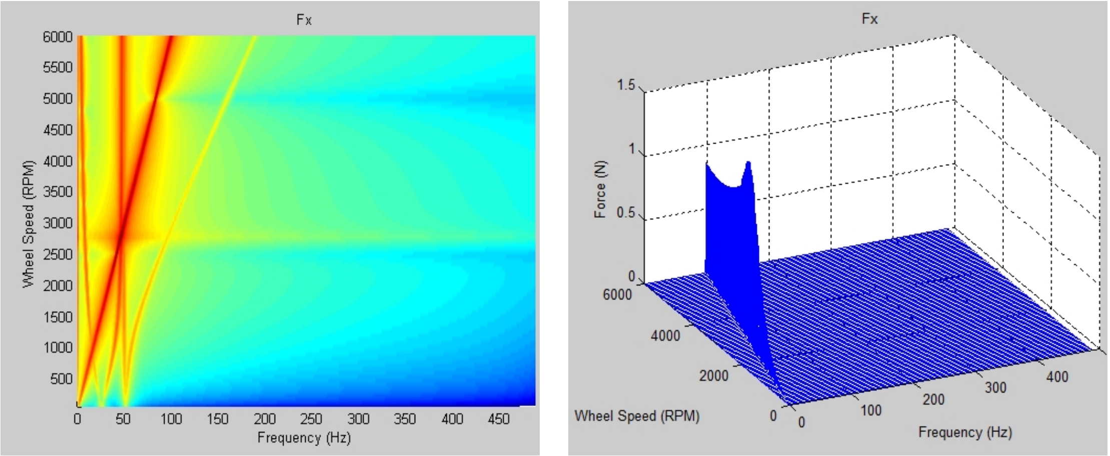

a) F_x spectral map c) F_x AS waterfall plots

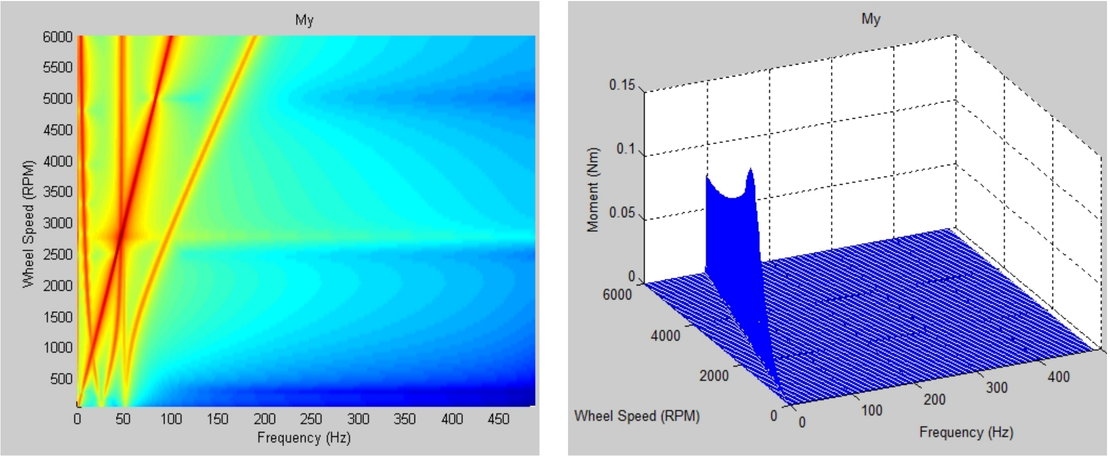

b) M_y spectral map d) M_y AS waterfall plots

Figure 5-11 Spectral maps and AS waterfall plots of F_x and M_y

In Figure 5-11 a) and b) since only fundamental harmonic responses are simulated from the WA microvibration model, the four WA structural modes intersect with it. For the AS waterfall plots in Figure 5-11 c) and d), it is clear that resonant amplitudes are significantly reduced by the high damping values applied in the model, and they also closely simulate the test results.

Note that in practice for this WA, higher harmonic responses are too small and unlikely contribute significant amount of energy to the overall microvibrations at any speed (see Figure 4-7 and Figure 4-13 for example), thus for simplicity higher harmonic response simulations can be ignored in the WA microvibration modeling. In contrast, all dynamic characteristics of the fundamental harmonic responses have been accurately simulated by the model (provided that ignoring nonlinearity influences).

In summary the method of applying damping values in the WA microvibration harmonic response simulations in this section is depicted in the following figure.

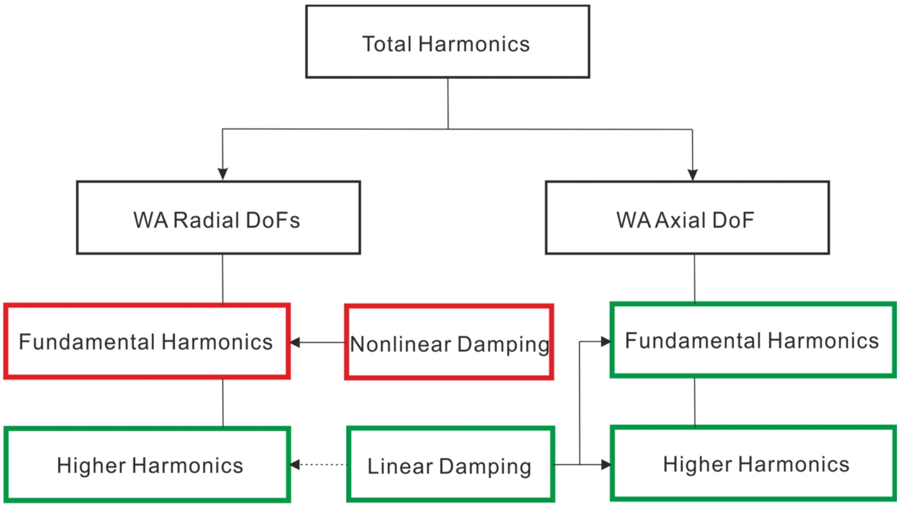

Figure 5-12 Damping implementation in the WA harmonic response simulation

- ***Linear*** damping values from low level input sine-sweep tests are used for fundamental harmonic response simulations in WA ***axial*** translational DoF.

- ***Nonlinear*** damping values from high level input sine-sweep tests are used for fundamental harmonic response simulations in WA ***radial*** DoFs.

- ***Linear*** damping values from low level input sine-sweep tests are used for ***higher harmonic*** response simulations in WA ***axial*** DoF, but with limitations in WA radial DoFs.

5.5. Broadband Noise Excitations

Generally, broadband noise is generated in the motor and bearing system and the amplitudes of broadband noise are much smaller compared to those of harmonics except at very low spin speeds. For a typical WA, they constantly accompany harmonics as long as the flywheel spins and exist in the entire frequency band analyzed. The WA and also the satellite structure are also continually excited by broadband noise. Due to their dynamic characteristics, broadband excitations in the WA are similar at all speeds, i.e. speed-independent. However their responses are speed-dependent as they are amplified by gyroscopic effects and structure modes the WA. Figure 4-6 b) is shown here again to demonstrate the significance of the broadband noise in typical WA-induced microvibrations.

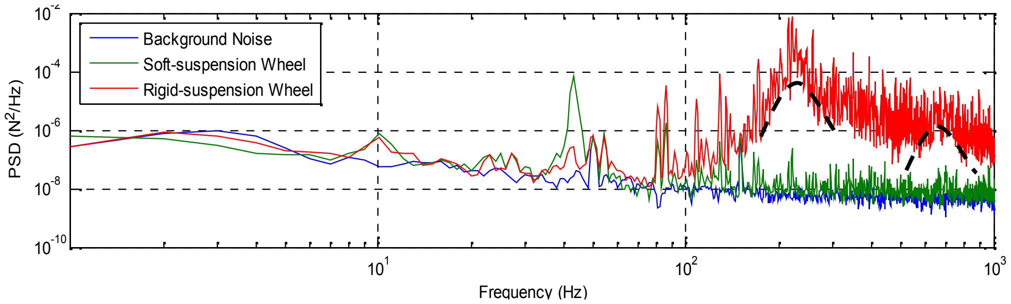

Figure 4-6 b) Examples of background noise and WA responses of F_z at 600 rpm

Firstly, broadband noise is clearly seen in the entire frequency band in both soft- and rigid-suspended WAs, but those induced by the rigid-suspended WA are the best examples. Remembering that the two broadband "mound" shaped peaks centered at 220 Hz and 690 Hz respectively are identified as the motor-bearing system natural frequencies. The two peaks are clearly excited by broadband noise, while the traditional WA microvibration modeling method ignores them completely. In contrast, the soft-suspended WA is much quieter due to its design. Note that the background noise is very close to the broadband noise of the soft-suspended WA in the figure.

Generally, the broadband excitation simulation method introduced in this section utilizes bandstop filters to block the identified spikes (harmonics and resonances) in a typical microvibration signal. The rest of the signal is thus the broadband noise. Therefore the modeling process mainly includes two parts: identify spikes and design filtering process. This can be presented in the following chart:

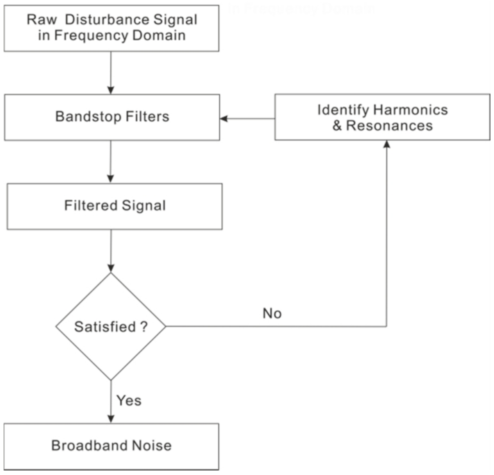

Figure 5-13 Broadband excitation simulation process

5.5.1. Spike Identification

Firstly, spikes such as harmonics and resonances in a raw microvibration force or moment signal are identified. The method shown here is based on the use of CRMS value plot produced from microvibration test results (see Chapter 4). For example, PSD and CRMS value plot of F_z at 1800 rpm is presented in Figure 5-14 a) between 0 to 500 Hz, its zoomed plot between 50 to 500 Hz is shown in Figure 5-14 b).

From the definition of CRMS value, if a spike exists at a frequency in the microvibration signal, a corresponding step jump appears in the CRMS value plot. The spike in this case could be either harmonic or resonance as long as it contributes "noticeable" energy to the signal. The difference in the amplitudes between steps indicates the amount of energy contributed, while the amplitude itself indicates the total amount of energy that has been accumulated so far. The CRMS value plot is often used for this purpose, i.e. to exam energy variation in a signal as shown in Chapter 4. It can also be used to identify spikes in a signal with extremely high accuracy, however this method has not been found in the literature.

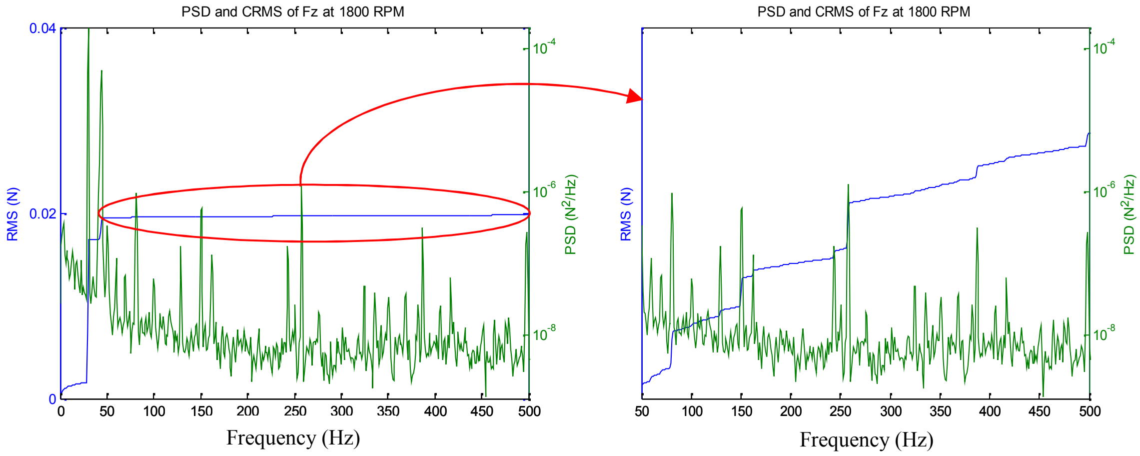

a) 0 to 500 Hz

b) 50 to 500 Hz

Figure 5-14 PSD and CRMS value plot of F_z at 1800 rpm

On the other hand, due to the different spike amplitudes in a signal, some will not be immediately blocked by the filters and an iteration filtering process must be performed. As the filtering iteration proceeds, the number of spikes is gradually reduced until the RMS values of the remaining spikes are within the defined critical value. Following this method, it is guaranteed that all "noticeable" spikes are blocked or removed, while the defined critical value determines if the spike is "noticeable" or not.

As mentioned previously, the general background noise is very close to the broadband noise for the soft-suspended WA. In this work the critical value is obtained from the CRMS value plot of background noise. Figure 5-15 presents a segment of PSD and CRMS value plot of background noise between 200 to 500 Hz.

Red arrows in the figure show some of the spikes used to calculate the critical value. From the figure, the frequency difference between the two neighboring spikes is approximately 20 Hz (identified manually), the difference in RMS values between them is calculated for a set of selected neighboring spikes and the average value is used. Note that the fact that the background noise CRMS value plot steady accumulates as speed increases indicates no significant amplification occurs as expected, thus this calculation process can be programmed and automatically performed. In this case, the critical RMS value is found approximately 1.5×10^{-5} N.

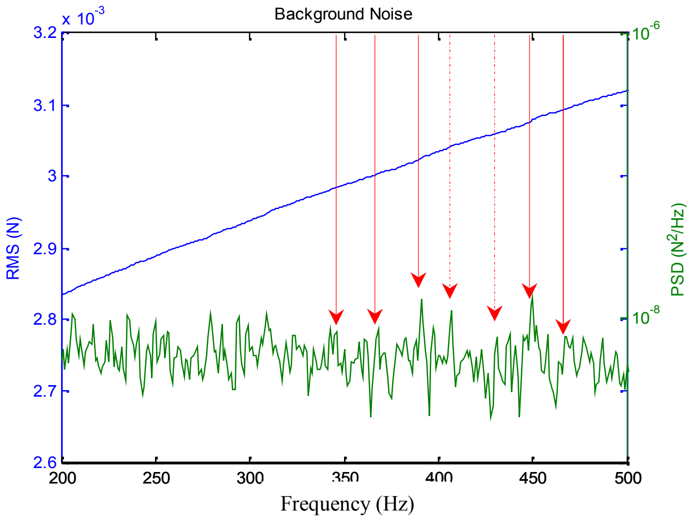

Figure 5-15 PSD and CRMS value of the background noise (200 to 500 Hz)

Following the process introduced above, the identified harmonics and resonances in F_z at 1800 rpm are shown in Figure 5-16 with red circles.

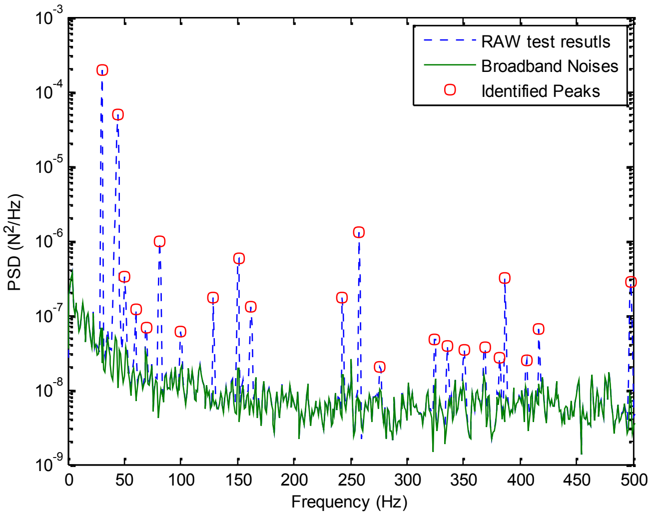

Figure 5-16 Identified spikes and broadband noise of F_z (1800 rpm)

Once the desired spikes are identified, one bandstop filter is assigned to each spike and filtering process begins. These are introduced in the following section.

5.5.2. Filtering Process

Typical Butterworth bandstop filters are used to block the identified spikes in the simulation of broadband excitations and are already programmed in MATLAB. Characteristics of the filter mainly depend on the frequency of spike that needs to be blocked and some pre-defined parameters. For example, filter parameters for the spike at 258 Hz are given in Table 5-2.

Parameters	Values
Passband corner frequency	257.9 Hz
Stopband corner frequency	258.1 Hz
Passband ripple	1
Stopband attenuation	3
The lowest order	1
normalized cut-off frequency band	257.5 to 258.5 Hz

Table 5-2 Parameters of the bandstop filter for the spike at 258 Hz

Note that frequencies in Table 5-2 need to be converted into radians for filter design. The resulting magnitude and phase of the filter for the spike at 258 Hz are plotted in Figure 5-17 a).

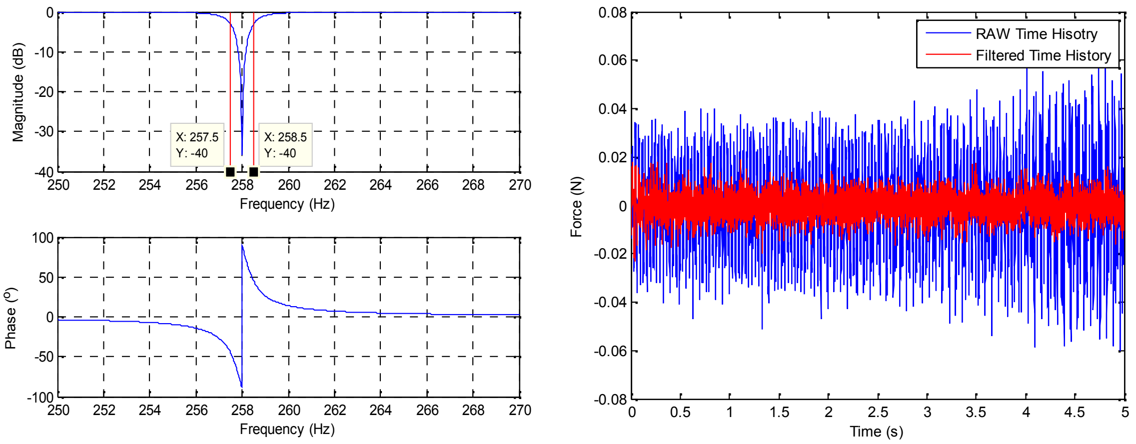

a) Butterworth bandstop filter at 258 Hz

b) Comparison of raw and filtered time signal at 1800 rpm (0 to 5 s only)

Figure 5-17 Bandstop filter and the filtered time history of F_z at 1800 rpm

From Figure 5-17 a), the bandstop filter has been designed with a narrow cut-off frequency band, in this example ± 0.5 Hz. The filter thus only blocks the identified spikes with very little influences to the surrounding responses. Note also that the maximum magnitude of the filter is defined at -36 dB. It is designed so that the resulting filtered amplitudes do not overshoot the general response level, however they are large enough to immediately block spikes with smaller amplitudes (e.g. spikes at 100 Hz and 276 Hz in Figure 5-16), while only partially reducing those with large amplitudes (e.g. spikes at 30 Hz and 44 Hz in Figure 5-16). An iteration filtering process mentioned earlier is therefore performed until all remaining responses in the signal are outside the critical value.

The finally filtered F_z microvibrations (i.e. broadband noise of F_z) at 1800 rpm are plotted in both frequency and time domain and compared to the raw microvibrations; they are shown in Figure 5-16 and Figure 5-17 b) respectively. In the frequency domain, it is clear that all identified spikes have been blocked and the remaining signal has approximately the same amplitudes; the same results are also seen in the time domain. The broadband noise obtained at any speed using this method can be applied as the universal broadband excitations to the WA microvibration model. In the microvibration model, since a linear assumption is used, they can be superimposed with harmonic excitations, such as in Eq. (3.80). The simulation of the complete WA microvibration responses under harmonic and broadband excitations are presented in the next section.

5.6. Full WA Microvibration Response Simulation

In this section, harmonic and broadband excitations are superimposed as the complete excitation to the WA microvibration model and their responses are simulated. The simulated results are compared to the test results.

F_z at 1800 rpm is first used as the demonstration example. In this case, all harmonics identified in Figure 5-16 are simulated using the method introduced in Section 5.3, including the integer and fractional higher harmonics. The broadband excitations are taken from Figure 5-17 b). The full responses are simulated from the WA microvibration model using the state space approach presented in Section 5.4. First of all, the simulated responses under harmonic excitations are presented; shown in Figure 5-18 a) on the next page. Next, the complete responses under harmonic and broadband excitations are presented; shown in Figure 5-18 b). Both simulated responses are compared with the same test results of F_z at 1800 rpm.

It is clear from Figure 5-18 a) if only harmonic excitations are considered in the model, frequency regions where no harmonic excitation modeled remain unexcited, i.e. "quiet regions". The general response level of these "quiet regions" is only raised for a very small amount by the dynamic amplification of the WA structural mode (in this case the axial translational mode only and at 44 Hz). Note also that the resonant amplitude is slightly lower than the test results due to the lack of broadband excitations, although harmonic responses have been well simulated, as also presented in previous sections.

Figure 5-18 a) also demonstrates the importance of broadband excitations in the WA microvibration modeling. Both results in the figure are plotted in logarithmic scale in PSD and show large differences between the model and test results in the "quiet regions". Note that they are hardly noticed in linear scale (see Section 4) and are generally ignored if the requirements of modeling accuracy limited, i.e. the traditional modeling method in the literature. Figure 5-18 b) presents the simulated responses under both harmonic and broadband excitations. In this case, the previous "quiet regions" have disappeared since responses are excited in the complete frequency band. In other words, the "quiet regions" are leveled up by broadband noise. Note that the resonant amplitude is accurately matched to the test results in this case, while harmonic responses are also increased slightly, however due to the small amplitudes of broadband noise responses in general, they are not significant.

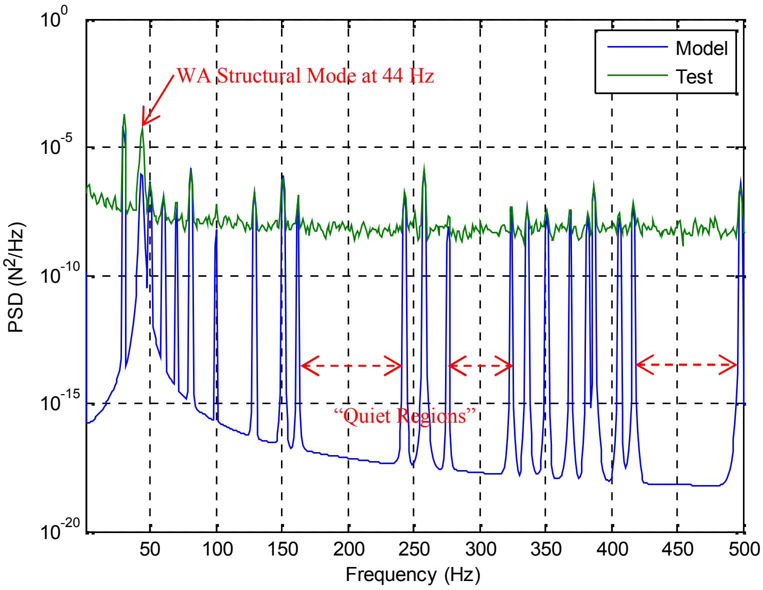

a) Harmonic responses only

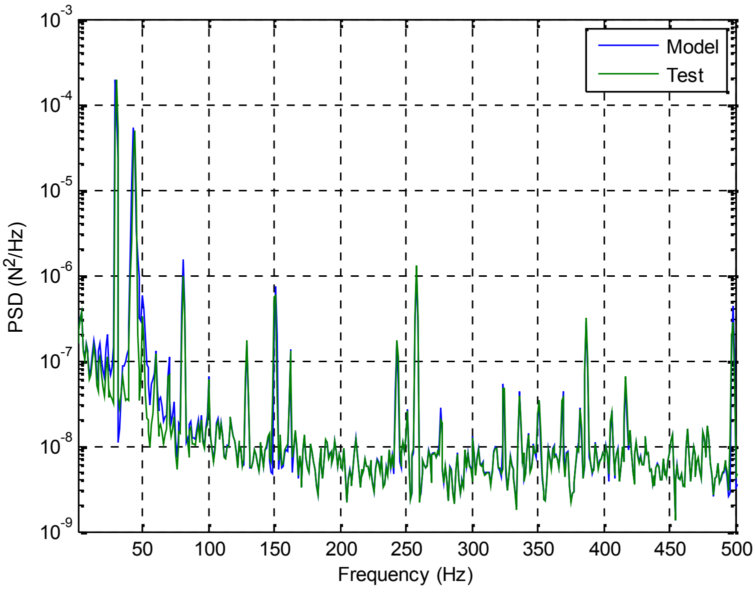

b) Full responses

Figure 5-18 Simulated full responses of F_z at 1800 rpm

As an example to demonstrate the speed-independent characteristic of broadband noise for this WA, harmonic responses are simulated at 3000 rpm of the WA spin speed and broadband excitations shown above (i.e. extracted from 1800 rpm) are superimposed with them under the linear assumption. The same simulation process and treatments are applied and the results are shown in the following figure.

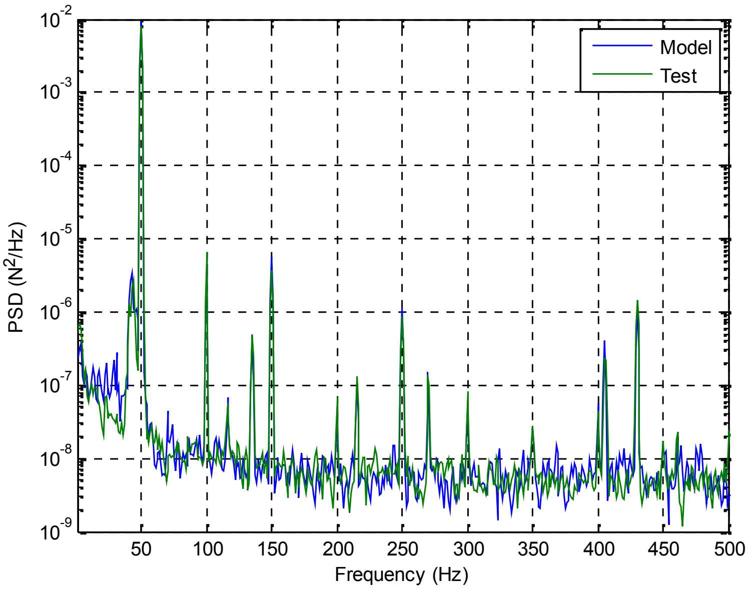

Figure 5-19 Simulated full responses of F_z at 3000 rpm

From Figure 5-19 firstly it is clear that the general broadband responses are simulated well compare to the test results, indicating the broadband noise is indeed speed-independent. Since broadband noise is random in nature, there are no identical broadband responses between any WA spin speeds, and therefore differences that are seen in the broadband responses in the figure. The overall RMS values for simulated and test results are 0.112 and 0.11 N (the error is about 1.8%). Harmonics and the WA axial translational mode are also simulated and are very close to the test results as expected.

5.7. Summary

The validation of the WA microvibration model and simulation of WA microvibration responses have been presented in this chapter. WA structural modes were first validated through Campbell diagrams. The peculiar dynamic characteristics of nonlinearity and high damping observed in the microvibration test results were discussed further. Harmonic excitation modeling strategies were also explained. A new systematic approach was developed to simulate the harmonic excitations from the test results based on several parameters and factors. The implementation of damping in the microvibration model was also discussed. Linear and nonlinear damping values were obtained from low and high level input sine-sweep tests respectively, and were applied to simulate the harmonic responses in different WA DoFs. The simulation of the traditionally ignored broadband excitations w introduced. Broadband excitations were obtained using an empirical method by identifying and blocking undesired spikes in the microvibration signal using typical bandstop filters. The complete WA responses were simulated at two WA spin speeds (1800 rpm and 3000 rpm). Both results show that the full WA microvibration responses simulated were very close to the test results, thus the modeling methods developed for WA microvibration analysis in a hard-mounted boundary condition were also validated.

6. Wheel Assembly-Seismic Mass Coupled Microvibration Analysis

In this chapter, a method is developed to measure the WA-induced microvibrations in a coupled boundary condition. The ultimate goal of the WA-structure coupled microvibration study is to establish the reaction loads (forces and moments) induced by the WA at its connection interface with the supporting structure (i.e. the driving point). This is achieved experimentally and analytically. Experimentally, a measurement system is designed that couples the WA to a rigid seismic mass which is used as the supporting structure in this study. When the flywheel spins, seismic mass response accelerations are measured while the interface forces and moments are calculated through a load-acceleration transfer matrix. Analytically, the coupled WA-seismic mass microvibration model is derived using the similar method as for the hard-mounted case shown in Chapter 3. Interface forces and moments induced by the WA in the coupled boundary condition are calculated from the model and validated with the coupled microvibration test results.

6.1. Coupled Microvibration Model Derivation

The measurement system developed for the WA-seismic mass coupled microvibration measurement is called the “Seismic Mass Vibration Measurement System” or “SMVMS”, it is presented in Figure 6-1 a). Its simplified model is presented in Figure 6-1 b). The WA is mounted upside-down on a seismic mass. The seismic mass is made of stainless steel and is thus a rigid body in the frequency band considered (up to 500 Hz). The only flexible component in this system is the WA soft-suspension system that connects the two rigid bodies (flywheel and seismic mass, while the WA base is considered as part of the seismic mass since they are rigidly connected). The whole system is suspended using elastic cords from a ground-fixed steal frame to simulate the “free-free” boundary condition.

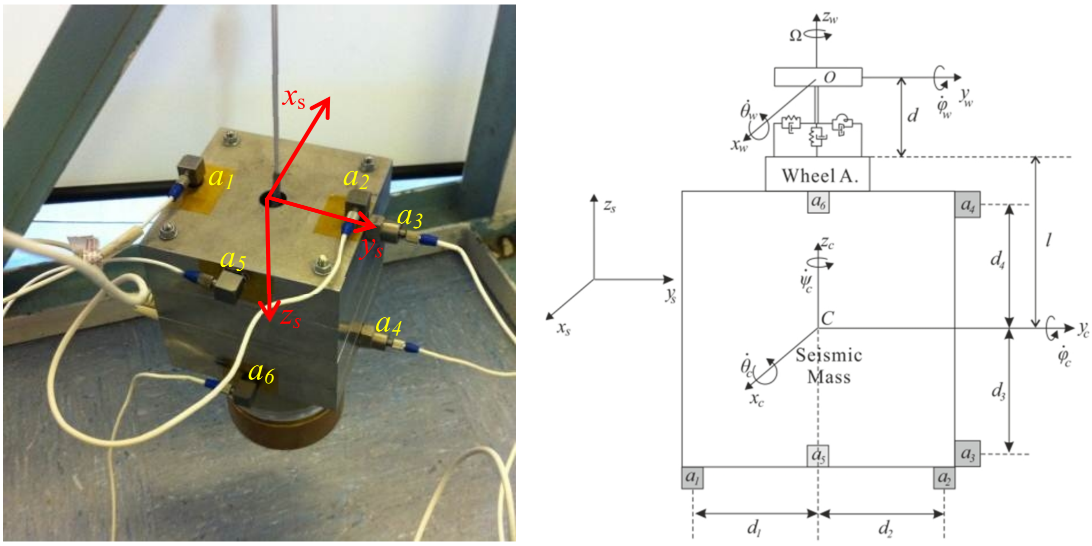

a) Test setup b) Simplified model

Figure 6-1 The SMVMS and its simplified model

In Figure 6-1, the seismic mass coordinate system is defined as $x_c y_c z_c$ with origin C at the seismic mass CoM. θ_c, φ_c and ψ_c are the corresponding rotations of the seismic mass about the three orthogonal axes shown in the figure. Note that in torsional DoF, the seismic mass perturbation speed is much smaller compared to the flywheel angular speed, thus ignored. M_c is the mass of seismic mass; I_{c_xx} and I_{c_yy} are its moment of inertias about x_c-axis and y_c-axis respectively. The vertical distance from the soft-suspension system to the seismic mass CoM is l. By assuming small angles of rotations, the linearized kinetic energy, T_c, of the seismic mass is derived:

$$T_c \approx \frac{1}{2}\left[M_c\left(\dot{x}_c^2+\dot{y}_c^2+\dot{z}_c^2\right)+I_{c\_xx}\dot{\theta}_c^2+I_{c\_yy}\dot{\varphi}_c^2\right] \tag{6.1}$$

Since the soft-suspension system connects the two rigid bodies in the model, the potential energy of the system involves both WA and seismic mass. Therefore the soft-suspension system somehow acts as a load transfer link between the two rigid bodies, thus to derive the potential energy and work done of the system, the relative displacements and velocities of springs and dashpots are required. The linearized potential energy of the system, U_c, in this case can be derived as:

$$\begin{aligned} U_c \approx \frac{1}{2}\Big[& k_z\left(z_c - z_w\right)^2 + k_r\left(\theta_c - \theta_w\right)^2 + k_t(-y_c + y_w + l\theta_c + d\theta_w)^2 \\ & + dk_t(-y_c + y_w + l\theta_c + d\theta_w)^2 + k_r(\varphi_c - \varphi_w)^2 - dk_t(x_c - x_w - l\varphi_c + d\varphi_w)^2 \\ & + k_t(x_c - x_w + l\varphi_c + d\varphi_w)^2 \Big] \end{aligned} \tag{6.2}$$

The work done is also derived and has a similar form to Eq. (6.2), it is not presented here. EoMs of the coupled microvibration model is also derived using an energy method. The system in this case has ten DoFs, five from WA and the other five from seismic mass. The linearized EoMs of the coupled system in matrix form is expressed as:

$$\boldsymbol{M}_s\ddot{\boldsymbol{q}}_s + \left(\boldsymbol{C}_s + \boldsymbol{G}_s\right)\dot{\boldsymbol{q}}_s + \boldsymbol{K}_s\boldsymbol{q}_s = \boldsymbol{F}_s \tag{6.3}$$

All matrices in Eq. (6.3) are listed in Appendix F. Note that if the seismic mass is fixed to ground, i.e. in a hard-mounted boundary condition, only five DoFs of WA are left in Eq. (6.3) and eventually the equation reduces to Eq. (3.79). Note that Eq. (6.3) also needs to be solved numerically due to the large number of unknowns and the coupled dynamics in WA radial translational and rotational DoFs as in the hard-mounted case.

6.2. The Coupled Microvibration Measurement System

WA-seismic mass coupled microvibration tests are performed using the SMVMS. The SMVMS utilizes several accelerometers mounted on the seismic mass to measure its response accelerations under the spinning flywheel. The measured accelerations allow microvibration forces and moments at their interface to be reconstructed. This can be considered as an indirect method to measure WA-induced microvibrations in a coupled boundary condition. In this section, the relationship between the response accelerations on seismic mass and interface loads, i.e. a transfer matrix between the two quantities, is derived and verified with test and numerical simulation results.

6.2.1. Seismic Mass Rigid Body Dynamics

The seismic mass is constructed from four stainless steel layers stacked together and connected by aluminum bars at its four corners; see Figure 6-2.

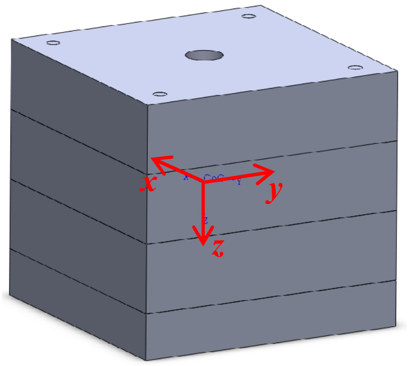

Figure 6-2 Seismic mass model

The coordinate system of the seismic mass is defined at its CoM. Note that the z-axis is defined positive as downwards. The six EoMs under the action of the generic force, F_i, and moment, M_i, exerted at its CoM can be written in the following classic form:

$$\begin{cases} F_x = m\ddot{x} \\ F_y = m\ddot{y} \\ F_z = m\ddot{z} \end{cases} \qquad \begin{cases} M_x = \dot{\omega}_x I_{xx} + \omega_y \omega_z (I_{zz} - I_{yy}) \\ M_y = \dot{\omega}_y I_{yy} + \omega_x \omega_z (I_{xx} - I_{zz}) \\ M_z = \dot{\omega}_z I_{zz} + \omega_x \omega_y (I_{yy} - I_{xx}) \end{cases} \tag{6.4}$$

The three force equations describe the translational motions and the three moment equations (known as Euler's equations) describe the rotational motions of a rigid body. Remembering that in theory both WA and seismic mass are axisymmetric, thus only one principle plane is necessary for this dynamics study. In this thesis the yz principle plane is used, so only F_y, F_z and M_x in Eq. (6.4) are necessary. Furthermore, there is no rotation about z-axis in the principle yz plane, thus ω_z is zero in M_x in Eq. (6.4). If the applied force is a sinusoidal excitation in y direction and the phase is assumed to be zero, the following relationship is derived from F_y and M_x:

$$\dot{\omega}_x I_{xx} = -F_y d_0 \sin(2\pi f t) \tag{6.5}$$

where d_0 is the moment arm from the applied sinusoidal force in y direction to the seismic mass CoM; f is the excitation frequency; t is time. The angular velocity about x-axis, ω_x, under the excitation force can therefore be solved numerically from Eq. (6.5).

Next, consider expressions relating the position, velocity and acceleration at any points A and B, particularize them to points of a rigid body, for example:

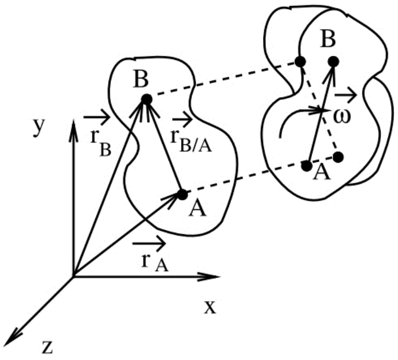

$$\begin{cases} \boldsymbol{r}_B = \boldsymbol{r}_A + \boldsymbol{r}_{B/A} \\ \boldsymbol{v}_B = \boldsymbol{v}_A + \boldsymbol{v}_{B/A} \\ \boldsymbol{a}_B = \boldsymbol{a}_A + \boldsymbol{a}_{B/A} \end{cases} \tag{6.6}$$

Figure 6-3 Rigid body motion representation

where $\boldsymbol{r}_{B/A}$ is the position vector of B relative to A, $\boldsymbol{v}_{B/A}$ is the velocity vector of B relative to A, and $\boldsymbol{a}_{B/A}$ is the acceleration vector of B relative to A.

Consider also that the rigid body moves in a plane, thus every movement of a rigid body can be decomposed as a translation of the vector $\boldsymbol{r}_{B/A}$ and a rotation around a point (A, for example). For a rigid body, the distance between any two points on the body is constant, thus the relative position vector has a constant modulus. As a consequence, the relative velocity is that associated with the rotation around A and can be written as:

$$\boldsymbol{v}_{B/A} = \boldsymbol{\omega} \times \boldsymbol{r}_{B/A} \tag{6.7}$$

where $\boldsymbol{\omega}$ is the angular velocity, a vector that is perpendicular to the plane of movement of the rigid body. With the aid of this equation, the velocity of B can be written as:

$$\boldsymbol{v}_B = \boldsymbol{v}_A + \boldsymbol{\omega} \times \boldsymbol{r}_{B/A} \tag{6.8}$$

The acceleration is the first derivative of velocity w.r.t. time, thus:

$$\boldsymbol{a}_B = \boldsymbol{a}_A + \frac{d\boldsymbol{\omega}}{dt} \times \boldsymbol{r}_{B/A} + \boldsymbol{\omega} \times \left(\boldsymbol{\omega} \times \boldsymbol{r}_{B/A}\right) \tag{6.9}$$

The first term on the right-hand-side of the equation is the translational acceleration, the second term is the tangential acceleration and the third one is the normal component of the relative acceleration of the point B w.r.t. A. For the seismic mass, applying the properties of the vectorial product, the following equation is derived:

$$\boldsymbol{a} = \frac{d\boldsymbol{v}}{dt} + \frac{d\boldsymbol{\omega}}{dt} \times \boldsymbol{r} - \boldsymbol{\omega}^2 \boldsymbol{r} \tag{6.10}$$

Remembering that ω_x is solved from Eq. (6.5), thus Eq. (6.10) can be used to predict accelerations at any point on the seismic mass in *yz* plane.

6.2.2. System Dynamics Validation Test

Vibration tests were performed to the seismic mass to validate Eq. (6.10). Figure 6-4 a) and b) show the test setup and the seismic mass model in *yz* plane. Positions of accelerometers on the seismic mass are also shown.

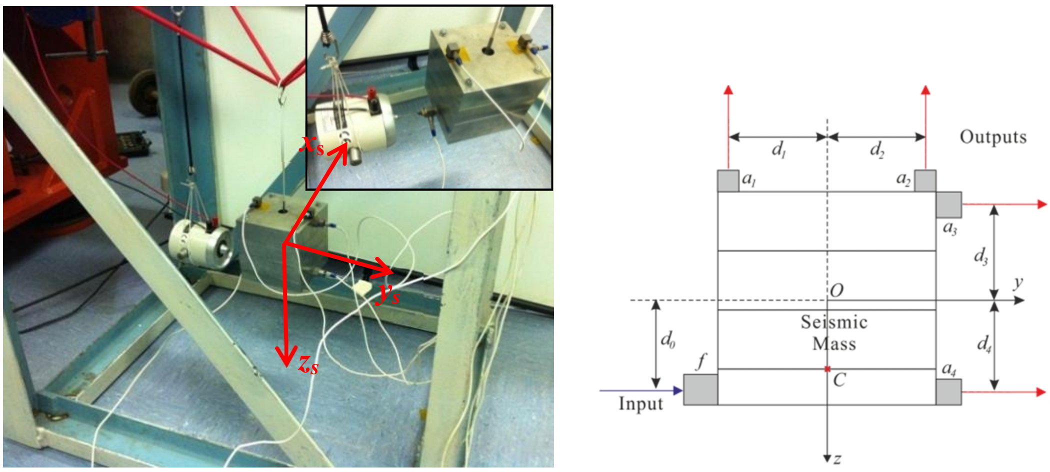

a) Validation test setup b) Seismic mass model

Figure 6-4 Seismic mass dynamics validation test

The complete test setup comprised of a seismic mass, a proof mass mini-shaker with a stinger, a force sensor, four accelerometers, bungee cords/wires and a ground-fixed steal frame. Both mini-shaker and seismic mass were lifted from the frame to simulate a “free-free” boundary condition. The attaching point from the bungee cords/wires to the seismic mass was placed at a position (red point C in Figure 6-4 b)) so that the system natural frequency in each of the six-DoFs was less than 1 Hz. The mini-shaker was used to generate input forces (and thus moments) to the seismic mass. The attaching point of the mini-shaker was chosen at the lower bottom surface of seismic mass, i.e. in practice where the WA was attached or the driving point. A stinger was used to connect the mini-shaker head and seismic mass, a calibrated force sensor was placed between them to measure the input forces. Response accelerations were measured from the four accelerometers. Accelerometers a_1 and a_2 were used to measure vertical response accelerations in z-axis, a_3 and a_4 were used to measure radial response accelerations in y-axis. Model parameters used in this analysis are listed in Table 6-1.

Stainless Steel Seismic Mass	**Parameters**	**Values**
4 Layers	Mass, m_c	10.58 kg (10.52 kg)
	Radial moment of inertia, I_{c_xx}	0.0216 kgm^2 (0.0213 kgm^2)
	Radial moment of inertia, I_{c_yy}	0.0214 kgm^2 (0.0213 kgm^2)
	Polar moment of inertia, I_{c_zz}	0.0215 kgm^2 (0.0213 kgm^2)
	Height	0.11 m
	Width	0.11 m
Piezoelectric Accelerometers		
a1 and a2 (PCB 333B50)	Sensitivity	1011 mv/g, 1017 mv/g
	Contact radius, r_a	0.0072 m
a3 and a4 (Endevco 752A13)	Sensitivity	1001 mv/g, 988.3 mv/g
	Contact radius, r_a	0.0072 m
Force Sensor		
PCB 208C02	Sensitivity	11.31 mv/N
	Contact Diameter	0.01588 m
Sensor Position w.r.t. system CoM		
	Force Sensor to system CoM distance, d_0	0.0471 m
	a_1 distance, d_1	0.0493 m
	a_2 distance, d_2	0.0493 m
	a_3 distance, d_3	0.0478 m
	a_4 distance, d_4	0.0478 m

Table 6-1 SMVMS parameters

Note that mass, m_c, and moment of inertia, I_{c_xx}, I_{c_yy} and I_{c_zz}, of the seismic mass include those of accelerometers and force sensors although they do not change the seismic mass properties significantly (see values in brackets for values of the seismic mass only). However, transducers dimensions are sensitive to the simulated results, and they must be included in the model to obtain their positions w.r.t the seismic mass CoM, i.e. d_1, d_2, d_3 and d_4 in the table.

Several input forces levels were applied by the mini-shaker in the test. They were sampled at 100 Hz from 0.1 to 1 N with an increasing step of 0.1 N hence ten tests were performed. In each test, five channels of signals (one force input and four acceleration responses) were acquired. Since only signals in the time domain were of interest in this case, the sampling frequency was set at 8192 Hz in order to obtain relatively smooth input and response plots, 10s data were acquired for each test.

6.2.3. System Dynamics Parameter Validation

From Eq. (6.10), acceleration expression of each accelerometer can be derived as following:

$$a_1 = \frac{d\omega_x}{dt} d_1 - \omega_x^2 d_1 \tag{6.11}$$

$$a_2 = -\frac{d\omega_x}{dt} d_2 - \omega_x^2 d_2 \tag{6.12}$$

$$a_3 = \frac{F_y \sin(2\pi ft)}{m_c} + \frac{d\omega_x}{dt} d_3 - \omega_x^2 d_3 \tag{6.13}$$

$$a_4 = \frac{F_y \sin(2\pi ft)}{m_c} - \frac{d\omega_x}{dt} d_4 - \omega_x^2 d_4 \tag{6.14}$$

Since there was no excitation applied in *z*-axis in the tests, only rotational terms exist in a_1 and a_2, but both translational and rotational terms exist in a_3 and a_4. With the system parameters given in Table 6-1 and ω_x obtained from Eq. (6.5), the theoretical accelerations of each accelerometer on the seismic mass can be obtained.

Background noise was measured for each test. Figure 6-5 presents the typical background noise in the frequency domain of all transducers.

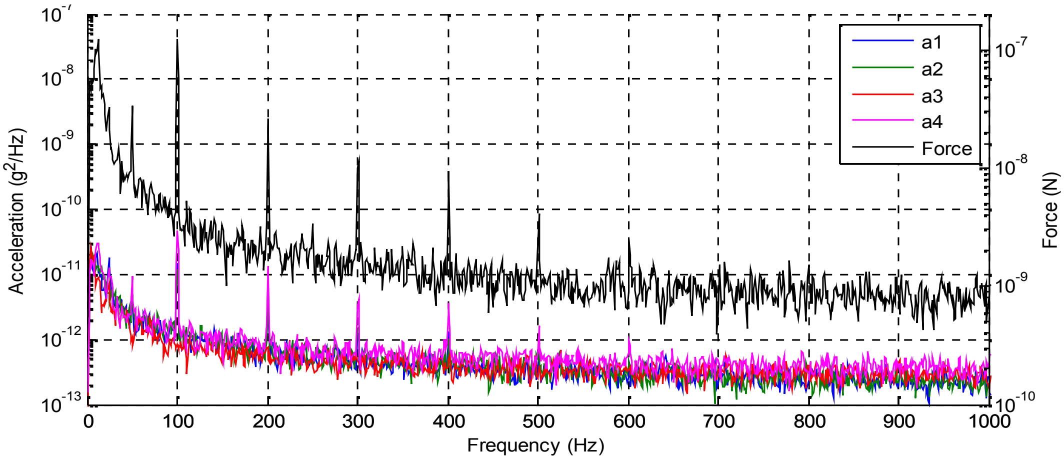

Figure 6-5 Background noise (PSDs) of transducers in SMVMS validation tests

Note that the spike at 50 Hz is due to the UK mains frequency. They cannot be completely avoided and efforts have been attempted to reduce them. The spikes at every 100 Hz up to 600 Hz might due to the electronics frequencies in the acquisition board or from transducers. They have small influences to the results and can be ignored.

Comparisons between the theoretical and experimental results were made for each input force test and each accelerometer channel. For example, Figure 6-6 shows the four theoretical accelerations calculated from Eqs. (6.11) to (6.14) superimpose with the corresponding test results for the 0.5 N input force test.

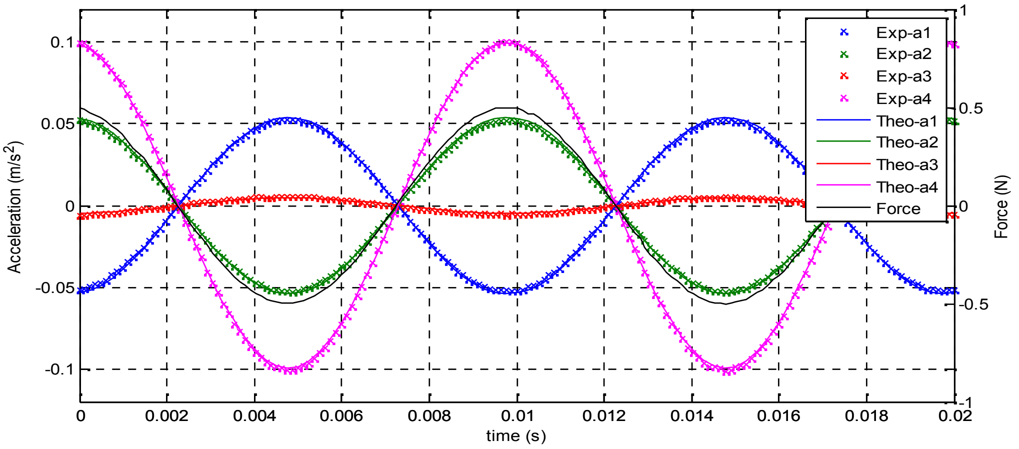

Figure 6-6 Comparisons of theoretical and experimental acceleration responses (0.5 N input force test)

In Figure 6-6, theoretical and experimental results have matched very well in each accelerometer, including magnitudes and phases. Figure 6-7 on the other hand presents quantitatively the disparity between theoretical and experimental results for all tests.

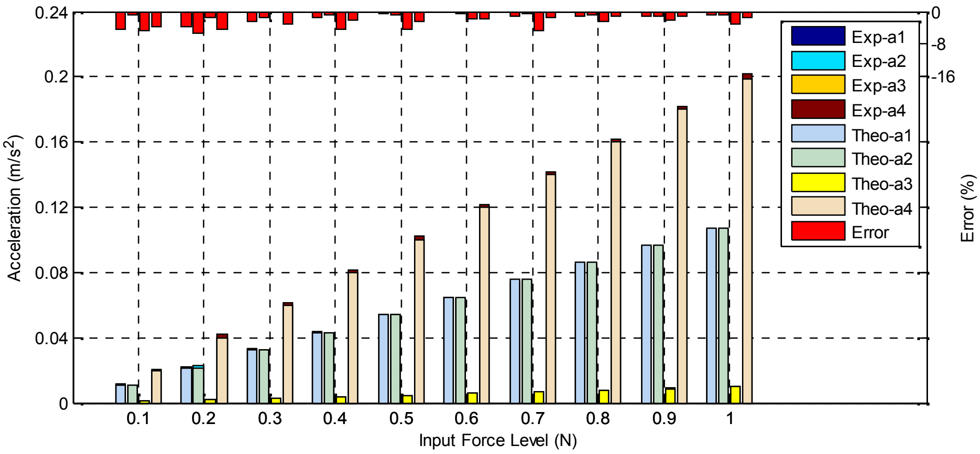

Figure 6-7 Comparisons of theoretical and experimental acceleration responses for all input force tests

In Figure 6-7, magnitudes of accelerations from both theory and test are clearly presented for each input force test. As expected from their positions on the seismic mass, accelerations a_1 and a_2 are almost identical for each test, while a_3 has the least magnitudes and a_4 has maximum magnitudes. In general, the largest error between the theory and test results occurs in a_4. This may be due to the accelerometer in the tests not being installed exactly at the position as it is defined in theory, and thus the disparate theory and test results. Meanwhile results have shown that theoretical values of a_4 are slightly lower than the test results in all cases, but the error in a_4 (the largest one is about 4%) is low enough to be accepted as experimental errors and can be ignored. For the other three accelerometers, errors are much smaller than a_4 (except at low input forces such as 0.1 N and 0.2 N). At low input forces, the signal-to-noise ratio is also very low, in these cases background noise is superimposed with the harmonic responses making estimations more difficult and thus relatively large uncertainties and errors. The common method is to calculate the average value between the upper and lower limits of each response curve as shown in Figure 6-7. Errors between theory and test results at low speeds are still low (less than 6%); these errors are also accepted.

In conclusion, the good agreements between the theory and test results shown that the analytical model (Eqs. (6.11) to (6.14)) was able to predict accelerations on the seismic mass accurately. The seismic mass was also validated with a model analyzed in MSC ADAMS. Results also correlate well with the rest results and thus to the analytical model presented in this section. The validated analytical model was used to derive the transfer matrix relating accelerations on the seismic mass to the forces and moments at the WA-seismic mass interface.

6.2.4. System Dynamics Transfer Matrices

The common approach to characterize WA-induced microvibrations in both hard-mounted and coupled boundary condition is to use the microvibration forces and moments either measured or predicted at the WA interface. These microvibration loads generally include three forces and three moments as shown in previous sections. In order to obtain them at the WA-seismic mass interface in SMVMS, response accelerations measured on the seismic mass must be transferred to the interface forces and moments.

It is found the dominant terms in Eqs. (6.11) to (6.14) are the linear and angular acceleration terms, but the second order term, $\omega^2\vec{r}$, has little influence to the predicted acceleration amplitudes and can thus be ignored. If so, F_y and M_x can be written from Eq. (6.13) and (6.14) as:

$$\begin{bmatrix} F_y \\ M_x \end{bmatrix} = \begin{bmatrix} \dfrac{m_c d_4}{d_3 + d_4} & \dfrac{m_c d_3}{d_3 + d_4} \\ \dfrac{I_{c\_xx}}{d_3 + d_4} & -\dfrac{I_{c\_xx}}{d_3 + d_4} \end{bmatrix} \begin{bmatrix} a_3 \\ a_4 \end{bmatrix} \tag{6.15}$$

Remembering that F_y and M_x are taken at the seismic mass CoM, they need to be transferred to the forces and moments at the interface, F_y' and M_x', thus:

$$\begin{bmatrix} F_y' \\ M_x' \end{bmatrix} = \begin{bmatrix} \dfrac{m_c d_4}{d_3 + d_4} & \dfrac{m_c d_3}{d_3 + d_4} \\ \dfrac{I_{c\_xx} + m_c d_4 \left(d_4 + r_a\right)}{d_3 + d_4} & -\dfrac{I_{c\_xx} - m_c d_3 \left(d_4 + r_a\right)}{d_3 + d_4} \end{bmatrix} \begin{bmatrix} a_3 \\ a_4 \end{bmatrix} \tag{6.16}$$

where r_a is the radius of the accelerometer.

In practice, once response accelerations are measured from a_3 and a_4, the radial force at the interface, F_y', and moment, M_x', can be obtained using Eq. (6.16). Due to SMVSM and WA axisymmetry, the other radial force, F_x', and moment, M_y', can also be obtained with response accelerations measured in the other principle plane (i.e. *xz* plane) using the same equation, they are not presented.

In practice, the WA also generates forces in *z*-axis and only translational terms exist in Eqs. (6.11) and (6.12). Axial translational force at the WA-seismic mass interface, F_z', can be simply derived as:

$$F_z' = -\frac{m_c}{2}(a_1 + a_2) \tag{6.17}$$

The two matrices between accelerations and forces/moments in Eqs. (6.16) and (6.17) are the transfer matrices of the SMVMS.

6.2.5. System Dynamic Performance

The practical minimum detectable force in the WA radial translational DoFs was found by attaching a 0.2 g point mass on the flywheel and spinning the flywheel from static with 10 rpm step increase until a distinct spike due to the point mass appears in the signal in the frequency domain. With the consideration of background noise, the first distinct spike, i.e. the fundamental harmonic of the 0.2 g point mass, was found at 140 rpm with amplitude of approximately 8 ×10^{-4} N; see Figure 6-8.

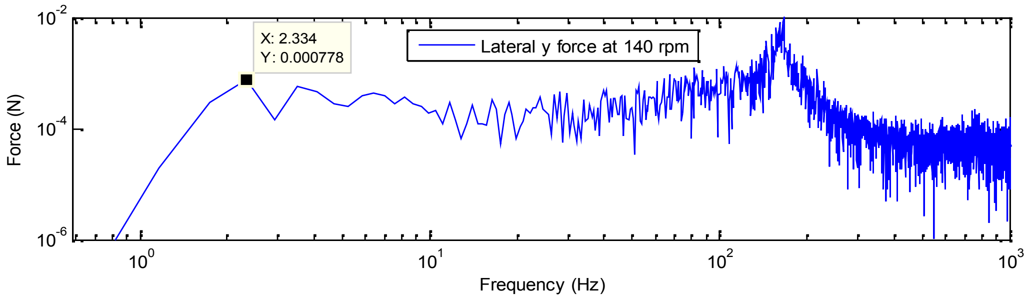

Figure 6-8 Minimum detectable force of SMVMS in radial DoF at 140 rpm

In axial translational DoF, the minimum detectable force was the same as in radial translational DoFs. The minimum detectable moment in radial DoFs was about 8 ×10^{-5}

Nm, however usually the minimum detectable force is used to assess a microvibration measurement system dynamic performance.

6.3. Coupled Microvibration Test

WA-seismic mass coupled microvibration tests were performed to demonstrate the new method of measuring WA-induced microvibrations in a coupled boundary condition. The transfer matrix derived in Section 6.2.4 was used to transfer the response accelerations on the seismic mass into the interface loads. In other words, this method is an indirect method to measure WA-induced forces and moments in a coupled boundary condition. In contrast, in traditional methods the interface loads are measured directly by a multi-DoF load cell typically installed between the two bodies.

The WA was mounted upside-down at the seismic mass bottom surface. The whole system was lifted by bungee cords/wires to simulate the "free-free" boundary condition (see Figure 6-9). The zoomed plot is shown in Figure 6-1 a) though.

Figure 6-9 WA-seismic mass coupled microvibration test setup

Six accelerometers were used to measure the response accelerations on the seismic mass. The six accelerometers had the same sensitivity around 1000 mV/g. Among the six accelerometers in Figure 6-1 a), a_1 and a_2 were to measure accelerations in z-axis, a_3 and a_4 were to measure accelerations in y-axis. This setup replicated accelerometer positions in the calibration tests and Eqs. (6.16) and (6.17) were used directly for analysis without transferring the coordinate system in loads calculations. a_5 and a_6 were similar to a_3 and a_4 but installed in x-axis, they were used to measure radial microvibration forces and moments in *xz* principle plane. Using the transfer matrix, the five interface loads, include three forces (F_x', F_y' and F_z') and two moments (M_x' and M_y'), could be measured simultaneously as WA spins.

In the test, the WA was spun from 240 to 4980 rpm with an increase step of 60 rpm. Microvibrations at speeds lower than 240 rpm were not stable due to WA control issues and were not shown. The sampling frequency was set at 2048 Hz and 5s of data were acquired for each channel. Background noise was also measured and results were similar to those shown in Figure 6-5. The coupled microvibration test results are shown in the next section.

6.4. Coupled Microvibration Test Results

WA-seismic mass coupled microvibrations were measured using the SMVMS. The measured accelerations were input into Eqs. (6.16) and (6.17) to obtain the interface forces and moments. Test results were analyzed in a similar manner as for the hard-mounted case. Results of F_y, M_x and F_z are plotted as spectral maps and PSD waterfall plots in Figure 6-10 on the next page, for examples.

Since the WA boundary condition has changed in the coupled system, it is expected that WA structural modes have also changed from those in a hard-mounted boundary condition. Meanwhile, since sine-sweep tests cannot be performed to the WA in the coupled system, natural frequencies of WA structural modes can only be determined from the coupled microvibration test results.

In Figure 6-10 a), the radial translational mode is identified at approximately 65 Hz, which is slightly higher than that in a hard-mounted boundary condition (50 Hz), while the vertical mode at 220 Hz due to the motor-bearing system has not changed. The "V" shaped "rocking" mode is clearly present in Figure 6-10 b). Due to lack of test results below 240 rpm, the "rocking" mode is estimated starting at approximately 28 Hz; this is almost identical to that in the hard-mounted boundary condition (27 Hz). In axial translational DoF in Figure 6-10 c), the axial translational mode is identified at 46 Hz, which is also somewhat higher than that in the hard-mounted boundary condition (44 Hz).

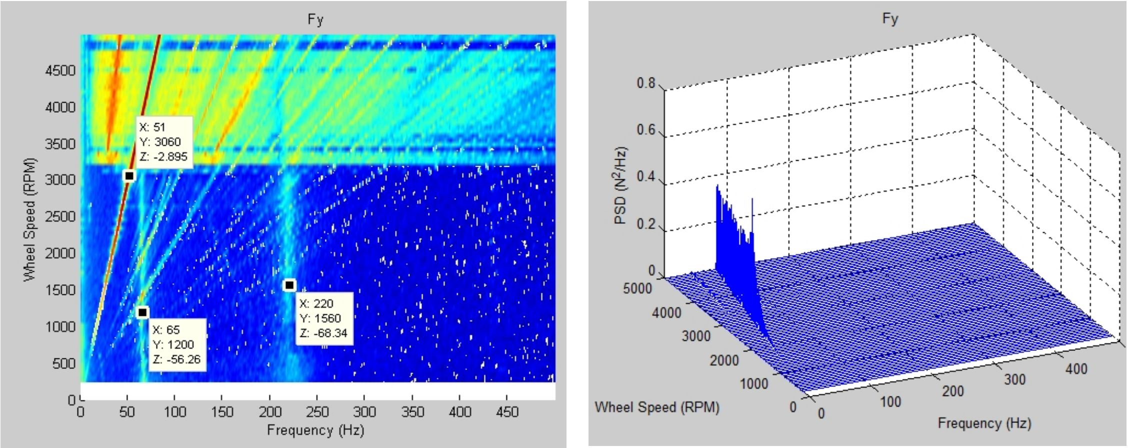

a) F_y spectral map d) F_y PSD waterfall plot

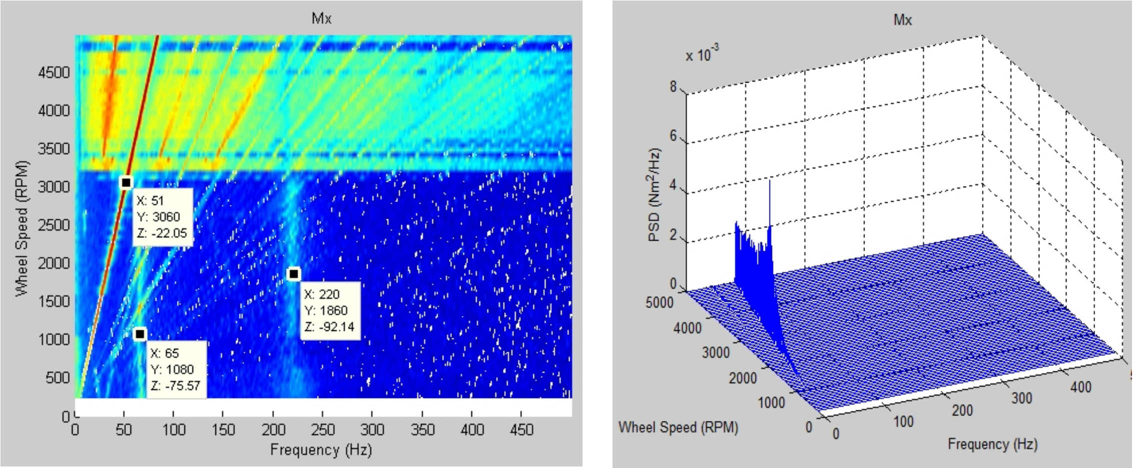

b) M_x spectral map e) M_x PSD waterfall plot

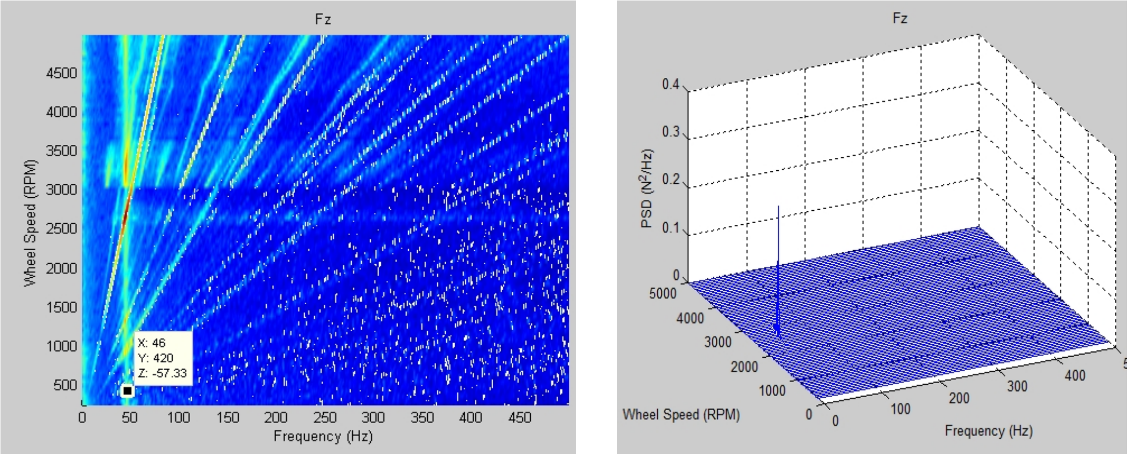

c) F_z spectral map f) F_z waterfall plot

Figure 6-10 Spectral maps and waterfall plots of coupled microvibrations

The influence of nonlinearity in axial translational DoF is not significant as also in the hard-mounted boundary condition case. In contrast, significant nonlinearity has also been observed in radial DoFs and is more severe than that in the hard-mounted boundary condition case. For example, from Figure 6-10 a) and b), primary resonances occur at approximately 51 Hz rather than the value that the radial translational mode interacted with fundamental harmonics. This is similar to that in the hard-mounted boundary condition where nonlinearity causes resonant frequencies to be shifted.

Fundamental harmonic responses of F_y, M_x and F_z are extracted from the microvibration test results and shown in Figure 6-12. In the figure, the test results of fundamental harmonic responses have shown similar dynamic characteristics as in the hard-mounted boundary condition case. Responses grow smoothly and exponentially before resonances and then slowly decrease. Note that fluctuated responses after resonances are due to unknown sources such as also seen in Figure 6-10 a), b) and c). Meanwhile, resonant amplitudes in WA radial DoFs are limited by the high damping of soft-suspension system, e.g. a sharp spike appears in F_z due to the low damping while in F_y is relatively flat. This is also similar to those in the hard-mounted boundary condition case.

Higher harmonics and broadband noise are not considered for the coupled microvibration modeling. Modeling methods of these additional excitations and responses have been validated for the hard-mounted boundary condition case shown in Chapter 5. In the next section, validation of the coupled WA microvibration model due to mass imbalances is presented, including structural modes with gyroscopic effects and simulation of fundamental harmonic responses.

6.5. Coupled Microvibration Model Validation

Coupled WA structural modes are first validated with microvibration test results. The theoretical structural modes are calculated from Eq. (6.3) under the free and undamped condition. Among the ten variables in the equation, the first five are from WA and the rest are from the seismic mass (see Appendix F for detail). M_x and F_z test results are used for structural modes validation in radial and axial translational DoFs respectively. They are presented in Figure 6-11.

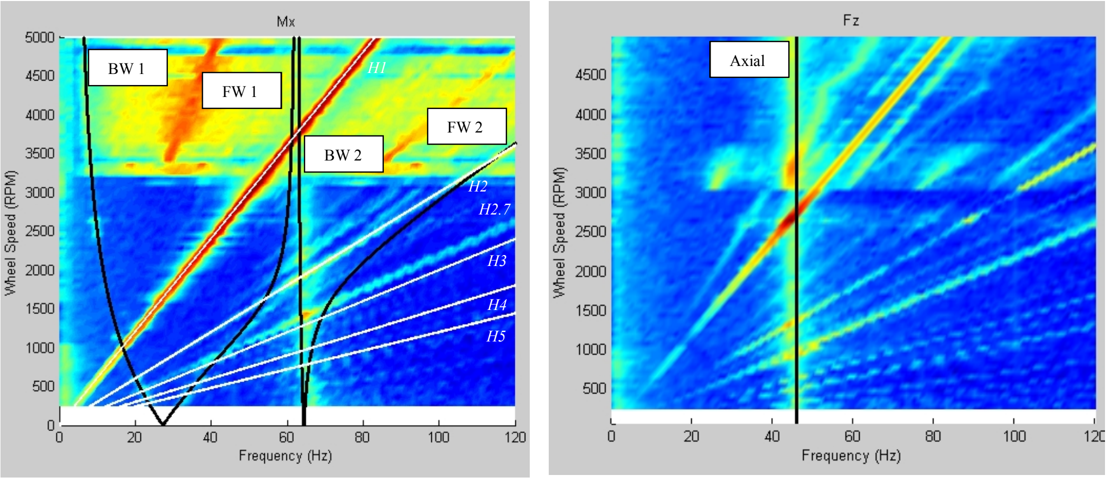

a) Radial DoFs (M_x) b) Axial translational DoF (F_z)

Figure 6-11 Coupled WA structural modes in radial and axial DoFs

In Figure 6-11 a) and b), all theoretical structural modes have matched well with test results. The four speed-dependent whirls are clearly shown in Figure 6-11 a). Similar nonlinearity influences on structural modes are also seen in the coupled boundary condition, these are not discussed.

Fundamental harmonic excitations of F_y, M_x and F_z were simulated using the method presented in Section 5.3, they were implemented into Eq. (6.3). Fundamental harmonic response forces and moments were calculated and they are superimposed with the corresponding test results shown in Figure 6-12.

Since damping values in the coupled boundary condition could not be obtained from sine-sweep tests, in this case the simulated harmonic responses were matched to microvibration test result and damping values were obtained using the traditional trial method. Damping ratios used in F_y, M_x and F_z harmonic response simulations are 0.2, 0.15 and 0.02 respectively. Damping ratios of M_x and F_z remain the same as those in the hard-mounted case, but slightly higher in F_y. Note that the coupled microvibration model shown in this chapter could neither accurately predict the harmonic responses after the resonances in WA radial DoFs as also in the hard-mounted case, but their general dynamics have been modeled well.

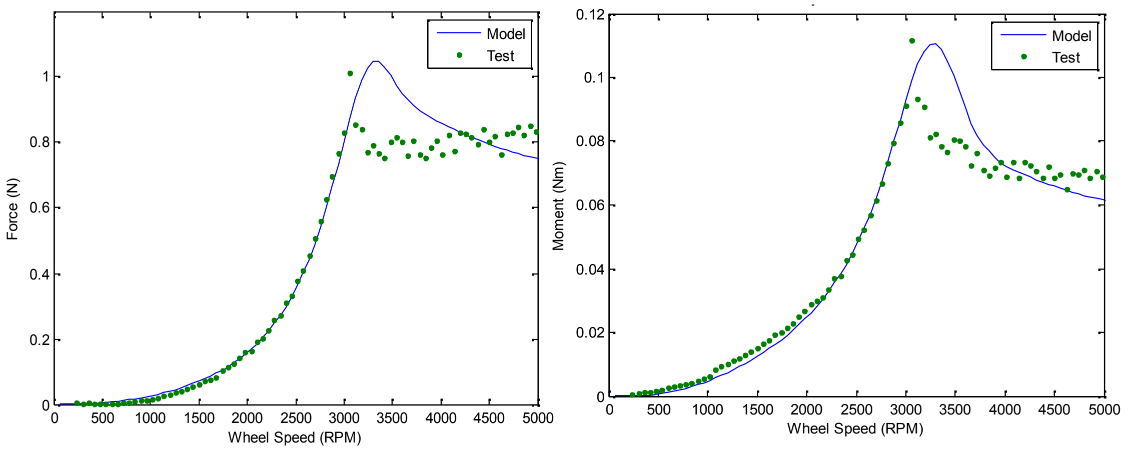

a) F_y b) M_x

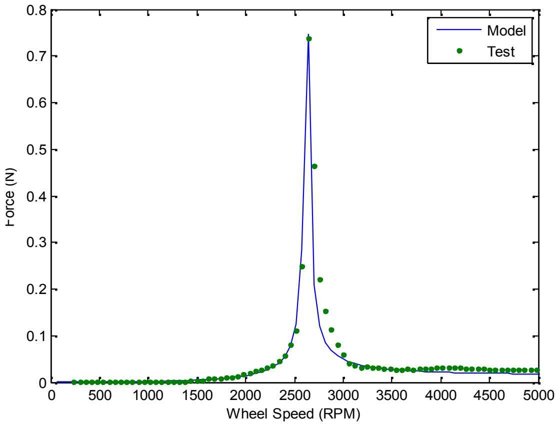

c) F_z

Figure 6-12 Validations of coupled fundamental harmonic responses (F_y, M_x and F_z)

6.6. Summary

In this chapter an alternative method to measure WA-induced microvibrations in a coupled boundary condition has been introduced. The WA-seismic mass coupled microvibration model was derived based on the method used for the hard-mounted case. A coupled microvibration measurement system, i.e. SMVMS, was designed and calibrated with a transfer matrix derived from SMVMS rigid body dynamics. The WA-induced loads at the interface could be accurately measured using this system. Coupled microvibration tests have been carried out and results have been analyzed. Structural modes were slightly different from those obtained in the hard-mounted boundary condition due to the different WA boundary conditions. Nonlinearity and high damping were also observed in coupled microvibration test results, similar dynamic characteristics were also seen here as in the hard-mounted case. The WA coupled microvibration model was validated from the structural modes and fundamental harmonic responses. The microvibration model was able to accurately simulate the WA dynamics before nonlinearity, but errors become large at and beyond resonances. The general WA dynamics behavior however, has been well modeled.

7. Wheel Assembly Accelerance and Coupled Microvibration Prediction

In this chapter, the coupled microvibration predictions, and especially the WA driving point accelerance calculations are discussed. Analytical and experimental methods are developed to find the WA driving point accelerance. The coupled microvibrations are predicted in the speed band considered. WA accelerance are obtained from two conditions: flywheel not spinning (i.e. static accelerance) or spinning (i.e. dynamic accelerance). A FE model of the WA is created and frequency response analysis is conducted in MSC NASTRAN for accelerance study. Experimentally, static and dynamic accelerance are measured using a designed measurement system utilizing common accelerometers and force sensors. Analytically, accelerance are derived from the WA microvibration model in a "free-free" boundary condition. WA static and dynamic accelerance are compared and used to predict the coupled microvibrations. Both predicted results are also compared to the traditional methods in the literature.

7.1. The Coupled Microvibration Analysis Theory

The WA-structure coupled microvibration analysis theory developed in the literature [140] is briefly introduced in this section. Generally, the relationship between the coupled and hard-mounted microvibrations is described mathematically as:

$$\boldsymbol{f}_c = \boldsymbol{f}_b + \boldsymbol{A}_w^{-1}\ddot{\boldsymbol{x}} \tag{7.1}$$

where $\boldsymbol{f}_c$ and $\boldsymbol{f}_b$ are 6×1 load vectors, each includes three forces and three moments. $\boldsymbol{f}_c$ is the coupled forces generated by the WA at the interface. $\boldsymbol{f}_b$ are those from hard-mounted boundary condition, either measured from WA grounded microvibration tests or predicted from WA hard-mounted microvibration model. $\ddot{\boldsymbol{x}}$ is a 6×1 acceleration vector, due to WA-structure interface coupled motion. $\boldsymbol{A}_w$ is the 6×6 WA driving point accelerance matrix.

Meanwhile for the satellite structure, the following equation can be expressed:

$$\ddot{\boldsymbol{x}} = -\boldsymbol{A}_s \boldsymbol{f}_c \tag{7.2}$$

where $\boldsymbol{A}_s$ is the driving point accelerance on the satellite structure.

If substituting Eq. (7.2) into Eq. (7.1) for $\ddot{\boldsymbol{x}}$, the following equation can be derived.

$$\boldsymbol{f}_c = \boldsymbol{f}_b \left[\boldsymbol{I} + \boldsymbol{A}_w^{-1} \boldsymbol{A}_s \right]^{-1} = \boldsymbol{f}_b \boldsymbol{G}_f \tag{7.3}$$

where $\boldsymbol{G}_f$ is termed the “load filter” between the coupled and hard-mounted loads:

$$\boldsymbol{G}_f \left(\omega, \Omega\right) = \left[\boldsymbol{I} + \boldsymbol{A}_w^{-1} \left(\omega, \Omega\right) \boldsymbol{A}_s \left(\omega\right) \right]^{-1} \tag{7.4}$$

If writing Eq. (7.3) into matrix form, the following equation is obtained:

$$\boldsymbol{\Phi}_{FF\_coupled} \left(\omega, \Omega\right) = \boldsymbol{G}_f \left(\omega, \Omega\right) \boldsymbol{\Phi}_{FF\_grounded} \left(\omega, \Omega\right) \boldsymbol{G}_f^H \left(\omega, \Omega\right) \tag{7.5}$$

$\boldsymbol{\Phi}_{FF\_grounded}$ and $\boldsymbol{\Phi}_{FF\_coupled}$ are both 6 × 6 complex matrices of WA-induced forces and moments written in spectral density form and corresponds to the hard-mounted and coupled loads, $\boldsymbol{f}_b$ and $\boldsymbol{f}_c$, respectively. The work extended in the coupled WA-structure microvibration analysis by the author is presented in the rest of this chapter.

7.2. Wheel Assembly Accelerance in Static Condition

As demonstrated in Chapter 2, accelerance of the WA and that of the supporting structure are crucial in the coupled microvibration analysis. While accelerance of the supporting structure is traditionally obtained from its FE model, for a spinning WA the process is much more complicated. In this section, WA accelerance in a static condition (or WA static accelerance) are obtained using analytical and experimental methods. Analytically, WA accelerance are obtained from frequency response analysis on a FE model of the WA analyzed in MSC NASTRAN. Experimentally, a measurement system is designed to measure the WA (static and dynamic) accelerance using common accelerometers and force sensors. WA static accelerance obtained from the two methods are compared and the results are used for further studies in this chapter.

7.2.1. Experimental Method

In general, the complete representation of the 6×6 WA accelerance matrix can be shown as following:

$$\begin{bmatrix} \ddot{x} \\ \ddot{y} \\ \ddot{z} \\ \ddot{\theta} \\ \ddot{\varphi} \\ \ddot{\psi} \end{bmatrix} = \begin{bmatrix} \enclose{circle}{\textcolor{red}{A_{w11}}} & A_{w12} & A_{w13} & A_{w14} & \textcolor{red}{A_{w15}} & A_{w15} \\ A_{w21} & \textcolor{red}{A_{w22}} & A_{w23} & \textcolor{red}{A_{w24}} & A_{w25} & A_{w26} \\ A_{w31} & A_{w32} & \enclose{circle}{\textcolor{red}{A_{w33}}} & A_{w34} & A_{w35} & A_{w36} \\ A_{w41} & \textcolor{red}{A_{w42}} & A_{w43} & \enclose{circle}{\textcolor{red}{A_{w44}}} & A_{w45} & A_{w46} \\ \enclose{circle}{\textcolor{red}{A_{w51}}} & A_{w52} & A_{w53} & A_{w54} & \textcolor{red}{A_{w55}} & A_{w56} \\ A_{w61} & A_{w62} & A_{w63} & A_{w64} & A_{w65} & \enclose{circle}{\textcolor{red}{A_{w66}}} \end{bmatrix} \begin{bmatrix} F_x \\ F_y \\ F_z \\ M_x \\ M_y \\ M_z \end{bmatrix} \tag{7.6}$$

Previous studies [141] have shown the diagonal elements (or the direct driving point accelerance): A_{w11}, A_{w22}, A_{w33}, A_{w44}, A_{w55}, A_{w66}, are the most important in the accelerance matrix. The four cross-DoF elements: A_{w15}, A_{w24}, A_{w51} and A_{w42} are also important especially when Cross Spectral Densities (CSDs) are considered in the microvibration loads. These elements are highlighted in red in Eq.(7.6). Other off-diagonal elements are not as important thus usually being ignored. Since the matrix is symmetric about its diagonal and due to WA axisymmetry, A_{w15} and A_{w24} are the same and also for A_{w42} and A_{w51}, i.e. the four cross-DoF elements are the same. In addition, diagonal elements A_{w11} and A_{w22} are the same and also A_{w44} and A_{w55}. Hence for simplicity, five elements in the matrix are chosen for the coupled microvibration analysis in this thesis. They are highlighted using blue circles in Eq. (7.6).

Experimentally, three independent tests were conducted to find the five elements in the accelerance matrix. Test setups are shown in Figure 7-1 b), c) and d) respectively. A mounting bracket was designed and rigidly connected to the WA in these tests. The detailed introductions on the mounting bracket are presented in Section 7.2.2. Accelerometer positions on the mounting bracket are shown in Figure 7-1 a).

In each test, the WA was rigidly attached to the mounting bracket and together hung "free-free" by bungee cords and nylon wires from a ground-fixed steel frame. The suspension was designed such that its natural frequency was less than 1 Hz in any of the six DoFs. Input forces and/or moments were applied by one or two mini-shakers and measured by the force sensors directly, while response accelerations were measured by eight accelerometers. The frame was verified previously by tap test and shown no influence in the frequency band of interest in accelerance tests.

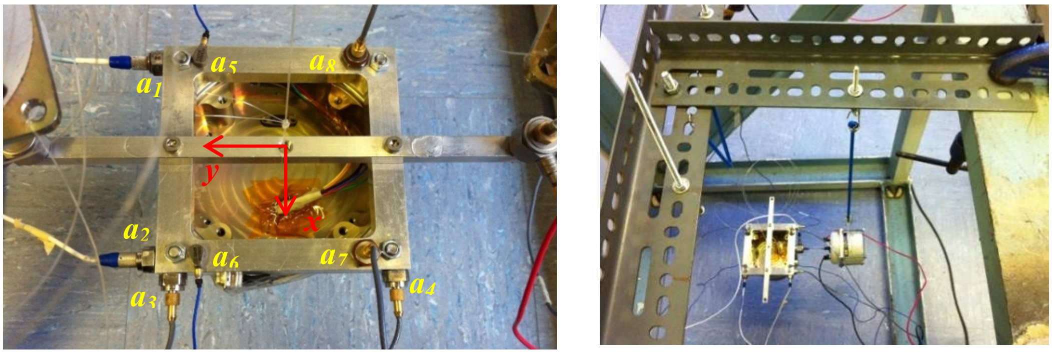

a) Accelerometer positions b) A_{w11} and A_{w51} test setup

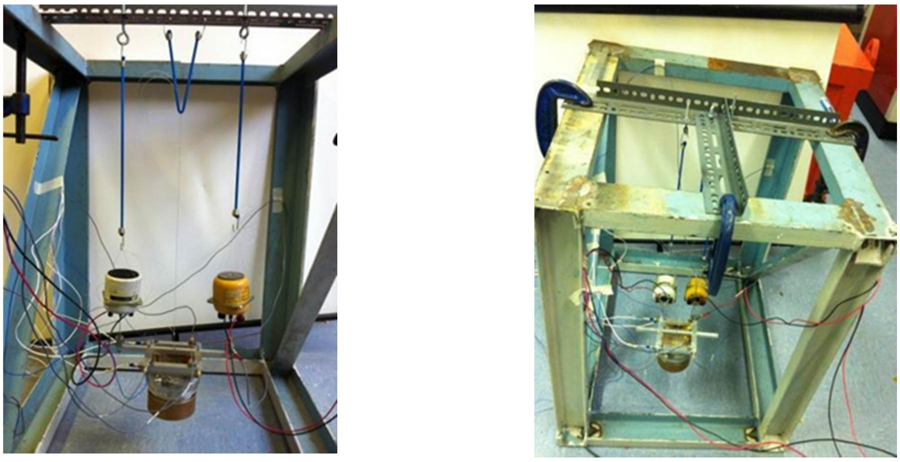

c) A_{w33} and A_{w44} test setup d) A_{w66} test setup

Figure 7-1 WA accelerance tests

Figure 7-2 shows force sensor positions in detail and force directions being applied, as well the accelerometer positions and response acceleration directions being measured.

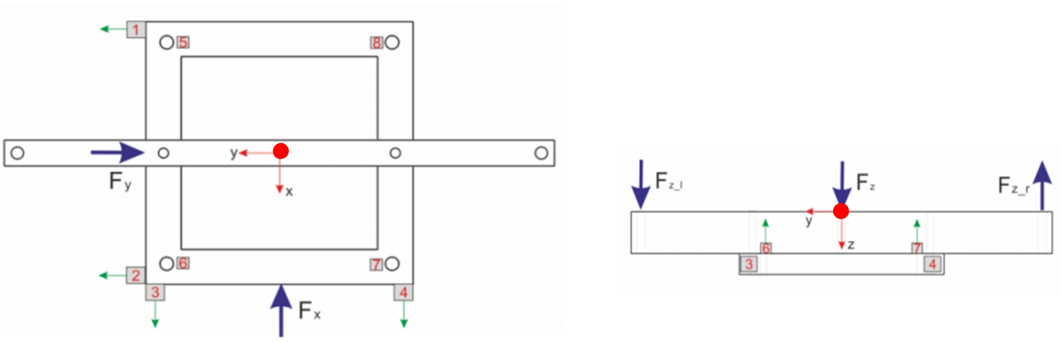

a) *xy*-plane b) *yz*-plane

Figure 7-2 Transducer positions and directions of forces being applied and accelerations being measured

The complete linear and angular accelerations at the driving point (high-lighted as red dots in Figure 7-2) can be calculated using the following set of equations.

$$\ddot{x}=\frac{1}{2}\left(a_3+a_4\right) \tag{7.7}$$

$$\ddot{y}=\frac{1}{2}\left(a_1+a_2\right) \tag{7.8}$$

$$\ddot{z}=-\frac{1}{4}\left(a_5+a_6+a_7+a_8\right) \tag{7.9}$$

$$\ddot{\theta}=\frac{1}{2d_{67}}\left(a_7+a_8-a_5-a_6\right) \tag{7.10}$$

$$\ddot{\varphi}=\frac{1}{2d_{56}}\left(a_6+a_7-a_5-a_8\right) \tag{7.11}$$

$$\ddot{\psi}=\frac{1}{d_{34}}\left(a_4-a_3\right) \tag{7.12}$$

where d_{67}, d_{56} and d_{34} are the distances between the two corresponding accelerometers in the defined coordinate system (see Figure 7-2 for detail). Note that accelerometer dimensions must be included in above equations due to their relative large size compared to the accelerometer distances between. Note that due to axisymmetry, only Eqs. (7.7), (7.9), (7.10) and (7.12) are required in this study.

In each test, mini-shaker(s) were controlled in open loop mode, i.e. a constant voltage of 1 V was applied. Force sensor(s) were inserted between mini-shaker(s) and the mounting bracket to directly measure the input forces, while moments were calculated subsequently. Sine-sweep tests were performed from 10 to 500 Hz and all signals were sampled at 2048 Hz. Each test is discussed in detail as following:

- Figure 7-1 b) depicts the setup for A_{w11} and A_{w51} tests. The WA was excited in positive x-axis using one mini-shaker. Linear and angular accelerations at the driving point were calculated using Eqs. (7.7) and (7.11) respectively. The driving point accelerance was calculated as the ratio of linear (or angular) acceleration to force (or moment). Note that both quantities were complex numbers.

- Figure 7-1 c) depicts the setup for A_{w33} and A_{w44} tests. For A_{w33} test, two mini-shakers were controlled in-phase, thus the total force in axial translational DoF was the sum of the two forcing signals. Linear accelerations at the driving point were calculated using Eq. (7.9). For A_{w44} test, two mini-shakers were controlled anti-phase and a moment at the driving point was produced. Angular accelerations at the driving point were calculated using Eq. (7.10).

- Figure 7-1 d) depicts the setup for A_{w66} test. The two mini-shakers were attached in positive x-axis and controlled anti-phase and a moment about z-axis at the driving point was produced. Eq. (7.12) was used to calculate the angular acceleration.

7.2.2. Analytical Method

Firstly, the 6×6 WA static accelerance matrix was first obtained from a FE model of the WA. Detailed modeling and validation of the WA FE model is shown in Appendix D. In addition, the WA was rigidly connected to a mounting bracket and suspended together to simulate the "free-free" boundary condition. The mounting bracket is shown in Figure 7-3 a). In the complete FE model in Figure 7-3 b), the mounting bracket was modeled using shell elements as also for the WA, the WA was attached to the mounting bracket using Rigid Body Element (RBE) elements (high-lighted as red lines). The mounting bracket was designed such that the system modal frequency in any of the six DoFs was much higher than the frequency band of interest in the accelerance study (700 Hz compared to 200 Hz for example), thus the mounting bracket did not influence accelerance test results.

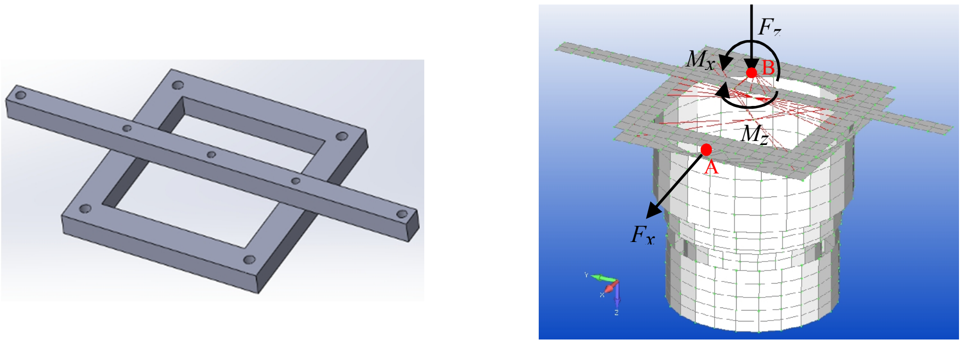

a) Mounting bracket CAD model b) WA attached to the mounting bracket

Figure 7-3 FE model of the WA with mounting bracket

In the frequency response analysis, a unit force or moment was applied at a selected node (the driving point "A" or "B" as high-lighted in Figure 7-3 b)) in one of the six DoFs, accelerations were calculated at the same node in the six DoFs, thus a 6×1 vector of accelerance at the driving point (one direct accelerance and five cross-DoF accelerance) was obtained. This process was repeated for the other five DoFs, and a 6×6 matrix was eventually obtained. The following calculations were performed using the modal frequency response analysis in MSC NASTRAN:

- 1 N F_x was applied at node A in positive x-axis; six accelerations and thus six accelerance were calculated;
- 1 N F_z was applied at node B in positive z-axis; six accelerations and thus six accelerance were calculated;
- 1 Nm M_x was applied at node B about positive x-axis; six accelerations and thus six accelerance were calculated;
- 1 Nm M_z was applied at node B about positive z-axis, six accelerations and thus six accelerance were calculated;

The frequency step was set at 1 Hz and frequency band was set between 0 to 500 Hz. WA parameters such as mass, inertia, stiffness and damping values, etc. were taken from the sine-sweep tests as shown in Appendix D. MSC NASTRAN results and test results are compared and discussed. They are shown in the next section.

7.2.3. Model Validation

The direct driving point accelerance elements, A_{w11}, A_{w33}, A_{w44} and A_{w66}, from the FE model and tests are compared first. They are shown in Figure 7-4.

In Figure 7-4, accelerance results obtained from the two methods are matched well in the frequency band considered. Results from the FE model and tests have accurately captured WA structural modes in each DoF. Note that due to the "free-free" boundary condition of WA in the tests, structural modes are slightly different from those observed in the hard-mounted microvibration tests. They will be further addressed in Section 7.3. Results of cross-DoF accelerance element, A_{w51}, are shown in Figure 7-5.

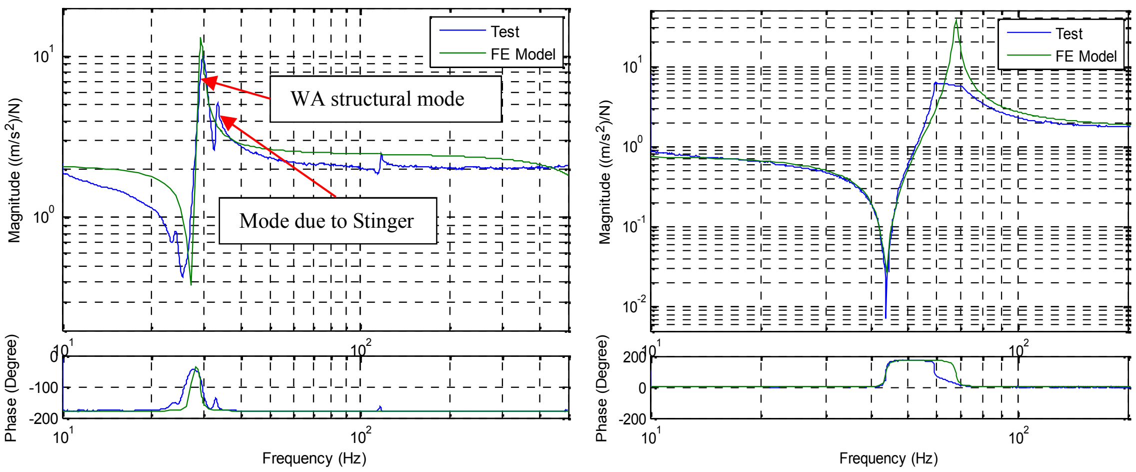

a) Radial translation DoF (A_{w11}) b) Axial translation DoF (A_{w33})

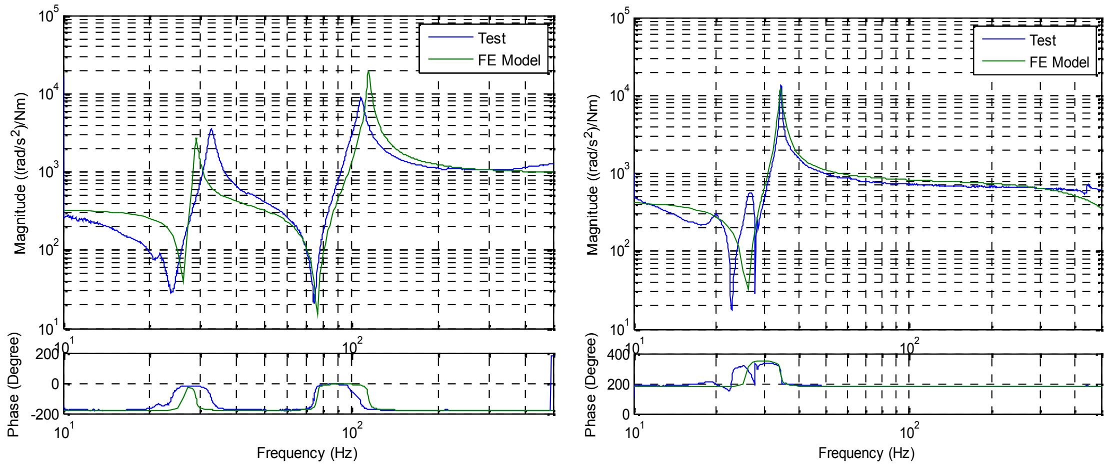

c) Radial rotational DoF (A_{w44}) d) Axial rotational DoF (A_{w66})

Figure 7-4 WA direct driving point accelerance from FE Model and tests

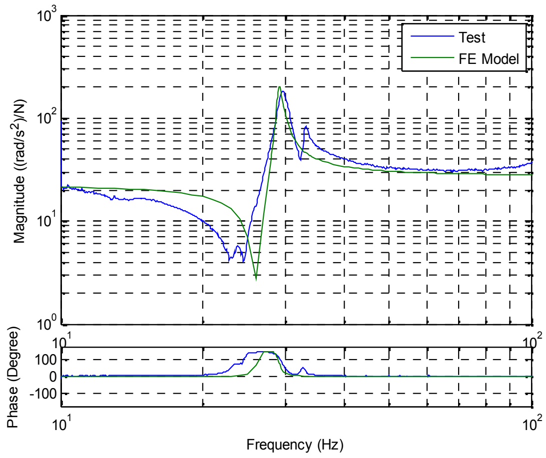

Figure 7-5 WA cross-DoF driving point accelerance (A_{w51}) from FE Model and test results

The driving point accelerance of the other three cross-DoF elements in Eq. (7.6) were also calculated and checked against A_{w51}. They were similar and matched well for the FE and test results in each case. Results from Figure 7-4 and Figure 7-5 show that the test method introduced in this section is able to accurately obtain the WA driving point accelerance. Note also that WA properties in the FE model were not updated with the accelerance test results and were taken directly from those used in the hard-mounted microvibration case, thus it has proved the consistency of the model used in different studies in this thesis.

Note that in Figure 7-4 a), c) and d) and Figure 7-5, in accelerance in radial DoFs, a small spike between 25 to 35 Hz was measured in each case. This spike has magnitude 5 to 6 times smaller than that of the WA structural mode in each DoF. Although in practice this spike can be ignored due to its much smaller amplitudes, however it was not expected in this frequency band and further investigations were carried out. It was found the spike was due to influences of mini-shaker stinger(s). The test setup of this investigation is shown in the Figure 7-6 a) for A_{w11}, while the updated test results are plotted in Figure 7-6 b).

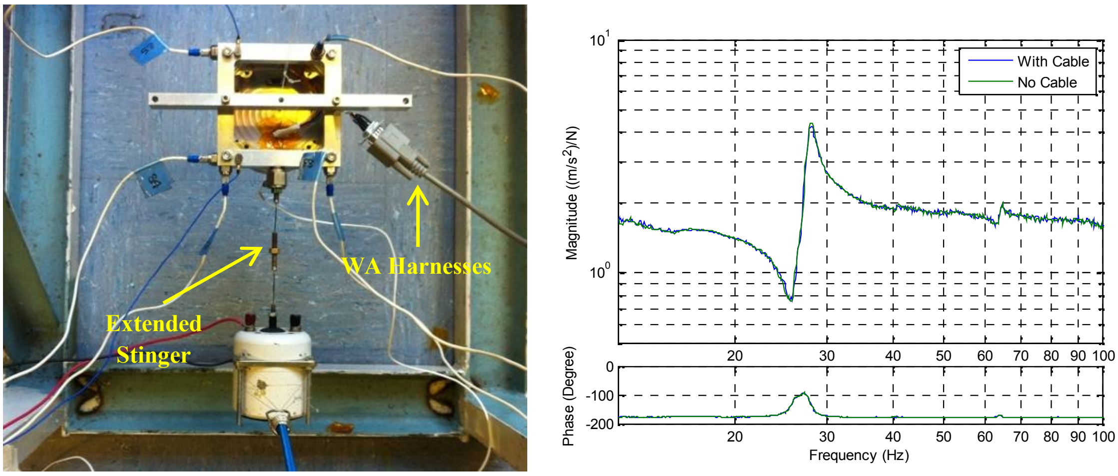

a) Test to investigate stinger and WA harnesses influences

b) Test results using an extended stinger with and without WA harnesses connected

Figure 7-6 Tests to investigate stinger and WA harnesses influences (A_{w11})

In this test, the stinger was extended and thus it was more flexible and in theory its natural frequency was reduced. Results were plotted in Figure 7-6 b) and show that the spike has been removed. In addition, WA external harnesses were plugged to the WA during the test. This was to investigate the influence of external harnesses to the accelerance measurements when flywheel spinning (i.e. the dynamic accelerance measurements, results are shown in Section 7.3). Test results in Figure 7-6 b) indicate WA harnesses do not show influences in the frequency band considered and are thus ignored.

In conclusion, WA structural modes at static condition in both FE and test results have been accurately captured, hence any method can be used for the coupled microvibration predictions in the traditional sense. However it must be noted that the WA accelerance obtained in static condition is flawed in that they do not take account of the gyroscopic effects of the flywheel. In other words, the coupled microvibrations predicted with the WA static accelerance matrix are only accurate when flywheel is static or spins at very low speeds (say up to 600 rpm). It is thus necessary to develop a method to include the gyroscopic effects so that the WA accelerance matrix can be used for the coupled microvibration analysis in broadband speeds.

7.3. Wheel Assembly Accelerance in Dynamic Condition

7.3.1. Gyroscopic Effects in Accelerance

Remembering that in Section 7.1, $\boldsymbol{G}_f(\omega, \Omega)$ is known as the "load filter". In addition, if microvibration test results are used as $\boldsymbol{\Phi}_{FF\_grounded}$ and $\boldsymbol{\Phi}_{FF\_coupled}$, it is called the "empirical load filter". The general form of $\boldsymbol{\Phi}_{FF\_grounded}$ and $\boldsymbol{\Phi}_{FF\_coupled}$ is:

$$\Phi_{FF}\left(\omega,\Omega\right)=\begin{bmatrix} \Phi_{F_xF_x} & \Phi_{F_xF_y} & \Phi_{F_xF_z} & \Phi_{F_xM_x} & \Phi_{F_xM_y} & \Phi_{F_xM_z} \\ \Phi_{F_yF_x} & \boxed{\Phi_{F_yF_y}} & \Phi_{F_yF_z} & \Phi_{F_yM_x} & \Phi_{F_yM_y} & \Phi_{F_yM_z} \\ \Phi_{F_zF_x} & \Phi_{F_zF_y} & \boxed{\Phi_{F_zF_z}} & \Phi_{F_zM_x} & \Phi_{F_zM_y} & \Phi_{F_zM_z} \\ \Phi_{M_xF_x} & \Phi_{M_xF_y} & \Phi_{M_xF_z} & \boxed{\Phi_{M_xM_x}} & \Phi_{M_xM_y} & \Phi_{M_xM_z} \\ \Phi_{M_yF_x} & \Phi_{M_yF_y} & \Phi_{M_yF_z} & \Phi_{M_yM_x} & \Phi_{M_yM_y} & \Phi_{M_yM_z} \\ \Phi_{M_zF_x} & \Phi_{M_zF_y} & \Phi_{M_zF_z} & \Phi_{M_zM_x} & \Phi_{M_zM_y} & \Phi_{M_zM_z} \end{bmatrix}$$

Traditionally, the coupled microvibration spectra, $\boldsymbol{\Phi}_{FF\_coupled}$, can be measured directly by inserting a load cell, for example, at the interface between the WA and the supporting structure. On the other hand, the hard-mounted microvibration spectra,

$\mathbf{\Phi}_{FF\_grounded}$, can be measured using a grounded Kistler table, for example. Microvibrations measured in both cases can be written as 6×6 spectral density matrices, where diagonal terms as PSDs and off-diagonal terms as CSDs such as in the matrix shown above. In order to study the gyroscopic effects in WA accelerance, microvibrations measured from the WA-seismic mass coupled system in Chapter 6 are used. Remembering also that in SMVMS, forces and moments that obtained at the interface between the WA and seismic mass directly represent those for $\mathbf{\Phi}_{FF\_coupled}$. The hard-mounted microvibrations are taken from Chapter 4.

For simplicity, only the microvibrations in the decoupled axial translational DoF are considered to demonstrate the "empirical load filter". From Eq. (7.5), if only considering axial translational DoF, the root of the ratio of the two microvibrations, i.e. $\Phi_{F_zF_z}$ of coupled and grounded cases, is directly the "empirical load filter" in axial translational DoF. If it is calculated for all speeds in the speed band considered, the complete decoupled "empirical load filter" can be obtained for axial translational DoF. Results are plotted as spectral maps shown in Figure 7-7.

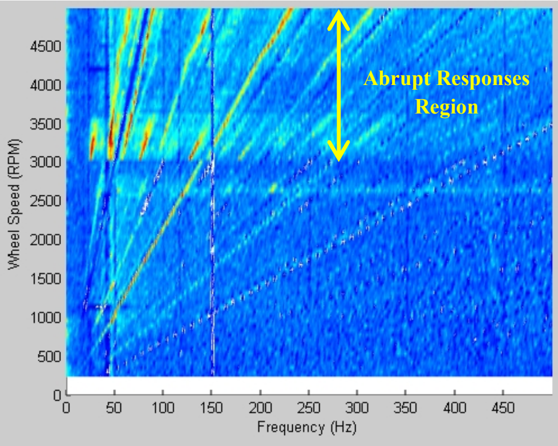

Figure 7-7 "Empirical load filter" (axial translational DoF)

From Figure 7-7 two important characteristics of WA driving point accelerance can be seen:

- Harmonic responses are almost eliminated in each DoF. Since amplitudes of the measured harmonic responses of hard-mounted and coupled microvibrations are very close to each other at each frequency each speed, their ratio is close to unity (see blue lines of harmonics in the figure). This observation indicates harmonics produced by the spinning WA are not part of the WA accelerance, which is as expected.

- The abrupt responses due to unknown sources also appear in the WA accelerance at high speeds (above 3000 rpm). Since influences of such responses are not modeled analytically in this thesis they cannot be included in the accelerance simulations, also the predicted coupled microvibrations at high speeds cannot be used for data comparison; this is shown in Section 7.2.3.

Both observations are used later in WA dynamic accelerance simulations and the coupled microvibration predictions. However the experimental method to obtain the “empirical load filter” introduced in this section cannot be used to directly predict accelerance in in-plane DoFs due to non-zero off-diagonal elements that cannot be ignored in the accelerance matrix. On the other hand, the fully populated “empirical load filter” is very difficult or impossible to be obtained experimentally.

The WA dynamic accelerance (i.e. accelerance with gyroscopic effects while flywheel spins) was measured at some selected speeds (1200 rpm to 3000 rpm at an step increase of 300 rpm) using the same test setup for static accelerance measurements (see Figure 7-1 for detail). In this case, the flywheel spun during sine-sweep tests that were performed by shakers, while forces and accelerations were measured simultaneously. Dynamic accelerance, A_{w11}, A_{w33}, A_{w44} and A_{w66}, at the selected speeds are plotted in Figure 7-8 respectively. Note that only magnitudes are plotted and signals are smoothed to reduce the broadband noise. The maximum speed was set at 3000 rpm as data were not reliable at higher speeds due to unknown sources.

Influences of gyroscopic effects are clearly shown in each measured dynamic accelerance. For example in Figure 7-8 a) and c), the WA “rocking” mode (27 Hz) appears and changes with speeds, thus A_{w11} and A_{w44} are also speed-dependent. Other structural modes such as the radial translational mode (100 Hz in Figure 7-8 a) and c)), the axial translational mode (63 Hz in Figure 7-8 b)) and the torque mode (14 Hz in Figure 7-8 d)) do not show significant sensitivity to speed. Another peak around 10 Hz in the test results is due to the overall natural frequency of the flywheel-base system. This is further discussed in Section 7.3.2.1. It is also noticed that the “rocking” mode decreases as speed increases (see red arrows in Figure 7-8 a) and c)). It was verified this decreasing trend follows the backward whirl of the "rocking mode".

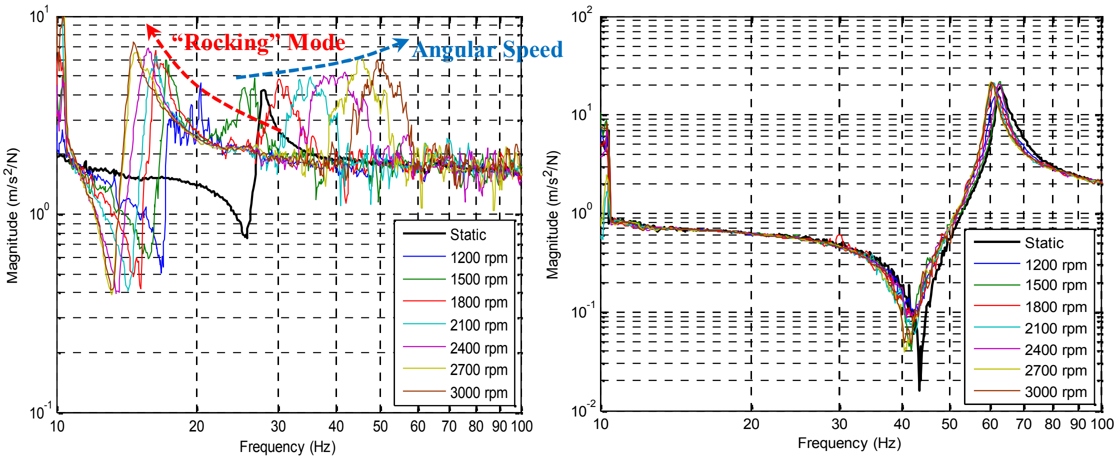

a) Radial translational DoF (A_{w11}) b) Axial translational DoF (A_{w33})

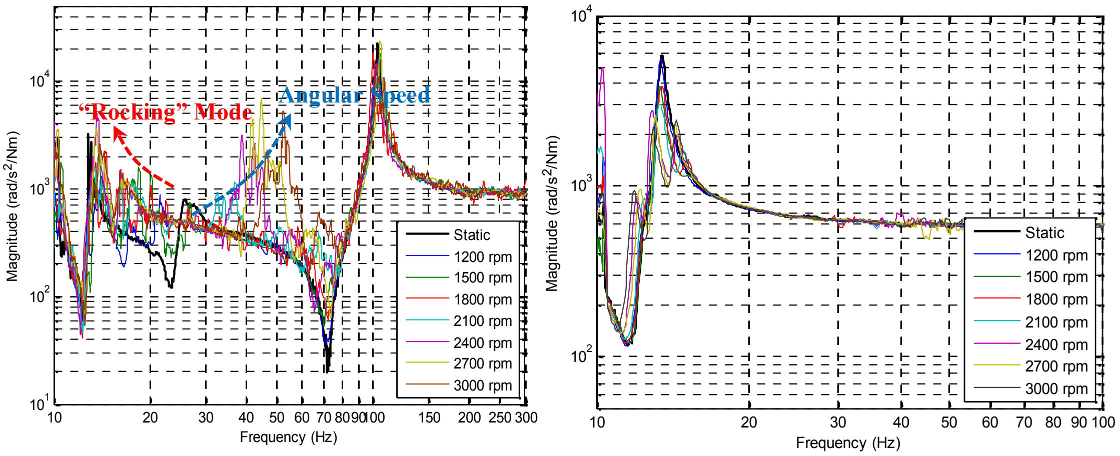

c) Radial rotational DoF (A_{w44}) d) Axial rotational DoF (A_{w66})

Figure 7-8 WA dynamic accelerance at some selected speeds

It should be mentioned that the measurement method introduced above is not practical due to several reasons. Firstly, dynamic accelerance were measured with the WA alone in "free-free" boundary condition and with a spinning flywheel. In this case, fundamental harmonics were also detected (see blue arrows in Figure 7-8 a) and c)). Remembering that from the "empirical load filter" in Figure 7-7, harmonics do not show significant influences in WA accelerance. This is as expected since harmonics are not accelerance by definition and should be avoided in calculating or measuring accelerance. This contradiction in the two experimental methods was mainly due to the different boundary conditions in the two types of test, however there is no difference at static. In practice, although harmonics influences in Figure 7-8 can be filtered out by appropriate signal post processing, it significantly increases the overall efforts, for example, this needs to be done at all speeds. Meanwhile, the direct measurement of dynamic accelerance requires that the WA spins at every speed while sine-sweep excitations are applied by shakers. This process is extremely time consuming and is not always reliable. In addition, the fundamental theory of coupled microvibration analysis shown in Section 7.1 also needs to be modified for accurate experimental measurements.

In conclusion, the two experimental methods introduced above to measure WA driving point dynamic accelerance are not practical in the coupled microvibration study. However, both results have clearly shown the difference between the WA static and dynamic accelerance, i.e. the gyroscopic effects must be included in WA dynamic accelerance. The most efficient approach is to obtain them analytically, an analytical method to calculate the WA driving point accelerance is introduced in the next section.

7.3.2. Analytical Method

Remembering that the accelerance of a mechanical system is the property of the system regardless of its boundary conditions, but the driving point accelerance depend on locations of input forces and response accelerations applied and measured on the system. The "driving point" for a typical WA is at its base interface and the mounting structure shares the same interface as the driving point. As WA and the mounting structure are usually rigidly connected (sometimes through vibration isolators), microvibrations induced by the WA are directly transmitted through the interface. The coupled WA-seismic mass system is depicted in the following figure and the driving point in this system is high-lighted.

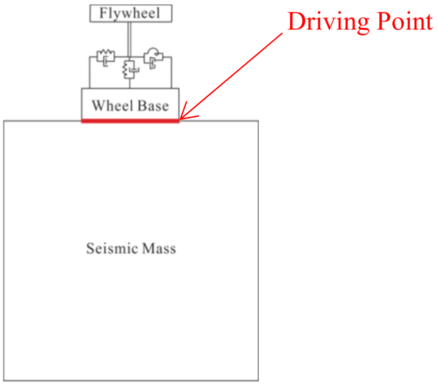

Figure 7-9 Coupled WA-seismic mass system

In previous work, analytical expressions of WA dynamic accelerance were derived considering the flywheel alone in the model, i.e. flywheel mass and moment of inertias only, but stiffness and damping values of the suspension system were not included. Thus at the static condition, WA accelerance calculated in the literature work were constant in all six DoFs in the frequency band, i.e. either flywheel mass or moment of inertias. This however, contradicts to those seen from the test results such as those shown in Figure 7-8 for example. This is because such a model did not correctly represent the WA driving point neither included properties of the suspension system, thus the coupled microvibrations predicted were inaccurate. For this reason, a new method must be developed to calculate the WA driving point dynamic accelerance.

7.3.2.1. WA Dynamic Accelerance Model

Remembering that microvibration models have been derived and validated for the WA in both hard-mounted boundary condition (see Chapter 3) and coupled with a seismic mass boundary condition (see Chapter 6). For WA accelerance derivation however, the hard-mounted model has been proved incorrectly predicts the quality in previous sections, while the WA-seismic mass coupled model can nether be used due to the seismic mass involved in the system. In this section, the WA driving point accelerance (either static or dynamic) is obtained when the WA is in a “free-free” boundary condition such as those in WA accelerance tests and its FE model introduced preciously. The WA in the “free-free” boundary condition can be depicted as in the following figure.

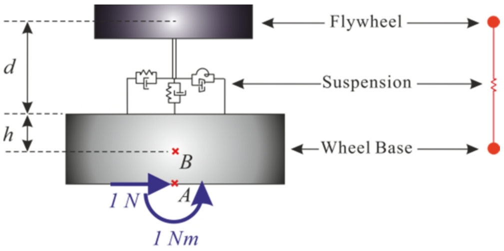

Figure 7-10 WA model in the “free-free” boundary condition

Similar to those previously introduced microvibration models, the flywheel is considered as a rigid and rotating disc and can be idealized as a point mass with moment of inertias, while the suspension system is modeled as a combination of springs and dashpots. If the WA is in a “free-free” boundary condition, the WA base must be considered in the model. The WA base can be modeled as a rigid point mass with its moment of inertias at its CoM. The model in Figure 7-10 is called the flywheel-base system unless mentioned otherwise.

Mathematically, the analytical expressions of the WA driving point dynamic accelerance can be derived from the WA microvibration model in the "free-free" boundary condition. In general, the EoM of a WA microvibration model can be written in the frequency domain as:

$$\boldsymbol{M}\ddot{\boldsymbol{q}}(\omega)+(\boldsymbol{C}+\boldsymbol{G})\dot{\boldsymbol{q}}(\omega)+\boldsymbol{K}\boldsymbol{q}(\omega)=\boldsymbol{F}(\omega) \tag{7.13}$$

Assuming zero initial conditions, the relationship between $\ddot{\boldsymbol{q}}(\omega)$, $\dot{\boldsymbol{q}}(\omega)$ and $\boldsymbol{q}(\omega)$ is:

$$\ddot{\boldsymbol{q}}(\omega)=j\omega\dot{\boldsymbol{q}}(\omega)=-\omega^2\boldsymbol{q}(\omega) \tag{7.14}$$

where j is the imaginary unit. Hence Eq. (7.13) can also be written as:

$$\boldsymbol{M}\ddot{\boldsymbol{q}}(\omega)+(\boldsymbol{C}+\boldsymbol{G})\frac{1}{j\omega}\ddot{\boldsymbol{q}}(\omega)-\boldsymbol{K}\frac{1}{\omega^2}\ddot{\boldsymbol{q}}(\omega)=\boldsymbol{F}(\omega) \tag{7.15}$$

and WA dynamic accelerance (with subscript "ss" for the flywheel-base system) can be expressed from Eq. (7.15) as:

$$\boldsymbol{A}_w(\omega,\Omega)=\left[\boldsymbol{M}_{ss}+(\boldsymbol{C}_{ss}+\boldsymbol{G}_{ss})\frac{1}{j\omega}-\boldsymbol{K}_{ss}\frac{1}{\omega^2}\right]^{-1} \tag{7.16}$$

Eq. (7.16) is both frequency-dependent (ω) and speed-dependent (Ω). The mass matrix, $\boldsymbol{M}_{ss}$, damping matrix, $\boldsymbol{C}_{ss}$, gyroscopic matrix, $\boldsymbol{G}_{ss}$, and stiffness matrix, $\boldsymbol{K}_{ss}$, include those of the flywheel and base. $\boldsymbol{F}$ is the excitation vector, $\ddot{\boldsymbol{q}}$ is the response vector, they are taken at the CoM of the flywheel and base respectively.

Since the torque accelerance can be ignored, the dimension of each matrix is 10×10; the dimension of each vector is 10×1. The EoM of the flywheel-base system can be derived following the same approach as for the WA-seismic mass coupled system. In this case, properties of the base are used, such as in the kinetic and potential energy expressions (see Eqs. (6.1) and (6.2)), thus giving the final EoM for the flywheel-base system. Elements of each matrix and vector in Eq. (7.16) are given in Appendix F. Values of each element are taken from previous microvibration models.

The definition of the driving point accelerance states that excitations and responses must be taken at the same point. In the flywheel-base system in Figure 7-10, the only microvibrations produced by WA are from its internal irregularities and are idealized at the flywheel CoM in the model. In order to find the driving point accelerance of the WA, forced motion must be applied at the base interface and its response accelerations are calculated there. Unit force or moment can be applied at the WA base interface (point A in the model in Figure 7-10 b)), they are required to be transferred to the base CoM (point B) in order to use as the forcing vector, $\boldsymbol{F}$, in the equation. The responses, $\ddot{\boldsymbol{q}}$, are then calculated at the base CoM (point B) but are required to be transferred back to the base interface (point A). The transfer functions of the two processes are the exactly opposite for a rigid body (i.e. the WA base), thus Eq. (7.16) does not ultimately change.

It also worth mentioning that $\boldsymbol{A}_w(\omega, \Omega)$ calculated from Eq. (7.16) is a 10×10 matrix at each speed (see Appendix F for its general form), if the unit load method is used to find accelerance at the base CoM, only the 25 elements from the WA base DoFs are eventually required. These elements are also highlighted in Appendix F. The 25 elements form a fully populated matrix (except the independent base axial translational DoF), thus the driving point accelerance of the flywheel-base system is a 5×5 symmetric matrix with non-zero off-diagonal terms, which is as expected. From the discussions so far, the analytical method introduced is more powerful than the two experimental methods shown in Section 7.3.1, since it is able to provide the fully populated WA accelerance rather than only diagonal elements in the accelerance matrix.

7.3.2.2. The Simulated Wheel Assembly Dynamic Accelerance

Eq. (7.16) is simulated in MATLAB in the frequency band between 1 to 500 Hz and speed band between 1 to 5000 rpm. Figure 7-11 shows comparisons of magnitudes of

A_{w33} and A_{w44} from analytical expressions and test results at static and 2400 rpm, for examples.

In Figure 7-11, analytical and test results are matched well for A_{w33}, the accelerance simply reveals the speed-independent axial translational mode in the frequency band. A_{w44} on the other hand have shown some differences between the two results, but the "rocking" mode due to gyroscopic effects has been successfully predicted and the general trend follows the test results quite well. The speed-independent mode around 100 Hz in A_{w44} have also quite well matched. Therefore the results shown in Figure 7-11 indicate that the analytical method introduced can be used to calculate the WA driving point dynamic accelerance.

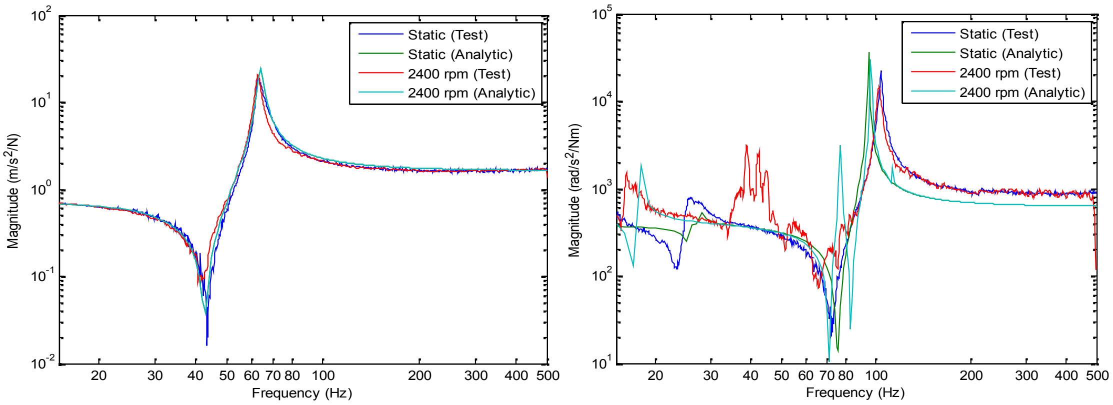

a) Axial translational DoF (A_{w33}) b) Radial rotational DoF (A_{w44})

Figure 7-11 Experimental and analytical WA accelerance comparison

Analytical results of the three WA direct driving point dynamic accelerance elements, A_{w11}, A_{w33} and A_{w44} and one selected cross-DoF driving point dynamic accelerance element, A_{w14}, are simulated in the speed band and results are shown in Figure 7-12 (magnitudes only).

From Figure 7-12 all speed-dependent and/or speed-independent modes of the WA are clearly seen in each plot. In Figure 7-12 a) and c), the forward and backward whirls of the "rocking mode" are clearly presented in radial DoFs, but unlike in the microvibration test results shown in Chapter 6, the forward whirl in accelerance is not as clear as the backward whirl. This observation matches the measured accelerance shown in Figure 7-8. This confirmation indicates that the backward whirl is much more important in WA dynamic accelerance, in other words, as speed increases gyroscopic effects mainly shift the “rocking” mode to lower frequencies in the dynamic accelerance. It is also seen that the speed independent modes around 100 Hz in Figure 7-12 a) and c) are not always constant. They are in fact a composition of the forward whirl (above 2700 rpm) and the radial translational mode (below 2700 rpm). Both modes are constant with speeds in the two speed bands, thus together are considered as the radial translational mode of the WA for modeling purpose.

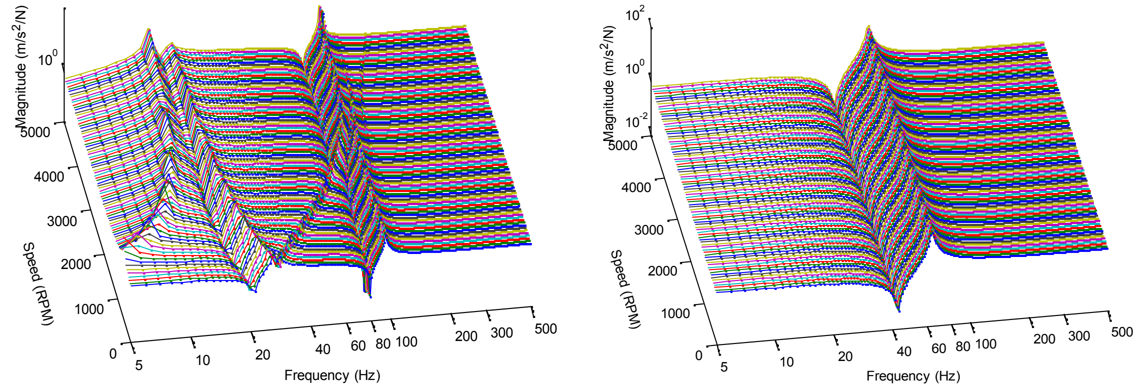

a) Radial translational DoF (A_{w11})

b) Axial translational DoF (A_{w33})

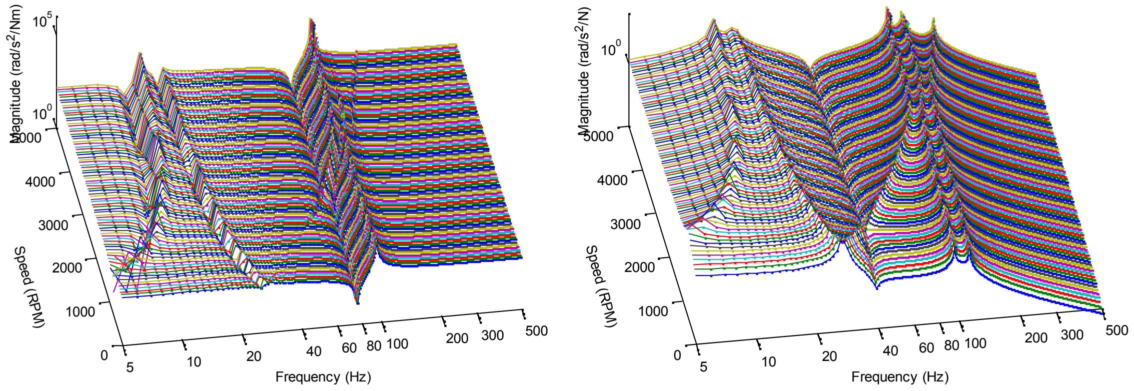

c) Radial rotational DoF (A_{w44})

d) Cross DoF (A_{w14})

Figure 7-12 Analytical results of the WA driving point dynamic accelerance

Another speed-dependent mode up to approximately 10 Hz is due to the overall natural frequency of the flywheel-base system. This mode is also influenced by gyroscopic effects as expected and also in the test results (see Figure 7-8), but it is not the major concern in accelerance in the frequency band of interest as it only grows up to 10 Hz.

It is also expected that in Figure 7-12 b), the axial translational mode is uncoupled from the four radial DoFs and speed-independent; also A_{w14} in Figure 7-12 d) include all modes in radial DoFs.

7.3.3. The Coupled Microvibration Prediction

The driving point accelerance of the mounting structure, $\boldsymbol{A}_s(\omega)$, can be obtained from the structure FE model. In this case, the seismic mass is a rigid body in the frequency band between 1 to 500 Hz and all elements in its accelerance matrix are constant values. The 5×5 accelerance matrix of the seismic mass was calculated from FE model in MSC NASTRAN, results are not shown here. The simulated results of the “analytical load filters”, $\boldsymbol{G}_f(\omega, \Omega)$, between hard-mounted and coupled microvibrations in Eq. (7.5) are neither shown here, as they are not very different from $\boldsymbol{A}_w(\omega, \Omega)$ due to the constant $\boldsymbol{A}_s(\omega)$, except that some modes are shifted and amplitudes are slightly changed.

The coupled microvibrations, $\boldsymbol{\Phi}_{FF\_coupled}$, of the WA-seismic mass system are predicted using two methods. First of all, the coupled microvibrations are obtained using the traditional method, where the WA static accelerance, $\boldsymbol{A}_w(\omega)$, is used in Eq. (7.5). On the other hand, the coupled microvibrations are obtained using the WA dynamic accelerance, $\boldsymbol{A}_w(\omega, \Omega)$. Both predicted coupled microvibrations in the speed band are compared to the test results. RMS values of Φ_{cFxFx}, Φ_{cFzFz} and Φ_{cMyMy} in the $\boldsymbol{\Phi}_{FF\_coupled}$ matrix at each speed are calculated in the speed band, results of Φ_{cFzFz} and Φ_{cMyMy} are shown in Figure 7-13 for examples.

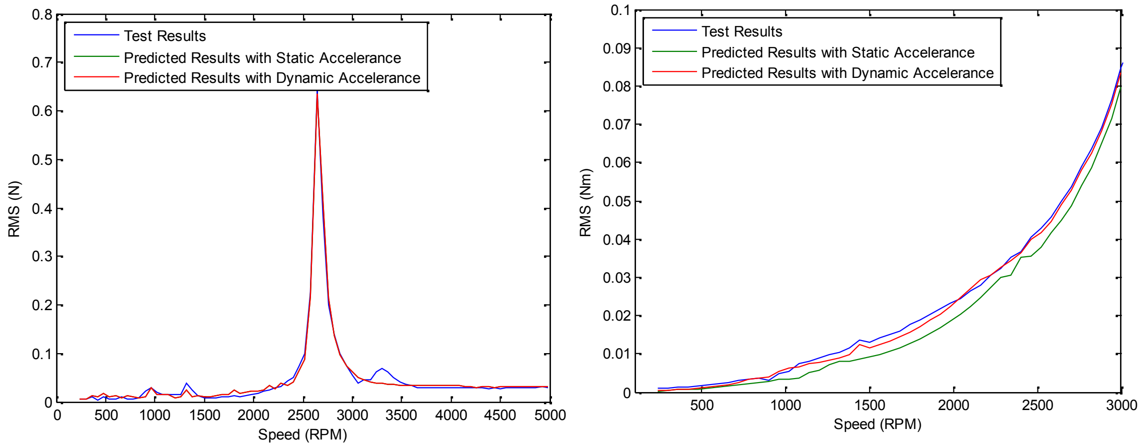

a) RMS value of Φ_{cFzFz} b) RMS value of Φ_{cMyMy}

Figure 7-13 Comparisons of RMS values of coupled microvibrations

In Figure 7-13 a), the predicted coupled microvibrations with static accelerance and dynamic accelerance are the same in the independent axial translational DoF as expected. Also, since nonlinearity is not significant in axial translational DoF, both predicted results match well with the test results in the whole speed band (up to 5000 rpm). Note that the small peak at approximately 3200 rpm in the test results are due to abrupt responses from unknown sources and are not captured in the analytical model (see Figure 7-7 for detail). In Figure 7-13 b) on the other hand, the predicted coupled microvibrations in radial DoFs have shown some divergence compared to the test results (performed up to 3000 rpm in radial DoFs). Nevertheless, the results predicted with dynamic accelerance are closer to the test results.

As an example, the predicted results of Φ_{cMyMy} at 2400 rpm are extracted and compared to the corresponding coupled microvibration test results. Also the microvibrations predicted using the traditional method (i.e. hard-mounted test results are used directly as inputs to the coupled system) is plotted for comparison. They are shown in Figure 7-14.

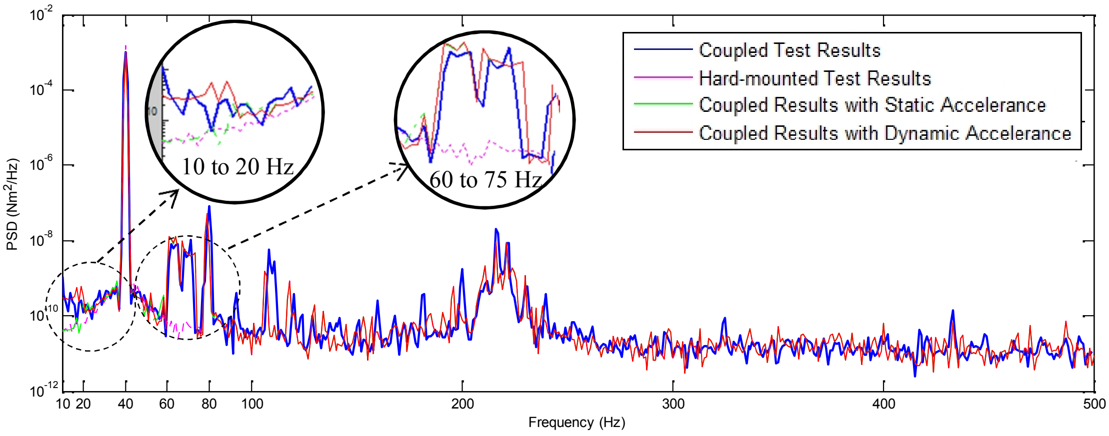

Figure 7-14 Predicted and test results of Φ_{cMyMy} at 2400 rpm

Generally, the coupled microvibrations predicted with static and dynamic accelerance match better to the coupled microvibration test results compared to those predicted with hard-mounted test results that are directly used as the inputs. In particular, results predicted with dynamic accelerance are most closely matched to the coupled test results, especially at low frequencies before fundamental harmonic (see the zoomed plot between 10 to 20 Hz in Figure 7-14). Compare between the coupled results predicted with WA static and dynamic accelerance, there are slight differences in two regions (10 to 20 Hz and 40 to 60 Hz (the zoomed plot is not shown here)). They are identified to be the regions where gyroscopic effects are present at 2400 rpm (see Figure 7-12 c) for reference). First of all, the “rocking” mode amplifies the hard-mounted test results (i.e. the inputs) between 10 to 20 Hz and thus the predicted coupled results. In the frequency region between 40 to 60 Hz however, amplifications are caused by the (beginning) interaction of the “rocking” mode and the radial translational mode, but its influences are not as obvious (see Figure 7-12 c) for reference). These additional amplifications are also the reason that the total RMS value of coupled microvibrations predicted with WA dynamic accelerance is larger than those predicted the WA static accelerance case (see Figure 7-13 b) at 2400 rpm for example).

Comparing both predicated results with WA accelerance to the hard-mounted microvibrations that are used directly as the inputs in the traditional method, not only are the amplifications below 20 Hz missed due to lack of the speed-dependent gyroscopic effects, but also those between 60 to 75 Hz due to lack of the “speed-independent” WA radial translational mode (see Figure 7-12 c) for detail). At high frequencies however, the two predicted coupled microvibrations and those predicted with hard-mounted are the same as there are no WA modes, neither gyroscopic effects. These results are therefore also very close to the measured coupled microvibrations as expected. Similar observations are also seen at other speeds and their results are plotted as the total RMS values in the speed band in Figure 7-13.

From the results and discussions presented in this section, it is clear that the coupled microvibration analysis method with WA dynamic accelerance has an advantage over the traditional method and the method with static accelerance. From the practicality point of view, since WA driving point dynamic accelerance are derived from the verified WA microvibration model, the complete analysis process can be programed following a systematic approach and easily to be modified for any type of WA.

7.4. Summary

In this chapter, microvibrations of coupled WA with its mounting structure are discussed in detail. Modeling and validation of the important WA driving point accelerance are studied in detail. Due to lack of the gyroscopic effects, the predicted microvibrations with WA static accelerance have been proved inaccurate. On the other hand, the method in the literature of including gyroscopic effects in WA accelerance derived from hard-mounted microvibration model does not correctly represent the boundary condition at its driving point. A new method for WA driving point dynamic accelerance modeling is thus developed. The method is based on the WA microvibration model in a “free-free” boundary condition by considering stiffness and damping of the suspension system. The modeling method has been validated with the coupled microvibration test results and have shown improved results, especially in regions where speed-dependent gyroscopic effects taken place. Also for practicality, the method is more efficient and accurate than any other available, thus it can be argued that it is the most advanced method to date.

8. Conclusion

The work presented in this thesis has focused on the development and validation of microvibration models for a satellite Wheel Assembly (WA). The particular WA which was analyzed consisted of a cantilevered configuration with the flywheel supported by a soft-suspension system. The peculiar WA dynamic characteristics such as nonlinearity in the motor and high damping of the soft-suspension system, as well as the more general dynamics not studied for the soft-suspended WA in the literature such as the coupled motion in WA radial directions and broadband excitations, etc., which are here considered, make the overall microvibration analysis significantly more complicated. On the other hand, the WA-structure coupled microvibrations are more representative than the hard-mounted ones. In particular, the WA driving point dynamic accelerance are often the most important and yet difficult parameters to obtain. These issues have been studied in this thesis for the state of the art of WA microvibration research and the conclusions are given this chapter. Furthermore, although the work presented in this thesis is considered as a complete microvibration analysis for a WA, some suggestions are also given for areas where future developments may be beneficial.

8.1. Main Achievements

Although satellite microvibrations and related issues have interested satellite engineers and researchers for more than four decades, the increasing structure stability requirements of satellites carrying highly sensitive payloads (i.e. receivers) such as cameras, telescopes, sensors and scientific instruments, etc., still pose challenges.

Even though there are many devices and events on board satellites which can generate microvibrations (i.e. sources), the high speed rotational mechanisms such as Reaction Wheel Assemblies (RWAs) and Momentum Wheel Assemblies (MWAs) are usually considered as one of the most significant.

The initial step in the satellite system level microvibration analysis (i.e. to predict the receiver performance or structure stability under microvibration environments) is to characterize the microvibration sources. The next step is to integrate the source-generated microvibrations as the input disturbances to the satellite structure model and to predict the receiver performance. In this thesis our research has focused on these two steps for a cantilever configured WA designed with a soft-suspension system. Main achievements are summarized as following.

➢ <u>WA Hard-mounted Boundary Condition</u>

- The analytical model of microvibrations has been derived for the cantilever configured WA designed with a soft-suspension system.

  To the best of the author's knowledge, only microvibration models of flywheel mid-span configuration of satellite WAs have been presented in literature. Here, based on standard assumptions such as linearity, small perturbation angles, small mass imbalances, WA (flywheel and base) symmetry and steady speed rotation, etc., an analytical model of the microvibrations produced by the flywheel mass imbalances has been derived by using the energy method for the cantilever configured WA with a soft-suspension system. This linearized analytical model accurately captures WA-induced fundamental harmonics, WA structural modes and gyroscopic effects of the spinning flywheel.

- Higher harmonic excitations have been modeled empirically using a more efficient and accurate method developed in this thesis.

  Due to the dynamics observed in the hard-mounted microvibration test results of the WA, such as nonlinearity in the motor and high damping in the soft-suspension system, harmonic excitations have been modeled empirically by retrieving values for the three related variables on each harmonic: amplitude coefficients, damping values and speed exponent. The modeling strategy was based on a "trade-off" process of these variables for each harmonic and an algorithm was developed to automate this process for practical use. In particular, a critical value termed the "cut-off speed" was estimated (in this case it was found at approximately 1500 rpm for the WA) from the fundamental harmonic responses of the test results. Amplitudes of all harmonic excitations were simulated up to this speed before the resonant dynamic amplifications began severely influence the harmonic responses in the test results.

The advantage of this method with respect to (w.r.t.) those previously proposed by other researchers was that it has covered the more general situations where resonance and its influences were not only limited to higher harmonics in the test speed band (usually no resonance appeared on the WA-induced fundamental harmonic responses in the speed band analyzed (e.g. up to 5000 rpm) in the literature for conventional WA designs due to rigid suspension systems used), but also on the fundamental harmonics, thus the method was more practical. Also, the speed exponent in the harmonic excitation amplitudes was considered as a variable (i.e. here it was not considered to be exactly the square of flywheel angular speed, which was true in practice), and thus the simulated harmonic excitations were more accurate.

- Broadband (noise) excitations have been simulated using an empirical method developed in this thesis.

The inclusion of the broadband excitations in the WA microvibration model completed the general excitation modeling under linear assumptions (including harmonic excitations and broadband excitations and they could be superimposed). The broadband excitations were simulated empirically by taking the typical WA-induced microvibrations at any speed in the test results and applying a number of designed bandstop filters to them, which were used to isolate the broadband noises from other disturbances.

The important issues of this part of the work were to identify the potential spikes (include harmonics and resonances) and design the filtering process. Spikes were identified using an energy variation method (also developed here) from the Cumulative Root Mean Square (CRMS) value plots of responses. These spikes were removed from the raw microvibrations by using a programed iteration filtering process. One of the improvements w.r.t. the previous work was that the simulated empirical broadband excitations in this thesis was a universal one, i.e. speed-independent, they could be applied to microvibrations at any speed due to their common broadband dynamic characteristics observed from the test results. Also the method did not require a specific analytical shape function of microvibrations for each speed, thus the efficiency of overall WA microvibration modeling process has been significantly improved.

- A microvibration measurement platform has been designed for hard-mounted WA-induced microvibration measurements, and from the peculiar dynamics observed in the test results, such as nonlinearity and high damping in the responses, modeling strategies have been developed and implemented in the WA microvibration modeling.

  The platform was designed from similar principles of a Kistler table, and in our case three common force sensors were used as the transducers and mounted on an aluminum platform. This relatively simple platform was able to simultaneously measure three WA-induced microvibration loads in the hard-mounted boundary condition. Assembling the payload in different orientations, it was possible to measure all six components of the reactions. The platform was much simpler to use and its performance was comparable to that of the much more expensive hardware (e.g. a Kistler table or a load cell) normally employed for these measurements.

In general, the limitations of the methods developed in this thesis for hard-mounted WA can be summarized as following:

- The microvibration model was able to accurately simulate the dynamics in WA axial Degree of Freedom (DoF) for all harmonics, but only for fundamental harmonics in WA radial DoFs. This was mainly due to different damping values of suspension system required for each harmonic in radial DoFs, and the consideration of overall modeling efficiency in practice.

- The platform designed was not able to simultaneously measure WA-induced reaction loads in its six DoFs, i.e. three forces and three moments. The change of WA orientations w.r.t platform in the tests may introduce undesired errors such as gravity effects to the spinning flywheel in the responses in x_w-axis and y_w -axis orientated tests (see Figure 4-1 for detail).

- Although the broadband excitation simulation method developed was a universal one for this WA, for conventional designs where structural modes appear at relatively high frequencies, it may require additional shape functions to describe their general response levels (due to excitations) by broadband noise (see Figure 4-3 for example).

➢ WA-Structure Coupled Boundary Condition

- A WA-seismic mass coupled microvibration measurement system, the "Seismic Mass Vibration Measurement System" or "SMVMS", has been designed.

  This measurement system implemented an indirect method to simultaneously measure the six components of microvibration loads induced by the WA. The six WA-seismic mass interface loads (three forces and three moments) were reconstructed from the system rigid body dynamics. With respect to the standard measurement systems, e.g. using a load cell or Kistler table, the measurement system developed here had the advantage to utilize simple hardware, like accelerometers and a seismic mass. It also had the benefit to be naturally isolated from the ground-borne noise, as the system was suspended using elastic cords. The accuracy of the system has been validated experimentally and its performance was similar to that of the considerably more expensive hardware normally employed for these measurements.

- An accelerance measurement system has been designed and measurement method has been developed to measure the WA driving point (static or dynamic) accelerance.

  This system primarily consisted of a specially designed mounting bracket attached to the WA and common accelerometers and force sensors for the measurements. The system was easy to setup compared to the one in the literature and able to provide the complete 6×6 WA accelerance matrix. It also had the advantage to measure the WA dynamic accelerance, which was the first time this has been performed in this research field. Furthermore, the direct application of input loads at the WA interface has reduced the unwanted modes in other DoFs, consequently the post-processing work and the accuracy of test results has improved.

- The WA driving point dynamic accelerance have been thoroughly studied from both experimental and analytical approaches.

  Firstly, to the best knowledge of the author, it was the first time that WA driving point dynamic accelerance were measured, i.e. an experimental analysis, for the coupled WA-structure microvibration analysis. Secondly and most importantly in this thesis, analytical expressions of the WA driving point dynamic accelerance have been derived and validated with the test results. The method presented here was more accurate than the only one available in the literature. In particular, the WA accelerance model has been developed from a new approach, i.e. from the WA microvibration model in a "free-free" boundary condition. In this case, the accelerance model not only included the gyroscopic effects but also the WA flexibilities, and this was verified with the WA accelerance test results. By using this model in the WA-structure coupled microvibration analysis, the accuracy of the predicted results has been improved w.r.t. all other available methods, especially at low frequencies where the backward whirl of the WA "rocking" mode (caused by gyroscopic effects) was more influential in the accelerance. This method was a universal one and has been applied to conventional WA designs with accurate results compared to the traditional method.

Although the WA-structure coupled microvibration analysis methods presented in this thesis significantly extended the work in the literature, some limitations can still be addressed:

- The measurement method developed for the WA driving point dynamic accelerance measurements need to be used carefully. Although it has been concluded that dynamic accelerance measured using this method was not able to be implemented into the coupled microvibration model due to the spinning flywheel (where unwanted harmonic responses were also measured along with WA structural modes), the fundamental coupled microvibration analysis theory need to be modified in order to obtain meaningful results.

8.2. Recommendations for Future Work

The recommendations for future work can be grouped into three main areas:

- Improvements of the WA hard-mounted microvibration model in its prediction accuracy and efficiency;

- Further developments in WA-structure coupled microvibration analysis methods;

- More application examples and thus, evidence of reliability and practicality of the WA microvibration analysis methods developed in this thesis;

They are briefly introduced as following:

- Improvements of the WA Hard-mounted Microvibration Modeling

- An analytical model of broadband excitations could be derived for the WA microvibration modeling.

  Although similar works have been attempted in the literature and failed in capturing the general dynamics of broadband noise, its modeling can still be developed. Generally, in order to obtain an analytical model of the low level broadband excitations, two factors of the model must be considered: a shape function to describe the general response level caused by response resonance amplifications and simulated random broadband vibrations (such as white noise defined in an analyzed frequency band). Under a linear assumption, the simulated random vibrations (with the more or less constant noise peak-peak amplitudes in the frequency band) can be brought up by an accurately modeled response shape function at that speed, and this will ensure the simulated broadband noise best matches to the test results. The difficulty here is to derive an analytical and universal shape function based on several factors, such as WA angular speed, response dynamic amplification and general response level, etc.

  Alternatively, the modeling of broadband noise can be considered from their causes, i.e. to physically model all irregularities and other dynamics which are sources of broadband excitations in the motor and bearing system, thus a completely analytical broadband noise model can be obtained.

- Further Extensions of the Coupled Microvibration Analysis Methods

Although in this thesis the presented method to calculate the WA driving point dynamic accelerance been improved from the previous methods, the process is not as efficient as it could ultimately be. For example as it has been presented in the thesis, WA driving point accelerance in six DoFs are required to be measured independently (i.e. one test in each DoF and a 6×1 accelerance vector is obtained in each test). The same process also applies in the analytical dynamic accelerance expressions (unit force needs to be applied six times at the WA interface). This process makes the overall microvibration analysis exceptionally time-consuming, especially in the experiments. Also the hard-mounted microvibrations must be included, which need to be measured or simulated independently, as also in the traditional methods.

During the WA-structure coupled microvibration research, we have also attempted several alternative methods to tackle the issues regarding WA driving point accelerance. These works are still in the progress of researching and details of the work have been provided in Appendix G. Some of them are briefly introduced below.

From Chapter 7, the WA-induced microvibration loads and the coupling accelerations between the WA and structure can be expressed in either vector form (in either time domain or frequency domain) or spectral density matrices form (in the frequency domain only). Starting from the fundamental equation of the coupled WA, i.e. Eq. (7.1):

$$\boldsymbol{f}_c = \boldsymbol{f}_b + \boldsymbol{A}_w^{-1}\ddot{\boldsymbol{x}} \tag{7.1}$$

In an alternative theory the WA accelerance, $\boldsymbol{A}_{\mathrm{w}}$, can be calculated as following: first of all, suspending the WA in a "free-free" boundary condition (i.e. in this case $\boldsymbol{f}_c$ is zero in the equation and $\boldsymbol{f}_b$, when WA is alone can be expressed in terms of the coupling accelerations, $\ddot{\boldsymbol{x}}$). Next, by mounting the WA on the seismic mass, the coupled forces, $\boldsymbol{f}_c$, can be measured. In both cases, if the flywheel spins and measurements are taken then the only unknown, $\boldsymbol{A}_{\mathrm{w}}$ in the equation can be calculated.

If the loads and coupling accelerations are expressed in vector form (see Eq. (8.1)), the problem then lies in the inversion of a vector, which mathematically does not have a unique solution.

$$\boldsymbol{A}_s^{-1}\ddot{\boldsymbol{x}}_c = \boldsymbol{A}_w^{-1}\left(\ddot{\boldsymbol{x}}_c - \ddot{\boldsymbol{x}}_f\right) \tag{8.1}$$

If they are expressed in matrix form, the difficulty then is to calculate the inverse of the 6 ×6 complex matrix, $\boldsymbol{A}_{\mathrm{w}}$, from the multiplication of the matrix with its Hermitian (even if $\boldsymbol{A}_{\mathrm{w}}$ is a symmetric matrix by assuming the WA is axisymmetric). The resulting equation is shown as following:

$$\left[\boldsymbol{A}_s^{-1}\right]\ddot{\boldsymbol{X}}_c\left[\boldsymbol{A}_s^{-1}\right]^H = -\left[\boldsymbol{A}_w^{-1}\right]\left(\ddot{\boldsymbol{X}}_c - \ddot{\boldsymbol{X}}_f\right)\left[\boldsymbol{A}_w^{-1}\right]^H \tag{8.2}$$

- Apart from the further developments of analytical methods, alternative WA accelerance measurement system may be designed to simultaneously measure all elements in the 6×6 WA driving point dynamic accelerance matrix, or at least to reduce the work that has been conducted in this thesis.

All these research works are being conducted in the Astronautics Research Group at the University of Southampton at present.

➢ More Test Applications to the Presented Modeling Methods

The modeling methods (hard-mounted and coupled) introduced in this thesis can also be applied to the conventional WA designs, e.g. the WA is mid-span configured with flywheel supported by a rigid system. In practice, the supporting structure is often flexible, i.e. with many DoFs, while in our case a rigid seismic mass has been used throughout the study. It is thus also necessary to verify the microvibration analysis methods developed in this thesis using a more representative flexible structure, e.g. strut-boom type structure or panel, to support the WA.

These two concerns have been applied in another project that the author and his colleagues are currently working on [8, 52-54]. In this case, a conventional mid-span configured RWA with a rigid system is used as the microvibration source and a real-life satellite panel (where the RWA is mounted at in practice) is used as its supporting structure.

8.3. Summary

Overall, this thesis has presented the microvibration research of a WA that has a cantilevered configuration designed with a soft-suspension system. WA-induced microvibrations have been modeled in hard-mounted and couple boundary conditions using methods developed in this thesis. This includes the implementation of several (microvibration and accelerance) measurement systems and analytical models of the WA. In general this study considers several aspects that have not been well addressed in the literature such as WA-induced broadband noise, general harmonic responses, WA driving point dynamic accelerance, etc. The methods proposed in this thesis have been shown to produce more accurate results and more efficient in practical applications than the previous techniques. Limitations of the methods are also addressed and future developments are given.

Appendix A Euler Rotation Transformation Matrices

Order: ***XYZ* → *abc* → *x'y'z'* → *xyz***		
From	**To**	**Transformation Matrices (*Z*-Convention)**
XYZ	*abc*	$\begin{Bmatrix} \hat{u}_a \\ \hat{u}_b \\ \hat{u}_c \end{Bmatrix} = \begin{bmatrix} \cos\varphi & 0 & -\sin\varphi \\ 0 & 1 & 0 \\ \sin\varphi & 0 & \cos\varphi \end{bmatrix} \begin{Bmatrix} \hat{u}_X \\ \hat{u}_Y \\ \hat{u}_Z \end{Bmatrix}$
abc	*x'y'z'*	$\begin{Bmatrix} \hat{u}_{x'} \\ \hat{u}_{y'} \\ \hat{u}_{z'} \end{Bmatrix} = \begin{bmatrix} 1 & 0 & 0 \\ 0 & \cos\theta & \sin\theta \\ 0 & -\sin\theta & \cos\theta \end{bmatrix} \begin{Bmatrix} \hat{u}_a \\ \hat{u}_b \\ \hat{u}_c \end{Bmatrix}$
x'y'z'	*xyz*	$\begin{Bmatrix} \hat{u}_x \\ \hat{u}_y \\ \hat{u}_z \end{Bmatrix} = \begin{bmatrix} \cos\psi & \sin\psi & 0 \\ -\sin\psi & \cos\psi & 0 \\ 0 & 0 & 1 \end{bmatrix} \begin{Bmatrix} \hat{u}_{x'} \\ \hat{u}_{y'} \\ \hat{u}_{z'} \end{Bmatrix}$
XYZ	*x'y'z'*	$\begin{Bmatrix} \hat{u}_{x'} \\ \hat{u}_{y'} \\ \hat{u}_{z'} \end{Bmatrix} = \begin{bmatrix} \cos\varphi & 0 & -\sin\varphi \\ \sin\theta\sin\varphi & \cos\varphi & \sin\theta\sin\varphi \\ \cos\theta\sin\varphi & -\sin\theta & \cos\theta\cos\varphi \end{bmatrix} \begin{Bmatrix} \hat{u}_X \\ \hat{u}_Y \\ \hat{u}_Z \end{Bmatrix}$
XYZ	*xyz*	$\begin{Bmatrix} \hat{u}_x \\ \hat{u}_y \\ \hat{u}_z \end{Bmatrix} = \begin{bmatrix} \cos\varphi\cos\psi + \sin\varphi\sin\theta\sin\psi & \cos\theta\sin\psi & -\sin\varphi\cos\psi + \cos\varphi\sin\theta\sin\psi \\ -\cos\varphi\sin\psi + \sin\varphi\sin\theta\cos\psi & \cos\theta\cos\psi & \sin\varphi\sin\psi + \cos\varphi\sin\theta\cos\psi \\ \sin\varphi\cos\theta & -\sin\theta & \cos\varphi\cos\theta \end{bmatrix} \begin{Bmatrix} \hat{u}_X \\ \hat{u}_Y \\ \hat{u}_Z \end{Bmatrix}$
abc	*xyz*	$\begin{Bmatrix} \hat{u}_x \\ \hat{u}_y \\ \hat{u}_z \end{Bmatrix} = \begin{bmatrix} \cos\psi & \cos\theta\sin\psi & \sin\theta\sin\psi \\ -\sin\psi & \cos\theta\cos\psi & \sin\theta\sin\psi \\ 0 & -\sin\theta & \cos\theta \end{bmatrix} \begin{Bmatrix} \hat{u}_a \\ \hat{u}_b \\ \hat{u}_c \end{Bmatrix}$

Table A- 1 Transformations from inertial frame (*XYZ*) to body frame (*xyz*)

Order: ***XYZ* ← *abc* ← *x'y'z'* ← *xyz***		
From	**To**	**Transformation Matrices (*Z*-Convention)**
abc	*XYZ*	$\begin{Bmatrix} \hat{u}_X \\ \hat{u}_Y \\ \hat{u}_Z \end{Bmatrix} = \begin{bmatrix} \cos\varphi & 0 & \sin\varphi \\ 0 & 1 & 0 \\ -\sin\varphi & 0 & \cos\varphi \end{bmatrix} \begin{Bmatrix} \hat{u}_a \\ \hat{u}_b \\ \hat{u}_c \end{Bmatrix}$
x'y'z'	*abc*	$\begin{Bmatrix} \hat{u}_a \\ \hat{u}_b \\ \hat{u}_c \end{Bmatrix} = \begin{bmatrix} 1 & 0 & 0 \\ 0 & \cos\theta & -\sin\theta \\ 0 & \sin\theta & \cos\theta \end{bmatrix} \begin{Bmatrix} \hat{u}_{x'} \\ \hat{u}_{y'} \\ \hat{u}_{z'} \end{Bmatrix}$
xyz	*x'y'z'*	$\begin{Bmatrix} \hat{u}_{x'} \\ \hat{u}_{y'} \\ \hat{u}_{z'} \end{Bmatrix} = \begin{bmatrix} \cos\psi & -\sin\psi & 0 \\ \sin\psi & \cos\psi & 0 \\ 0 & 0 & 1 \end{bmatrix} \begin{Bmatrix} \hat{u}_x \\ \hat{u}_y \\ \hat{u}_z \end{Bmatrix}$
x'y'z'	*XYZ*	$\begin{Bmatrix} \hat{u}_X \\ \hat{u}_Y \\ \hat{u}_Z \end{Bmatrix} = \begin{bmatrix} \cos\varphi & \sin^2\theta & \cos\theta\sin\varphi \\ 0 & \cos\theta & -\sin\theta \\ 0 & \sin\theta\cos\varphi & \cos\theta\cos\varphi \end{bmatrix} \begin{Bmatrix} \hat{u}_{x'} \\ \hat{u}_{y'} \\ \hat{u}_{z'} \end{Bmatrix}$
xyz	*XYZ*	$\begin{Bmatrix} \hat{u}_X \\ \hat{u}_Y \\ \hat{u}_Z \end{Bmatrix} = \begin{bmatrix} \cos\varphi\cos\psi + \sin\varphi\sin\theta\sin\psi & -\cos\varphi\sin\psi + \sin\varphi\sin\theta\cos\psi & \sin\varphi\cos\theta \\ \cos\theta\sin\psi & \cos\theta\cos\psi & -\sin\theta \\ -\sin\varphi\cos\psi + \cos\varphi\sin\theta\sin\psi & \sin\varphi\sin\psi + \cos\varphi\sin\theta\cos\psi & \cos\varphi\cos\theta \end{bmatrix} \begin{Bmatrix} \hat{u}_x \\ \hat{u}_y \\ \hat{u}_z \end{Bmatrix}$
xyz	*abc*	$\begin{Bmatrix} \hat{u}_a \\ \hat{u}_b \\ \hat{u}_c \end{Bmatrix} = \begin{bmatrix} \cos\psi & -\sin\psi & 0 \\ \cos\theta\sin\psi & \cos\theta\cos\psi & -\sin\theta \\ \sin\theta\sin\psi & \sin\theta\sin\psi & \cos\theta \end{bmatrix} \begin{Bmatrix} \hat{u}_x \\ \hat{u}_y \\ \hat{u}_z \end{Bmatrix}$

Table A- 2 Transformations from body frame (*xyz*) to inertial frame (*XYZ*)

Appendix B Wheel Assembly Kinetic Energy

B1 Kinetic Energy of Statically Mass Imbalanced Flywheel

From the total displacement vector of the static mass imbalance given in Chapter 3, i.e. Eq. (3.63), by differentiating the equation w.r.t. time *t*, the resulting velocity vector is inserted into the following kinetic energy expression.

$$T_{m_s} = \frac{1}{2} m_s \boldsymbol{V}_{m_s}^T \boldsymbol{V}_{m_s} \tag{B1-1}$$

This gives the kinetic energy expression as:

$$\begin{aligned}
T_{m_s} = \frac{1}{2} m_s \Big(& \Omega^2 r_s^2 - 2\Omega r_s \dot{x}_w \cos\Omega t \cos\varphi_w - 2\Omega r_s \dot{x}_w \sin\Omega t \sin\theta_w \sin\varphi_w + \dot{x}_w^2 \\
& -2\Omega r_s \dot{y}_w \cos\theta_w \sin\Omega t + \dot{y}_w^2 - 2\Omega r_s \dot{z}_w \cos\varphi_w \sin\Omega t \sin\theta_w + 2\Omega r_s \dot{z}_w \cos\Omega t \sin\varphi_w \\
& +\dot{z}_w^2 + 2 r_s \dot{x}_w \dot{\theta}_w \cos\Omega t \cos\theta_w \sin\varphi_w - 2 r_s \dot{y}_w \dot{\theta}_w \cos\Omega t \sin\theta_w \\
& +2 r_s \dot{z}_w \dot{\theta}_w \cos\Omega t \cos\theta_w \cos\varphi_w + \frac{1}{2} r_s^2 \dot{\theta}_w^2 + \frac{1}{2} r_s^2 \dot{\theta}_w^2 \cos^2\Omega t - \frac{1}{2} r_s^2 \dot{\theta}_w^2 \sin^2\Omega t \\
& -2\Omega r_s^2 \dot{\varphi}_w \sin\theta_w + 2 r_s \dot{x}_w \dot{\varphi}_w \cos\Omega t \cos\varphi_w \sin\theta_w + 2 r_s \dot{x}_w \dot{\varphi}_w \sin\Omega t \sin\varphi_w \\
& +2 r_s \dot{z}_w \dot{\varphi}_w \cos\varphi_w \sin\Omega t - 2 r_s \dot{z}_w \dot{\varphi}_w \cos\Omega t \sin\theta_w \sin\varphi_w + 2 r_s^2 \dot{\theta}_w \dot{\varphi}_w \cos\Omega t \cos\theta_w \sin\Omega t \\
& +\frac{3}{4} r_s^2 \dot{\varphi}_w^2 - \frac{1}{4} r_s^2 \dot{\varphi}_w^2 \cos^2\Omega t - \frac{1}{4} r_s^2 \dot{\varphi}_w^2 \cos^2\theta_w - \frac{1}{4} r_s^2 \dot{\varphi}_w^2 \cos^2\Omega t \cos^2\theta_w + \frac{1}{4} r_s^2 \dot{\varphi}_w^2 \sin^2\Omega t \\
& +\frac{1}{4} r_s^2 \dot{\varphi}_w^2 \cos^2\theta_w \sin^2\Omega t + \frac{1}{4} r_s^2 \dot{\varphi}_w^2 \sin^2\theta_w + \frac{1}{4} r_s^2 \dot{\varphi}_w^2 \cos^2\Omega t \sin^2\theta_w - \frac{1}{4} r_s^2 \dot{\varphi}_w^2 \sin^2\Omega t \sin^2\theta_w \Big)
\end{aligned} \tag{B1-2}$$

Eq. (B1-2) can be further simplified using the typical trigonometric properties. Due to the complexity, it is first broken down into the following form:

$$\begin{aligned}
T_{m_s} = \frac{1}{2} m_s \Big[\Big(& \dot{x}_w^2 + \dot{y}_w^2 + \dot{z}_w^2 + \Omega^2 r_s^2 - 2\Omega r_s \dot{x}_w \cos\Omega t \cos\varphi_w - 2\Omega r_s \dot{x}_w \sin\Omega t \sin\theta_w \sin\varphi_w \\
& - 2\Omega r_s \dot{y}_w \cos\theta_w \sin\Omega t + 2 r_s \dot{x}_w \dot{\theta}_w \cos\Omega t \cos\theta_w \sin\varphi_w - 2 r_s \dot{y}_w \dot{\theta}_w \cos\Omega t \sin\theta_w \Big) \rightarrow (1) \\
& + \Big(-2\Omega r_s^2 \dot{\varphi}_w \sin\theta_w + 2 r_s \dot{x}_w \dot{\varphi}_w \cos\Omega t \cos\varphi_w \sin\theta_w + 2 r_s \dot{x}_w \dot{\varphi}_w \sin\Omega t \sin\varphi_w \\
& \qquad + 2 r_s^2 \dot{\theta}_w \dot{\varphi}_w \cos\Omega t \cos\theta_w \sin\Omega t \Big) \rightarrow (2) \\
& + \left(-\frac{1}{4} r_s^2 \dot{\varphi}_w^2 \cos^2\Omega t \cos^2\theta_w + \frac{1}{4} r_s^2 \dot{\varphi}_w^2 \cos^2\theta_w \sin^2\Omega t - \frac{1}{4} r_s^2 \dot{\varphi}_w^2 \cos^2\theta_w \right) \rightarrow (3) \\
& + \left(\frac{1}{4} r_s^2 \dot{\varphi}_w^2 \cos^2\Omega t \sin^2\theta_w - \frac{1}{4} r_s^2 \dot{\varphi}_w^2 \sin^2\Omega t \sin^2\theta_w + \frac{1}{4} r_s^2 \dot{\varphi}_w^2 \sin^2\theta_w \right) \rightarrow (4) \\
& + \left(\frac{1}{4} r_s^2 \dot{\varphi}_w^2 \sin^2\Omega t - \frac{1}{4} r_s^2 \dot{\varphi}_w^2 \cos^2\Omega t + \frac{3}{4} r_s^2 \dot{\varphi}_w^2 \right) \rightarrow (5) \\
& + \left(\frac{1}{2} r_s^2 \dot{\theta}_w^2 + \frac{1}{2} r_s^2 \dot{\theta}_w^2 \cos^2\Omega t - \frac{1}{2} r_s^2 \dot{\theta}_w^2 \sin^2\Omega t \right) \rightarrow (6) \\
& + r_s \dot{z}_w \Big(-2\Omega \cos\varphi_w \sin\Omega t \sin\theta_w + 2\Omega \cos\Omega t \sin\varphi_w + 2\dot{\theta}_w \cos\Omega t \cos\theta_w \cos\varphi_w \\
& + 2\dot{\varphi}_w \cos\varphi_w \sin\Omega t - 2\dot{\varphi}_w \cos\Omega t \sin\theta_w \sin\varphi_w \Big) \Big] \rightarrow (7)
\end{aligned}$$

In this form, some of the terms (or sub-equations numbered with (1), etc.), can be simplified. Amongst them, (1), (2) and (7) are not changed.

- (3) is simplified as:

$$\begin{aligned}
& -\frac{1}{4} r_s^2 \dot{\varphi}_w^2 \cos^2\Omega t \cos^2\theta_w + \frac{1}{4} r_s^2 \dot{\varphi}_w^2 \cos^2\theta_w \sin^2\Omega t - \frac{1}{4} r_s^2 \dot{\varphi}_w^2 \cos^2\theta_w \\
& = \frac{1}{4} r_s^2 \dot{\varphi}_w^2 \left[-\cos^2\Omega t \cos^2\theta_w + \cos^2\theta_w \left(1 - \cos^2\Omega t\right) - \cos^2\theta_w \right] \\
& = \frac{1}{4} r_s^2 \dot{\varphi}_w^2 \left(-2\cos^2\Omega t \cos^2\theta_w \right) \\
& = -\frac{1}{2} r_s^2 \dot{\varphi}_w^2 \cos^2\Omega t \cos^2\theta_w
\end{aligned}$$

- (4) is simplified as:

$$\begin{aligned}
&\frac{1}{4}r_s^2\dot{\varphi}_w^2\cos^2\Omega t\sin^2\theta_w-\frac{1}{4}r_s^2\dot{\varphi}_w^2\sin^2\Omega t\sin^2\theta_w+\frac{1}{4}r_s^2\dot{\varphi}_w^2\sin^2\theta_w\\
&=\frac{1}{4}r_s^2\dot{\varphi}_w^2\sin^2\theta_w\left(\cos^2\Omega t-\sin^2\Omega t+1\right)\\
&=\frac{1}{2}r_s^2\dot{\varphi}_w^2\sin^2\theta_w\cos^2\Omega t\\
&=\frac{1}{2}r_s^2\dot{\varphi}_w^2\cos^2\Omega t-\frac{1}{2}r_s^2\dot{\varphi}_w^2\cos^2\theta_w\cos^2\Omega t
\end{aligned}$$

- Summing the simplified (3) and (4) with (5), it gives:

$$\begin{aligned}
&-\frac{1}{2}r_s^2\dot{\varphi}_w^2\cos^2\Omega t\cos^2\theta_w+\frac{1}{2}r_s^2\dot{\varphi}_w^2\cos^2\Omega t-\frac{1}{2}r_s^2\dot{\varphi}_w^2\cos^2\theta_w\cos^2\Omega t\\
&\qquad\qquad\qquad\qquad+\frac{1}{4}r_s^2\dot{\varphi}_w^2\sin^2\Omega t-\frac{1}{4}r_s^2\dot{\varphi}_w^2\cos^2\Omega t+\frac{3}{4}r_s^2\dot{\varphi}_w^2\\
&=-r_s^2\dot{\varphi}_w^2\cos^2\Omega t\cos^2\theta_w+\left(\frac{1}{2}r_s^2\dot{\varphi}_w^2\cos^2\Omega t-\frac{1}{4}r_s^2\dot{\varphi}_w^2\cos^2\Omega t\right)+\frac{1}{4}r_s^2\dot{\varphi}_w^2\sin^2\Omega t+\frac{3}{4}r_s^2\dot{\varphi}_w^2\\
&=-r_s^2\dot{\varphi}_w^2\cos^2\Omega t\cos^2\theta_w+r_s^2\dot{\varphi}_w^2
\end{aligned}$$

- (6) is simplified as:

$$\begin{aligned}
&\frac{1}{2}r_s^2\dot{\theta}_w^2+\frac{1}{2}r_s^2\dot{\theta}_w^2\cos^2\Omega t-\frac{1}{2}r_s^2\dot{\theta}_w^2\sin^2\Omega t\\
&=\frac{1}{2}r_s^2\dot{\theta}_w^2+\frac{1}{2}r_s^2\dot{\theta}_w^2\cos^2\Omega t-\frac{1}{2}r_s^2\dot{\theta}_w^2\left(1-\cos^2\Omega t\right)\\
&=r_s^2\dot{\theta}_w^2\cos^2\Omega t
\end{aligned}$$

By summing all terms, the following equation is obtained:

$$
\begin{aligned}
T_{m_s} &= \frac{1}{2} m_s \Big\{ \dot{x}_w^2 + \dot{y}_w^2 + \dot{z}_w^2 + r_s^2 \Big[\dot{\varphi}_w^2 \left(1 - \cos^2 \Omega t \cos^2 \theta_w\right) + \dot{\theta}_w^2 \cos^2 \Omega t + \Omega^2 \Big] \\
&-2 r_s \dot{y}_w \left(\dot{\theta}_w \cos \Omega t \sin \theta_w + \Omega \cos \theta_w \sin \Omega t \right) \\
&+2 r_s^2 \dot{\varphi}_w \left(-\Omega \sin \theta_w + \dot{\theta}_w \cos \Omega t \cos \theta_w \sin \Omega t \right) \\
&+2 r_s \dot{x}_w \Big[\dot{\theta}_w \cos \Omega t \cos \theta_w \sin \varphi_w - \Omega \left(\cos \Omega t \cos \varphi_w + \sin \Omega t \sin \theta_w \sin \varphi_w \right) \\
&\qquad\qquad + \dot{\varphi}_w \left(\cos \Omega t \cos \varphi_w \sin \theta_w + \sin \Omega t \sin \varphi_w \right) \Big] \\
&+ r_s \dot{z}_w \Big(-2\Omega \cos \varphi_w \sin \Omega t \sin \theta_w + 2\Omega \cos \Omega t \sin \varphi_w + 2\dot{\theta}_w \cos \Omega t \cos \theta_w \cos \varphi_w \\
&+2 \dot{\varphi}_w \cos \varphi_w \sin \Omega t - 2\dot{\varphi}_w \cos \Omega t \sin \theta_w \sin \varphi_w \Big) \Big\}
\end{aligned}
$$

From Chapter 3, the total kinetic energy of the mass balanced flywheel is:

$$
T_w = \frac{1}{2} \Big[M_w \left(\dot{x}_w^2 + \dot{y}_w^2 + \dot{z}_w^2 \right) + \left(\dot{\theta}_w^2 + \dot{\varphi}_w^2 \cos^2 \theta_w \right) I_r + \left(\dot{\varphi}_w^2 \sin^2 \theta_w + \Omega^2 - 2\Omega \dot{\varphi}_w \sin \theta_w \right) I_z \Big]
$$

Thus, the total kinetic energy of the statically mass imbalanced flywheel is derived as:

$$
\begin{aligned}
T_{w+m_s} &= \frac{1}{2} \Big[\left(M_w + m_s \right) \left(\dot{x}_w^2 + \dot{y}_w^2 + \dot{z}_w^2 \right) \\
&+ \dot{\theta}_w^2 \left(m_s r_s^2 \cos^2 \Omega t + I_r \right) \rightarrow \text{(i)} \\
&+ \dot{\varphi}_w^2 \left(m_s r_s^2 - m_s r_s^2 \cos^2 \Omega t \cos^2 \theta_w + \cos^2 \theta_w I_r + \sin^2 \theta_w I_z \right) \rightarrow \text{(ii)} \\
&+ \Omega^2 \left(m_s r_s^2 + I_z \right) \rightarrow \text{(iii)} \\
&-2 m_s r_s \dot{y}_w \left(\dot{\theta}_w \cos \Omega t \sin \theta_w + \Omega \cos \theta_w \sin \Omega t \right) \rightarrow \text{(iv)} \\
&+2 m_s r_s \dot{x}_w \Big(\dot{\theta}_w \cos \Omega t \cos \theta_w \sin \varphi_w - \Omega \cos \Omega t \cos \varphi_w - \Omega \sin \Omega t \sin \theta_w \sin \varphi_w \\
&\qquad\qquad + \dot{\varphi}_w \cos \Omega t \cos \varphi_w \sin \theta_w + \dot{\varphi}_w \sin \Omega t \sin \varphi_w \Big) \rightarrow \text{(v)} \\
&+2 \dot{\varphi}_w \left(m_s r_s^2 \dot{\theta}_w \cos \Omega t \cos \theta_w \sin \Omega t - m_s r_s^2 \sin \theta_w - \Omega \sin \theta_w I_z \right) \rightarrow \text{(vi)} \\
&+ m_s r_s \dot{z}_w \Big(-2\Omega \cos \varphi_w \sin \Omega t \sin \theta_w + 2\Omega \cos \Omega t \sin \varphi_w + 2\dot{\theta}_w \cos \Omega t \cos \theta_w \cos \varphi_w \\
&+2 \dot{\varphi}_w \cos \varphi_w \sin \Omega t - 2\dot{\varphi}_w \cos \Omega t \sin \varphi_w \sin \varphi_w \Big) \Big] \rightarrow \text{(vii)}
\end{aligned}
\tag{B1-3}
$$

The terms numbered with (*i*) etc. in Eq. (B1-3) can be further simplified if applying the following assumptions:

- small (perturbation) angle assumption;
- small mass imbalance assumption;
- flywheel angular speed domination assumption;

The detailed simplification process is introduced as following:

- (*i*) term; The magnitude of flywheel moment of inertia is much larger than that of the mass imbalance, thus this term is simplified as: $\dot{\theta}_w^2 I_r$.

- (*ii*) term; similarly to (*i*), the two mass imbalance terms and the two inertia terms are in the same bracket, ignoring mass imbalances, the term reduces to: $\dot{\varphi}_w^2\left(\cos^2\theta_w I_r + \sin^2\theta_w I_z\right)$. Using the small angle assumption, i.e. $\cos\theta \approx 1$, it is further simplified as: $\dot{\varphi}_w^2\left(\cos^2\theta_w I_r + \sqrt{1-\cos^2\theta_w} I_z\right) \approx \dot{\varphi}_w^2 I_r$.

- (*iii*) term; similar to (*ii*), it can be simplified as: $\Omega^2 I_z$.

- (*iv*) term; in practice since the flywheel angular speed Ω is much larger than disturbance velocity terms, the term is simplified as: $-2m_s r_s \dot{y}_w \Omega \sin\Omega t$.

- (*v*) term; similar to (*iv*), if the flywheel angular speed dominates in the bracket, using a small angle assumption, the second order rotational angles term: $-\Omega\sin\Omega t\sin\theta\sin\varphi$, is very small compares to other terms thus can be ignored. Hence (*v*) is simplified as following:

  $$2m_s r_s \dot{x}_w\left(-\Omega\cos\Omega t\cos\varphi_w - \Omega\sin\Omega t\sin\theta_w\sin\varphi_w\right) \approx -2m_s r_s \dot{x}_w \Omega\cos\Omega t.$$

- (*vi*) term; the mass imbalance term is very small thus can be ignored. Also using the small angle assumption, the term can be simplified as: $-2\dot{\varphi}_w \Omega \theta_w I_z$.

- (*vii*) term; the following process shows it is simplified to be zero.

$$
\begin{aligned}
& m_s r_s \dot{z}_w \Big(-\Omega\cos\varphi_w \sin\Omega t \sin\theta_w + \Omega\cos\Omega t \sin\varphi_w + \dot{\theta}_w \cos\Omega t \cos\theta_w \cos\varphi_w \\
& +\dot{\varphi}_w \cos\varphi_w \sin\Omega t - \dot{\varphi}_w \cos\Omega t \sin\varphi_w \sin\varphi_w\Big) \\
& = m_s r_s \dot{z}_w \left(-\Omega\cos\varphi_w \sin\Omega t \sin\theta_w + \Omega\cos\Omega t \sin\varphi_w\right) \\
& = m_s r_s \dot{z}_w \Omega\left(-\theta_w \sin\Omega t + \varphi_w \cos\Omega t\right) \\
& \approx 0
\end{aligned}
$$

From the above discussions, the simplified kinetic energy of the statically mass imbalanced flywheel is thus:

$$
\begin{aligned}
T_{w+m_s} \approx \frac{1}{2}\Big[& M_w\left(\dot{x}_w^2 + \dot{y}_w^2 + \dot{z}_w^2\right) + \dot{\theta}_w^2 I_r + \dot{\varphi}_w^2 I_r + \Omega^2 I_z - 2m_s r_s \dot{y}_w \Omega \sin\Omega t \\
& -2m_s r_s \dot{x}_w \Omega\cos\Omega t - 2\dot{\varphi}_w \Omega \theta_w I_z \Big]
\end{aligned}
$$

B2 Kinetic Energy of Dynamically Mass Imbalanced Flywheel

In this section, discussions of the kinetic energy of the dynamically mass imbalanced flywheel are introduced. From the two displacement vectors of dynamic mass imbalances given in Chapter 3, i.e. Eqs. (3.72) and (3.73), by differentiating the two vectors respectively w.r.t. time *t*, the resulting velocity vectors are inserted into the following kinetic energy expression:

$$
T_{md} = \frac{1}{2} m_d \boldsymbol{V}_{m_{d1}}^T \boldsymbol{V}_{m_{d1}} + \frac{1}{2} m_d \boldsymbol{V}_{m_{d2}}^T \boldsymbol{V}_{m_{d2}} \qquad \text{(B1-4)}
$$

This gives the kinetic energy expression as:

$$
\begin{gathered}
T_{m_d} = m_d \left(r_d^2\Omega^2 + \dot{x}_w^2 + \dot{y}_w^2 + \dot{z}_w^2 - 2hr_d\Omega\dot{\theta}_w \sin\Omega t + h^2\dot{\theta}_w^2 + \frac{1}{2}r_d^2\dot{\theta}_w^2 + \frac{1}{2}r_d^2\dot{\theta}_w^2\cos^2\Omega t \right. \\
-\frac{1}{2}r_d^2\dot{\theta}_w^2\sin^2\Omega t + 2hr_d\Omega\dot{\varphi}_w\cos\Omega t\cos\theta_w - 2r_d^2\Omega\dot{\varphi}_w\sin\theta_w + 2r_d^2\dot{\theta}_w\dot{\varphi}_w\cos\Omega t\cos\theta_w\sin\Omega t \\
+2hr_d\dot{\theta}_w\dot{\varphi}_w\sin\Omega t\sin\theta_w + \frac{1}{2}h^2\dot{\varphi}_w^2 + \frac{3}{4}r_d^2\dot{\varphi}_w^2 - \frac{1}{4}r_d^2\dot{\varphi}_w^2\cos^2\Omega t + \frac{1}{2}h^2\dot{\varphi}_w^2\cos^2\theta_w - \frac{1}{4}r_d^2\dot{\varphi}_w^2\cos^2\theta_w \\
-\frac{1}{4}r_d^2\dot{\varphi}_w^2\cos^2\Omega t\cos^2\theta_w + \frac{1}{4}r_d^2\dot{\varphi}_w^2\sin^2\Omega t + \frac{1}{4}r_d^2\dot{\varphi}_w^2\cos^2\theta_w\sin^2\Omega t - 2hr_d\dot{\varphi}_w^2\cos\Omega t\sin\theta_w\cos\theta_w \\
\left. -\frac{1}{2}h^2\dot{\varphi}_w^2\sin^2\theta_w + \frac{1}{4}r_d^2\dot{\varphi}_w^2\sin^2\theta_w + \frac{1}{4}r_d^2\dot{\varphi}_w^2\cos^2\Omega t\sin^2\theta_w - \frac{1}{4}r_d^2\dot{\varphi}_w^2\sin^2\Omega t\sin^2\theta_w \right)
\end{gathered}
\tag{B1-5}
$$

Eq. (B1-5) can also be simplified using the typical trigonometric properties. It is first broken down into the following form:

$$
\begin{gathered}
T_{m_d} = m_d \Big[\Big(\dot{x}_w^2 + \dot{y}_w^2 + \dot{z}_w^2 + r_d^2\Omega^2 - 2hr_d\Omega\dot{\theta}_w\sin\Omega t + h^2\dot{\theta}_w^2 + 2hr_d\Omega\dot{\varphi}_w\cos\Omega t\cos\theta_w \\
+2r_d^2\dot{\theta}_w\dot{\varphi}_w\cos\Omega t\cos\theta_w\sin\Omega t + 2hr_d\dot{\theta}_w\dot{\varphi}_w\sin\Omega t\sin\theta_w - 2hr_d\dot{\varphi}_w^2\cos\Omega t\sin\theta_w\cos\theta_w \Big) \rightarrow (1) \\
+\left(-\frac{1}{4}r_d^2\dot{\varphi}_w^2\cos^2\Omega t\cos^2\theta_w + \frac{1}{4}r_d^2\dot{\varphi}_w^2\cos^2\theta_w\sin^2\Omega t - \frac{1}{4}r_d^2\dot{\varphi}_w^2\cos^2\theta_w \right) \rightarrow (2) \\
+\left(\frac{1}{4}r_d^2\dot{\varphi}_w^2\cos^2\Omega t\sin^2\theta_w - \frac{1}{4}r_d^2\dot{\varphi}_w^2\sin^2\Omega t\sin^2\theta_w + \frac{1}{4}r_d^2\dot{\varphi}_w^2\sin^2\theta_w \right) \rightarrow (3) \\
+\left(\frac{1}{4}r_d^2\dot{\varphi}_w^2\sin^2\Omega t - \frac{1}{4}r_d^2\dot{\varphi}_w^2\cos^2\Omega t + \frac{3}{4}r_d^2\dot{\varphi}_w^2 \right) \rightarrow (4) \\
+\left(\frac{1}{2}h^2\dot{\varphi}_w^2\cos^2\theta_w - \frac{1}{2}h^2\dot{\varphi}_w^2\sin^2\theta_w + \frac{1}{2}h^2\dot{\varphi}_w^2 \right) \rightarrow (5) \\
+\left(\frac{1}{2}r_d^2\dot{\theta}_w^2 + \frac{1}{2}r_d^2\dot{\theta}_w^2\cos^2\Omega t - \frac{1}{2}r_d^2\dot{\theta}_w^2\sin^2\Omega t \right) \Big] \rightarrow (6)
\end{gathered}
$$

Similarly, some terms in the above equation can be simplified. In this case, (1) is not changed.

- (2) is simplified as:

$$
\begin{aligned}
&-\frac{1}{4}m_d r_d^2\dot{\varphi}_w^2\cos^2\Omega t\cos^2\theta_w+\frac{1}{4}m_d r_d^2\dot{\varphi}_w^2\cos^2\theta_w\sin^2\Omega t-\frac{1}{4}m_d r_d^2\dot{\varphi}_w^2\cos^2\theta_w\\
&=\frac{1}{4}m_d r_d^2\dot{\varphi}_w^2\left(-\cos^2\Omega t\cos^2\theta_w+\cos^2\theta_w\left(1-\cos^2\Omega t\right)-\cos^2\theta_w\right)\\
&=-\frac{1}{2}m_d r_d^2\dot{\varphi}_w^2\cos^2\Omega t\cos^2\theta_w
\end{aligned}
$$

- (3) is simplified as:

$$
\begin{aligned}
&\frac{1}{4}m_d r_d^2\dot{\varphi}_w^2\cos^2\Omega t\sin^2\theta_w-\frac{1}{4}m_d r_d^2\dot{\varphi}_w^2\sin^2\Omega t\sin^2\theta_w+\frac{1}{4}m_d r_d^2\dot{\varphi}_w^2\sin^2\theta_w\\
&=\frac{1}{4}m_d r_d^2\dot{\varphi}_w^2\sin^2\theta_w\left(\cos^2\Omega t-\sin^2\Omega t+1\right)\\
&=\frac{1}{4}m_d r_d^2\dot{\varphi}_w^2\sin^2\theta_w\left(\cos^2\Omega t-\left(1-\cos^2\Omega t\right)+1\right)\\
&=\frac{1}{2}m_d r_d^2\dot{\varphi}_w^2\left(1-\cos^2\theta_w\right)\cos^2\Omega t\\
&=\frac{1}{2}m_d r_d^2\dot{\varphi}_w^2\cos^2\Omega t-\frac{1}{2}m_d r_d^2\dot{\varphi}_w^2\cos^2\Omega t\cos^2\theta_w
\end{aligned}
$$

- The sum of the simplified (2) and (3) is:

$$
\begin{aligned}
&-\frac{1}{2}m_d r_d^2\dot{\varphi}_w^2\cos^2\Omega t\cos^2\theta_w+\frac{1}{2}m_d r_d^2\dot{\varphi}_w^2\cos^2\Omega t-\frac{1}{2}m_d r_d^2\dot{\varphi}_w^2\cos^2\Omega t\cos^2\theta_w\\
&=\frac{1}{2}m_d r_d^2\dot{\varphi}_w^2\left(-2\cos^2\Omega t\cos^2\theta_w+\cos^2\Omega t\right)
\end{aligned}
$$

by adding (4), it gives:

$$
\begin{aligned}
&\frac{1}{2}m_d r_d^2\dot{\varphi}_w^2\left(-2\cos^2\Omega t\cos^2\theta_w+\cos^2\Omega t\right)-\frac{1}{4}m_d r_d^2\dot{\varphi}_w^2\cos^2\Omega t+\frac{1}{4}m_d r_d^2\dot{\varphi}_w^2\sin^2\Omega t+\frac{3}{4}m_d r_d^2\dot{\varphi}_w^2\\
&=\frac{1}{2}m_d r_d^2\dot{\varphi}_w^2\left(-2\cos^2\Omega t\cos^2\theta_w+\cos^2\Omega t-\frac{1}{2}\cos^2\Omega t\right)+\frac{1}{4}m_d r_d^2\dot{\varphi}_w^2\sin^2\Omega t+\frac{3}{4}m_d r_d^2\dot{\varphi}_w^2\\
&=\frac{1}{2}m_d r_d^2\dot{\varphi}_w^2\left(-2\cos^2\Omega t\cos^2\theta_w+\frac{1}{2}\cos^2\Omega t+\frac{1}{2}\sin^2\Omega t\right)+\frac{3}{4}m_d r_d^2\dot{\varphi}_w^2\\
&=m_d r_d^2\dot{\varphi}_w^2-m_d r_d^2\dot{\varphi}_w^2\cos^2\Omega t\cos^2\theta_w
\end{aligned}
$$

- (5) is simplified as:

$$\begin{aligned}&\frac{1}{2}m_d h^2\dot{\varphi}_w^2\cos^2\theta_w-\frac{1}{2}m_d h^2\dot{\varphi}_w^2\sin^2\theta_w+\frac{1}{2}m_d h^2\dot{\varphi}_w^2\\&=\frac{1}{2}m_d h^2\dot{\varphi}_w^2\left(\cos^2\theta_w-\sin^2\theta_w+1\right)\\&=m_d h^2\dot{\varphi}_w^2\cos^2\theta_w\end{aligned}$$

- (6) is simplified as:

$$\begin{aligned}&\frac{1}{2}m_d r_d^2\dot{\theta}_w^2+\frac{1}{2}m_d r_d^2\dot{\theta}_w^2\cos^2\Omega t-\frac{1}{2}m_d r_d^2\dot{\theta}_w^2\sin^2\Omega t\\&=\frac{1}{2}m_d r_d^2\dot{\theta}_w^2\left(1+\cos^2\Omega t-\sin^2\Omega t\right)\\&=m_d r_d^2\dot{\theta}_w^2\cos^2\Omega t\end{aligned}$$

B3 Kinetic Energy of Fully Mass Imbalanced Flywheel

Summing all simplified terms with (1), the following expression of the total kinetic energy of the two dynamic mass imbalances is obtained:

$$\begin{aligned}T_{m_d}&=m_d\left\{\dot{x}_w^2+\dot{y}_w^2+\dot{z}_w^2+r_d^2\Omega^2+\dot{\theta}_w^2\left(r_d^2\cos^2\Omega t+h^2\right)\right.\\&+\dot{\varphi}_w^2\left[h^2\cos^2\theta_w+r_d^2\left(1-\cos^2\Omega t\cos^2\theta_w\right)-2r_d h\sin\theta_w\cos\theta_w\cos\Omega t\right]\\&-2r_d\dot{\theta}_w\sin\Omega t\left[h\Omega-\dot{\varphi}_w\left(r_d\cos\theta_w\cos\Omega t+h\sin\theta_w\right)\right]\\&\left.-2r_d\dot{\varphi}_w\Omega\left(r_d\sin\theta_w-h\cos\Omega t\cos\theta_w\right)\right\}\end{aligned}$$

Remembering that the kinetic energy of the statically mass imbalanced flywheel was derived in Section B1 and thus the kinetic energy of the fully mass imbalanced flywheel, i.e. the sum of T_{w+m_s} and T_{m_d}, gives:

$$
\begin{aligned}
T_{w+m_s+m_d} = \frac{1}{2}\Big[& \left(M + m_s + 2m_d\right)\left(\dot{x}_w^2 + \dot{y}_w^2 + \dot{z}_w^2\right) \\
& +\dot{\theta}_w^2\left(m_s r_s^2 \cos^2 \Omega t + I_r + 2m_d r_d^2 \cos^2 \Omega t + 2m_d h^2\right) \rightarrow \text{(i)} \\
& +\dot{\varphi}_w^2\Big(m_s r_s^2 - m_s r_s^2 \cos^2 \Omega t \cos^2 \theta_w + \cos^2 \theta_w I_r + \sin^2 \theta_w I_z + 2m_d h^2 \cos^2 \theta_w + 2m_d r_d^2 \\
& \qquad - 2m_d r_d^2 \cos^2 \Omega t \cos^2 \theta_w - 4m_d r_d h \sin \theta_w \cos \theta_w \cos \Omega t\Big) \rightarrow \text{(ii)} \\
& +\Omega^2\left(m_s r_s^2 + I_z + 2m_d r_d^2\right) \rightarrow \text{(iii)} \\
& -2m_s r_s \dot{y}_w\left(\dot{\theta}_w \cos \Omega t \sin \theta_w + \Omega \cos \theta_w \sin \Omega t\right) \rightarrow \text{(iv)} \\
& +2m_s r_s \dot{x}_w\Big(\dot{\theta}_w \cos \Omega t \cos \theta_w \sin \varphi_w - \Omega \cos \Omega t \cos \varphi_w - \Omega \sin \Omega t \sin \theta_w \sin \varphi_w \\
& \qquad +\dot{\varphi}_w \cos \Omega t \cos \varphi_w \sin \theta_w + \dot{\varphi}_w \sin \Omega t \sin \varphi_w\Big) \rightarrow \text{(v)} \\
& +2\dot{\varphi}_w\left(m_s r_s^2 \dot{\theta}_w \cos \Omega t \cos \theta_w \sin \Omega t - m_s r_s^2 \sin \theta_w - \Omega \sin \theta_w I_z\right) \rightarrow \text{(vi)} \\
& -4r_d \dot{\theta}_w \sin \Omega t\left(m_d h \Omega - m_d \dot{\varphi}_w r_d \cos \Omega t \cos \theta_w - m_d \dot{\varphi}_w h \sin \theta_w\right) \rightarrow \text{(vii)} \\
& -4r_d \dot{\varphi}_w \Omega\left(m_d r_d \sin \theta_w - m_d h \cos \Omega t \cos \theta_w\right) \rightarrow \text{(viii)} \\
& +m_s r_s \dot{z}_w\Big(-2\Omega \cos \varphi_w \sin \Omega t \sin \theta_w + 2\Omega \cos \Omega t \sin \varphi_w + 2\dot{\theta}_w \cos \Omega t \cos \theta_w \cos \varphi_w \\
& +2\dot{\varphi}_w \cos \varphi_w \sin \Omega t - 2\dot{\varphi}_w \cos \Omega t \sin \varphi_w \sin \varphi_w\Big)\Big] \rightarrow \text{(ix)}
\end{aligned}
$$

Similarly, each term in the above equation can be further simplified, details are shown as following:

- (*i*) term; since the magnitude of flywheel moment of inertia is much larger than that of the mass imbalances, it is simplified as: $\dot{\theta}_w^2 I_r$.

- (*ii*) term; similar to (*i*), since inertia terms dominate, it can be simplified as: $\dot{\varphi}_w^2\left(\cos^2 \theta_w I_r + \sin^2 \theta_w I_z\right)$. Also using the small angle assumption, it can be further simplified as: $\dot{\varphi}_w^2 I_r$.

- (*iii*) term; the magnitude of flywheel moment of inertia is much larger than that of mass imbalances, thus the term is simplified as: $\Omega^2 I_z$.

- (*iv*) term; since the flywheel angular speed dominates in the bracket, using the small angle assumption; it can be simplified as: $-2m_s r_s \dot{y}_w \Omega \sin \Omega t$.

- (*v*) term; since the flywheel angular speed dominates, using the small angle assumption and the second order rotation terms are ignored, thus: $-2m_s r_s \dot{x}_w \Omega \cos \Omega t$.

- (*vi*) term; since the flywheel angular speed dominates and the magnitude of flywheel moment of inertia is much larger than that of mass imbalances, also using the small angle assumption, it is simplified as: $-2\dot{\varphi}_w \Omega \theta_w I_z$.

- (*vii*) term; since the flywheel speed dominates, it is simplified as: $-4r_d m_d h \dot{\theta}_w \Omega \sin \Omega t$.

- (*viii*) term; since the flywheel angular speed is the common term, using the small angle assumption, it is simplified as: $-4r_d \dot{\varphi}_w \Omega \left(m_d r_d \theta_w - m_d h \cos \Omega t \right)$.

- (*ix*) term; it is simplified to be zero as for the statically mass imbalance case.

Finally, the kinetic energy of the fully mass imbalanced flywheel includes those of the statically mass imbalanced and dynamically mass imbalanced cases, it is:

$$
\begin{aligned}
T_{w+m_s+m_d} \approx\; & M_w \left(\dot{x}_w^2 + \dot{y}_w^2 + \dot{z}_w^2 \right) + \dot{\theta}_w^2 I_r + \dot{\varphi}_w^2 I_r + \Omega^2 I_z - 2m_s r_s \dot{y}_w \Omega \sin \Omega t - 2m_s r_s \dot{x}_w \Omega \cos \Omega t \\
& -2\dot{\varphi}_w \Omega \theta_w I_z - 4r_d m_d h \dot{\theta}_w \Omega \sin \Omega t - 4r_d \dot{\varphi}_w \Omega \left(m_d r_d \theta_w - m_d h \cos \Omega t \right)
\end{aligned}
$$

Appendix C Hard-mounted Microvibration Measurement Platform

C1 Introduction

In this section, a microvibration measurement platform is designed to measure WA-induced microvibrations in the hard-mounted boundary condition. The platform is shown in Figure C- 1 a).

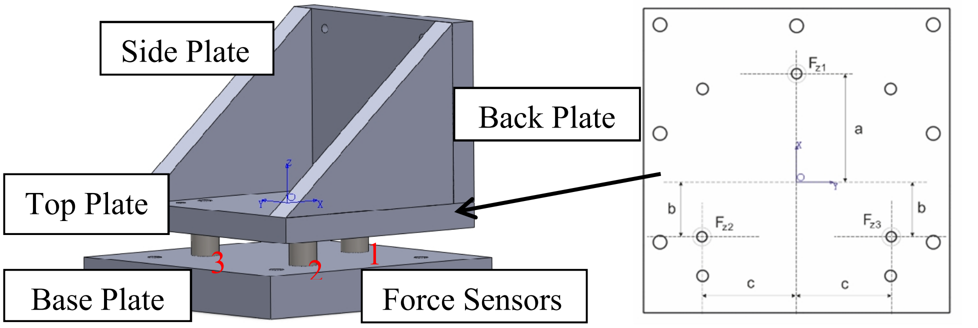

a) Platform model b) Top plate (bottom view)

Figure C- 1 WA hard-mounted microvibration measurement platform

The platform utilizes three unidirectional force sensors: one PCB 208C01 force sensor at position 1 and two PCB 208C02 force sensors at position 2 and 3 respectively. They are installed between the top and base plates, see Figure C- 1 b). The three forces sensors form an equilateral triangle shape. If the platform coordinate system is defined at the triangle geometric center, *O*, the three force sensors measure forces in the positive *z*-axis. The resulting forces and moments at *O* can be calculated from the three force sensor measurements as:

$$F_z\big|_p = F_{z1} + F_{z2} + F_{z3} \tag{C1-1}$$

$$M_y\big|_p = -F_{z1}a + \left(F_{z2} + F_{z3}\right)b \tag{C1-2}$$

$$M_x\big|_p = -F_{z2}c + F_{z3}c \tag{C1-3}$$

$$M_z\big|_p = \left(F_{x2} - F_{x3}\right)c + F_{y1}a - \left(F_{y2} + F_{y3}\right)b \tag{C1-4}$$

where $a = 50$ mm, $b = 25$ mm, $c = 43.3$ mm; subscript ‘p’ indicates the “platform” local coordinates. Note that Eq. (C1-1) is also used to calculate F_x and F_y but requires the WA to be installed in orthogonal w.r.t the platform.

Therefore, the WA-induced microvibration forces and moments in all six DoFs can be measured using this platform.

C2 Platform Dynamics Calibration

In the platform dynamics calibration process, one of the tests was to verify if there were undesired motions of force sensors during the microvibration measurements. In this test, one accelerometer (Endevco 256-100) was attached near each force sensor. Another test was to verify Eqs. (C1-1) to (C1-4), as they were used to calculate microvibration forces and moments induced by the WA. Three verification test setups were designed, see Figure C- 2. The force test was to verify F_z or Eq. (C1-1), and the two moment tests were to verify M_y or Eq. (C1-2) and M_x or Eq. (C1-3). The other forces and moments, i.e. F_x, F_y and M_z were verified indirectly from these verifications.

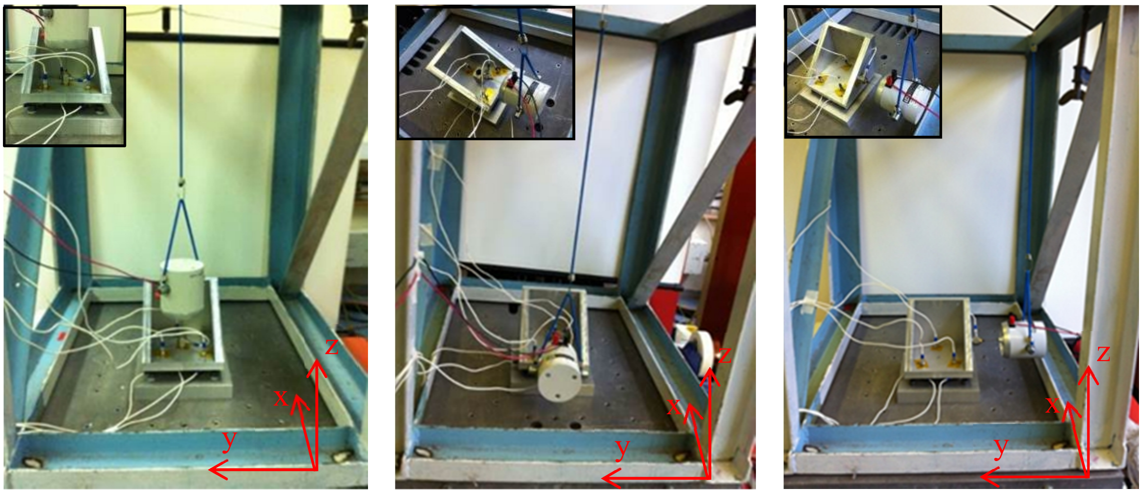

a) F_z verification test b) M_y verification test c) M_x verification test

Figure C- 2 Microvibration measurement platform dynamics calibration tests

In all tests, a LDS V201 shaker was suspended “free-free” using flexible bungee cords from a ground-fixed steal frame. The shaker generated input forces and/or moments to the platform. A unidirectional force sensor (PCB 208C03) was attached between the shaker stinger and the platform to measure the input forces. Constant sinusoidal forces at three input levels: 0.5 N, 1 N and 1.5 N (all sampled at 100 Hz) were applied respectively and the response accelerations and forces were measured. Note that in practice these input forces were the typical WA-induced microvibrations.

- For F_z verification test, the input forces were applied directly at O in negative z-axis, see Figure C- 2 a).

- For M_y verification test, a small stainless steel cube was placed at O, the shaker was attached to the cube along the positive x-axis thus producing the positive M_y, see Figure C- 2 b).

- For M_x verification test, the shaker was attached on right side plate of the platform along positive y-axis thus producing a negative M_x, see Figure C- 2 c).

Moment arms between the input forces and force sensors were 0.05 m (including force sensor dimension and top plate thickness), the corresponding theoretical moments were therefore 0.025 Nm, 0.05 Nm and 0.075 Nm respectively for the three input forces. All response signals were measured with a sampling frequency of 2048 Hz and a block size of 2048. This gives the frequency resolution as 1 Hz. 5 s data were acquired for each test.

C3 Results and Discussions

As an example, Figure C- 3 presents the background noise (i.e. the platform in static condition) compared to the response accelerations during shaker excitations (i.e. the platform in working condition) from the F_z verification test.

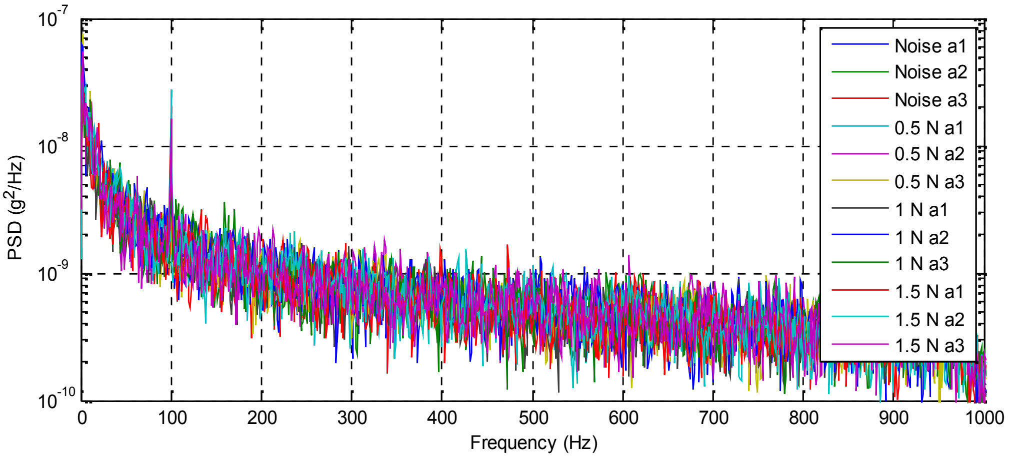

Figure C- 3 Response accelerations and background noise of F_z verification test

RMS values were also calculated for each curve, results are listed in Table C- 1.

Accelerometer No.	**Noise Level (RMS/g)**	**0.5 N Input (RMS/g)**	**1 N Input (RMS/g)**	**1.5 N Input (RMS/g)**	**Comparison (Largest)**
1	0.00103	0.00103	*0.00100*	0.00103	3%
2	0.00105	0.00109	*0.00110*	0.00109	5%
3	0.00102	*0.00106*	0.00105	0.00105	4%

Table C- 1 Total RMS values of accelerations and background noise of F_z verification test

From Table C- 1, RMS values of all accelerations were very close to each other and also to that of the background noise, regardless accelerometers or input force level. The largest difference (or error) between acceleration signals and the background noise was about 5%. These errors were mainly from the small input forces being detected by accelerometers during vibrations, e.g. peaks at 100 Hz in Figure C- 3. These errors could not be completely avoided in practice, but their amplitudes were very small thus had no significant influences to the measured signals. The two moment verification tests have shown similar results. Therefore the three force sensors were considered fixed during microvibration measurements, i.e. the measured microvibrations were not contaminated from this point of view.

Figure C-4 presents the 1.5 N input force and the three response forces from F_z verification test. Force signals are plotted for the first 0.05 s and 0-P amplitudes of all force signals are given in Table C- 2.

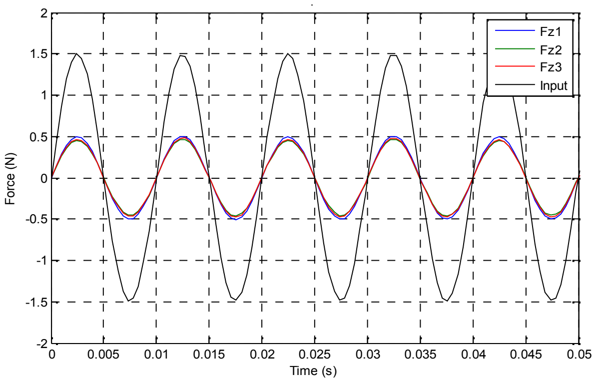

Figure C- 4 Input forces and response forces from F_z verification test (1.5 N input case)

Force Channels	**Values**
Input	1.5 N
F_{z1}	0.50 N
F_{z2}	0.49 N
F_{z3}	0.49 N

Table C- 2 0-P amplitudes of the input and response forces from F_z verification test (1.5 N input case)

In Table C- 2, the sum of the three response forces is 1.48 N which was about 1.3% different from the input force of 1.5 N. For the other two input forces (0.5 N and 1 N), the differences are about 1% and 1.1% respectively. These differences were due to the small offsets of force sensors being installed slightly away from their defined positions in theory. Thus they are considered as experimental errors and Eq. (C1-1) is verified.

Figure C- 5 a) and b) present the results of M_y and M_x verification tests of the 1.5 N input case.

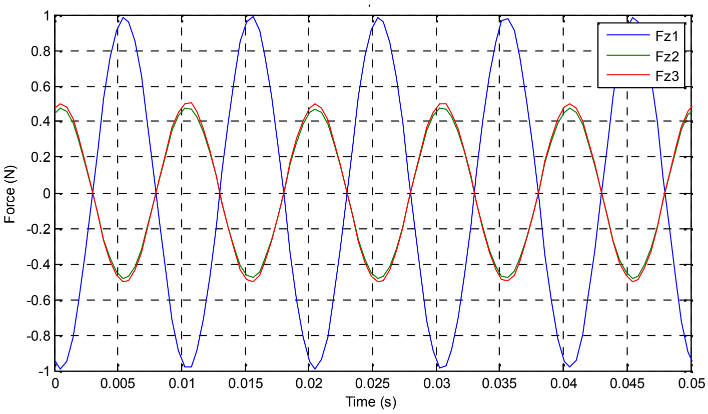

a) M_y

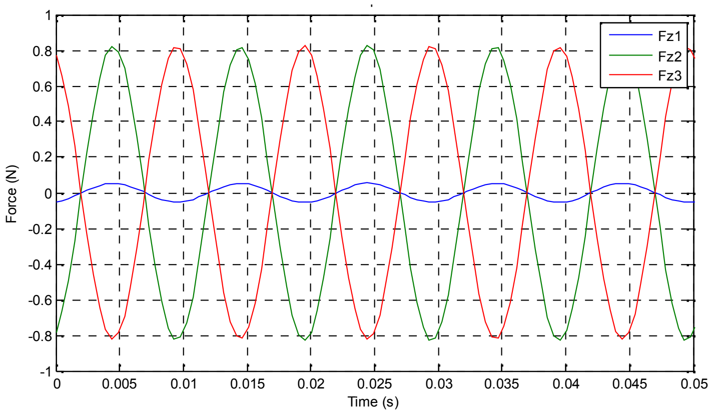

b) M_x

Figure C- 5 Input and responses of verification test (1.5 N input)

M_y and M_x were calculated using Eqs. (C1-2) and (C1-3) respectively and compared to the input moments. For M_y test, errors are about 0.8%, 0.9% and 1% for the three input forces 0.5 N, 1 N and 1.5 N respectively. For M_x test, errors are about 0.3%, 1% and 0.8%. Note that in Figure C- 5 b), small responses in F_{z1} are detected (which in theory should be zero). They were mainly due to small offsets of force sensor 1 being installed slightly distant from its defined position in theory along x-axis, thus very small responses were detected. F_{z1} responses were included in the above error calculations and clearly shown no significant influences to the results, thus Eqs. (C1-2) and (C1-3) were also verified.

In addition, the FE model of the platform was created for the normal and x_w-axis oriented test setups. In each model, the WA was modeled as a point mass at its CoM and rigidly connected to the platform model. Modal analyses were performed in MSC NASTRAN. Frequencies of the first mode were 930 Hz and 913 Hz for the normal and x-orientated setup respectively. These frequencies were distant from the coarse frequency band of interest (from several Hz to 500 Hz) and the fine frequency band of interest (from several Hz to 200 Hz) in this study. Thus the platform would not influence the measured microvibrations from this view point.

Appendix D WA Suspension System Stiffness and Damping Value Estimation

In this appendix, the estimations of WA suspension system stiffness (k_t, k_z and k_r) and damping values (c_t, c_z and c_r) are introduced. Estimations were carried out using both experimental and analytical methods. Experimentally, grounded sine-sweep tests were performed to the WA. In the test, in order to investigate the nonlinearity that was observed in the WA microvibration test results, sine-sweep tests were performed with high and low level inputs respectively. Analytically, a WA FE model was first created using solid elements, i.e. a full WA FE model. Modal analyses were performed and natural frequencies of the suspension system in all six DoFs were obtained. Next, a simplified WA FE model was created using shell elements. Frequency response analyses were performed to extract the suspension system damping values, along with the high and low level input sine-sweep test results.

D1 Wheel Assembly Sine-sweep Tests

Grounded sine-sweep tests were performed to estimate the suspension system stiffness and damping values. Low level input sine-sweep tests were performed first. Due to the low level inputs, nonlinearity in the WA did not appear, and the test results could be used to estimate the stiffness and damping values of the suspension system in linear condition. Next, high level input sine-sweep tests were performed. In this case, nonlinearity became apparent and stiffness and damping values of the suspension system in nonlinear condition were obtained. In addition, sine-sweep tests were performed in forward and backward directions for each input case to investigate the nonlinearity.

Both high and low level input sine-sweep tests were performed in WA radial DoF (or horizontal in x-axis) and axial DoF (or vertical in z-axis); see Figure D- 1 for the test setups. The WA was fixed on a shaker and the input accelerations were applied. Note that an aluminum cube was used as the adaptor in the test. The cube shown no influences to the test results in the frequency band interested (5 to 100 Hz in this case).

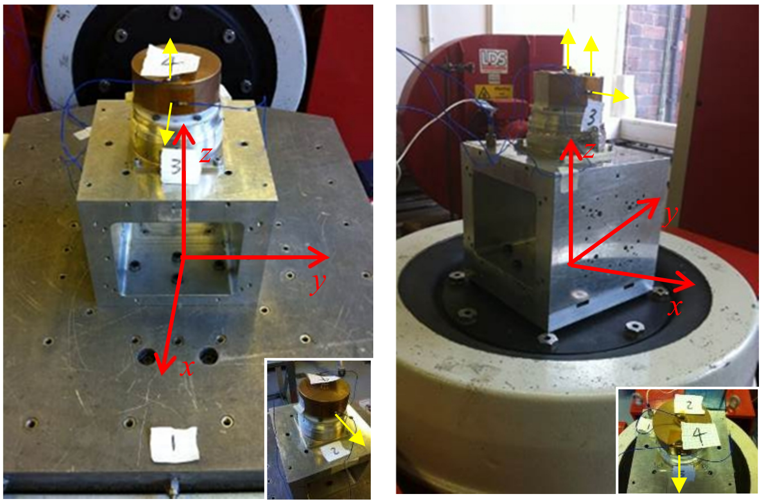

a) Radial DoF b) Axial DoF

Figure D- 1 WA grounded sine-sweep tests

Note that the freely rotating flywheel must be constrained during sine-sweep tests, meanwhile the setup has to maintain the suspension system properties in order to reveal WA structural modes from the test results. The flywheel was thus externally taped (see Figure D- 1 a) for detail). In this way, certain flexibilities in tapes were allowed and the flywheel was able to excite the WA structural modes but did not rotate.

Three accelerometers (no. 2, 3 and 4) were attached on the “non-spinning” flywheel; see Figure D- 1 a) and b). Another accelerometer (no. 1) was used as control signals in both cases. In radial DoF tests, two accelerometers no. 2 and 3 were attached on the flywheel peripheral surface in *x*-axis and opposite to each other. Both accelerations were used to measure the radial translational mode. Accelerometer no. 4 was attached on the flywheel top surface near its edge in positive *z*-axis. It was primarily used to measure the “rocking” mode. In axial DoF tests, accelerometer no. 2 was attached in positive *z*-axis to measure the axial translational mode.

D1.1 Low Level Input Sine-sweep Test Results

During the low level input sine-sweep tests it was found that the lowest possible acceleration inputs were 0.008 g and 0.015 g in WA radial and axial DoFs respectively in order to retain the suspension system behaves linear. Test results in radial and axial DoFs are presented in Figure D- 2 a) and b) respectively.

Firstly, control signals in both cases follow the defined profiles very well indicating both tests were successfully performed. Forward and backward sine-sweep test results are almost identical between each other in the frequency band in each case, indicating nonlinearity is not raised. Note also that all major spikes are sharp, indicating suspension system shows low damping characteristic.

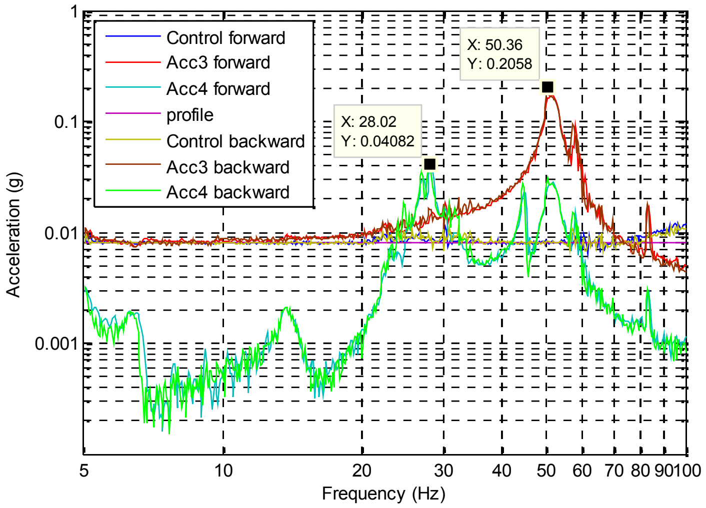

a) Radial DoF (0.008 g input)

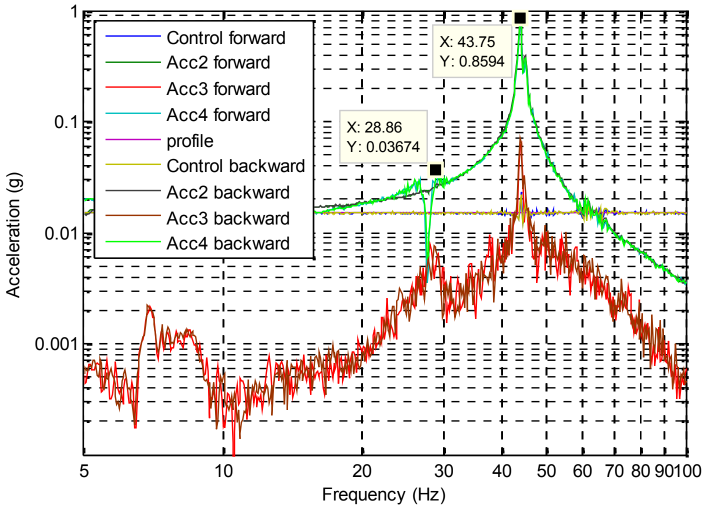

b) Axial DoF (0.015 g input)

Figure D- 2 Low level input sine-sweep test results

WA natural frequencies of structural modes identified from low level input sine-sweep tests are listed in Table D- 1.

Natural Frequency (Test)	
f_t	50.4 Hz
f_r	28.9 Hz
f_z	43.8 Hz

Table D- 1 WA natural frequencies (low level input sine-sweep tests)

D1.2 High Level Input Sine-sweep Test Results

High level input sine-sweep tests were performed in order to raise nonlinearity in the WA. The input forces used were 0.25 g and 0.1 g in WA radial and axial DoFs respectively. Results are presented in Figure D- 3.

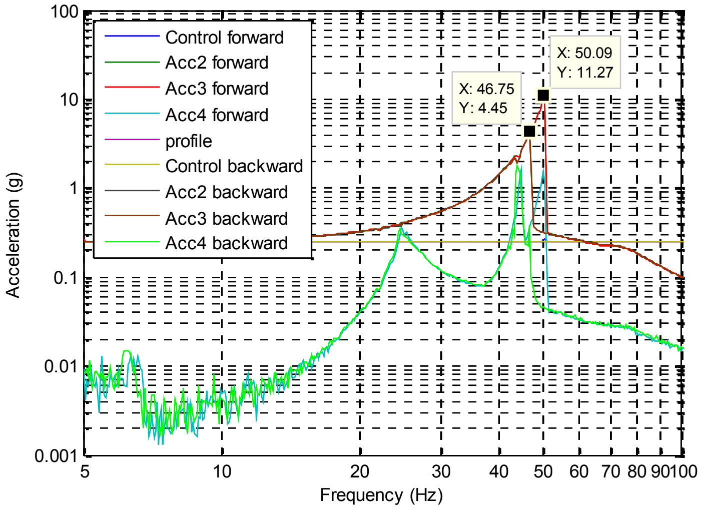

a) Radial DoF (0.25 g input)

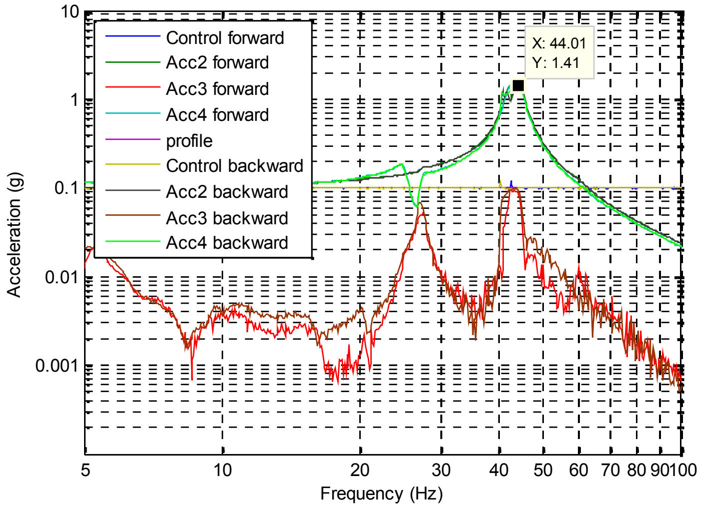

b) Axial DoF (0.1 g input)

Figure D- 3 High level input sine-sweep test results

Nonlinearity is clearly presented in each case in Figure D- 3. For example, the response accelerations in Figure D- 3 a) have shown the typical nonlinear dynamic characteristics, e.g. a sudden response decline after 50 Hz. Furthermore, forward and backward sine-sweep test results are not matched at some resonances in frequencies and amplitudes in the figure. For example, the frequency of the WA radial translational mode at 50 Hz that appeared in the forward test shifts to 47 Hz in the backward test; the peak amplitudes are reduced.

If comparing the sine-sweep test results to the microvibration test results presented in Chapter 4, nonlinearity in the microvibration tests starts at about 38 Hz (or 2280 rpm), which is lower than the sine-sweep test results shown above (47 to 50 Hz). This is primarily due to the different WA test conditions, in one case the WA spins and reaction loads are measured but in the other case, it is at static and sine-sweep tests are performed. In WA axial DoF in Figure D- 3 b), nonlinearity is not as influential as that in radial DoFs. Forward and backward test results have matched well for all accelerometers.

The strong nonlinearity observed in high level input sine-sweep test results makes it difficult to estimate the natural frequencies of the suspension system in this condition, especially in radial DoFs. Due to this reason, the results obtained from low level input sine-sweep tests (shown in Table D- 1) are used as the experimental natural frequencies of the WA suspension system. The results obtained from high level input sine-sweep tests on the other hand, are used for damping value extractions in nonlinear condition. They are discussed in detail in Section D3.

D2 Wheel Assembly FE Model (Solid Elements)

After some simplifications, the WA model includes four main parts: WA base, suspension system, motor and flywheel. They are made from aluminum, Delrin, steel and brass respectively. Note that the motor is first assumed as steel, its density in the model is then tuned so that its model mass is the same as its physical mass. The WA base and suspension system together are considered as the stator, while motor and flywheel are considered as the rotor. Each component was modeled using solid element. WA FE model was created in FEMAP (see Figure D- 4 a) for detail). Note that the web-spring has been partitioned from the suspension system and it is modeled with a finer mesh (see Figure D- 4 b) for detail).

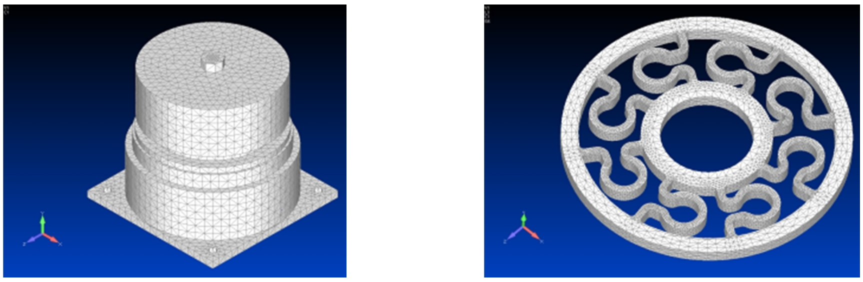

a) The complete model b) The web-spring model

Figure D- 4 WA FE model (solid elements)

Modal analysis was performed to the FE model in MSC NASTRAN. The WA base interface was fixed to simulate the hard-mounted boundary condition as in the sine-sweep tests. Figure D- 5 shows the three major mode shapes: the WA "rocking" mode, radial and axial translational mode respectively.

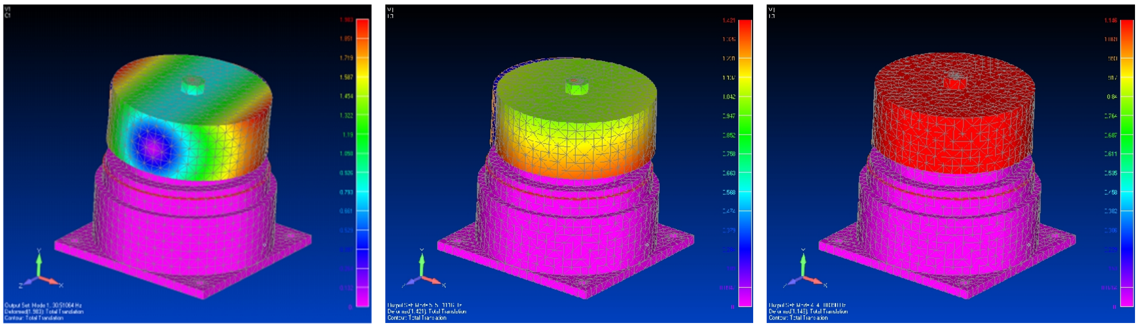

a) "Rocking" mode b) Radial translational mode c) Axial translational mode

Figure D- 5 Mode shapes of the WA

Frequencies calculated from the modal analysis are listed in Table D- 2.

Natural Frequency (FE Model)	
f_t	50 Hz
f_r	30 Hz
f_z	46 Hz

Table D- 2 WA suspension system natural frequencies (FE results)

The analytical results of the WA suspension system stiffness, k_t, k_z and k_r, were calculated using Eqs. (D2-1) to (D2-3). The rotor mass, m_w, is 0.75 kg (including flywheel and motor). Rotor radial moment of inertia about the suspension system CoM, I_r, is about 5.1×10^{-4} kgm^2.

$$k_t = \left(2\pi f_t\right)^2 m_w \tag{D2-1}$$

$$k_z = \left(2\pi f_z\right)^2 m_w \tag{D2-2}$$

$$k_r = \left(2\pi f_r\right)^2 I_r \tag{D2-3}$$

By comparing to the WA microvibration test results and Table D- 1, the final WA natural frequencies are determined and their corresponding stiffness are calculated. They are listed in Table D- 3. These values are used as the model parameters in the WA microvibration model development.

Natural Frequency		**Stiffness**	
f_t	50 Hz	k_t	6.9×10^4 N/m
f_r	27 Hz	k_r	15 Nm/rad
f_z	44 Hz	k_z	5.8×10^4 N/m

Table D- 3 WA stiffness for microvibration modeling

D3 Wheel Assembly FE Model (Shell Elements)

WA FE model was also created using shell elements (i.e. the simplified WA FE model). This model was created for damping values extraction purpose and later also used for WA driving point accelerance study. The simplified WA FE model is shown in Figure D- 6 a). The WA suspension system was modeled using a CBUSH element (which has a six DoF stiffness and damping property). It is high-lighted as the red point in Figure D-6 b). The six stiffness values were taken from Table D- 3. Frequency response analyses were performed to the simplified WA FE model in MSC NASTRAN. The results output nodes were chosen to be the accelerometer positions in the corresponding sine-sweep tests (see Figure D- 1 for detail).

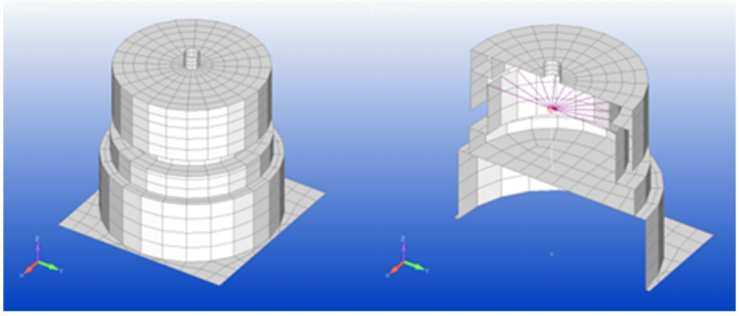

a) Full model b) Cross-section

Figure D- 6 WA simplified FE model

Damping values were tuned with low and high level input sine-sweep test results respectively. In damping value extractions, only damping values in WA radial and axial translational DoFs (i.e. c_t and c_z) were extracted. Note that the total damping of the "rocking" mode, c_R, was assumed to be same as c_t. The damping value of the torsional spring, c_r, was directly related to c_R from the following equations.

$$\varsigma_R = d^2\varsigma_t + \varsigma_r \tag{D3-1}$$

$$c_R = d^2 c_t + c_r \tag{D3-2}$$

where d is the distance from rotor CoM to suspension system, it is 0.008 m. Note that $\varsigma_R \approx \varsigma_r$ if ς_t is small. The final curve-fittings between the FE model and test results are shown in Figure D- 7; damping ratios are also given.

From Figure D- 7, curves of FE model and test results have matched very well in most cases. In Figure D- 7 c) however, since nonlinearity has been raised in WA radial DoFs, forward and backward test results are very different in frequencies and amplitudes at the resonances. Thus an exact estimation of the damping value was not possible. In our case, damping value in high level input sine-sweep tests was first estimated from the value obtained in WA axial translational DoF, i.e. Figure D- 7 d). It was then assumed that the damping value in WA radial DoF was the same (this can be proved from Figure D- 7 a) and b) of low level input sine-sweep tests). Therefore the curve produced in Figure D- 7 c) was a compromise between the forward and backward test results.

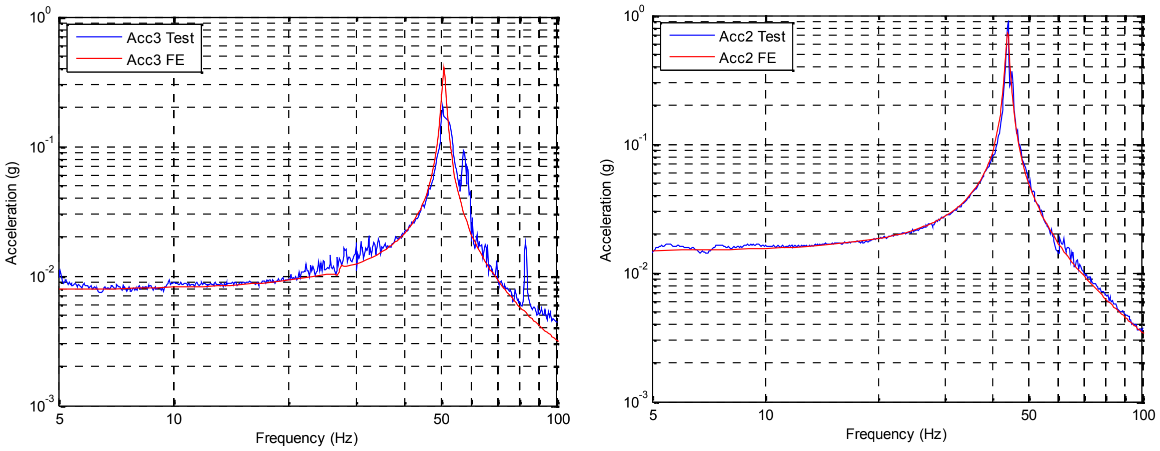

a) Low level input sine-sweep: radial DoFs ($\varsigma_t = 0.02$)

b) Low level input sine-sweep: axial translational DoF ($\varsigma_z = 0.02$)

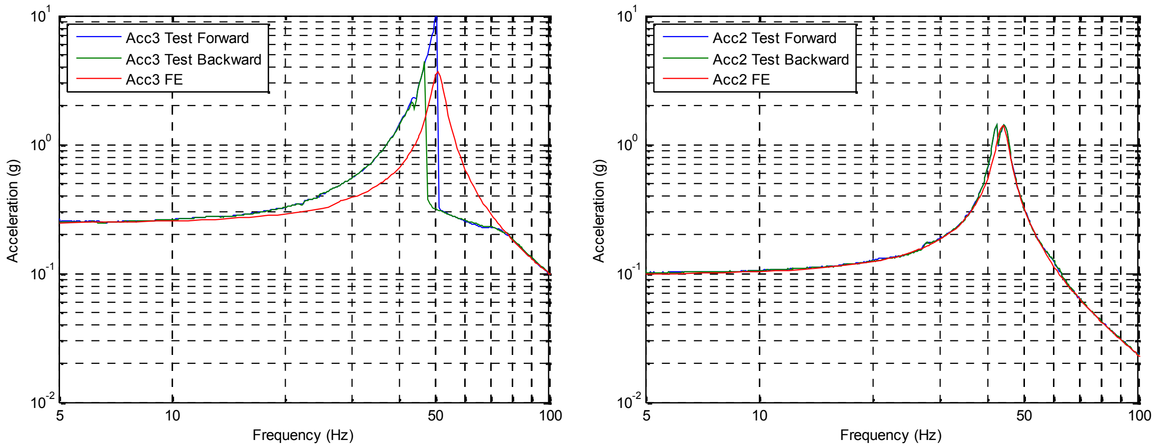

c) High level input sine-sweep: radial DoFs ($\varsigma_t = 0.15$)

d) High level input sine-sweep: axial translational DoF ($\varsigma_z = 0.15$)

Figure D- 7 WA suspension system damping value extractions

Damping values were calculated using the following equations:

$$c_t = 2\varsigma_t \sqrt{k_t m_w} \tag{D3-3}$$

$$c_z = 2\varsigma_z \sqrt{k_z m_w} \tag{D3-4}$$

$$c_r = 2\varsigma_r \sqrt{k_r I_r} \tag{D3-5}$$

In practice, WA microvibration test results have shown that the dynamics in WA axial translational DoF was mostly linear, however that in WA radial DoFs are highly nonlinear. It was therefore decided to use the damping values obtained from low input level sine-sweep tests for WA axial translational DoF microvibrations modeling, while damping values obtained from high level input sine-sweep test for WA radial DoF microvibration modeling. They are discussed in the thesis.

The final damping ratios and damping values for WA microvibration modeling are listed in Table D- 4.

Damping Ratio		**Damping Value**	
ζ_t	0.15	c_t	68.2 kg/s
ζ_z	0.02	c_z	8.3 kg/s
ζ_r	0.15	c_r	0.026 kg m^2/s/rad

Table D- 4 WA damping values for microvibration modeling

Appendix E Signal Processing Techniques

E1 Data Processing

Generally, the microvibration measurements normally involves large amounts of data, thus specific attention has to be given to automation of the entire signal acquisition, management and analysis.

Regarding the basic structure of relevant vibration signatures and the corresponding signal treatment, the following classification is recommended particularly for satellite/mechanism microvibration analysis.

- **Stationary (or quasi-stationary) signals**; including special cases like cyclostationary signals (e.g. generated by WA, cryocooler, rotating or translating device-generated microvibrations, continuously operating scanners, etc.). The signal statistics remain constant, or they are only slowly varying over time. Stationary signals are typically analyzed in the frequency domain.

- **Non-stationary signals**; including transient signals (e.g. generated by waveguide switches, valves, piezoelectric thruster, thermal snap, etc.). The signal statistics may change rapidly, and computing a spectral density for a transient signal is not mathematically correct since the pulsing sequence is neither random (ergodic) nor periodic in nature, thus non-stationary signals are typically analyzed in the time domain.

For stationary signals such as those generated by WAs, several analysis methods have been established and various parameters have been used, for instance:

- Time domain: signal statistics, e.g. variance, standard deviation and higher order central moments (skewness and kurtosis), histogram-based estimation of probability density functions, (auto-) correlation function, etc.

- Frequency domain: PSD and AS (also known as magnitude Fourier transformation), considering the effects of spectral averaging and window functions as well as higher order spectra (e.g. bispectrum, trispectrum and spectral maps), etc. RMS values and CRMS value plots are also commonly used.

- Further processing for automated feature extraction, e.g. identification and estimation of spectral and order peaks, dedicated filtering, etc.

For non-stationary signals, the scope of available analysis tools may be extended by:

- Time-frequency analysis, including Short-Time Fourier Transform, Spectrogram, Wigner-Ville Distribution, Continuous Wavelet Transform & Scalogram, etc.

The best approach of analyzing transient microvibration data is to use the spectrogram, which is a graph of time versus frequency where the FFT amplitude is represented by the color intensity. The spectrogram is more accurate than the spectral density plot for assessing the time varying spectral content of transient microvibrations.

- Further processing for automated feature extraction, e.g. order analysis, Campbell diagram, etc.

For WA-induced microvibrations, measurements are usually analyzed in the frequency domain. In particular, algorithms are written in this thesis to calculate the FFT, PSD, AS, RMS value and CRMS value of forces and moments. Singles are also analyzed in the time domain. All algorithms are compiled in MATLAB. Theories and equations implemented in the algorithms are introduced in the rest of this chapter.

E2 Energy in Signal

The energy in a signal can be determined by its RMS value, which is a useful metric in microvibration analysis. In general, there are three approaches to define the RMS value of a signal:

- Statistical approach (time and frequency domain).

- Energy approach (time and frequency domain).
- PSD approach (frequency domain).

In the time domain, the expected value of a continuous signal $x(t)$ is the same as the signal's mean value, $\mu_x(t)$:

$$\mu_x(t) = E\left[x(t)\right] \tag{E2-1}$$

The variance, $\sigma_x^2(t)$, of the signal is then:

$$\sigma_x^2(t) = E\left[\left\{x(t) - \mu_x(t)\right\}^2\right] \tag{E2-2}$$

The square root of Eq. (E2-2), i.e. $\sigma_x(t)$, is the standard derivation of the time signal. The mean square of the signal is the expected value of the square of the time signal and can be expressed in terms of the signal mean and variance through Eq. (E2-2) as:

$$r_x^2(t) = E\left[x(t)^2\right] = \sigma_x^2(t) + \mu_x^2(t) \tag{E2-3}$$

The square root of the mean square, $r_x(t)$, is referred as the RMS value of the time signal. It is easy to see from Eq. (E2-3) that for a zero-mean process, i.e. $\mu_x(t) = 0$, the RMS value simply equals to the square root of the variance. For simplicity, the assumption is made in this thesis that all stochastic microvibrations in this thesis are zero-mean, otherwise singles are corrected to have zero-mean.

The RMS value definition in Eq. (E2-3) is based on the statistical approach and regardless the domain in which they are analyzed. As long as the signal (in either time or frequency domain) has a finite number of data, its RMS value can be calculated. However, this approach of estimating RMS value is generally not used for estimating the energy in the signal. An alternative approach of calculating the area under the discretized (or digitized) signal curve is commonly used for calculating the energy in the signal. It is introduced as following.

In the time domain, the energy of a signal, E_t, can be defined as:

$$E_t = \int_{-\infty}^{\infty} x^2(t)dt \tag{E2-4}$$

and the power of discretized time domain signal, P_t, can be derived from as:

$$P_t = \frac{1}{N}\sum_{n=0}^{N-1} x^2(n) \tag{E2-5}$$

where $x(n)$ is the discretized time domain signal of $x(t)$; N is the total number of data in the signal; n is the data index. The power of discretized frequency domain signal can be written in a similar way, it gives:

$$P_f = \frac{1}{N^2}\sum_{k=0}^{N-1} |x(k)|^2 \tag{E2-6}$$

where $x(k)$ is the discretized frequency domain signal of $x(f)$; k is the data index; f is frequency in Hz.

According to Parseval's theorem, the power (and thus energy) of a signal in the time domain equals to the power of the same signal in the frequency domain. From Eqs. (E2-5) and (E2-6), it gives:

$$\frac{1}{N}\sum_{n=0}^{N-1} x^2(n) = \frac{1}{N^2}\sum_{k=0}^{N-1} |x(k)|^2 \tag{E2-7}$$

By definition, the RMS value of a signal in the time domain is the square root of the power of the signal, thus:

$$r_x(t) = \sqrt{\frac{1}{N}\sum_{n=0}^{N-1} x^2(n)} \tag{E2-8}$$

The same argument applies to the RMS value in the frequency domain, thus:

$$r_x(f) = \sqrt{\frac{1}{N^2}\sum_{k=0}^{N-1}|x(k)|^2} \qquad \text{(E2-9)}$$

This also means that the RMS values of the signal are the same in the time and frequency domain. This definition of the RMS value from the energy approach reveals its physical meaning. Therefore in the microvibration data processing, Eq. (E2-8) is usually used to present the energy of the signal in the time domain and Eq. (E2-9) to present the energy of the signal in the frequency domain. An equivalent definition of the RMS value is based on the PSD of the signal. In addition, the CRMS value plot can be produced from this approach. It is introduced in Section E6.

In general, the different RMS values introduced above can be applied in a typical microvibration data processing as following.

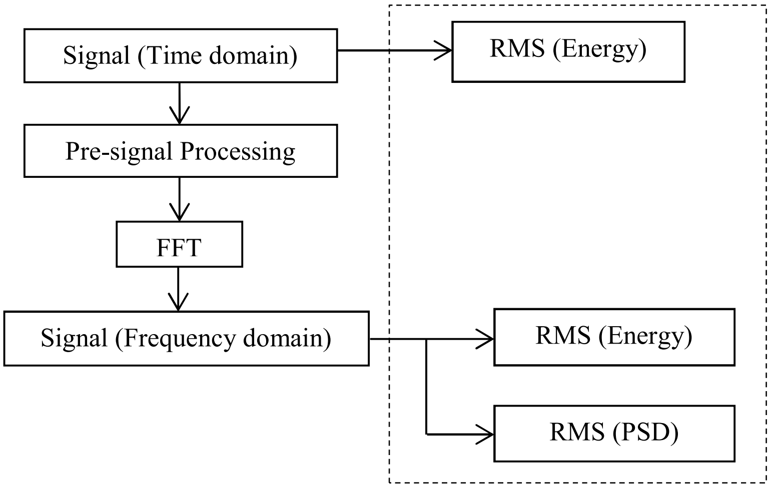

Figure E- 1 WA microvibration data processing process and RMS values

Eq. (E2-8) is commonly used to define the target RMS value of a signal, since it is based on the raw time domain data without any pre-signal processing. In the general signal processing process, the initially acquired time signals are usually transformed into the frequency domain using the Fourier transform (or FFT more precisely) and then can be calculated as PSDs, for example. The RMS values calculated from PSDs can be compared to those calculated in the time domain, and they should be similar for the same signal. In this manner, RMS values can be used to access the quality of the transformation process, including sampling size, window (size and type), overlapping and averaging, etc., which are commonly applied in this process.

E3 Fourier Transformation

Fourier transformation is used to transform the time signals into frequency domain. This process is performed by FFT function built in MATLAB. The FFT results can be used to calculate other functions such as AS, PSD, CSD, RMS value and CRMS value.

The forward Fourier transform of a time domain signal, $x(t)$, is defined as:

$$X(\omega) = \int_{-\infty}^{+\infty} x(t) e^{-i\omega t} dt \tag{E3-1}$$

where $X(\omega)$ is complex and $\omega = 2\pi f$.

A limitation of Eq. (E3-1) is that it integrates over infinite time, and does not hold for stationary signals since they are not completely integratable. Also in practice it is impossible to measure an infinitely-long signal $x(t)$. Instead, it is useful to define the finite Fourier transform of $x(t)$ over the interval $(0,T)$ as:

$$X(\omega,T) = \int_{0}^{T} x(t) e^{-i\omega t} dt \tag{E3-2}$$

where T is the length of the time of the signal.

E4 Amplitude Spectrum

A useful frequency domain representation of a stochastic process with FFT results is the AS of the signal. It provides an estimate of the signal amplitude as a function of frequency. It is defined in continuous form as:

$$A_x(f) = \frac{1}{T} \left| \int_{0}^{T} x(t) e^{-i2\pi f t} dt \right| \tag{E4-1}$$

The discretized form of Eq. (E4-1) can be expressed as:

$$A_x(f) = \frac{|x(k)|}{N} \tag{E4-2}$$

Unlike the Fourier transform, the AS is a real-valued function and gives a direct view of the amplitude distribution in a signal in the frequency domain. Note that due to two-side characteristics of FFT results, Eq. (E4-2) needs to be halved. Also in practice, a correction factor may be applied to the AS.

E5 Auto- and Cross-correlation Function

Generally, a signal can be characterized as either purely deterministic or stochastic (random). A deterministic signal is exactly predictable over the time period of interest. For example:

$$x(t) = A \cdot \sin(\omega t) \tag{E5-1}$$

where A is the amplitude (0-peak) of the signal, ω is the angular frequency.

A stochastic signal, on the other hand, is one that has some random elements associated with it. In addition, a stochastic signal can be further characterized as deterministic or non-deterministic. For example:

$$x(t) = A \cdot \sin(\omega t + \varphi) \tag{E5-2}$$

where φ is the random phase evenly distributed between 0 and 2π. This example is a deterministic stochastic process because it is deterministic in form but has a random element, φ. Pure white noise, on the other hand, is a non-deterministic stochastic process, since it is purely determined by chance and has no particular structure at all.

RWA-induced microvibrations are generally modeled as deterministic random processes similar to the example of Eq. (E5-2). Such a process can be characterized by its auto-correlation and cross-correlation functions. Both functions contain information about the frequency content of the process.

Auto-correlation function describes how well a signal is correlated with itself at two different times and is defined as:

$$R_x(t_1,t_2) = E\left[x(t_1)x(t_2)\right] \tag{E5-3}$$

and cross-correlation function measures the correlation between two different sign, it is defined as:

$$R_{xy}(t_1,t_2) = E\left[x(t_1)y(t_2)\right] \tag{E5-4}$$

A weakly stationary process is one whose mean and variance are time invariant and whose auto-correlation and cross-correlation functions depend only on the difference, τ, between t_1 and t_2, so that:

$$R_x(\tau) = R_x(t,t+\tau) = E\left[x(t)x(t+\tau)\right] \tag{E5-5}$$

and

$$R_{xy}(\tau) = R_{xy}(t,t+\tau) = E\left[x(t)y(t+\tau)\right] \tag{E5-6}$$

All signals presented in this thesis are considered weakly stationary, zero-mean microvibrations, so the auto-correlation and cross-correlation functions will be written as Eq. (E5-5) and (E5-6), the variance is considered to be constant.

E6 Power Spectrum Density

The PSD of a time signal is a frequency domain variable often employed in microvibration analysis. It has two equivalent definitions. The first one is based on the time history of the signal, defined as the Fourier transform of the signal’s auto-correlation function. For example, taking the Fourier transform of Eq. (E5-5), the PSD can be derived as:

$$S_x(f) = \int_{-\infty}^{+\infty} R_x(\tau) e^{-i2\pi f \tau} d\tau \qquad \text{(E6-1)}$$

Remembering that the RMS value of a signal in the frequency domain can be derived from the signal's PSD. Since the power in a signal is the area under the signal, the area under the discretized PSD curve gives the RMS value of the signal (the square root of the area). In general, the power in a signal in the frequency domain can be defined as:

$$P_f = \int_{-\infty}^{\infty} S_x(f) df \qquad \text{(E6-2)}$$

Applying the trapezium rule to Eq. (E6-2), its discretized form is obtained:

$$P_f \approx \sum_{k=0}^{N/2-1} S_x(k) \Delta f \qquad \text{(E6-3)}$$

On the other hand, according to the Parseval's theorem and also the two-side characteristics of PSD due to FFT, Eq. (E2-6) can be written as:

$$P_f = \frac{2}{N^2} \sum_{k=0}^{N/2-1} |x(k)|^2 \qquad \text{(E6-4)}$$

From Eqs. (E6-3) and (E6-4), it gives:

$$\sum_{k=0}^{N/2-1} S_x(k) \Delta f = \frac{2}{N^2} \sum_{k=0}^{N/2-1} |x(k)|^2 \qquad \text{(E6-5)}$$

The PSD of a time signal in discretized form is thus obtained as:

$$S_x(k) = \frac{2}{N^2 \Delta f} |x(k)|^2 \qquad \text{(E6-6)}$$

For any stationary, zero-mean signal, the RMS value can be computed as the square root of the area under the PSD curve. Therefore from Eq. (E6-6), an alternative definition of the RMS value can be obtained as:

$$r_x(f) = \sqrt{\sum_{k=0}^{N/2-1} S_x(k)\Delta f} \qquad \text{(E6-7)}$$

In practice, Eqs. (E6-6) and (E6-7) can be programmed as they are in discretized form. In this thesis they are used for estimating PSD and RMS values of signals in the frequency domain.

A useful extension of this result is the CRMS value function. It is defined in continuous form as:

$$r_{cx}(f_0) = \sqrt{2\int_{f_{\min}}^{+f_0} S_x(f)df} \qquad \text{(E6-8)}$$

where $f_0 \in [f_{\min}, f_{\max}]$ and $f_{\min}$ and $f_{\max}$ are the upper and lower limits of the frequency band considered. In practice, the CRMS value function of a signal can be calculated using the build-in function in MATLAB. In such case, the PSD of the signal is first divided into smaller segments. RMS values of these segments are calculated by integrating over the frequency band of each segment respectively and the cumulative sum is computed for all segments.

The CRMS value function represents a cumulative contribution of the total RMS value in a signal as a function of frequency. Usually, the CRMS value function is plotted with the corresponding PSD of the signal. Any value change in the CRMS value plot represents a determined amount of energy contributed to the signal. Thus CRMS value plot is a useful tool in this study because it allows one to visualize the variation of vibrational modes and responses in terms of energy. It can also be used to identify these changes w.r.t. frequency, such as for identifying spikes in a signal in broadband excitation modeling.

E7 Sampling Techniques

The fidelity of all frequency domain metrics introduced so far are dependent on the quality of data acquisition in the time domain. One of the key rules in this matter is that the digital sampling frequency must be greater than at least twice the frequency band interested, known as the Nyquist frequency, f_{nq}, in order to avoid aliasing of the data. The sampling frequency, f_s, should be 2.56 times greater than Nyquist frequency in addition to compensate the roll-off effect of the anti-aliasing filter.

$$f_s = 2.56 f_{nq} \tag{E7-1}$$

For example, if the desired frequency bandwidth is [0, 400] Hz, then the recommended sampling frequency is 1024 Hz.

Other parameters involve in a signal sampling process include time length T, number of sampling points, N, frequency resolution, Δf, and time resolution, Δt. They are also related to one another, their relationships are listed in Table E- 1.

Sampling Parameters	**Relationship**
Sampling frequency	$f_s = \frac{1}{\Delta t} = \frac{N}{T}$
Frequency resolution	$\Delta f = \frac{f_s}{N} = \frac{1}{T}$
Time length	$T = N\Delta t = \frac{N}{f_s}$
Time resolution	$\Delta t = \frac{T}{N} = \frac{1}{f_s}$

Table E- 1 Relationships of signal sampling parameters

Appendix F Matrices of Coupled System

F1 Wheel Assembly-Seismic Mass Coupled System

$$
\boldsymbol{M}_s = \begin{bmatrix}
M_w & 0 & 0 & 0 & 0 & 0 & 0 & 0 & 0 & 0 \\
0 & M_w & 0 & 0 & 0 & 0 & 0 & 0 & 0 & 0 \\
0 & 0 & M_w & 0 & 0 & 0 & 0 & 0 & 0 & 0 \\
0 & 0 & 0 & I_r & 0 & 0 & 0 & 0 & 0 & 0 \\
0 & 0 & 0 & 0 & I_r & 0 & 0 & 0 & 0 & 0 \\
0 & 0 & 0 & 0 & 0 & M_c & 0 & 0 & 0 & 0 \\
0 & 0 & 0 & 0 & 0 & 0 & M_c & 0 & 0 & 0 \\
0 & 0 & 0 & 0 & 0 & 0 & 0 & M_c & 0 & 0 \\
0 & 0 & 0 & 0 & 0 & 0 & 0 & 0 & I_{c\_xx} & 0 \\
0 & 0 & 0 & 0 & 0 & 0 & 0 & 0 & 0 & I_{c\_yy}
\end{bmatrix}
$$

$$
\boldsymbol{G}_s = \begin{bmatrix}
0 & 0 & 0 & 0 & 0 & 0 & 0 & 0 & 0 & 0 \\
0 & 0 & 0 & 0 & 0 & 0 & 0 & 0 & 0 & 0 \\
0 & 0 & 0 & 0 & 0 & 0 & 0 & 0 & 0 & 0 \\
0 & 0 & 0 & 0 & \Omega I_z & 0 & 0 & 0 & 0 & 0 \\
0 & 0 & 0 & -\Omega I_z & 0 & 0 & 0 & 0 & 0 & 0 \\
0 & 0 & 0 & 0 & 0 & 0 & 0 & 0 & 0 & 0 \\
0 & 0 & 0 & 0 & 0 & 0 & 0 & 0 & 0 & 0 \\
0 & 0 & 0 & 0 & 0 & 0 & 0 & 0 & 0 & 0 \\
0 & 0 & 0 & 0 & 0 & 0 & 0 & 0 & 0 & 0 \\
0 & 0 & 0 & 0 & 0 & 0 & 0 & 0 & 0 & 0
\end{bmatrix}
$$

$$
\boldsymbol{C}_s \approx \begin{bmatrix}
c_t & 0 & 0 & 0 & -dc_t & -c_t & 0 & 0 & 0 & -lc_t \\
0 & c_t & 0 & dc_t & 0 & 0 & -c_t & 0 & lc_t & 0 \\
0 & 0 & c_z & 0 & 0 & 0 & 0 & -c_z & 0 & 0 \\
0 & dc_t & 0 & d^2c_t + c_r & 0 & 0 & -dc_t & 0 & ldc_t - c_r & 0 \\
-dc_t & 0 & 0 & 0 & d^2c_t + c_r & dc_t & 0 & 0 & 0 & ldc_t - c_r \\
-c_t & 0 & 0 & 0 & dc_t & c_t & 0 & 0 & 0 & lc_t \\
0 & -c_t & 0 & -dc_t & 0 & 0 & c_t & 0 & -lc_t & 0 \\
0 & 0 & -c_z & 0 & 0 & 0 & 0 & c_z & 0 & 0 \\
0 & lc_t & 0 & ldc_t - c_r & 0 & 0 & -lc_t & 0 & l^2c_t + c_r & 0 \\
-lc_t & 0 & 0 & 0 & ldc_t - c_r & lc_t & 0 & 0 & 0 & l^2c_t + c_r
\end{bmatrix}
$$

$$\boldsymbol{K}_s \approx \begin{bmatrix} k_t & 0 & 0 & 0 & -dk_t & -k_t & 0 & 0 & 0 & -lk_t \\ 0 & k_t & 0 & dk_t & 0 & 0 & -k_t & 0 & lk_t & 0 \\ 0 & 0 & k_z & 0 & 0 & 0 & 0 & -k_z & 0 & 0 \\ 0 & dk_t & 0 & d^2k_t + k_r & 0 & 0 & -dk_t & 0 & ldk_t - k_r & 0 \\ -dk_t & 0 & 0 & 0 & d^2k_t + k_r & dk_t & 0 & 0 & 0 & dlk_t - k_r \\ -k_t & 0 & 0 & 0 & dk_t & k_t & 0 & 0 & 0 & lk_t \\ 0 & -k_t & 0 & -dk_t & 0 & 0 & k_t & 0 & -lk_t & 0 \\ 0 & 0 & -k_z & 0 & 0 & 0 & 0 & k_z & 0 & 0 \\ 0 & lk_t & 0 & ldk_t - k_r & 0 & 0 & -lk_t & 0 & l^2k_t + k_r & 0 \\ -lk_t & 0 & 0 & 0 & ldk_t - k_r & lk_t & 0 & 0 & 0 & l^2k_t + k_r \end{bmatrix}$$

$$\boldsymbol{F}_s = \begin{Bmatrix} -\sum_{i=1}^{n_{rt}} C_i^{rt}\Omega^2 \sin\left(h_i^{rt}\Omega t\right) + W_x(\Omega) \\ \sum_{i=1}^{n_{rt}} C_i^{rt}\Omega^2 \cos\left(h_i^{rt}\Omega t\right) + W_y(\Omega) \\ \sum_{i=1}^{n_{at}} C_i^{at}\Omega^2 \sin\left(h_i^{at}\Omega t\right) + W_z(\Omega) \\ \sum_{i=1}^{n_{rr}} C_i^{rr}\Omega^2 \cos\left(h_i^{rr}\Omega t\right) + W_\theta(\Omega) \\ \sum_{i=1}^{n_{rr}} C_i^{rr}\Omega^2 \sin\left(h_i^{rr}\Omega t\right) + W_\varphi(\Omega) \\ 0 \\ 0 \\ 0 \\ 0 \\ 0 \end{Bmatrix} \qquad \boldsymbol{q}_s = \begin{Bmatrix} x_w \\ y_w \\ z_w \\ \theta_w \\ \varphi_w \\ x_c \\ y_c \\ z_c \\ \theta_c \\ \varphi_c \end{Bmatrix}$$

F2 Flywheel-Base Coupled System

$$\boldsymbol{M}_{ss} = \begin{bmatrix} M_w & 0 & 0 & 0 & 0 & 0 & 0 & 0 & 0 & 0 \\ 0 & M_w & 0 & 0 & 0 & 0 & 0 & 0 & 0 & 0 \\ 0 & 0 & M_w & 0 & 0 & 0 & 0 & 0 & 0 & 0 \\ 0 & 0 & 0 & I_r & 0 & 0 & 0 & 0 & 0 & 0 \\ 0 & 0 & 0 & 0 & I_r & 0 & 0 & 0 & 0 & 0 \\ 0 & 0 & 0 & 0 & 0 & M_b & 0 & 0 & 0 & 0 \\ 0 & 0 & 0 & 0 & 0 & 0 & M_b & 0 & 0 & 0 \\ 0 & 0 & 0 & 0 & 0 & 0 & 0 & M_b & 0 & 0 \\ 0 & 0 & 0 & 0 & 0 & 0 & 0 & 0 & I_{b\_xx} & 0 \\ 0 & 0 & 0 & 0 & 0 & 0 & 0 & 0 & 0 & I_{b\_yy} \end{bmatrix}$$

$$\boldsymbol{G}_{ss} = \begin{bmatrix} 0 & 0 & 0 & 0 & 0 & 0 & 0 & 0 & 0 & 0 \\ 0 & 0 & 0 & 0 & 0 & 0 & 0 & 0 & 0 & 0 \\ 0 & 0 & 0 & 0 & 0 & 0 & 0 & 0 & 0 & 0 \\ 0 & 0 & 0 & 0 & \Omega I_z & 0 & 0 & 0 & 0 & 0 \\ 0 & 0 & 0 & -\Omega I_z & 0 & 0 & 0 & 0 & 0 & 0 \\ 0 & 0 & 0 & 0 & 0 & 0 & 0 & 0 & 0 & 0 \\ 0 & 0 & 0 & 0 & 0 & 0 & 0 & 0 & 0 & 0 \\ 0 & 0 & 0 & 0 & 0 & 0 & 0 & 0 & 0 & 0 \\ 0 & 0 & 0 & 0 & 0 & 0 & 0 & 0 & 0 & 0 \\ 0 & 0 & 0 & 0 & 0 & 0 & 0 & 0 & 0 & 0 \end{bmatrix}$$

$$\boldsymbol{C}_{ss} \approx \begin{bmatrix} c_t & 0 & 0 & 0 & -dc_t & -c_t & 0 & 0 & 0 & -hc_t \\ 0 & c_t & 0 & dc_t & 0 & 0 & -c_t & 0 & hc_t & 0 \\ 0 & 0 & c_z & 0 & 0 & 0 & 0 & -c_z & 0 & 0 \\ 0 & dc_t & 0 & d^2c_t + c_r & 0 & 0 & -dc_t & 0 & hdc_t - c_r & 0 \\ -dc_t & 0 & 0 & 0 & d^2c_t + c_r & dc_t & 0 & 0 & 0 & hdc_t - c_r \\ -c_t & 0 & 0 & 0 & dc_t & c_t & 0 & 0 & 0 & hc_t \\ 0 & -c_t & 0 & -dc_t & 0 & 0 & c_t & 0 & -hc_t & 0 \\ 0 & 0 & -c_z & 0 & 0 & 0 & 0 & c_z & 0 & 0 \\ 0 & hc_t & 0 & hdc_t - c_r & 0 & 0 & -hc_t & 0 & h^2c_t + c_r & 0 \\ -hc_t & 0 & 0 & 0 & hdc_t - c_r & hc_t & 0 & 0 & 0 & h^2c_t + c_r \end{bmatrix}$$

$$
\boldsymbol{K}_{ss} \approx \begin{bmatrix}
k_t & 0 & 0 & 0 & -dk_t & -k_t & 0 & 0 & 0 & -hk_t \\
0 & k_t & 0 & dk_t & 0 & 0 & -k_t & 0 & hk_t & 0 \\
0 & 0 & k_z & 0 & 0 & 0 & 0 & -k_z & 0 & 0 \\
0 & dk_t & 0 & d^2k_t + k_r & 0 & 0 & -dk_t & 0 & hdk_t - k_r & 0 \\
-dk_t & 0 & 0 & 0 & d^2k_t + k_r & dk_t & 0 & 0 & 0 & hdk_t - k_r \\
-k_t & 0 & 0 & 0 & dk_t & k_t & 0 & 0 & 0 & hk_t \\
0 & -k_t & 0 & -dk_t & 0 & 0 & k_t & 0 & -hk_t & 0 \\
0 & 0 & -k_z & 0 & 0 & 0 & 0 & k_z & 0 & 0 \\
0 & hk_t & 0 & hdk_t - k_r & 0 & 0 & -hk_t & 0 & h^2k_t + k_r & 0 \\
-hk_t & 0 & 0 & 0 & hdk_t - k_r & hk_t & 0 & 0 & 0 & h^2k_t + k_r
\end{bmatrix}
$$

$$
\boldsymbol{q}_{ss} = \begin{Bmatrix} x_w \\ y_w \\ z_w \\ \theta_w \\ \varphi_w \\ x_b \\ y_b \\ z_b \\ \theta_b \\ \varphi_b \end{Bmatrix}
$$

F3 Accelerance of Flywheel-Base Coupled System

$$
A_w = \begin{bmatrix}
A_{w11} & A_{w12} & 0 & A_{w14} & A_{w15} & A_{w16} & A_{w17} & 0 & A_{w19} & A_{w110} \\
A_{w21} & A_{w22} & 0 & A_{w24} & A_{w25} & A_{w26} & A_{w27} & 0 & A_{w29} & A_{w210} \\
0 & 0 & A_{w33} & 0 & 0 & 0 & 0 & A_{w38} & 0 & 0 \\
A_{w41} & A_{w42} & 0 & A_{w44} & A_{w45} & A_{w46} & A_{w47} & 0 & A_{w49} & A_{w410} \\
A_{w51} & A_{w52} & 0 & A_{w54} & A_{w55} & A_{w56} & A_{w57} & 0 & A_{w59} & A_{w510} \\
A_{w61} & A_{w62} & 0 & A_{w64} & A_{w65} & A_{w66} & A_{w67} & 0 & A_{w69} & A_{w610} \\
A_{w71} & A_{w72} & 0 & A_{w74} & A_{w75} & A_{w76} & A_{w77} & 0 & A_{w79} & A_{w710} \\
0 & 0 & A_{w83} & 0 & 0 & 0 & 0 & A_{w88} & 0 & 0 \\
A_{w91} & A_{w92} & 0 & A_{w94} & A_{w95} & A_{w96} & A_{w97} & 0 & A_{w99} & A_{w910} \\
A_{w101} & A_{w102} & 0 & A_{w104} & A_{w105} & A_{w106} & A_{w107} & 0 & A_{w109} & A_{w1010}
\end{bmatrix}
$$

WA Base DoFs

Appendix G Alternative Methods to Calculate Wheel Assembly Accelerance

Some alternative methods to calculate the WA driving point dynamic accelerance which are still being developed are presented in this appendix. They are summarized as following:

- With reference to the Eqs. (7.1) to (7.5) in Section 7.1, the relationship between the WA coupled and hard-mounted loads is:

  $$\boldsymbol{f}_c = \boldsymbol{f}_b + \boldsymbol{A}_w^{-1}\ddot{\boldsymbol{x}} \tag{7.1}$$

  If instead we let the WA alone to be suspended in a "free-free" boundary condition and spinning while measurements are taken (where accelerometers can be attached at its base interface), $\boldsymbol{f}_c$ then equals zero in the above equation, i.e. there are no coupled forces, and an expression for $\boldsymbol{f}_b$ can be expressed:

  $$\boldsymbol{f}_b = -\boldsymbol{A}_w^{-1}\ddot{\boldsymbol{x}}_f \tag{G.1}$$

  where subscript *f* indicates the WA is in the "free-free" boundary condition.

  On the other hand, if the WA is mounted on the seismic mass, the WA-induced coupled loads can be directly measured using the methods developed in this thesis, so from the following equation:

  $$\boldsymbol{f}_c = \boldsymbol{A}_s^{-1}\ddot{\boldsymbol{x}}_c \tag{G.2}$$

  Substituting Eqs. (G.1) and (G.2) into Eq. (7.1), the following equation can be derived:

  $$\boldsymbol{A}_s^{-1}\ddot{\boldsymbol{x}}_c = \boldsymbol{A}_w^{-1}\left(\ddot{\boldsymbol{x}}_c - \ddot{\boldsymbol{x}}_f\right) \tag{G.3}$$

where the only unknown in the equation is the WA driving point accelerance, $\boldsymbol{A}_w$.

However, the problem here lies in the inversion of a vector, which mathematically does not have a unique solution.

- If expressing Eq. (7.1) into vector and matrix spectral density form:

$$\boldsymbol{\Phi}_c = \boldsymbol{\Phi}_b + \left[\boldsymbol{A}_w^{-1}\right]\ddot{\boldsymbol{X}}_c\left[\boldsymbol{A}_w^{-1}\right]^H \tag{G.4}$$

Applying the same derivation procedure, the following equation can be obtained:

$$\left[\boldsymbol{A}_s^{-1}\right]\ddot{\boldsymbol{X}}_c\left[\boldsymbol{A}_s^{-1}\right]^H = -\left[\boldsymbol{A}_w^{-1}\right]\left(\ddot{\boldsymbol{X}}_c - \ddot{\boldsymbol{X}}_f\right)\left[\boldsymbol{A}_w^{-1}\right]^H \tag{G.5}$$

where again the only unknown is the WA driving point accelerance, $\boldsymbol{A}_w$, and the problem here lies in the calculation of Hermitian matrix cross-product with the matrix itself as unknowns.

The above two methods require the WA to be measured in a "free-free" boundary condition and coupled with the structure.

- Another method involves using different supporting structure (in our case, the seismic mass with different layers assembled) and the measurements of their coupled microvibrations at their interface. It is introduced as following:

The relationship between the coupled forces and hard-mounted forces for the two measurements (with different layers) can be expressed respectively as:

$$\boldsymbol{\Phi}_{c_1} = \left(\left[\boldsymbol{I} + \boldsymbol{A}_w^{-1}\boldsymbol{A}_{s_1}\right]^{-1}\right)\boldsymbol{\Phi}_b\left(\left[\boldsymbol{I} + \boldsymbol{A}_w^{-1}\boldsymbol{A}_{s_1}\right]^{-1}\right)^H \tag{G.6}$$

$$\boldsymbol{\Phi}_{c_2} = \left(\left[\boldsymbol{I} + \boldsymbol{A}_w^{-1}\boldsymbol{A}_{s_2}\right]^{-1}\right)\boldsymbol{\Phi}_b\left(\left[\boldsymbol{I} + \boldsymbol{A}_w^{-1}\boldsymbol{A}_{s_2}\right]^{-1}\right)^H \tag{G.7}$$

If dividing the two equations, the hard-mounted loads matrix Φ_b is eliminated, thus:

$$\frac{\boldsymbol{\Phi}_{c_1}}{\boldsymbol{\Phi}_{c_2}}=\frac{\left(\left[\boldsymbol{I}+\boldsymbol{A}_w^{-1}\boldsymbol{A}_{s_1}\right]^{-1}\right)\left(\left[\boldsymbol{I}+\boldsymbol{A}_w^{-1}\boldsymbol{A}_{s_1}\right]^{-1}\right)^H}{\left(\left[\boldsymbol{I}+\boldsymbol{A}_w^{-1}\boldsymbol{A}_{s_2}\right]^{-1}\right)\left(\left[\boldsymbol{I}+\boldsymbol{A}_w^{-1}\boldsymbol{A}_{s_2}\right]^{-1}\right)^H} \tag{G.8}$$

Again, the only unknown is the WA driving point accelerance, $\boldsymbol{A}_w$, and the same problem lies in the Hermitian matrix calculation.

Articles Produced by the Author

The content of this thesis has contributed to the following publications and internal technical reports:

Journal Papers

- Zhang, Z., Aglietti, G. S., and Zhou, W. *Microvibrations Induced by a Cantilevered Wheel Assembly with a Soft-Suspension System*, AIAA Journal, Vol. 49, No. 5, 2011, pp. 1067-1079.

- Zhou, W., Aglietti, G. S., and Zhang, Z. *Modelling and Testing of a Soft Suspension Design for a Reaction/momentum Wheel Assembly*, Journal of Sound and Vibration, Vol. 330, No. 18-19, 2011, pp. 4596-4610.

- Zhang, Z., Aglietti, G. S., and Ren, W. *Coupled Microvibration Analysis of a Reaction Wheel Assembly including Gyroscopic Effects in its Accelerance*, accepted by Journal of Sound and Vibration in December 2012.

Conference Papers

- Zhang, Z., Zhou, W., Aglietti, G. S., and Bianchi, G. *Modelling Microvibrations emitted by Satellites Reaction Wheel Assemblies*, The 10th International Conference on Recent Advances in Structural Dynamics (RASD), Southampton, UK, 2010.

- Zhang, Z., Ren, W., and Aglietti, G. S. *Microvibration Modeling, Validation and Coupled Analysis of a Reaction Wheel in Satellite*, The 12th European Conference on Spacecraft Structures, Materials & Environmental Testing (ECSSMET), Noordwijk, the Netherlands, 2012.

- Zhang, Z., Aglietti, G. S., and Le Page, B. H. *Microvibration Modelling and Testing of a Satellite Reaction Wheel Assembly*, The 10th International Conference on Vibrations in Rotating Machinery (VIRM), London, UK, 2012.

- Zhang, Z., Aglietti, G. S., and Ren, W. *Microvibration Model Development and Validation of a Cantilevered Reaction Wheel Assembly*, The 2nd International Conference on Vibration, Structural Engineering and Measurement (ICVSEM), Shanghai, China, 2012.

- Remedia, M., Aglietti, G. S., Zhang, Z., Le Page, B. H., and Richardson, G. *Modeling Methodologies for Microvibration-related Analysis of Spacecraft Structures*, The 12th European Conference on Spacecraft Structures, Materials & Environmental Testing (ECSSMET), Noordwijk, the Netherlands, 2012.

- Remedia, M., Aglietti, G. S., Zhang, Z., Le Page, B. H., and Richardson, G. *A General Methodology to Study the Transmission of Micro-vibrations in Satellites*, The 63rd International Astronautical Congress (IAC), Naples, Italy, 2012.

Internal Technical Report

- Zhang, Z., Remedia, M., Aglietti, G. S., Le Page, B. H., and Richardson, G. *Methodology for Analysis of Structure-Borne Micro-Vibration*. Internal Report for ESA and SSTL joint project, ITT No. AO/1-6135/09/NL/NA, 2011.

EFERENCES

1. Toyoshima, M., and Araki, K. *In-orbit Measurements of Short Term Attitude and Vibrational Environment on the Engineering Test Satellite VI using Laser Communication Equipment*, Optical Engineering, Vol. 40, No. 5, 2001, pp. 827-832.

2. Jono, T., Toyoshima, M., Takahashi, N., Yamawaki, T., Nakagawa, K., and Yamamoto, A. *Laser Tracking Test under Satellite Microvibrational Disturbances by OICETS ATP System*, Acquisition, Tracking, and Pointing XVI, Orlando, FL, USA, 2002.

3. Toyoshima, M., Takayama, Y., Kunimori, H., Jono, T., and Yamakawa, S. *In-orbit Measurements of Spacecraft Microvibrations for Satellite Laser Communication links*, Optical Engineering, Vol. 49, No. 8, 2010, pp. 083604-083604-10.

4. Pavarin, D., Lambert, M., Francesconi, A., Destefanis, R., Bettella, A., Debei, S., de Cecco, M., Faraud, M., Giacomuzzo, C., Marucchi-Chierro, P. C., Parzianello, G., Saggin, B., and Angrilli, F. *Analysis of GOCE's Disturbances Induced by Hypervelocity Impact*, Proceedings of the 4th European Conference on Space Debris, Darmstadt, Germany, 2005.

5. Wacker, T., Weimer, L., and Eckert, K. *GOCE Platform Micro-vibration Verification by Test and Analysis*, European Conference on Spacecraft Structures, Materials & Mechanical Testing, Noordwijk, the Netherlands, 2005.

6. Koekkoek, E., Guénégo, P., and Bureo Dacal, R. *A Realistic Approach in the Prediction of the ACES Micro-gravity Environment*, European Conference on Spacecraft Structures, Materials & Mechanical Testing, Noordwijk, the Netherlands, 2005.

7. Deng, F., He, X., Zhang, J., Li, L., and Dong, X. *Research on the Effects of Microgravity Vibration Enviroment in the Spacelab*, Journal of Vibration and Shock, Vol. 24, No. 3, 2005, pp. 103-107.

8. Zhang, Z., Remedia, M., Aglietti, G. S., Le Page, B. H., and Richardson, G. *Methodology for Analysis of Structure-Borne Micro-Vibration*. Internal Technical Report for ESA and SSTL joint project, ITT No. AO/1-6135/09/NL/NA, 2011.

9. Vaillon, L., Petitjean, B., Frapard, B., and Lebihan , D. *Active Isolation in Space Truss Structures: From Concept to Implementation*, Smart Materials and Structures, Vol. 8, No. 6, 1999.

10. Aglietti, G. S. *Active Control of Microvibrations for Equipment Loaded Spacecraft Panels*, Ph.D thesis, University of Southampton, 1999.

11. Hyde, T. T., Ha, K. Q., Johnston, J. D., Howard, J. M., and Mosier, G. E. *Integrated Modeling Activities for the James Webb Space Telescope: Optical*

Jitter Analysis, SPIE Conference on Astronomical Telescopes and Instrumentation, Glasgow, Scotland, 2004.

12. Oh, C.-S., Lee, W., and Bang, H. *Passive Jitter Isolation for Reaction Wheel of Satellites*, SICE-ICASE International Joint Conference, Busan, Korea, 2006.

13. European Space Agency, European Cooperation for Space Standardization (ESA ECSS), Spacecraft Mechanical Loads Analysis, Chapter 13 Micro-gravity & Micro-vibrations, ECSS-E-HB-32-26, 2012

14. Bialke, B. *Microvibration Disturbance Fundamentals for Rotating Mechanisms*, 34th AAS Annual Guidance and Control Conference, Breckenridge, CO, USA, 2011.

15. Collins, S. A. *Multi-axis Analog Adaptive Feedforward Cancellation of Cryocooler Vibration*, Ph.D thesis, Massachusetts Institute of Technology, 1994.

16. Clapp, B., Sills, J., and Voorhees, C. *Hubble Space Telescope Pointing Performance Due to Micro-Dynamic Disturbances from the NICMOS Cryogenic Cooler* 43rd AIAA/ASME/ASCE/AHS/ASC Structures, Structural Dynamics, and Materials Conference, Denver, Colorado, USA, 2002.

17. Jedrich, N., Zimbelman, D., Turczyn, M., Sills, J., Voorhees, C., and Clapp, B. *Cryo Cooler Induced Micro-Vibration Disturbances to the Hubble Space Telescope*, 5th Cranfield Dynamics and Control of Systems and Structures in Space Conference, Cambridge, UK, 2002.

18. Blaurock, C., Liu, K. C., and Mule, P. *Solar Dynamics Observatory (SDO) HGAS Induced Jitter* 49th AIAA/ASME/ASCE/AHS/ASC Structures, Structural Dynamics, and Materials Conference Schaumburg, IL, USA, 2008.

19. Bourkland, K. L., Liu, K. C., and Blaurock, C. *A Jitter-Mitigating High Gain Antenna Pointing Algorithm for the Solar Dynamics Observatory*, Proceedings of the 20th International Symposium on Space Flight Dynamics, Greenbelt, MD, USA, 2007.

20. Capitanio, R. S., and Stavrinidis, C. *Analysis of Satellite in-orbit Dynamic Disturbances due to Tape Recorder Excitations* 35th AIAA/ASME/ASCE/AHS/ASC Structures, Structural Dynamics, and Materials Conference, Washington, DC, USA, 1994.

21. Bely, P. Y. *The Design and Construction of Large Optical Telescopes*: New York: Springer-Verlag, 2003.

22. Woodard, S. E. *Upper Atomshpere Research Satellite In-Flight Dyamics Study: Lessons Learned*, Journal of Spacecraft and Rockets, Vol. 37, No. 6, 2000, pp. 794-800.

23. Mason, P. A. C., and Starin, S. R. *Propellant Slosh Analysis for the Solar Dynamics Observatory*. Goddard Space Flight Center, 2005.

24. Marsell, B., Gangadharan, S., Chatman, Y., Sudermann, J., Schlee, K., and Ristow, J. *A CFD Approach to Modeling Spacecraft Fuel Slosh* 47th AIAA Aerospace Sciences Meeting including The New Horizons Forum and Aerospace Exposition, Orlando, FL, USA, 2009.

25. Lenahen, B. A., Sances, D. J., and Gangadharan, S. N. *Accurately Correlating Experimental and Computational Spacecraft Fuel Slosh Models Using Diaphragm-Implemented Propellant Tanks* 34th Annual Guidance and Control Conference, Breckenridge, CO, USA, 2011.

26. Ingham, M., Kim, Y., Crawley, E., McManus, H., and Miller, D. *Experimental Characterization of Thermal Creak Response of Deployable Structures*, Journal of Spacecraft and Rockets, Vol. 37, No. 3, 2000.

27. Grillenbeck, A., Deutsch, G., and Pouilloux, B. *Micro-vibration Measurements on Thermally Loaded Multi-layer Insulation Samples*, 10th European Conference on Spacecraft Structures, Materials and Mechanical Testing, in Connection with the 1st CEAS European Air and Space Conference, Berlin, Germany, 2007.

28. Magg, M., and Grillenbeck, A. *Micro-vibration and Centre of Gravity Shift Measurements on Thermally Stressed Thermal-Control Blanket*, Proceedings of the 5th International Symposium on Environmental Testing for Space Programmes, Noordwijk, the Netherlands, 2004.

29. Luhía, C., and A., M. *Sudden Stress Release Tests Performed on GOCE Spacecraft Component Samples*, European Conference on Spacecraft Structures, Materials & Mechanical Testing, Noordwijk, the Netherlands, 2005.

30. Zhang, Z., Yang, L., and Pang, S. *Jitter Environment Analysis for Micro-precision Spacecraft*, Spacecraft Enviroment Engineering, Vol. 26, No. 6, 2009, pp. 528-534.

31. Fujita, T., Hattori, T., Suzuki, Y., Yasuda, M., and Tsuchiya, M. *Study on the Method of Evaluating Microvibration Influence on Spacecraft Gyroscopes*, Nihon Kikai Gakkai Nenji Taikai Koen Ronbunshu, Vol. 2002, No. 6, 2002, pp. 177-178.

32. Bradley, A. J., Connor, C. T., Del Toro, Y., Andersen, G. C., Bely, P. Y., Decker, J., Franz, O. G., Wasserman, L. H., and Van Altena, W. F. *Determination and Characterization of the Hubble Space Telescope Pointing Stability*, Spaceflight dynamics 1993 and the 8th AAS & NASA International Symposium, Greenbelt, MD, USA, 1993.

33. Blair, M. A., and Vadlamudi, N. *Jitter Performance Test for the Hubble Space Telescope - Method and Results*, 6th International Modal Analysis Conference, Kissimmee, FL, USA, 1988.

34. Bely, P. Y., Lupie, O. L., and Hershey, J. L. *The Line-of-sight Jitter of the Hubble Space Telescope*, Space Astronomical Telescopes and Instruments II, Orlando, FL, USA, 1993.

35. Wittig, M. E., van Holtz, L., Tunbridge, D. E. L., and Vermeulen, H. C. *In-orbit Measurements of Microaccelerations of ESA's Communication Satellite OLYMPUS*, Free-Space Laser Communication Technologies II Los Angeles, CA, USA, 1990.

36. Dyne, S., Collins, P., and Tunbridge, D. *Satellite Mechanical Health Monitoring*, IEE Colloquium on Advanced Vibration Measurements, Techniques and Instrumentation for the Early Prediction of Failure, London, UK, 1992.

37. Wittig, M. E. *The Use of In-orbit Measurements of Microaccelerations of ESA's Communication Satellite OLYMPUS for the Optimization of the Tracking Control Loop of an Optical Communication Payload*, 18th International Symposium on Space Technology and Science, Kagoshima, Japan, 1992.

38. Tunbridge, D. *The Olympus PAX, Measurement of Mechanism induced Vibration*, 5th European Space Mechanisms and Tribology Symposium, Paris, France, 1993.

39. Dyne, S. J. C., Tunbridge, D. E. L., and Collins, P. P. *The Vibration Environment on a Satellite in Orbit*, IEE Colloquium on High Accuracy Platform Control in Space, London, UK, 1993.

40. de Gaujac, A. C., Monteil, D., and Bousquet, C. *In Orbit Microvibration Test on SPOT 1 Satellite - Experimental Principle and Results*, Proc. 1st ESA International Conference on Spacecraft Guidance, Navigation and Control Systems, Noordwijk, the Netherlands, 1991.

41. Betermier, J. M., Charmeau, M. C., Jourdon, N., and Guillaud, V. *Microvibration Tests on Satellites - Lessons Learned from the SPOT 3 Experiment*, Proceedings of the 1st International Symposium on Space Microdynamics and Accurate Control, Nice, France, 1992.

42. Marucchi-Chierro, P. C., and Galeazzi, C. *The Microvibration Environment on ARTEMIS : A Strategy for Its Characterization and Control*, 46th International Astronautical Congress, Oslo, Norway, 1995.

43. Marucchi-Chierro, P. C., Balestra, L., and Galeazzi, C. *ARTEMIS Microvibration Environment: Verification Strategy and Test Methodologies*, 16th Aerospace Testing Seminar, Manhattan Beach, CA, USA, 1996.

44. Marchante, E. M., and Munoz, L. *ARTEMIS Satellite Microvibrations Testing and Analysis Activities*, Proceedings of the 48th International Astronautical Congress, Torino, Italy, 1997.

45. Ullio, R., and Marta, F. *ARTEMIS Micro-Vibration Environment Prediction*, European Conference on Spacecraft Structures, Materials & Mechanical Testing, Braunschweig, Germany, 1998.

46. Sevilla, M. L. *Microvibration Tests of the ARTEMIS Structural Model*, European Conference on Spacecraft Structures, Materials & Mechanical Testing, Braunschweig, Germany, 1999.

47. Laurens, P., P., F., Collados, E., Capitaine, A., and Desplats, E. *Line-of-sight Jitter of SILEX Optical Terminals, Analysis and Verification Activities*, Proceedings of the 3rd International Conference on the Dynamics and Control of Structures in Space, Cranfield, UK, 1996.

48. Le Duigou, J. M. *Microvibration Measurements on Spot 4, Results of the Micromedy Experiment*, European Conference on Spacecraft Structures, Materials & Mechanical Testing, Braunschweig, Germany, 1998.

49. Privat, M. *On Ground and in Orbit Microvibrations Measurement Comparison*, Space Mechanisms and Tribology, Proceedings of the 8th European Symposium, Toulouse, France, 1999.

50. Sudey, J. J., Dellinger, W., and Hagopian, M. *On-orbit Jitter Performance of the GOES Spacecraft and Instruments*, Proceedings of GOES-8 and Beyond Denver, CO, USA, 1996.

51. Laurens, P., Decoux, E., and Janvier, M. *SOHO Microvibrations: Analyses, Tests and Flight Results*, Spacecraft Guidance, Navigation and Control Systems, Proceedings of the 3rd ESA International Conference, Noordwijk, the Netherlands, 1997.

52. Remedia, M., Aglietti, G. S., Zhang, Z., Le Page, B. H., and Richardson, G. *Modeling Methodologies for Microvibration-related Analysis of Spacecraft Structures*, 12th European Conference on Spacecraft Structures, Materials & Environmental Testing (ECSSMET), Noordwijk, the Netherlands, 2012.

53. Remedia, M., and Aglietti, G. S. *Modeling Micro-vibrations Transmission in Spacecraft Structures*, 62rd International Astronautical Congress (IAC), Cape Town, South Africa, 2011.

54. Remedia, M., Aglietti, G. S., Zhang, Z., Le Page, B. H., and Richardson, G. *A General Methodology to Study the Transmission of Micro-vibrations in Satellites*, 63rd International Astronautical Congress (IAC), Naples, Italy, 2012.

55. Toyoshima, M., Jono, T., Takahashi, N., Yamawaki, T., Nakagawa, K., and Arai, K. *Transfer Functions of Microvibrational Disturbances on a Satellite*, 21st International Communications Satellite Systems Conference and Exhibit, Yokohama, Japan, 2003.

56. Shi, S. *Study on High Precision Attitude Control Systems of Foreign Earth-Observation Satellites*, Aerospace Shanghai, No. 6, 2000, pp. 49-53.

57. Takahara, O., Ichimoto, K., Kosugi, T., Shimada, S., and Yoshida, N. *Evaluation of Pointing Error for SOLAR-B Using Optical Measurement*, Uchu Kagaku Gijutsu Rengo Koenkai Koenshu, Vol. 50, 2006, pp. 271-275.

58. Yoshida, N., Takahara, O., Kosugi, T., Ninomiya, K., Hashimoto, T., Minesugi, K., Tsuneta, S., Ichimoto, K., and Shimada, S. *Systematic Approach to Achieve Fine Pointing Requirement of Solar-B*, 16th Symposium on Automatic Control in Aerospace, St. Petersburg, Russia, 2004.

59. Yoshida, N., Ichimoto, K., Kosugi, T., Ninomiya, K., Hashimoto, T., Minesugi, K., Shimada, S., and Saito, H. *System Technology for the Achievement of Ultra-High Pointing Accuracy of Solar-B*, Proceedings of the Space Sciences and Technology Conference, Japan, 2001.

60. Liu, K. C., Kenney, T., Maghami, P., Mule, P., Blaurock, C., and Haile, W. B. *Jitter Test Program and On-Orbit Mitigation Strategies for Solar Dynamic Observatory*, Proceedings of the 20th International Symposium on Space Flight Dynamics, Greenbelt, MD, USA, 2007.

61. Liu, K. C., Maghami, P., and Blaurock, C. *Reaction Wheel Disturbance Modeling, Jitter Analysis, and Validation Tests for Solar Dynamics Observatory* AIAA Guidance, Navigation and Control Conference and Exhibit, Honolulu, Hawaii, USA, 2008.

62. Katsukawa, Y., Masada, Y., Shimizu, T., Sakai, S., and Ichimoto, K. *Pointing Stability of Hinode and Requirements for the Next Solar Mission Solar-C*, International Conference on Space Optics, Rhodes, Greece, 2010.

63. Meza, L., Tung, F., Anandakrishnan, S., Spector, V., and Hyde, T. *Line of Sight Stabilization of James Webb Space Telescope*, 27th Annual AAS Guidance and Control Conference, Breckenridge, CO, USA, 2005.

64. Nella, J., Atcheson, P. D., Atkinson, C. B., Au, D., Bronowicki, A. J., Bujanda, E., Cohen, A., Davies, D., Lightsey, P. A., Lynch, R., Lundquist, R., Menzel, M. T., Mohan, M., Pohner, J., Reynolds, P., Rivera, H., Texter, S. C., Shuckstes, D. V., Simmons, D. D. F., Smith, R. C., Sullivan, P. C., Waldie, D. D., and Woods, R. *James Webb Space Telescope (JWST) Observatory architecture and performance*, Optical, Infrared, and Millimeter Space Telescopes, Glasgow, United Kingdom, 2004.

65. Tanguy, P., Spalinger, E., Sghedoni, M., and Guichon, D. *MTG Microvibration Requirements and Associated Potential Impact on the Satellite Design*, 34th Annual Guidance and Control Conference, Breckenridge, CO, USA, 2011.

66. Li, Y.-Y., Hamlin, L. A., Wirz, R., Adams, D., Moore, G., Coppolino, R., Peng, C.-Y., and Levine, M. *Dynamic Simulations for the Terrestrial Planet Finder Interferometer*, UV/Optical/IR Space Telescopes: Innovative Technologies and Concepts II, San Diego, CA, USA, 2005.

67. LoBosco, D. M., Blaurock, C., Chung, S.-J., and Miller, D. W. *Integrated Modeling of Optical Performance for the Terrestrial Planet Finder Structurally Connected Interferometer*, Modeling and Systems Engineering for Astronomy Glasgow, United Kingdom, 2004.

68. Miller, D. W., de Weck, O. L., Uebelhart, S. A., Grogan, R., and Basdogan, I. *Integrated Dynamics and Controls Modeling for the Space Interferometry Mission (SIM)*, IEEE Proceedings of Aerospace Conference, Big Sky, MT, USA, 2001.

69. Neat, G. W. *The Micro-arcsecond Measurement Testbed and its Relationship to the Space Interferometer Mission*, Interferometry in Space, Waikoloa, HI, USA, 2003.

70. Grogan, R. L., and Laskin, R. A. *On Multidisciplinary Modeling of the Space Interferometry Mission*, Proceedings of the American Control Conference, Philadelphia, PA, USA, 1998.

71. de Weck, O. L., Miller, D. W., and Mosier, G. E. *Multidisciplinary Analysis of the NEXUS Precursor Space Telescope*, Highly Innovative Space Telescope Concepts Waikoloa, HI, USA, 2002.

72. LoBosco, D. M., and Miller, D. W. *Integrated Modeling of Optical Performance for the Terrestrial Planet Finder Structurally Connected Interferometer*, M.Sci. thesis, Massachusetts Institute of Technology, 2004.

73. Briggs, H. C., Phillips, C. J., and Orzewalla, M. A. *Integrated Modeling of Advanced Opto-mechanical Systems*, 47th AIAA/ASME/ASCE/AHS/ASC Structures, Structural Dynamics, and Materials Conference, Newport, RI, USA, 2006.

74. Basdogan, I., Elias, L. M., Dekens, F., and Sievers, L. *Predicting the Optical Performance of the Space Interferometry Mission using a Modeling, Testing, and Validation*, Journal of Vibration and Acoustics, Vol. 129, No. 2, 2007, pp. 148-157.

75. Uebelhart, S. A., and Miller, D. A. *Conditioning, Reduction, and Disturbance Analysis of Large Order Integrated Models for Space-Based Telescopes*, M.Sc. thesis, Massachusetts Institute of Technology, 2001.

76. Pittelkau, M. E. *Pointing Error Definitions, Metrics, and Algorithms*, AAS/AIAA Astrodynamics Specialists Conference, Big Sky, MT, USA, 2003.

77. Fausz, J., Wilson, B., Hall, C., Richie, D., Lappas, V., Wie, B., and Tsiotras, P. *Survey of Technology Developments in Flywheel Attitude Control and Energy Storage Systems*, Journal of Guidance, Control, and Dynamics, Vol. 32, No. 2, 2009, pp. 354-365.

78. Zhang, Z., Aglietti, G. S., and Le Page, B. H. *Microvibration Modelling and Testing of a Satellite Reaction Wheel Assembly*, 10th International Conference on Vibrations in Rotating Machinery (VIRM10), London, UK, 2012.

79. Zhang, Z., Zhou, W., Aglietti, G. S., and Bianchi, G. *Modelling Microvibrations emitted by Satellites Reaction Wheel Assemblies*, 10th International Conference on Recent Advances in Structural Dynamics (RASD 2010), Southampton, UK, 2010.

80. Zhang, Z., Aglietti, G. S., and Zhou, W. *Microvibrations Induced by a Cantilevered Wheel Assembly with a Soft-Suspension System*, AIAA Journal, Vol. 49, No. 5, 2011, pp. 1067-1079.

81. Zhou, W., Aglietti, G. S., and Zhang, Z. *Modelling and Testing of a Soft Suspension Design for a Reaction/momentum Wheel Assembly*, Journal of Sound and Vibration, Vol. 330, No. 18-19, 2011, pp. 4596-4610.

82. Zhang, Z., Ren, W., and Aglietti, G. S. *Microvibration Modeling, Validation and Coupled Analysis of a Reaction Wheel in Satellite*, 12th European Conference on Spacecraft Structures, Materials & Environmental Testing (ECSSMET), Noordwijk, the Netherlands, 2012.

83. Zhang, Z., Aglietti, G. S., and Ren, W. *Microvibration Model Development and Validation of a Cantilevered Reaction Wheel Assembly*, International Conference on Vibration, Structural Engineering and Measurement (ICVSEM 2012), Shanghai, China, 2012.

84. Zhang, Z., Aglietti, G. S., and Ren, W. *Coupled Microvibration Analysis of a Reaction Wheel Assembly including Gyroscopic Effects in its Accelerance*, submitted to Journal of Sound and Vibration in August 2012.

85. Fortescue, P., Stark, J., and Swind, G. *Spacecraft Systems Engineering*: Chichester: John Wiley & Sons Ltd., 2003.

86. Stromswold, E., and Bialke, B. *Behavior of Reaction Wheels Near Zero Speed*, Proceedings of the Annual AAS Guidance and Control Conference, Breckenridge, CO, USA, 2004.

87. Varatharajoo, R., and Fasoulas, S. *Methodology for the Development of Combined Energy and Attitude Control Systems for Satellites*, Aerospace Science and Technology, Vol. 6, No. 4, 2002, pp. 303-311.

88. Varatharajoo, R., and Fasoulas, S. *The Combined Energy and Attitude Control System for Small Satellites—Earth Observation Missions*, Acta Astronautica, Vol. 56, No. 1–2, 2005, pp. 251-259.

89. Lappas, V., Wie, B., Schaub, H., and Peck, M. *Robust Control Moment Gyroscope Steering Logic with Gimbal Angle Constraints*, Journal of Guidance, Control, and Dynamics, Vol. 32, No. 5, 2009, pp. 1662-1666.

90. Wang, Q., and Hu, G. *Analysis of Flywheel Disturbance and Measuring Technology*, Chinese Journal of Space Science, Vol. 29, No. 1, 2009, pp. 39-44.

91. Muszynska, A. *Rotordynamics*: CRC Press, 2005.

92. Genta, G. *Dynamics of Rotating Systems*: Springer Science + Business Media, Inc., 2005.

93. *An Evaluation of Reaction Wheel emitted Vibrations for Large Space Telescope*. NASA Technical Report N76-18213, NASA/Marshall Space Flight Center, 1976.

94. Bosgra, J. A., and Prins, J. J. M. *Testing and Investigation of Reaction Wheels*, 9th Symposium on Automatic Control in Space, 1982.

95. Hasha, M. D. *Reaction Wheel Mechanical Noise Variations*, *Space Telescope Program Engineering Memo SSS 218*. 1986.

96. Melody, J. W. *Discrete-frequency and Broadband Reaction Wheel Disturbance Models*. JPL Interoffce Memo #3411-95-200csi (Internal Document), 1995.

97. Bialke, B. *Microvibration Disturbance Sources in Reaction Wheels and Momentum Wheels*, European Conference on Spacecraft Structures, Materials & Mechanical Testing, Noordwijk, the Netherlands, 1996.

98. Bialke, B. *A Compilation of Reaction Wheel induced Spacecraft Disturbances*, 20th Annual American Aeronautical Society Guidance and Control Conference, 1997.

99. Bialke, B. *High Fidelity Mathematical Modeling of Reaction Wheel Performance*, Proceedings of the Annual AAS Guidance and Control Conference, Breckenridge, CO, USA, 1998.

100. Laurens, P., and Decoux, E. *Understanding and Monitoring Space Mechanisms through their Microdynamic Signature*, The 7th European Space Mechanisms and Tribology Symposium, Noordwijk, the Netherlands, 1997.

101. Laurens, P., and Decoux, E. *Microdynamic Behaviour of Momentum and Reaction Wheels*, Proceedings of the Second Space Microdynamics and Accurate Symposium, Toulouse, Fracne, 1997.

102. Laurens, P., Dupuis, P. E., Phillips, N., and Kugel, U. *Noise Identification Models and Benchmark Testing of Mechanisms*, Proceedings of the 2nd Space Microdynamics and Accurate Control Symposium, Toulouse, France, 1997.

103. Dupuis, P. E., Bugeat, L. P., Privat, M., and Borrien, A. *Industrialisation of a Microdynamics Test Bench*, Conference on Spacecraft Structures, Materials & Mechanical Testing, Noordwijk, the Netherlands, 1996.

104. Galeazzi, C., Marucchi-Chierro, P. C., and Holtz, L. V. *Experimental Activitis on ARTEMIS for the Microvibration Verification*, Proc. Conference on Spacecraft Structures, Materials & Mechanical Testing, Noordwijk, the Netherlands, 1996.

105. Martin, G. *Portable Microvibration Test Facility for Spacecrafts*, 20th Space Simulation Conference: The Changing Testing Paradigm, Annapolis, MD, USA, 1998.

106. Oh, H.-S., Kwon, J.-W., Lee, H., Nam, M.-R., and Park, D.-J. *Torque and Force Measurement of a Prototype HAU Reaction Wheel and the Effect of Disturbance on the Attitude Stability of Spacecraft*, Journal of Mechanical Science and Technology, Vol. 15, No. 6, 2001, pp. 743-751.

107. Collins, P. *Important Factors in Microvibration Testing*, Proc. Conference on Spacecraft Structures, Materials & Mechanical Testing, Noordwijk, the Netherlands, 1996.

108. Santiago-Prowald, J., Oz-Sevilla, L. M., Reina-Barragán, F. J., and Sanz-Andrés, Á. *Calibration of Accelerometers for the Measurement of Microvibrations*, Journal of Spacecraft and Rockets, Vol. 35, No. 5, 1998, pp. 695-702.

109. Monteil, D., Guillaud, V., and Laurens, P. *Mastering the Effect of Microvibrations on the Performances of Reconnaissance Satellites*, AGARD Flight Vehicle Integration Panel Symposium on "Space Systems Design and Development Testing, Cannes, France, 1994.

110. Taniwaki, S., and Ohkami, Y. *Experimental and Numerical Analysis of Reaction Wheel Disturbances*, JSME International Journal Series C Mechanical Systems, Machine Elements and Manufacturing, Vol. 46, No. 2, 2003, pp. 519-526.

111. Taniwaki, S., Hatsutori, Y., and Ohkami, Y. *Development of Lower Frequency Disturbance Detector for Reaction Wheel Analysis*, ASME Internal Mechanical Engineering Congress and Exposition, Orlando, FL, USA, 2005.

112. Taniwaki, S., Kudo, M., Sato, M., and Ohkami, Y. *Analysis of Retainer Induced Disturbances of Reaction Wheel*, Journal of System Design and Dynamics, Vol. 1, No. 2, 2007, pp. 307-317.

113. Taniwaki, S., and Kanazawa, T. *Sensing of Micro Noise Caused by Satellite Fly-Wheel Using Air Floating Disturbance Detector*, INTER-MAC Joint Technical Conference, Tokyo, Japan, 2001.

114. Heimel, H. *Spacewheel Microvibration - Sources, Appearance, Countermeasures*, 8th International ESA Conference on Guidance & Navigation Control Systems, Karlovy Vary, Czech Republic, 2011.

115. Bo, L., Goddu, G., and Mo-Yuen, C. *Detection of Common Motor Bearing Faults using Frequency-domain Vibration Signals and a Neural Network Based Approach*, Proceedings of American Control Conference, Philadelphia, PA, USA, 1998.

116. Carpine, A. *Microvibrations Dynamic Perturbation Predictions of Motor or Complex Mechanism Excitations*, Spacecraft structures, materials and mechanical testing, Proceedings of a European Conference, Braunschweig, Germany, 1999.

117. Hightower, R. A., and Bailey, D. *Ball Bearing Vibrations Amplitude Modeling and Test Comparisons*, The 29th Aerospace Mechanisms Symposium, Johnson Space Center, Houston, TX, USA, 1995.

118. Le, M. P., van der Heide, E., Seiler, R., and Cottaar, E. J. E. *Detection and Diagnosis of Ball Bearing Imperfections in Reaction Wheels by Micro-vibration Test*, 12th European Conference on Spacecraft Structures, Materials and Enviroment Testing, Noordwijk, the Netherlands, 2012.

119. Wagner, M., Airey, S., Piret, G., and Le, P. *European Space Agency - ESA New Reaction Wheel Characterisation Test Facility (RCF)*, 35th Annual AAS Guidance and Control Conference, Breckenridge, CO, USA, 2012.

120. de Weck, O. L., and Miller, D. W. *Integrated Modeling and Dynamics Simulation for the Next Generation Space Telescope*, M.Sc. thesis, Massachusetts Institute of Technology, 1999.

121. Masterson, R. A., Miller, D. W., and Grogan, R. L. *Development and Validation of Reaction Wheel Disturbance Models: Empirical Model*, Journal of Sound and Vibration, Vol. 249, No. 3, 2002, pp. 575-598.

122. Masterson, R. A., Miller, D. W., and Grogan, R. L. *Development of Empirical and Analytical Reaction Wheel Disturbance Models*, Structures, Structural Dynamics and Materials Conference, St. Louis, MO, USA, 1999.

123. Oh, S.-H., and Rhee, S.-W. *Micro-Vibration Measurement, Analysis and Attenuation Techniques of Reaction Wheel Assembly in Satellite*, Journal of the Korean Society for Aeronautical & Space Sciences, Vol. 30, No. 8, 2002, pp. 126-132.

124. Li, L., and Dai, J. *Inner Disturbance Modelling and Simulation Analysis of Reaction Wheel System*, Journal of System Simulation, Vol. 17, No. 8, 2005, pp. 1855-1863.

125. Oh, H.-S., and Cheon, D.-I. *Precision Measurements of Reaction Wheel Disturbances with Frequency Compensation Process*, Journal of Mechanical Science and Technology, Vol. 19, No. 1, 2005, pp. 136-143.

126. Cheon, D.-I., Lee, H.-H., and Oh, H.-S. *Three Dimensional Measurements and Parameter Identification of Force and Torque Distmbances of High Speed Rotating Actuators*, Transactions of the Korean society of Mechanical Engineers, Vol. 31, No. 4, 2007, pp. 409-416.

127. Sun, J., and Zhao, Y. *Model Reaction Wheel Assembly and Research of Parameters Identification Method*, System Simulation Technology & Application, Vol. 7, 2005, pp. 64-69.

128. Sun, J., Zhao, Y., and Tian, H. *Identification Method to Improve Disturbance Model Parameters of Reaction Wheel*, Chinese Journal of Aeronautics, Vol. 26, No. 1, 2006, pp. 70-74.

129. Sun, J., Zhao, Y., and Wang, B. *Development of Precise Disturbance Model of Reaction Wheel Assembly on a Spacecraft*, Journal of Harbin Institute of Technology, Vol. 38, No. 4, 2006, pp. 520-522.

130. Zhao, Y., Sun, J., and Tian, H. *Development of methods identifying parameters in reaction wheel assembly disturbance model*, Aircraft Engineering and Aerospace Technology, Vol. 78, No. 4, 2006, pp. 326-330.

131. Kim, D.-K., Oh, S.-H., Yong, K.-L., and Yang, K.-H. *Numerical Study on a Reaction Wheel and Wheel-Disturbance Modeling*, Journal of the Korean Society for Aeronautical & Space Sciences, Vol. 38, No. 7, 2010, pp. 702-708.

132. Shin, Y.-H., Heo, Y.-H., Oh, S.-H., Kim, D.-K., Kim, K.-J., and Yong, K.-L. *Identification of Input Force for Reaction Wheel of Satellite by Measured Action*

Forceon Decelerating, Transactions of the Korean society for noise and vibration engineering, Vol. 20, No. 3, 2010, pp. 263-271.

133. Zhang, P., Cheng, W., Wang, H., and Zhao, Y. *Disturbance Modelling and Parameters Identification of Reaction Wheel Assembly on Spacecraft*, Journal of Beijing University of Aeronautics and Astronautics, 2010.

134. Zhou, W., Li, D., Luo, Q., and Liu, K. *Analysis and Testing of Microvibrations Produced by Momentum Wheel Assemblies*, Chinese Journal of Aeronautics, Vol. 25, No. 4, 2012, pp. 640-649.

135. Blaurock, C. *Method and System for Extracting a Model of Disturbances Induced by Rotating Mechanisms*. USA, 2009.

136. Ponslet, E. *System Level Modeling of the SNAP Instrument and Analysis of Reaction-Wheel-Induced Jitter*. NASA Internal Report, 2000.

137. Seiler, R., and Allegranza, C. *Mechanism Noise Signatures: Identification and Modelling*, 14th European Space Mechanisms and Tribology Symposium, Vienna, Austria, 2009.

138. Masterson, R. A., and Miller, D. W. *Development and Validation of Empirical and Analytical Reaction Wheel Disturbance Models*, M.Sc. thesis, Massachusetts Institute of Technology, 1999.

139. Elias, L. M., and Miller, D. W. *A Structurally Coupled Disturbance Analysis Method Using Dynamic Mass Measurement Techniques with Application to Spacecraft Reaction Wheel Systems*, Ph.D thesis, Massachusetts Institute of Technology, 2001.

140. Elias, L. M., and Miller, D. W. *A Coupled Disturbance Analysis Method using Dynamic Mass Measurement Techniques*, 43rd AIAA/ASME/ASCE/AHS/ASC Structures, Structural Dynamics, and Materials Conference, Denver, CO, USA, 2002.

141. Elias, L. M., Dekens, F. G., Basdogan, I., Sievers, L. A., and Neville, T. *A Methodology for Modeling the Mechanical Interaction between a Reaction Wheel and a Flexible Structure*, Interferometry in Space, Waikoloa, HI, USA, 2003.

142. Elias, L. M., and Miller, D. W. *Dynamics of Multi-Body Space Interferometers Including Reaction Wheel Gyroscopic Stiffening Effects: Structurally Connected and Electromagnetic Formation Flying Architectures*, Ph.D thesis, Massachusetts Institute of Technology, 2004.

143. Zhao, Y., Zhang, P., and Cheng, W. *Measurement and Study of Disturbance Characteristics of Reaction Wheel Assembly* Journal of Experimental Mechanics, Vol. 24, No. 6, 2009, pp. 532-538.

144. Narayan, S. S., Nair, P. S., and Ghosal, A. *Dynamic Interaction of Rotating Momentum Wheels with Spacecraft Elements*, Journal of Sound and Vibration, Vol. 315, No. 4-5, 2008, pp. 970-984.